Experimental and theoretical investigation of semiconductor optical amplifier (SOA) based all-optical switches

Nielsen, Mads Lønstrup; Dittmann, Lars; Clausen, Anders; Mørk, Jesper

Publication date:
2004

Document Version
Publisher's PDF, also known as Version of record

Experimental and Theoretical investigation of Semiconductor Optical Amplifier (SOA) based All-Optical Switches

Mads Lønstrup Nielsen

April 2004

Research Center COM
Technical University of Denmark

Acknowledgements

I would like to start out by thanking my advisors Lars Dittmann, Anders Clausen, and Jesper Mørk. Lars for providing a great social atmosphere, and allowing me to pursue my interest in optics in the Networks Group, Anders for good collaboration with the Systems area, and Jesper for invaluable inspiration and theoretical assistance.

In addition, a great number of former and current colleagues at COM are thanked for joint efforts in the lab, for solving computer-related problems (including fejl 40), helpful scientific discussions, and all the non-scientific stuff that made all it worth the effort. In particular, I would like to thank Tina Fjelde, David Wolfson, Allan Kloch, Leif Oxenlöwe, Henrik N. Poulsen, Anders Clausen, Tommy Berg, Kresten Yvind, Christophe Peucheret, Jakob Buron, Henning Christiansen, Jørn Hedegaard Poulsen, Michael Berger, Henrik Christiansen, Martin Nordal Petersen and Martin "Havrenakke" Nord.

Alcatel Research and Innovation are acknowledged for supplying state-of-the-art devices for the experiments, and in particular I would like to thank Beatrice Dagens and Bruno Lavigne for a good collaboration during my three visits to Marcoussis.

Moreover, I am grateful to Allan Kloch for boosting my self esteem every weekend on the squash court, and to Dolkene & Co. for the good life.

Last, but not least, I am indebted to Rikke for putting up with me, and taking care of me, during the last four months.

Kgs. Lyngby, 14/4/2004 Mads Lønstrup Nielsen

List of Abbreviations

1R (regeneration)	Re-amplification
2R (regeneration)	1R + Re-shaping
3R (regeneration)	2R + Re-timing
FD-BPM	Finite-Difference Beam Propagation Model
A.O.	Acousto-optic
A/N	Any Number
A-P	Active-Passive
A-A	All-Active
AM	Amplitude Modulation
AMZI/AMZ	Asymmetric MZI
ASE	Amplified Spontaneous Emission
BER	Bit Error-Rate
BERT	Bit Error-Rate Test Set
BPF	Band-Pass Filter
BRF	Birefringent Fiber
BRS	Buried Ridge Structure
CDR	Carrier Density Response
CH	Carrier Heating
CLK	Clock
CMR	Carrier-to-Modulation Ratio
CR	Contrast Ratio
CW	Continuous Wave
DCF	Dispersion Compensating Fiber
DEMUX	Demultiplexing / Demultiplexer
DFB	Distributed FeedBack
DFF	Decision Flip-Flop
DFG	Difference Frequency Generation
DISC	Delayed-Interference Signal Converter
DM	Differential-Mode / Dual-Mode
DOMO	Dual-Order MOde
DPSK	Differential Phase Shift Keying
DSF	Dispersion Compensating Fiber
DUT	Device Under Test

EAM	Electro-Absorption Modulator
ECL	External Cavity Laser
EDFA	Erbium-Doped Fiber Amplifier
EIM	Effective Index Method
EO	Electro-Optic
EPC	Equivalent Photo Current
ER	Extinction Ratio
ESA	Electrical Spectrum Analyzer
FBG	Fiber Bragg Grating
FEC	Forward Error Correction
FFT-BPM	Fast Fourier Transform Beam Propagation Model
FM	Frequency Modulation
FSR	Free Spectral Range
FWHM	Full Width at Half Maximum
FWM	Four Wave Mixing
GPIB	General Purpose Interface Bus
GS-DFB	Gain Switched DFB (laser)
IP	In-Phase
IPDR	Input Power Dynamic Range
IWC	Interferometric Wavelength Converter
LCM	Least Common Multiple
MEMS	Micro Electro Mechanical Systems
MI	Michelson Interferometer
ML-FRL	Mode-Locked Fiber Ring Laser
MLL	Mode-Locked Laser
MMI	Multi-Mode Interference
MP	Mark Patterning
MUX	Multiplexing / Multiplexer
MZI	Mach-Zehnder Interferometer
NLE	Non-Linear Element
NLF	NonLinear Fiber
NOLM	Nonlinear Optical Loop Mirror
NRZ	Non Return-to-Zero
OCS	Optical Circuit Switching
OE	Opto-Electronic
OOP	Out-Of-Phase
OPC	Optical Phase Conjugator
OPS	Optical Packet Switching
OSA	Optical Spectrum Analyzer
OSNR	Optical Signal-to-Noise-Ratio
OTDM	Optical Time Division Multiplexing
OXC	Optical Cross Connect
P.C.	Polarization Controller

P.D.	Photo Diode
PBS	Polarization Beam Splitter
PCF	Photonic Crystal Fiber
PD-EAM	Photo Diode Electro-Absorption Modulator
Pdf	Probability Density Function
PMD	Polarization Mode Dispersion
PD-MZI	Polarization Discriminating Mach-Zehnder Interferometer
PLC	Planar Lightwave Circuit
PLL	Phase-Locked Loop
PM	Phase Modulation / Polarization Maintaining
PPG	Pulse Pattern Generator
PPLN	Periodically Poled Lithium Niobate
PPM	Pulse Position Modulation
PRBS	Pseudo-Random Bit Sequence
PRZ	Pseudo Return-to-Zero
RF	Radio Frequency
Rx	Receiver
RZ	Return-to-Zero
SE	Spontaneous Emission
SHB	Spectral Hole Burning
SI	Sagnac Interferometer
SLALOM	Semiconductor Laser Amplifier Loop Mirror
SM	Standard-Mode / Single-Mode
SMF	Single Mode Fiber
SM-MZI	Standard-Mode MZI
SM-XPM	Standard-Mode Cross-Phase Modulation
SOA	Semiconductor Optical Amplifier
SPM	Self-Phase Modulation
SRS	Stimulated Raman Scattering
SSFR	Small-Signal Frequency Response
StC	Sideband-to-Carrier
SVEA	Slowly Varying Envelope Approximation
TOAD	TeraHertz Optical Asymmetric Demultiplexer
TOF	Time Of Flight
Tx	Transmitter
TW-EAM	Traveling Wave Electro Absorption Modulator
UNI	Ultra-fast Nonlinear Interferometer
UTC-PD	Uni-Traveling-Carrier Photo Diode
WDM	Wavelength Division Multiplexing
XAM	Cross-Absorption Modulation
XGM	Cross-Gain Modulation
XOR	Exclusive OR
XPM	Cross-Phase Modulation

Abstract

This thesis analyzes semiconductor optical amplifier (SOA) based all-optical switches experimentally and through numerical simulations. These devices are candidates for optical signal processing functionalities such as wavelength conversion, regeneration, and logic processing in future transparent optical networks.

The factors governing the modulation bandwidth of SOAs are determined, and schemes for reducing detrimental patterning effects are discussed. Three types of SOA-based switches are investigated numerically: so-called standard-mode and differential-mode switches, and the filtering assisted switch. Differential -mode switches are shown to eliminate one contribution to the patterning effects, referred to as the *linear patterning*. This enables operation at bitrates far beyond the limit set by the carrier lifetime, but ultimately a saturation-induced patterning effect, *nonlinear patterning*, is found to limit the performance. Two implementations of differential-mode switches, the Mach-Zehnder interferometer (MZI) and the delayed-interferometer signal converter (DISC), are compared at bitrates up to 160 Gb/s, and fundamental differences in terms of noise filtering are demonstrated.

The DISC, consisting of an SOA and an asymmetric MZI filter, is analyzed in the small-signal regime, and the obtainable modulation bandwidth is expressed analytically. A new optical spectrum approach to small-signal analysis is introduced, and is used to assess the bandwidth enhancing effect of different optical filters, as well the impact of the filter phase response. Experiments at 40 Gb/s verify the predictions of the small-signal analysis.

Wavelength conversion is demonstrated experimentally at 40 Gb/s using a simple filtering-assisted scheme with an ultra-low optical switching energy, and up to 80 Gb/s employing MZIs operated in the standard-mode, also assisted by bandwidth enhancing filtering.

The impact of 2R regeneration (re-amplification and re-shaping) is explained through simulations, and demonstrated using MZIs at 10 Gb/s. In addition, the 2R regenerative capability of a novel all-active $2x2$ coupler is verified, also at 10 Gb/s. 3R regeneration (2R + re-timing), based on a cross-gain modulation wavelength converter and a MZI, is demonstrated at 40 Gb/s in a recirculating loop experiment over 4000 km. Moreover, an optical subsystem for NRZ clock recovery, based on self-phase modulation and cross-phase modulation in an SOA,

and capable of generating the 40 GHz spectral component from a 40 Gb/s NRZ signal, is presented.

All-optical Boolean logic gates and functionalities involving several gates are investigated experimentally and numerically. Boolean AND and XOR gates are realized experimentally with MZIs, at 20 Gb/s and 10 Gb/s, respectively, whereas combinations of Boolean functions in MZIs are used to demonstrate a 3-input XOR gate, a data segment bit comparator, and a compact parity checking scheme, all at 10 Gb/s.

Resumé (in Danish)

Denne afhandling analyserer rent optiske switche baseret på optiske halvlederforstærkere gennem eksperimenter og numeriske simuleringer. Disse komponenter er kandidater til at realisere optisk signalprocessering såsom bølgelængdekonvertering, regenerering og logisk processering i fremtidens transparente optiske netværk.

Faktorer bestemmende for halvlederforstærkeres modulationsbåndbredde er bestemt, og metoder til reducering af skadelige mønstereffekter diskuteres. Tre typer halvlederforstærker-baserede switche er undersøgt numerisk: Såkaldte standard -mode og differentiel-mode switche og den filtreringsassisterede switch. Det vises at differentiel-mode switche eliminerer et af bidragene til mønstereffekterne, kaldet *lineær mønstereffekt*, mens den endelige begrænsning for ydelsen sættes af en mætningsinduceret effekt, kaldet *ulineær mønstereffekt*. To implementationer af differentiel-mode switche, Mach-Zehnder interferometret (MZI) og delayed-interferometer signal convertereren (DISC), sammenlignes for bitrater op til 160 Gb/s og fundamentale forskelle i deres støj-filtrerende egenskaber demonstreres.

DISC komponenten, der består af en halvlederforstærker og et asymmetrisk MZI filter, er analyseret i små-signal grænsen, og den opnåelige modulationsbåndbredde er udtrykt analytisk. En ny metode til små-signal analyse, der baserer sig på det optiske spektrum, introduceres og benyttes til at bestemme den båndbreddeforøgelse der kan opnås med forskellige optiske filtre. Ydermere analyseres effekten af filtres faserespons på modulationsbåndbredden. Eksperimenter ved 40 Gb/s bekræfter små-signal analysens forudsigelser.

Bølgelængdekonvertering er demonstreret eksperimentelt ved 40 Gb/s v. hj. a. en filtreringsassisteret teknik med ultra-lav switch-energi, og ved bitrater op til 80 Gb/s v. hj. a. MZI'er opereret i standard-mode konfiguration, også assisteret af båndbreddeforøgende filtrering.

Indvirkningen og betydningen af 2R regenerering (forstærkning og støjundertrykkelse) forklares gennem simuleringer, og demonstreres ved 10 Gb/s med MZI'er. Ydermere verificeres de regenererende egenskaber af en ny type rent-aktiv $2x2$ kobler, også ved 10 Gb/s. 3R regenerering (2R + jitterundertrykkelse), baseret på en bølgelængdekonverter opereret i kryds-gain modulation og et MZI, er demonstreret ved 40 Gb/s i et loopeksperiment over 4000 km. Derudover præsenteres et delsystem til klokkegendannelse for NRZ signaler, baseret på selv-

fasemodulation (SPM) og kryds-fasemodulation (XPM) i en halvlederforstærker. Systemet genererer den spektrale komponent ved 40 GHz udfra et 40 GHz NRZ signal.

Rent-optiske Boolske logiske gates, og funktionaliteter der involverer flere gates, er undersøgt eksperimentelt og numerisk. Boolsk AND og XOR er realiseret eksperimentelt v. hj. a. MZI'er, ved henholdsvis 20 Gb/s og 10 Gb/s, hvorimod kombinationer af Boolske funktioner i MZI'er anvendes til at demonstrere en 3-input XOR gate, en datasegment bit-komparator og en kompakt paritetschecker. Alle funktionaliteter er undersøgt ved 10 Gb/s.

Contents

Chapter 1

Introduction

At the onset of the new millennium there seemed to be a clear consensus in the fiber-optic community about the future role of optics in communication networks. Already, fiber-optic transmission had provided very impressive increases of the system capacity through the Wavelength Division Multiplexing (WDM) technology. Such systems were widely implemented by network operators, and it was expected that within the foreseeable future, optics would also replace an increasing number of electronic functionalities. This should pave way for the transparent optical network, capable of routing an optical signal from its source to destination, entirely in the optical domain. Hence, the vision was that the optical signal should propagate through the transmission fibers, and avoid being converted into an electrical signal for switching- or signal processing purposes. The main motivation for implementing a transparent optical network was to overcome the so-called electronic bottleneck - the limitation in terms of capacity imposed by electronics in general.

Today, 4-5 years down the line, the industry seems to be in the early phase of a recovery after a historic crash that brought down giant corporations and numerous start-up companies alike [1,2]. So what happened? Industry magazines have had 4-5 years to answer the question, and have not missed the opportunity. Most analysts agree that the heavy investment in WDM equipment by network operators lead to an overcapacity that is yet to be exploited, and that this is the primary reason the telecommunication market turned bad [3]. Moreover, in hindsight experts agree that the expectations to the telecom business before the down-turn were blown out of proportion, and that a crash was inevitable [3]. However, it was not all hype. The exponential growth of Internet traffic - a claim regularly found in the introduction of scientific publications a few years back - really did happen, and did prompt a huge demand for bandwidth. The demand was met by the WDM technology, which proved to be a cost-effective way of upgrading existing fiber infrastructure from carrying a single channel to supporting a large number of channels at different wavelengths. In combination with the Erbium-Doped Fiber Amplifier (EDFA), WDM technology provided a

huge capacity, which is still growing, due to introduction of new types of fiber and optical amplifiers [4, 5]. As it turned out, even the exponential growth of the Internet - currently unfolding at an overall rate of 20% per year [6] - was not enough to exploit the enormous capacity brought about by the new optical technologies. Bandwidth-demanding "killer applications" were needed to fill the spare capacity, but did not arrive, and finally the boom ended in a bust in 2001.

The forecast for the future looks promising though, and money is being made again. According to a recently published report, US optical network equipment vendors experienced double-digit revenue growth rates in the fourth quarter of 2003 [7], and the tendency is the same for optical component vendors. Systems implemented today are still primarily point-to-point, which means that all WDM channels are terminated and processed electrically at each node. Since converting signals between the optical and electrical domains at high bitrates is costly and power consuming [8], keeping the signals in the optical domain may be attractive from a technical and economical point of view. This is feasible, since photonic space switches have been commercially available for several years, and have been successfully tested in field trials [9]. Such switches, or Optical Cross Connects (OXC), can e.g. be based on Micro Electro-Mechanical Systems (MEMS), in which the angle of tiny mirrors are controlled to steer the signal light from its input port to its correct output port. One manufacturer claims that basing a network on its MEMS switches provides savings of 50-90% [9]. Such savings are made possible by avoiding the signal termination at each node, thereby eliminating lasers, receivers, and transponders by replacing the costly high-speed electronic switch core with an OXC.

Implementation of all-optical switch fabrics in the networks is the first step on the way to the transparent optical network. To avoid collisions between WDM channels, termed "blocking", no two channels can be assigned the same wavelength on the same WDM link between two nodes. For large networks this requirement is difficult to fulfil without wavelength conversion, i.e. the ability to change the wavelength of a channel from one link to another [10].

Transparency implies that optical signals may traverse numerous OXCs before being terminated. This accelerates signal impairments such as accumulation of noise from EDFAs, chromatic dispersion, jitter, and fiber nonlinearities, which puts a serious constraint on the size of the transparent network. However, by implementing all-optical regeneration, a function equivalent to that of the optoelectronic (OEO) repeater, the impact of signal impairments can be reduced dramatically, which enables network scalability [11–14].

Optical Packet Switching (OPS) has been proposed as a technology for better exploiting the network resources [10]. Apart from fast (ns) switch fabrics, optical packet routers benefit from 3R[1] regeneration, and require header/payload separation, header re-insertion, and buffering. In addition, a control unit is required

[1] 3R: Re-amplification, Re-shaping, Re-timing

to schedule e.g. the output port and output wavelength of each packet, and to control the switch resources to ensure correct switching [10, 11, 15, 16]. Most of these tasks have been demonstrated in laboratory environments, but in all cases the control unit has been electronic. However, in a future scenario, where optics has reached a higher level of maturity, it is envisioned that optical solutions may move all the way into the control plane to perform e.g. address recognition [17–19], and header update/label-swapping [20–22] at bitrates exceeding the limits of electronic processing. The promise of all-optical processing is not limited to packet switching, but may find applications in high-speed circuit switched networks as well. Either way, optical implementations of Boolean logic gates are expected to play a key role.

This thesis focuses on some of the key building blocks for realizing transparent optical networking, namely all-optical wavelength conversion, regeneration, and logic gates. Although several technologies are available for implementing these functionalities, the focus is mainly on Semiconductor Optical Amplifier (SOA) based switches, in particular SOA-based Mach-Zehnder Interferometers (MZIs). These switches are superior on a number of key points, as they are potentially ultra-fast, extremely versatile with respect to applications, have a large optical bandwidth, and can be integrated [23],[p9].

The work represents a physical layer perspective on SOA-based optical switches, where experimental demonstrations are supported by detailed physical modeling. As a result, the density of mathematical manipulations is quite extensive. Although this may come at the expense of 'reader-friendlyness', the mathematical description provides valuable insight into the operation, performance, and optimization of SOA-based switches.

The structure of the thesis is as follows: Chapter 2 motivates switching and signal processing in the optical domain and provides an overview of relevant technologies and schemes.

In Chapter 3, a detailed one-dimensional large-signal time-domain model of an all-optical MZI switch is given. The model forms the basis of the modeling effort, and is employed extensively in Chapters 4, 5, 6, and 8. In addition, a two-dimensional Finite-Difference Beam Propagation Model (2D FD-BPM) is presented, which is used to investigate a novel multi-moded optical switch in Chapter 6.

Chapter 4 uses a small-signal approach to analyze the carrier dynamics of SOAs. It focuses on the influence on a continuous wave (CW) probe signal, which either propagates in the same direction (co-propagation), or in the opposite direction (counter-propagation) as the modulated signal. Conclusions based on the small-signal analysis are tested against the large-signal model. Patterning effects are described, and divided into two categories: linear and nonlinear patterning. Alleviation of both types of patterning is discussed.

In Chapter 5 a detailed numerical investigation of the SOA-based MZI switch is given. The switch may be operated in two different modes, referred to as the

standard-mode (SM) and differential-mode (DM), and both are optimized with respect to interferometer phase-bias, input powers, and bias currents. Another DM-type wavelength converter switch - the Delayed-Interference Signal Converter (DISC) - is compared to the DM-MZI at bitrates up to 160 Gb/s, and fundamental differences are identified and quantified. Following this, a small-signal analysis, based on the analysis of the field envelope, is presented. This approach provides a convenient way of investigating the effect on the small-signal frequency response of placing an arbitrary optical filter after an SOA.

In Chapter 6, all-optical wavelength conversion at 40 Gb/s and above is demonstrated experimentally. In one experiment a single SOA followed by a band-pass filter (BPF) is used to wavelength convert a 40 Gb/s Return-to-Zero (RZ) data signal with a record-low data pulse energy of 3 fJ, while maintaining the data format and polarity. Wavelength conversion at 40 Gb/s is demonstrated in two other experiments, using an active-passive and an all-active MZI, both operated in the standard-mode. The response of the all-active MZI proved fast enough for 80 Gb/s. Moreover, the all-active device is employed as a 2x20 Gb/s to 40 Gb/s WDM to Optical Time Division Multiplexing (OTDM) translator and multiplexer. Finally, a numerical investigation of a novel Dual-Order MOde (DOMO) wavelength converter is carrier out. The work presented in sections 6.2.2 and 6.3 was done in collaboration with Martin Nord (COM).

The topic of Chapter 7 is all-optical regeneration, and it starts with an introduction to the principle of reshaping, before presenting a demonstration of 2R[2] regeneration in a MZIs at 10 Gb/s. The tolerance at 10 Gb/s of a MZI-based 3R regenerator towards chromatic dispersion is then analyzed, followed by a 40 Gb/s recirculating loop demonstration of a 3R regenerator based on a cascade of a Cross-Gain Modulation (XGM) wavelength converter and an active-passive MZI operated in standard-mode. Subsequently, a novel and very compact 2R regenerator based on a Multi-Mode Interference SOA (MMI-SOA) is introduced, and demonstrated at 10 Gb/s. Finally, all-optical extraction of the 40 GHz base frequency from a 40 Gb/s Non-Return-to-Zero (NRZ) signal is demonstrated using self-phase modulation (SPM) and Cross-Phase Modulation (XPM) in an SOA. The work in section 7.3 was done in collaboration with Martin Nord (COM) and Martin Nordal Petersen (COM), the results in section 7.4 were obtained with Elodie Balmefrezol and Bruno Lavigne (Alcatel CIT, France), whereas the work in section 7.5 was obtained with Jan De Merlier (formerly IMEC, University of Gent, Belgium).

Chapter 8 demonstrates all-optical Boolean logic gates, implemented with all-active MZIs, and logic functionalities obtained by combining Boolean functions. The principle of obtaining the NOT, OR, AND, and XOR functions with MZIs is explained, and all-optical AND and XOR is demonstrated at 20 Gb/s and 10 Gb/s, respectively. XOR with NRZ input data is found to introduce pattern

[2] 2R: Re-amplification, Re-shaping, although 2R is often used even though amplification does not take place

dependent jitter, and the tolerance of the XOR gate towards poor temporal synchronization of the input signal is investigated experimentally and numerically. Then, two XOR gates are cascaded to demonstrate a 3-input XOR gate operating at 10 Gb/s, followed by a scheme for bit-comparison in segments of input data, implemented with a single MZI operated at 10 Gb/s. Finally, an all-optical bit-parity calculator with SOA-amplified feedback is demonstrated with a single all-active MZI. Simulations asses the maximum bitrate at which the parity calculator may be operated. The experimental results in sections 8.1.4, 8.2.1, and 8.2.2 were obtained with Jakob Buron (COM), while the experimental work in section 8.2.3 was made in collaboration with Martin Nordal Petersen (COM) and Martin Nord (COM).

Chapter 9 concludes the thesis.

Chapter 2

Towards transparent optical networks

The vision of complete transparency in optical networks, and its potential benefits in terms of cost and performance, is fuelling a world-wide research effort in all-optical technologies. Employing optics for switching and signal processing, in addition to transmission, enables transparent switching of entire wavelength channels or even bands of wavelengths. Avoiding termination, electrical switching, and electrical processing has the potential benefit of saving cost by avoiding a lot of electronic and optoelectronic hardware at intermediate nodes. Whilst both electrical- and optical systems are transparent to content, only optical systems are to a certain degree transparent to signal format and bitrate [24]. Such transparency makes the network more flexible, being able to handle different signal types from potentially different edge node interfaces, and may make upgrades more cost-effective, by enabling re-use of installed equipment.

This Chapter motivates the work presented in the thesis, with a realistic view on the future of all-optical signal processing. First, the motivation for switching signals in the optical domain is elaborated on, followed by a discussion of transparency in a network employing all-optical wavelength conversion, regeneration, and logic functionalities. Then, the current state of optoelectronic interfaces for 3R regeneration and wavelength conversion is presented, which sets a reference to compare all-optical solutions against. Finally, different technologies for implementing all-optical wavelength converters and regenerators are presented and compared.

2.1 The benefits of transparency

Switching in the optical domain is expected to lead to a higher bitrate per WDM channel, since the switch fabric, if implemented using e.g. MEMS technology, is truly bitrate transparent, and not restricted to a single bitrate, as opposed to

OEO switches, which use electronic processing. The upgrade from 2.5 Gb/s to 10 Gb/s per channel, that took place towards the end of the last century, offered a reduction in the cost per bit, and this is expected to be the case again with the forthcoming upgrade to 40 Gb/s [25]. This is anticipated even if switching remains in the electrical domain, so in combination with optical switching the cost saving may be even larger [9]. Switching in the optical domain is receiving attention for another - more practical - reason. As the port-count of electrical cross-connects increases the number of internal high-speed electrical interconnects scales poorly due to the need for parallelization. This leads to a large power consumption, which dictates a minimum physical size of the switch fabric [8, 26]. The long electrical interconnects represent a source of loss and distortion, which limits the total throughput of the switch. An optical switch fabric, or an electrical switch using optical fibers for interconnections, is not bound by the same constraint, since fiber is a superior transmission medium.

The fact that MEMS switches as large as 256x256 are still being offered by a number of vendors [9, 27, 28] at the end of the industry downturn, seems to indicate that implementation of optical space switching is a matter of *when* and not *if*. Today, wavelength conversion and 3R regeneration is carried out in the electrical domain. This means that introducing an optical switch fabric actually removes functionality that needs to be replaced by optical solutions.

As the size of the network increases, finding an available wavelength that can carry the signal on all links to the destination node becomes increasingly difficult [29]. This can be alleviated by decreasing utilization, by either decreasing the network load, or by increasing the number of wavelengths per link [30]. Low utilization is bad economics, and there is a physical limit to the number of wavelengths that may be carried per link. These are main reasons why optical networks will benefit from wavelength conversion capability. Wavelength conversion ensures a reduced probability of wavelength blocking with a modest total number of wavelengths, since the same wavelength may be re-used and assigned on a link-basis, rather than on a global scale [31]. Moreover, the added flexibility of wavelength conversion allows for simpler network management, protection and restoration [32].

For Optical Circuit Switched (OCS) networks, wavelength conversion can to some extend be avoided by careful wavelength assignment [33], or by using multiple fibers between nodes [30]. However, if a fiber breaks and traffic must be routed along alternative paths, the flexibility of wavelength conversion enables faster and simpler restoration [34]. For OPS networks wavelength conversion is needed to resolve contention issues [35] in the absence of an all-optical random access memory.

Optical signals accumulate detrimental effects when propagating through the network, and require 2R or 3R regeneration to enable scalability. To some extent, new modulation formats, Forward Error Correction (FEC), and Raman amplification [4, 5] represent alternatives to regeneration, as they all increase the power

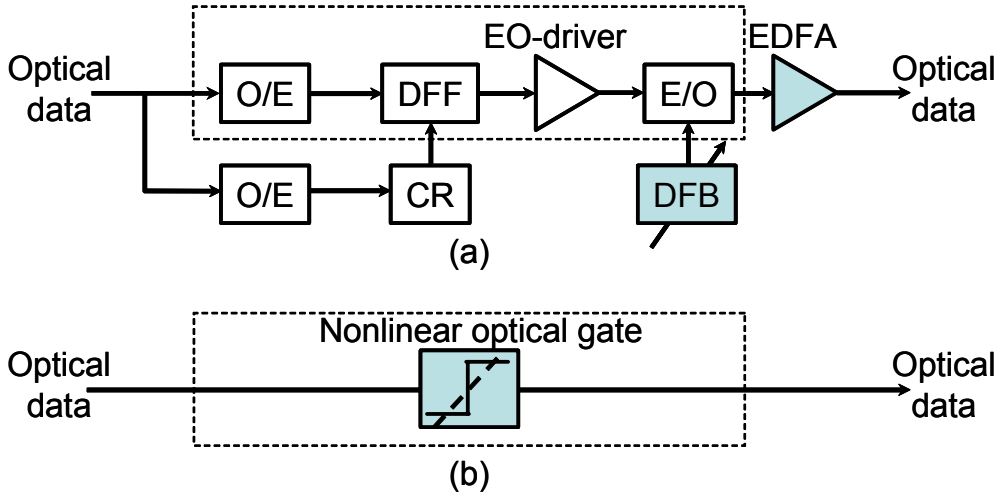

Figure 2.1: (a) optoelectronic 3R regenerator based on a decision flip-flop (DFF) [36]. The 2R part (dashed box) may be replaced by an optical gate (b)

budget in one way or the other. However, this is only the case for point-to-point links, where all WDM channels have equal properties at the input. In a network scenario, individual WDM channels pass through numerous nodes on the way to their destinations. A specific link between two nodes may carry WDM channels with different accumulated dispersion, Optical Signal-to-Noise Ratio (OSNR), etc, but regardless the link must be able to transport all the channels to the next node. This prompts the need for an interface that equalizes the quality of the individual channels, to make sure that equipment such as Dispersion Compensating Fiber (DCF) and optical amplifiers in the link have similar impact on all channels. A regenerator - all-optical or optoelectronic - is such an interface.

Logic functionalities in the optical domain are likely to be implemented after regeneration and wavelength conversion functionalities, since logic gates are less mature, and their implementation generally more complex. The potential impact of all-optical logic is by no means clear at this point, since optical logic gates are at least 50 years behind their electronic counterparts in terms of maturity. It seems likely though, that a first introduction of optical logic in a real network will implement a very simple function at the line rate, which reduces the required bandwidth of the surrounding electronics, which will still be needed for functions of higher complexity.

2.2 Optoelectronic interfaces

An option, which is being considered for a short to medium-term approach to optical networking, is using optoelectronic (OEO) interfaces on an optical switch fabric [37]. In this approach, which is illustrated in Fig. 2.1 (a), each WDM channel is detected, 3R regenerated electronically, and modulated on a new op-

tical carrier, possibly with a new wavelength, before entering the optical switch fabric. The electronic and optoelectronic components required in such an interface are fast photodetectors, a clock recovery circuit, a decision flip-flop (DFF), driver amplifier, an electro-optic modulator, and a tunable Distributed FeedBack (DFB) laser. An all-optical solution carrying out the same function may be realized with fewer components, since the OE and EO conversion is bypassed. This is illustrated in Fig. 2.1 (b), where the dashed box of Fig. 2.1 (a) is replaced by a single nonlinear optical gate, which carries out the reshaping function equivalent to the DFF. The remainder of the interface in Fig. 2.1 (a) is needed, regardless of the whether regeneration is carried out electrically or optically. From Fig. 2.1 it seems obvious that the all-optical solution has greater potential on the long-term, as the simpler design and the lower component count may be a cost-saver. Moreover, the continued development of optical technology may provide a significantly higher bandwidth. However, at present, this does not seem to be the case. In a recent 40 Gb/s demonstration of the optoelectronic 3R regenerator setup in Fig. 2.1 (a) [36], using a commercial DFF [38], the cascaded performance was better than for the most recent all-optical SOA-based implementations [39, 40]. As it will be detailed in the introduction to Chapter 7, the power consumption of the two schemes is very similar, and since this particular all-optical 3R regenerator is a quite complex two-stage design, the optoelectronic solution has the upper hand.

Another approach, based on the integration of a photo diode and an Electro Absorption Modulator (EAM), is described as OEO [41], but is bordering an all-optical solution, has been used to demonstrate retiming and wavelength conversion, at a bitrate of 100 Gb/s [42]. The potential of this technology is detailed in section 2.3, but here it should just be noted that all-optical solutions will not necessarily outperform optoelectronics. The best scheme may be a hybrid between the two.

2.3 State-of-the-art all-optical switches

All-optical regenerators, wavelength converters and logic gates are all based on optical switches. An all-optical switch is here defined very generally as a device capable of controlling one optical signal, the probe signal, by means of one or more externally applied optical signals, which will be referred to as control signals. The properties of the probe signal are described fully by the amplitude and phase of the electric field representing the probe. Thus, all-optical switches rely on the modulation of the amplitude and/or the phase of the probe signal through an interaction with a physical medium, or on generation of a new signal by interaction between the control signal and a pump signal through the medium. The medium must be nonlinear in order for the interaction to take place, and for practical reasons, the nonlinear medium usually takes the shape of an optical waveguide. This enables confinement of the fields, which increases the intensity,

and thereby the effective nonlinearity, compared to a homogeneous nonlinear medium.

The choice of medium determines properties such as response time, efficiency[1], physical size, etc. In the following the fundamental properties of the nonlinear media most widely used in all-optical switching are briefly reviewed, and subsequently the current state-of-the-art demonstrations of wavelength conversion and regeneration are presented. All-optical logic gates reported so far are without exception based on the same optical switches as wavelength converters and regenerators. The requirements are thus the same, and a review of the current state of all-optical logic is left to Chapter 8.

Switches based on resonant semiconductor waveguides such as SOAs or EAMs can be made very compact, and for SOAs in particular, the control pulse energy required to change the state of the switch - the switching energy - is lower than any other practical medium available today [43, 44],[p4]. The main problem in using SOAs and EAMs as nonlinear elements is their finite response time, which limits the bitrate at which the switch can be operated. For an SOA, the response time is governed by the carrier lifetime [45], which will be discussed in detail in the following Chapter. For an EAM the limiting time constant is defined by the magnitude of the external electric field, i.e. by the reverse bias voltage, which is responsible for "sweeping-out" carriers from the active region [46]. Both SOAs and EAMs can be designed to be polarization independent by compensating for the different modal confinement of the TE and TM modes by straining the active layer [47].

NonLinear Fiber (NLF) based switches exploit the third-order nonlinearity of Silica (SiO_2), which has a response time limited by the stimulated Raman scattering (SRS) response of 60-70 fs [48]. Thus, for pulse widths larger than $\approx$1 ps, the response may be considered instantaneous. The down-side to NLF as a nonlinear medium is the relatively low nonlinearity, which is at least 3 orders of magnitude smaller than that of SOAs [43] - even when highly nonlinear Photonic Crystal Fibers (PCFs) are employed [49]. This means that in order to accumulate a nonlinear effect equivalent to that of an SOA, the interaction length, i.e. the length of the NLF in an all-optical switch is typically 10s-100s of meters long in order to keep the switching energy at a level that can be facilitated by Erbium-Doped Fiber Amplifiers (EDFAs). The long interaction length makes the switch inherently sensitive to mechanical and thermal fluctuations, which makes NLF-based switches ill-suited for practical systems applications. However, a lot of effort is going into developing highly nonlinear PCFs, and progress is being made. In [50], wavelength conversion at 10 Gb/s, based on Four-Wave Mixing (FWM) in a 15 m long Holey PCF, was demonstrated. NLF-based all-optical switches exploit either XPM [51–53] or FWM [50, 54], and both processes require co-polarized probe and control signals [48], which make the switches polarization

[1] Efficiency is often defined as the ratio of switched output probe power to input control power

dependent.

Another medium receiving a lot of attention is Periodically Poled $LiNbO_3$ (PPLN) waveguides. Interaction between the control signal and an intense pump signal takes place through the second-order Difference Frequency Generation (DFG) process, which generates a new signal at a wavelength determined by the wavelengths of the two input signals [55–58]. The efficiency, in terms of energy transfer from control signal to probe, is quite high [59], and is estimated to be as high as 0 dB, not counting coupling losses [60]. The main advantage of PPLN waveguides over SOAs is their almost instantaneous response, providing a modulation bandwidth in excess of several Terahertz [60]. In addition, the efficiency does not depend on the control signal power, which gives rise to a very large Input Power Dynamic Range[2] (IPDR), measured to >30 dB in [60]. Finally, compared to NLF the PPLN waveguides are relatively compact (< 10 cm) [56], which makes them robust. However, as for XPM and FWM in fiber, DFG is inherently polarization dependent, which may be reduced considerably however, through polarization diversity schemes [61, 62].

At present, active semiconductor waveguides are still believed to be prime candidates for nonlinear elements in all-optical switches, as they consume less power, and are potentially polarization independent. Furthermore, they allow for integration with interferometers to form nonlinear gates [63], or with e.g. electronics on an InP substrate [64].

2.3.1 Wavelength conversion

The requirements to an all-optical wavelength converter apply, for the most part, generally to all-optical switches and include [23]: independence of input data wavelength, polarization, extinction ratio, and OSNR, operation with low optical/electrical power levels, low chirp of output signal, simple and robust implementation, bitrate and format transparency, high IPDR, large optical wavelength bandwidth, and high output OSNR. Not all these requirements can be fulfilled by a single wavelength conversion scheme, but as describes in the following, some techniques come close.

SOA-based techniques

Using that the probe gain provided by an SOA can be saturated by a control signal, wavelength conversion by XGM has been demonstrated at 40 Gb/s [65]. This technique is very simple and provides a large IPDR (10 dB at 10 Gb/s [23]), but reduces the extinction ratio of the converted signal when the wavelength of the probe is higher than that of the control signal (up conversion). In addition, the converted signal may be significantly chirped, which accelerates the impact

[2] IPDR is often measured as the input power range of the control signal for which the excess power penalty is < 1 dB

of chromatic dispersion [23], and the signal polarity of the converted signal is inverted compared to the input data.

XGM is accompanied by XPM, and this may be exploited by inserting SOA(s) into an interferometer, which converts the phase modulation (PM) into amplitude modulation (AM). Compared to XGM, SOA-based Interferometric Wavelength Converters (IWCs) allow for a lower switching energy and chirp [23], controllable polarity of the converted signal, and similar performance for up and down conversion [p7],[p9]. Moreover, reshaping is an inherent property of IWCs, which enables cascadability of many wavelength converters [12]. A drawback to IWCs is an inherently low IPDR, which, however, may be compensated for through active control of the input power [p7]. IWCs have been monolithically integrated in the Mach-Zehnder (MZI), Michelson (MI), and Sagnac (SI) configurations [66–68], but due to a higher speed potential the MZI configuration is receiving the most attention. The MZI and MI configurations may be operated in the so-called standard-mode, in which the bitrate is limited to below $\approx$ 80 Gb/s, due to the finite carrier lifetime. However, by employing a so-called differential control scheme, in which the trailing part of the probe phase response is cancelled, operation at bitrates exceeding 100 Gb/s is possible. Fiber - SOA hybrid implementations of the MZI operated in the differential-mode, referred to as the Ultra-fast Nonlinear Interferometer (UNI) [69] or Polarization Discriminating MZI (PD-MZI) [70], have been demonstrated with Bit Error-Rate (BER) measurements at 84 Gb/s [70]. The differential control scheme may also be realized in a fiber Sagnac interferometer with an SOA as the nonlinear medium. This configuration is dubbed Terahertz Optical Asymmetric Demultiplexer (TOAD) [71] or Semiconductor Laser Amplifier LOop Mirror (SLALOM) [72]. Finally, a very simple differential-mode IWC, referred to as the Delayed-Interference Signal Converter (DISC), and consisting of a single SOA followed by an asymmetric MZI filter, has been used to demonstrate wavelength conversion up to 168 Gb/s [73, 74] in a hybrid setup, and up to 100 Gb/s with a monolithically integrated version [75]. Replacing the Asymmetric MZI filter of the DISC with a simple BPF gives rise to similar broadband operation [p2],[p4]. In [76], this was demonstrated using a Fiber Bragg Grating (FBG), which enabled wavelength conversion at 100 Gb/s.

Wavelength conversion by FWM in SOAs has been investigated intensely as the technique is coherent, and consequently preserves not only the polarity, but also the phase information, which is a necessity for wavelength converting signals with advanced modulation formats such as e.g. Differential Phase Shift Keying (DPSK). Another advantage of FWM is the ability to convert a whole band of WDM channels to a band of new wavelengths, demonstrated at 10 Gb/s for a band of 32 channels in [77]. Moreover, since the FWM product is proportional to the complex conjugate of the data (control) signal, a FWM wavelength converter may be used as an Optical Phase Conjugator (OPC), which is able to reverse the impact of the accumulated dispersion if positioned between two identical fiber spans. This technique was used to transmit an 80 Gb/s signal over 208

km of standard single-mode fiber (SMF) in [78]. Although high-speed operation at bitrates up to 100 Gb/s has been demonstrated [79], and tunability in excess of 20 nm at 40 Gb/s [80] and 80 nm at 2.5 Gb/s [81] has been shown, the conversion efficiency and OSNR are limited by the fact that the SOA must be heavily saturated by the probe signal in order to reduce the effect of XGM [80]. The low OSNR limits the cascadability of wavelength converters based on FWM, and so far recirculating loop experiments have not been carried out to quantify this. Cascading two FWM wavelength converters at 10 Gb/s lead to a reduction of the OSNR from $\approx$ 50 dB/0.1 nm to only $\approx$ 20 dB/0.1 nm after the second conversion [82].

EAM-based techniques

Just as the gain can be saturate in an SOA and facilitate wavelength conversion by XGM, the absorption can be saturated in an EAM by cross-absorption modulation (XAM). This technique is equally simple as XGM, and has been reported at bitrates up to 40 Gb/s [83]. As explained previously the modulation bandwidth of EAMs is limited by the "sweep-out" time, which decreases as the applied reverse bias is increased [84]. This leads to a trade-off between insertion loss and speed, which translates into a poor conversion efficiency at high speeds [84]. XPM in an EAM has also been exploited by using a hybrid implementation of the DISC [84], and in this configuration wavelength conversion at 80 Gb/s has been reported [84].

In a novel OEO scheme, a Travelling-Wave EAM (TW-EAM) is switched by an ultra-short electrical pulse generated by a Uni-Traveling-Carrier Photo Diode (UTC-PD) integrated with the EAM [41]. So far, this configuration, referred to as the PD-EAM, has demonstrated power penalty free wavelength conversion at 100 Gb/s in a fully integrated device with modest dimensions of 1 mm x 0.4 mm [42]. Details on the power consumption have not been published, but it could potentially be very low.

NLF-based techniques

Wavelength converters based on XPM in NLF are realized much in the same way as with the SOA counterparts, namely either by using a filter to perform the PM-to-AM conversion, or by inserting the nonlinear fiber into an interferometer. Using the former approach conversion has been demonstrated at 80 Gb/s [21, 53], and by exploiting polarization rotation in a 1 km long nonlinear fiber proceeded by a Polarization Beam Splitter (PBS), a PD-MZI type interferometer was realized at a bitrate of 160 Gb/s in [85]. In the same reference the wavelength converted signal is converted a second time by means of Super Continuum Generation (SCG) and spectral slicing. Using a Nonlinear Optical Loop

Mirror[3] (NOLM) with 1 km highly nonlinear Dispersion Shifted Fiber (DSF), wavelength conversion at 80 Gb/s over 50 nm was reported in [86].

PPLN-based techniques

Since DFG is a coherent process, wavelength conversion in PPLN waveguides provides full transparency towards modulation format, as it is the case for FWM. Penalty-free wavelength conversion of 160 Gb/s RZ data has been reported in a 6 cm long device with an efficiency better than -10 dB [87]. However, to obtain this efficiency the device was heated to $>90°$ C to avoid photorefractive effects, which is not realistic in a deployed system. In another demonstration a PPLN wavelength converter was made polarization independent by applying a compact diversity scheme, involving counter propagating the TE and TM components [62]. This device was tested in a 500 km field trial at 40 Gb/s with negligible power penalty.

2.3.2 Regeneration

Regenerators must fulfill the same requirement as wavelengths converters. In addition, the nonlinearity of the gate is a key parameter, as it determines the extent to which the fluctuations around the "0" and "1" levels of the signal may be reduced [63]. Whether 3R regeneration is required in a system, or 2R regeneration is sufficient, depends on the application. 1R regeneration, i.e. simple re-amplification, is sufficient for carefully optimized long-haul submarine systems, but in an optical network where signals may be split and reamplified several times when traversing a network node, the accumulation of Amplified Spontaneous Emission (ASE) will limit the size of the network, and prompt installation of 2R regenerators. For even larger networks with more hops, the performance may be limited by jitter introduced by noise from active components, environmental fluctuations, XPM, or Polarization-Mode Dispersion (PMD) [88], which makes it necessary to retime the signal as well [89].

SOA-based interferometers

2R regeneration is an inherent property of IWCs due to the nonlinear transfer function [23, 90]. Extensive recirculating loop experiments have been carried out with integrated SOA-based MZIs to assess the cascadability and regenerative capability. At 2.5 Gb/s, a 2R regenerator based on a cascade of an SOA-XGM wavelength converter, with co-propagating data and probe signals, and a MZI operated in standard-mode turned a BER floor[4] after 4 spans of 400 km SMF into a power penalty of only 3 dB after 9 spans [91]. In a similar experiment, the XGM converter was operated with counter-propagating data and probe signals,

[3] A NOLM is a NLF-assisted Sagnac interferometer switch

[4] BER floor: Minimum BER approached asymptotically as received power is increased

and the regenerated signal was passed through a $16x16$ SOA-gate array in each lap, containing 55 km of DSF. Due to the noise added by the gate array, and the introduction of jitter from the counter-propagation XGM converter [92], only 8 laps could be tolerated. Adding sampling functionality to the MZI by replacing the CW probe with a recovered clock signal, thereby realizing 3R regeneration, the power penalty remained constant and < 1 dB after 70 laps [89]. At 40 Gb/s, a 3R regenerator consisting of a cascade of two MZIs operated in differential-mode has demonstrated 100 laps of 40 km DSF with fixed receiver sensitivity after 2 laps. Finally, a simplified 3R regenerator made up of a SOA-XGM co-propagation wavelength converter and a MZI operated in the standard-mode has been demonstrated at 42.66 Gb/s with a BER of 10^{-4} (corresponding to a BER$<10^{-9}$ using FEC) after 100 laps of 300 km of SMF/DCF [39].

3R regeneration using the PD-MZI gate has been reported at bitrates up to 84 Gb/s in a single-regenerator experiment [93], and at 40 Gb/s in a recirculating loop demonstration over 20 laps of 100 km DSF [94]. The retiming capability of the DISC has been verified in a single-regenerator demonstration [95], and in a loop experiment over 2500 laps of 400 km non-zero dispersion fiber and DCF [96].

EAM-based techniques

As for IWCs, 2R regeneration is inherent for EAMs operated as XAM wavelength converters [46]. Replacing the CW probe signal with a recovered optical clock enables 3R regeneration, which has been demonstrated at bitrates up to 40 Gb/s in a single-regenerator experiment, where regeneration was performed between two 500 km fiber links [97], with significant improvement of the signal quality.

The PD-EAM switch introduced in section 2.3.1 has been used to realize retiming at 100 Gb/s in a single-regenerator experiment [42]. This is possible because the switching window generated by the electrical pulse is rectangular-like and slightly broader than the data pulse exciting the photo diode, which provides tolerance towards jitter.

NLF-based techniques

2R regeneration is an inherent property of wavelength converters based on the NOLM [98], due to the nonlinear transfer function of the Sacnac interferometer. A detailed single-regenerator investigation at 10 Gb/s is presented in [99], but should be observed at higher bitrates as well [86, 98]. Another way in which 2R regeneration can be obtained, is by launching a high signal power into a nonlinear fiber, and exploiting that the amount of SPM-induced spectral broadening has a nonlinear dependence on the pulse peak power. By positioning a sharp filter away from the carrier wavelength, only pulses with a certain 'threshold peak power' are transmitted [100]. This technique has been used as the decision function in a 40 Gb/s 3R regenerator demonstration over 1 million km, where the retiming is obtained through in-line synchronous modulation [14]. The latter implies that

the data pulses align to the timeslot during propagation [88]. In [96], a DISC was used for retiming instead of synchronous modulation in a similar experiment, also spanning 1 million km.

The highest bitrate at which 3R regeneration has been reported is 160 Gb/s, and the implementation is based on the PD-MZI type wavelength converter described in [85]. By broadening the data pulses before launching them into the decision gate, consisting of 1 km nonlinear fiber followed by a PBS, an increased tolerance towards jitter is obtained. The regenerative capability was investigated in a recirculating loop with 62.2 km of fiber per lap, and after 3 laps (184 km), the sensitivity improvement was > 3 dB [101].

2.4 Summary

In this Chapter it was argued that implementing all-optical switch fabrics may save cost on the short to medium term, and possibly become necessary on the longer term, to combat long electrical interconnects in the switch backplanes. With the introduction of an all-optical switch fabric, all-optical wavelength conversion and regeneration of individual WDM channels enables transparent optical networking. Technologies and techniques for realizing optoelectronic and all-optical wavelength conversion and regeneration were reviewed, and it was concluded that since optoelectronic solutions for the coming upgrade to 40 Gb/s are mature and commercially available, all-optical solutions are not likely to be implemented at bitrates ≤ 40 Gb/s. On the medium term 40 Gb/s optoelectronic interfaces may be used in connection with all-optical MEMS switches, but in a future scenario, with line rates approaching 160 Gb/s, all-optical solutions for wavelength conversion, 3R regeneration, and simple logic functionalities will be needed to enable transparency. The most promising technologies for realizing the required optical functionalities include SOAs, PPLN waveguides, and highly nonlinear PCFs.

Chapter 3

Simulation tool for SOA-based switches

Physical modeling of complex devices, such as all-active MZIs, is necessary in order to understand their potential and limitations. In addition, a reliable physical model may be used to investigate new configurations leading to superior ways of operating devices, or possibly to development of entirely new device structures. In this Chapter, the simulation tool used throughout the thesis is presented. The tool is based on a detailed one-dimensional model, assuming homogeneity of the field-intensity in the cross-section of the SOA, and is capable of modeling an all-active MZI with up to six independent SOAs. Following this, a Finite-Difference Beam Propagation Method (FD-BPM) with an inhomogeneous transversal grid is introduced. This model accounts for field propagation in multi-moded SOAs and is used to simulate the Dual-Order-MOde (DOMO) wavelength converter detailed in Chapter 6.

The simulation tool may be broken into four parts as shown in the block diagram in Fig. 3.1: an optical signal generator part, the SOA-based switch itself, a signal processing toolbox, and finally an optoelectronic receiver. The theory behind the model of the SOA-based switch is explained in detail in the

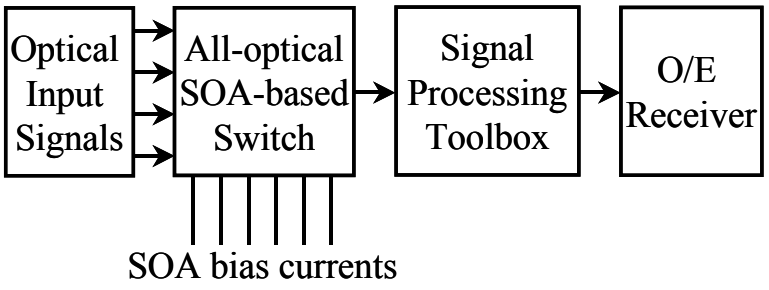

Figure 3.1: Block diagram of large-signal simulation tool

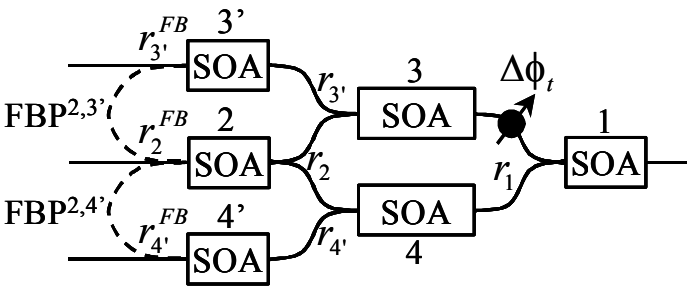

Figure 3.2: Schematic of the MZI switch, as it is represented in the model, including six SOAs, tunable passive phase shift, and feedback paths (FBPs)

following, whereas the description of the interfaces to the model, i.e. the optical inputs, signal processing options, and the receiver, is left to Appendix A.

The block dubbed "All–optical SOA-based switch" in Fig. 3.1 is basically six SOAs connected through a number of couplers to form an all-active MZI switch, with active input and output SOAs, also referred to as peripheral SOAs, or an active/passive MZI switch, where only the interferometer arms are active, or alternatively an advanced gate with optical feedback. The layout is depicted in Fig. 3.2, which shows the six SOAs in a Mach-Zehnder configuration, along with a number of optional feedback paths (FBPs) connecting inputs and outputs, shown as dashed curves. Signals and ASE can enter all inputs/outputs. However, optional isolators may be included in the FBPs to prevent bi-directional propagation, and they play an important role for some applications, as will be described in chapter 8. Apart from the optional isolator, the FBPs are characterized by the propagation delays $\tau_{2,3'}$, $\tau_{2,4'}$, as well as the coupling ratios of the 2x1 couplers at the entry and exit points. These coupling ratios are labelled like the SOA at the input/output in question, i.e.: $r_{3'}^{FB}$, r_2^{FB}, and $r_{4'}^{FB}$. Since the couplers have only two outputs, the two FBPs may not be active at the same time, as this would require a 3x1 coupler at the input of SOA 2. Internally in the MZI, the coupling ratios are also adjustable, and labelled $r_{3'}$, r_2, $r_{4'}$, and r_1 (see Fig. 3.2). Moreover, the upper arm of the MZI is equipped with a passive phase tuning section, which modifies the phase by $\Delta\phi_t$.

It is assumed that polarization effects can be neglected, and consequently solving the field propagation becomes a matter of solving the scalar wave equation. Contributions to the carrier dynamics from intraband effects such as carrier heating (CH) and spectral holeburning (SHB) are excluded in this model, which sets a lower limit for the pulse width of signals that may be accurately propagated through the SOA. This so-called critical pulse width may be expressed as [102]

$$\tau_{cr} = \frac{\varepsilon}{(\partial g/\partial N)\, v_g} \tag{3.1}$$

where ε is the nonlinear gain-suppression parameter due to CH and SHB, $\partial g/\partial N$

is the differential gain, and v_g is the group velocity. For realistic values of $\varepsilon = 1 \cdot 10^{-23} m^3$ and $\partial g/\partial N = 5 \cdot 10^{-20}$ m^2, the critical pulse width is ≈ 2.4 ps.

3.1 One-dimensional SOA-model

In the time domain, the forward propagating electric field can be expressed as [103]

$$\begin{aligned}\overrightarrow{E}(z,t) = E(z,t)\overrightarrow{e_x} &= \tfrac{1}{2}\left(A(z,t)e^{j(\beta z-\omega_0 t)} + A^*(z,t)e^{-j(\beta z-\omega_0 t)}\right)\overrightarrow{e_x} \\ &= \tfrac{1}{2}\left(\sqrt{P(z,t)}e^{j\phi(z,t)}e^{j(\beta z-\omega_0 t)} + \sqrt{P(z,t)}e^{-j\phi(z,t)}e^{-j(\beta z-\omega_0 t)}\right)\overrightarrow{e_x}\end{aligned} \tag{3.2}$$

where $*$ denotes complex conjugation, $\overrightarrow{e_x}$ is a unit vector directed along the x-axis, and $A(z,t)$ is the complex slowly varying field envelope, with instantaneous power and phase given by $P(z,t)$ and $\phi(t)$, respectively. This description is referred to as the slowly varying envelope approximation (SVEA), since the bandwidth of $A(t)$ must be negligible compared to the carrier angular frequency ω_0 for the separation of signal and carrier in (3.2) to be valid. The field envelope is assumed spatially invariant in the $(x,y)-$ plane, and thus propagation is limited to the $z-$dimension. The propagation constant β is defined as $\beta = \overline{n}k_0$, with $\overline{n}$ being the mode index. Eq. (3.2) is normalized such that the power averaged over a period of the carrier is obtained as $P(z,t) = A(z,t)A^*(z,t)$[1]. Defining the Fourier transform operator $\mathbf{F}$ as

$$E(\omega) = \mathbf{F}\left[E(t)\right](\omega) = \int_{-\infty}^{\infty} E(t)e^{j\omega t}dt \tag{3.3}$$

the field may be described analogously in the frequency domain

$$E(z,\omega) = \frac{1}{2}\left(A(z,\omega-\omega_0)e^{j\beta z} + A^*(z,-\omega-\omega_0)e^{-j\beta z}\right) \tag{3.4}$$

with $A(z,\omega)$ and $A(z,t)$ being related through (3.3). For (3.4) to satisfy Maxwell's equations, $E(z,\omega)$ must satisfy the scalar wave equation

$$\frac{\partial^2 E}{\partial z^2} + k_0^2\left(\overline{n}^2(\omega) + \chi_{NL}(N,\omega)\right)E = 0 \tag{3.5}$$

where χ_{NL} is the nonlinear susceptibility given by [103]

$$\begin{aligned}\chi_{_{NL}}(N,\lambda) &= \frac{c_0\overline{n}}{\omega}\left(\frac{4\pi}{\lambda}\frac{d\overline{n}/dN}{dg/dN} - j\Gamma\right)g(N,\lambda) \\ &= 2\Gamma\overline{n}\frac{\partial n_{core}}{\partial N}\left(N-N_r\right) - j\Gamma\frac{c\overline{n}}{\omega}g(N,\lambda)\end{aligned} \tag{3.6}$$

[1] This is a common definition in the literature (see e.g. [103]), but strictly, the equality sign in the second line of (3.2) is incorrect, as the power, per definition, is given by $\frac{1}{2}|A(z,t)|^2$. However, this discrepancy is absorbed by the input boundary condition, and thus has no implications on results or conclusions in this work.

Here, c_0 is the speed of light in vacuum, and $g(N,\lambda)$ is the material gain, expanded around a reference carrier density N_r in the second line of (3.6). According to the Effective Index Method (EIM) [104], the mode index $\overline{n}$ can be approximated by $\overline{n} \approx n_{clad} + \Gamma(n_{core} - n_{clad})$ for weak step index waveguides, where n_{core} and n_{clad} are the refractive indices of the active core of the waveguide and the surrounding cladding, respectively, and Γ is the optical confinement factor. Consequently, a carrier density induced change in the mode index $\frac{\partial \overline{n}}{\partial N}\Delta N$ can be approximated by $\Gamma\frac{\partial n_{core}}{\partial N}\Delta N$. This is convenient, since the effect of the waveguide is then only contained in Γ. Another convenient definition is the linewidth enhancement factor, α, related to the differential index change $\partial n_{core}/\partial N$ by

$$\alpha = -2k_0 \frac{\partial n_{core}/\partial N}{\partial g/\partial N} \tag{3.7}$$

Taylor expanding the squared propagation constant to first order around $\omega = \omega_0$, and ignoring chromatic dispersion, yields[2]

$$\beta^2 = \overline{n}^2 k_0^2 = \frac{\omega^2}{c_0^2}\overline{n}^2 \approx \frac{\omega_0^2}{c_0^2}\overline{n}^2(\omega_0) + \frac{2k_0\overline{n}(\omega_0)}{v_g}(\omega - \omega_0) \tag{3.8}$$

where v_g is the group velocity, defined as $v_g^{-1} = \left[\overline{n} + \omega\left(d\overline{n}/d\omega\right)\right]_{\omega_0}/c_0$. Inserting (3.4) and (3.8) into (3.5), using

$$\mathbf{F}\left[\frac{\partial A}{\partial t}e^{-j\omega_0 t}\right] = -j(\omega - \omega_0)A(z, \omega - \omega_0) \tag{3.9}$$

and neglecting $\partial^2 A/\partial z^2$, which corresponds to assuming a slowly varying field envelope in the $z-$direction, the wave equation for the forward propagating field is reduced to

$$\frac{\partial A}{\partial z} + \frac{1}{v_g}\frac{\partial A}{\partial t} = \frac{1}{2}\left(\Gamma g(N,\lambda) - \alpha_l + j2k_0\Gamma\frac{\partial n_{core}}{\partial N}(N - N_r)\right)A \tag{3.10}$$

where the internal scattering loss, α_l, is added phenomenologically, and approximated by [105, 106]

$$\alpha_l = \Gamma(a_1 + a_2 N) + a_3 \tag{3.11}$$

Here, the constants a_1 and a_2 both depend on the amplifier length, and their values may be found in Appendix D. The equation governing the propagation of a backwards propagating field may be obtained by substituting β for $-\beta$ in (3.2), which changes $(1/v_g)\,\partial A/\partial t$ into $-(1/v_g)\,\partial A/\partial t$ in (3.10). Eq. (3.10) can be split into two equations, governing the power and phase, respectively, of the forward and backward propagating field

$$\frac{\partial P^{\pm}}{\partial z} \pm \frac{1}{v_g}\frac{\partial P^{\pm}}{\partial t} = \left(\Gamma g(N,\lambda) - \alpha_l\right)P^{\pm} \tag{3.12}$$

$$\frac{\partial \phi^{\pm}}{\partial z} \pm \frac{1}{v_g}\frac{\partial \phi^{\pm}}{\partial t} = k_0\Gamma\frac{\partial n_{core}}{\partial N}(N - N_r) \tag{3.13}$$

[2] Expansion of β^2 around $\omega = -\omega_0$ is obtained by replacing $\omega - \omega_0$ by $-(\omega + \omega_0)$.

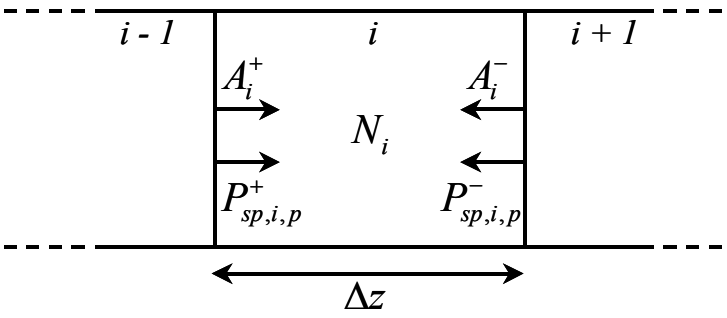

Figure 3.3: Discretization of SOA with definition of forward and backwards traveling fields and ASE spectra

where $\pm$ identifies the direction of propagation. It is important to point out that $P^{\pm}(z,t)$ is interpreted as the field power confined in the active core of the waveguide, i.e. $P^{\pm}(z,t) = \Gamma P^{\pm}_{TOT}(z,t)$, where $P^{\pm}_{TOT}(z,t)$ is the total modal power. This has implications for the boundary conditions at $z = 0$ and $z = L$, where L is the length of the SOA, as well as for the carrier rate equation given below.

Eqs. (3.12) and (3.13) can in general not be solved analytically, due to the inhomogeneity of the carrier density N along the SOA. However, by dividing the SOA into a number of sections, as illustrated in Fig. 3.3, small enough that the carrier density may be considered constant within each section, (3.12) and (3.13) may be solved numerically. Fig. 3.3 shows that the forward and backward propagating fields associated with section i, A_i^+ and A_i^-, are defined on the left and right section border, respectively. The symbols $P^{\pm}_{sp,i,p}$ represent the forward and backward propagating ASE power in a specific bandwidth identified by the index p.

Using the following finite forward-difference approximations for the differential coefficients

$$\begin{aligned} \left.\frac{\partial P}{\partial z}\right|_{i,t} &\approx \frac{P^t_{i+1} - P^t_i}{\Delta z} \\ \left.\frac{\partial P}{\partial t}\right|_{i,t} &\approx \frac{P^{t+\Delta t}_i - P^t_i}{\Delta t} \end{aligned} \tag{3.14}$$

where $P^t_i = P(z = z_i, t = t)$, the forward propagating field power (+) of eq. (3.12), may be expressed

$$\left.\frac{\partial P^+}{\partial z}\right|_{i,t} \pm \frac{1}{v_g}\left.\frac{\partial P^+}{\partial t}\right|_{i,t-\Delta t} = \left(\Gamma g(N,\lambda) - \alpha_l\right) P^+_{i,t-\Delta t} \tag{3.15}$$

This leads to

$$\begin{aligned} P_{i+1}^{+,t} &= \left(1+\left(\Gamma g(N_i^{t-\Delta t},\lambda)-\alpha_l\right)\Delta z\right)P_i^{+,t-\Delta t} \\ &\approx \exp(\left(\Gamma g(N_i^{t-\Delta t},\lambda)-\alpha_l\right)\Delta z)P_i^{+,t-\Delta t} \\ &= G_i^{t-\Delta t}(\lambda)P_i^{+,t-\Delta t} \end{aligned} \tag{3.16}$$

where

$$G_i^{t-\Delta t}(\lambda)=\exp\left[\left(\Gamma g(N_i^{t-\Delta t},\lambda)-\alpha_l\right)\Delta z\right] \tag{3.17}$$

is the single pass gain of section i at the wavelength λ, Δt is the transit time of one grid-spacing from i to $i+1$, and thus $\Delta z = v_g\Delta t$. The phase $\phi(z,t)$ does not include the phase change due to propagation (see e.g. 3.2), but this can easily be incorporated through the following Taylor expansion around the reference wavelength λ_r

$$k_0\overline{n}=\frac{2\pi}{\lambda}\overline{n}\approx 2\pi\left(\frac{\overline{n}}{\lambda_r}+n_g\left(\frac{1}{\lambda}-\frac{1}{\lambda_r}\right)\right) \tag{3.18}$$

with n_g being the group index $n_g = c_0/v_g$. Using (3.13), (3.14), (3.16), and (3.18), the finite difference equation for the forward propagating complex field envelope $A_i^{+,t} = A^+(z=z_i,t=t)$ can be expressed

$$A_{i+1}^{+,t}=\sqrt{G_i^{t-\Delta t}(\lambda)}\exp\left(j\Delta\phi_i^{t-\Delta t}(\lambda)\right)A_i^{+,t-\Delta t} \tag{3.19}$$

where $\Delta\phi_i^t$ is the single-pass phase shift of section i at wavelength λ

$$\begin{aligned} \Delta\phi_i^t(\lambda) &= \Delta\phi_i(t,\lambda) \\ &= 2\pi\Delta z\left(\frac{\overline{n}}{\lambda_r}+n_g\left(\frac{1}{\lambda}-\frac{1}{\lambda_r}\right)+\frac{\Gamma}{\lambda_r}\frac{\partial n_{core}}{\partial N}\left(N_i^t-N_r\right)\right) \end{aligned} \tag{3.20}$$

An expression for the backwards travelling field envelope $A_i^{-,t} = A^-(z=z_i,t=t)$ is obtained analogously, and the results is

$$A_{i-1}^{-,t}=\sqrt{G_i^{t-\Delta t}(\lambda)}\exp\left(j\Delta\phi_i^{t-\Delta t}(\lambda)\right)A_i^{-,t-\tau} \tag{3.21}$$

3.1.1 ASE generation and propagation

The Einstein relation states that the spontaneous emission rate per optical mode, r_{sp}, equals the stimulated emission rate per photon E_{cv} [104]. This may be expressed in terms of the material gain and the inversion parameter $n_{sp}(\lambda)$

$$r_{sp}(\lambda)=E_{cv}=(E_{cv}-E_{vc})\frac{E_{cv}}{E_{cv}-E_{vc}}=g(\lambda)n_{sp}(\lambda) \tag{3.22}$$

where the stimulated absorption rate, E_{vc}, as well as E_{cv} and r_{sp}, are in units of $(length)^{-1}$. The inversion parameter, which is also referred to as the spontaneous-emission factor, or the population-inversion factor, is given by [104]

$$n_{sp}(\lambda) = \frac{E_{cv}}{E_{cv} - E_{vc}} = \left[1 - \exp\left(\frac{hc_0/\lambda - \Delta E_{qF}}{k_B T}\right)\right]^{-1} \tag{3.23}$$

Here, $\Delta E_{qF} = E_{qF,c} + E_{qF,v} + E_g$ is the quasi Fermi-level separation, with $E_{qF,c}$ and $E_{qF,v}$ being the quasi Fermi-levels for electrons and holes in the conduction and valence bands, respectively. Eq. (3.22) implies that the number of spontaneously emitted photons at a given wavelength λ, coupled into the single guided mode of the waveguide per second, is given by $v_g \Gamma g(\lambda) n_{sp}(\lambda)$. The material gain spectrum $g(\lambda)$ is known from Appendix B, and the spontaneous-emission factor from (3.23), and thus the generation and propagation of spontaneous emission (SE), and amplified spontaneous emission (ASE), may now be described.

The equation governing the propagation of SE and ASE is analogous to (3.12), except for the addition of the spontaneous emission source term $\Gamma r_{sp}(\lambda) E(\lambda) \Delta f$, which accounts for the mean SE-power coupled into the mode in an optical bandwidth Δf around the wavelength λ

$$\frac{\partial P_{sp}^{\pm}(\lambda)}{\partial z} \pm \frac{1}{v_g} \frac{\partial P_{sp}^{\pm}(\lambda)}{\partial t} = (\Gamma g - \alpha_l) P_{sp}^{\pm}(\lambda) + \Gamma r_{sp}(\lambda) E(\lambda) \Delta f \tag{3.24}$$

Here, $P_{sp}^{\pm}(\lambda)$ is the forward/backward travelling (amplified) spontaneous emission modal power in one polarization state in the optical bandwidth Δf, and $E(\lambda) = hc_0/\lambda$ is the photon energy. Introducing a (z, t, λ_p) grid, where p identifies the spectral component of bandwidth $\Delta\lambda$, the forward propagating ASE power may be expressed

$$\begin{aligned} P_{sp,i+1,p}^{+,t} &= P_{sp,i+1}^{+,t}(\lambda_p) = G_i^{t-\Delta t}(\lambda_p) P_{sp,i}^{+,t-\Delta t} \\ &+ \frac{\Gamma g(\lambda_p, N_i^{t-\Delta t}) n_{sp}(\lambda_p, N_i^{t-\Delta t})}{\Gamma g(\lambda_p, N_i^{t-\Delta t}) - \alpha_i^{t-\Delta t}} \left(G_i^{t-\Delta t}(\lambda_p) - 1\right) \frac{hc_0^2}{\lambda_p^3} \Delta\lambda \end{aligned} \tag{3.25}$$

where $P_{sp,i+1,p}^{+,t} = P_{sp}^{+}(z = z_{i+1}, t = t, \lambda = \lambda_p)$, and $\Delta\lambda = \left(\lambda^2/c_0\right) \Delta f$ is the noise bandwidth in the wavelength domain. As for the field description, the backwards propagating ASE is obtained analogously, and the results is

$$\begin{aligned} P_{sp,i-1,p}^{-,t} &= P_{sp,i-1}^{-,t}(\lambda_p) = G_i^{t-\Delta t}(\lambda_p) P_{sp,i}^{-,t-\Delta t} \\ &+ \frac{\Gamma g(\lambda_p, N_i^{t-\Delta t}) n_{sp}(\lambda_p, N_i^{t-\Delta t})}{\Gamma g(\lambda_p, N_i^{t-\Delta t}) - \alpha_i^{t-\Delta t}} \left(G_i^{t-\Delta t}(\lambda_p) - 1\right) \frac{hc_0^2}{\lambda_p^3} \Delta\lambda \end{aligned} \tag{3.26}$$

In each spatial grid-section the carrier density can be assumed constant if Δz is small enough, and thus the solution of (3.16) and (3.25) becomes a matter of calculating the single-pass gain (3.17) and phase shift (3.20) over the entire (z, t, λ) space. In the following, the carrier rate equation is introduced, which relates the carrier density and the optical intensities in a self-consistent manner.

3.1.2 The carrier rate equation

The rate equation provides the relationship between the injected current and removal of carriers from the active region through spontaneous and stimulated recombination

$$\frac{\partial N}{\partial t} = \frac{I}{eHWL} - R(N) - \frac{1}{hc_0HW}\sum_{direction}\left(\sum_{signal,s} g(\lambda_s)\lambda_s P_s + 2\Gamma\int g(\lambda_p)\lambda_p\widetilde{P}_{sp}(\lambda_p)d\lambda_p\right) \tag{3.27}$$

Here $I, H, W, R(N)$, and $\widetilde{P}_{sp}(\lambda_p)$ is the bias current, height and width of the active region, the spontaneous recombination rate, and the spectral power density, respectively. The spontaneous recombination rate is approximated by a third-order polynomial [104]

$$R(N) = c_1N + c_2N^2 + c_3N^3 \tag{3.28}$$

where c_1, c_2, and c_3 are recombination coefficients identified as the nonradiative recombination coefficient due to traps and defects, the spontaneous radiative recombination coefficient, and the Auger coefficient, respectively. The first sum in (3.27) includes the forward and backward travelling signals, whereas the second sum represents the stimulated recombinations from the different input signals. The integration is over the entire gain bandwidth of the SOA, and accounts for the stimulated recombinations due to SE and ASE. The factor of 2 in front of the integration takes into account that spontaneous emission is random and thus distributed evenly between the two independent polarization states. In most references, e.g. [103] and [107], the signal power in (3.27) is multiplied by the confinement factor. This is not the case here, because P_s accounts for the *confined* signal power. The boundary conditions below reflect this choice of normalization.

The integration in (3.27) is carried out numerically by approximating the product $\widetilde{P}_{sp}(\lambda_p)d\lambda_p$ by $P_{sp}(\lambda_p)$, introduced in (3.25) and (3.26), and summing over the discrete wavelengths with index p.

$$\frac{\partial N_i}{\partial t} = \frac{I}{eHWL} - R(N_i) - \frac{1}{hc_0HW}\left(\sum_{signals,s} g(\lambda_s, N_i)\lambda_s P^{av}_{s,i} + 2\Gamma\sum_{p} g(\lambda_p, N_i)\lambda_p P^{av}_{sp,i,p}\right) \tag{3.29}$$

The assumption that the carrier density is constant in each section of the SOA implies that the total power is constant in each section. Thus, the summation over propagation directions has been eliminated, and the signal and ASE powers

replaced by the average powers $P_{s,i}^{av}$ and $P_{sp,i,p}^{av}$, given by

$$\begin{aligned} P_{s,i}^{av} &= \frac{1}{\Delta z}\int_i \left[\left|A_{s,i}^{+}(z)\right|^2 + \left|A_{s,i}^{-}(z)\right|^2\right] dz \\ &= \frac{G_i - 1}{\ln(G_i)}\left[\left|A_{s,i}^{+}\right|^2 + \left|A_{s,i}^{-}\right|^2\right] \end{aligned} \tag{3.30}$$

where $\left|A_{s,i}^{+}\right|$ and $\left|A_{s,i}^{-}\right|$ are the field amplitudes of the forward and backward propagating fields of wavelength λ_s, respectively, calculated on the left and right edge, respectively, of section i. Analogously, the average ASE power in section i, in the bandwidth $\Delta\lambda$ around λ_p, is given by

$$\begin{aligned} P_{sp,i,p}^{av} &= \frac{G_i(\lambda_p) - 1}{\ln(G_i(\lambda_p))}\Big[P_{sp,i,p}^{+} + P_{sp,i,p}^{-} + \\ &\quad 2\frac{\Gamma n_{sp}(\lambda_p, N_i) g(\lambda_p, N_i) h c_0^2}{\lambda_p^3 \ln(G_i(\lambda_p))}\left(G_i(\lambda_p) - 1 - \ln(G_i(\lambda_p))\right)\Big] \end{aligned} \tag{3.31}$$

3.1.3 Boundary conditions

The only thing missing for the above description to be self-consistent, is the boundary conditions of the fields and ASE power at the input and output facet of the SOA. If the sections are numbered $i = 0...N_z - 1$, from left to right, the boundary conditions for the left facet may be expressed

$$A_{out}^{-,t} = \sqrt{\xi_L} A_0^{-,t-\Delta t}\sqrt{G_0^{t-\Delta t}} e^{j\Delta\phi_0^{t-\Delta t}} \tag{3.32}$$

$$P_{sp,out,p}^{-,t} = 2\xi_L P_{sp,0,p}^{-,t-\Delta t} G_0^{t-\Delta t}(\lambda_p) \tag{3.33}$$

$$A_0^{+,t} = \sqrt{\xi_L \Gamma (1 - R_1) P_{in}^{+}(t)} + \sqrt{R_1} A_0^{-,t-\Delta t}\sqrt{G_0^{t-\Delta t}} e^{j\Delta\phi_0^{t-\Delta t}} \tag{3.34}$$

$$P_{sp,0,p}^{+,t} = R_1 P_{sp,0,p}^{-,t-\Delta t} G_0^{t-\Delta t}(\lambda_p) + (1 - R_1)\xi_L P_{sp,in,p}^{+,t}/2 \tag{3.35}$$

where A_{out}^{-} is the output field envelope at the left facet, and $P_{sp,out,p}^{-}$ is the modal ASE power at wavelength λ_p, with both independent polarization states taken into account, at the left facet. R_1, ξ_L, $P_{in}^{+}(t)$, and $P_{sp,in,p}^{+}$ are the reflectance of the left facet, the fiber/SOA coupling, the modal input signal power, and the modal input ASE power at λ_p, respectively. The latter represents the ASE power in both independent polarization states, and is thus divided by 2. For the same reason (3.33) contains a factor of 2. $P_{sp,in,p}^{+,t}$ is zero unless there is a noise source in front of the SOA, such as e.g. an additional SOA. If $P_{sp,in,p}^{+,t}$ is generated by another SOA in an integrated MZI, the coupling loss ξ_L in (3.35) is neglected ($\xi_L = 1$). Since $\left|A_{out}^{-,t}\right|^2$ in (3.32) represents the confined power, the modal output signal power from the left facet is normalized by Γ, and given by $P_{out}^{-,t} = \left|A_{out}^{-,t}\right|^2/\Gamma$.

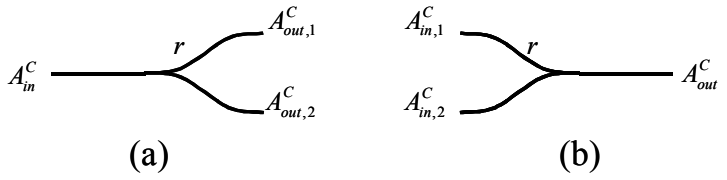

Figure 3.4: Schematic of (a) $1x2$ and (b) $2x1$ couplers, with coupling ratio γ.

Similarly for the right facet

$$A^{+,t}_{out} = \sqrt{\xi_L} A^{+,t-\Delta t}_{N_z-1} \sqrt{G^{t-\Delta t}_{N_z-1}} e^{j\Delta\phi^{t-\Delta t}_{N_z-1}} \tag{3.36}$$

$$P^{+,t}_{sp,out,p} = 2\xi_L P^{+,t-\Delta t}_{sp,N_z-1,p} G^{t-\Delta t}_{N_z-1}(\lambda_p) \tag{3.37}$$

$$A^{-,t}_{N_z-1} = \sqrt{\xi_L \Gamma (1-R_2) P^-_{in}(t)} + \sqrt{R_2} A^{+,t-\Delta t}_{N_z-1} \sqrt{G^{t-\Delta t}_{N_z-1}} e^{j\Delta\phi^{t-\Delta t}_{N_z-1}} \tag{3.38}$$

$$P^{-,t}_{sp,N_z-1,p} = R_2 P^{+,t}_{sp,out,p} + (1-R_2)\xi_L P^{-,t}_{sp,in,p}/2 \tag{3.39}$$

Here, $A^{+,t}_{out}$ is the field envelope at the right facet, and $P^+_{sp,out,p}$ is the modal ASE power at λ_p (both polarization states). R_2 is the facet reflectance and $P^-_{sp,in,p}$ is the modal ASE power at λ_p (both polarization states) launched from the right facet. As for the left facet, the modal output signal power becomes $P^{+,t}_{out} = \left|A^{+,t}_{out}\right|^2 / \Gamma$. If more than one signal is injected at either facet, which is generally the case when the SOA is part of an all-optical switch, all the signals must satisfy (3.32), (3.34), (3.36), and (3.38).

For an SOA in a MZI, there are additional boundary conditions, as several SOAs are interconnected through potentially asymmetric couplers. The asymmetric 1x2 splitter, which is sketches in Fig. 3.4 (a), may be modeled as

$$\begin{aligned} \begin{bmatrix} A^C_{out,1} \\ A^C_{out,2} \end{bmatrix} &= \underline{\underline{T}}_C(r) A^C_{in} \\ &= \begin{bmatrix} \sqrt{r} & \sqrt{1-r} \\ \sqrt{1-r} & \sqrt{r} \end{bmatrix} A^C_{in} \end{aligned} \tag{3.40}$$

where $\underline{\underline{T}}_C(r)$ is the coupler transfer matrix for the power coupling ratio r. Similarly, the 2x1 combiner in Fig. 3.4 (b) is described by

$$A^C_{out} = \underline{\underline{T}}^T_C(r) \begin{bmatrix} A^C_{in,1} \\ A^C_{in,2} \end{bmatrix} \tag{3.41}$$

where $\underline{\underline{T}}^T_C(r)$ is the transpose of $\underline{\underline{T}}_C(r)$. Due to the symmetry, these couplers do not introduce a phase shift between the two arms, as it is the case for a 2x2 coupler [108]. With the definition of the coupler transfer matrices in (3.40) and (3.41) the propagation of *signals* through the MZI in Fig. 3.2 is described in full,

and the forward propagating output field at the right facet of SOA 1, $A^+_{out,1}$, may be expressed

$$\begin{aligned} A^+_{out,1} &= A^+_{in,2}\sqrt{G_{T,1}G_{T,2}}e^{j\phi_{T,1}}e^{j\phi_{T,2}}\left[\sqrt{r_2(1-r'_3)r_1G_{T,3}}e^{j\phi_{T,3}}e^{j\Delta\phi_t}\right. \\ &\quad \left.+\sqrt{(1-r_2)r'_4(1-r_1)G_{T,4}}e^{j\phi_{T,4}}\right] \end{aligned} \tag{3.42}$$

where the time index has been omitted for clarity, and $G_{T,j}$ and $\phi_{T,j}$ are the total single pass gain and phase shift for SOA j. The corresponding output power, $P^+_{out,1}$, becomes

$$\begin{aligned} P^+_{out,1} &= P^+_{in,2}G_{T,1}G_{T,2}\left[r_2(1-r'_3)r_1G_{T,3}+(1-r_2)r'_4(1-r_1)G_{T,4}\right. \\ &\quad +2\sqrt{r_2(1-r_2)r_1(1-r_1)(1-r'_3)r'_4}\sqrt{G_{T,3}G_{T,4}} \\ &\quad \left.\times\cos\left(\phi_{T,3}-\phi_{T,4}+\Delta\phi_t\right)\right] \end{aligned} \tag{3.43}$$

Interchanging the indices 1 and 2, and + and −, an expression for the backward propagating output field at the left facet of SOA 2, $A^-_{out,2}$, is obtained. Notice that by setting $r_1 = r_2 = r'_3 = r'_4 = \frac{1}{2}$, (3.43) is reduced to the familiar expression

$$P^+_{out,1} = \frac{1}{8}P^+_{in,2}G_{T,1}G_{T,2}\left[G_{T,3}+G_{T,4}+2\sqrt{G_{T,3}G_{T,4}}\cos\left(\phi_{T,3}-\phi_{T,4}+\Delta\phi_t\right)\right] \tag{3.44}$$

ASE generated in SOA 2 propagates through the MZI, and is assumed to be modulated by a transfer function equivalent to (3.43). Thus, the contribution from SOA 2 to the forward propagating ASE at λ_p on the left (input) facet of SOA 1 becomes

$$\begin{aligned} P^+_{sp,in,p,2\to1} &= P^+_{sp,out,p,2}\left[r_2(1-r'_3)r_1G_{T,3}(\lambda_p)+(1-r_2)r'_4(1-r_1)G_{T,4}(\lambda_p)\right. \\ &\quad +2\sqrt{r_2(1-r_2)r_1(1-r_1)(1-r'_3)r'_4}\sqrt{G_{T,3}(\lambda_p)G_{T,4}(\lambda_p)} \\ &\quad \left.\times\cos\left(\phi_{T,3}(\lambda_p)-\phi_{T,4}(\lambda_p)+\Delta\phi_t\right)\right] \end{aligned} \tag{3.45}$$

ASE components generated in different SOAs have no phase correlation, and thus the interference-term vanishes. Consequently, the contribution to the forward propagating ASE power at the left facet of SOA 1 from SOAs 3 and 4 becomes

$$P^+_{sp,in,p,3/4\to1} = \begin{bmatrix} r_1 & 1-r_1 \end{bmatrix}\begin{bmatrix} P^+_{sp,out,p,3} \\ P^+_{sp,out,p,4} \end{bmatrix} \tag{3.46}$$

Here, $P^+_{sp,out,p,3}$ and $P^+_{sp,out,p,4}$ represent the ASE power at λ_p at the right facets of SOA 3 and 4, respectively, including potential ASE contributions from SOA $3'$ and $4'$. Finally, the total ASE power at λ_p at the input of SOA 1 may be expressed

$$P^+_{sp,in,p,1} = P^+_{sp,in,p,2\to1} + P^+_{sp,in,p,3/4\to1} \tag{3.47}$$

At this boundary, (3.35) relates $P^{+}_{sp,in,p,1}$ to the forward propagating ASE inside SOA 1. For ASE generated in SOA 1, propagating through the interferometer in the backward direction towards SOA 2, analogous expressions may be derived by interchanging the indices 1 and 2, and + and −.

The OSNR of each of the four possible input signals to the MZI may be set to a finite value through the input interface, as described in Appendix A. The OSNR of the signal launched into a specific port is specified in a resolution bandwidth of 1 nm. Before the signal enters the MZI it passes through a rectangular shaped BPF of width $\Delta\lambda_F$, which simulates a WDM demultiplexer, and thus the ASE power at the input of the port is given by

$$P^{\pm}_{sp,in,p} = \frac{P^{\pm}_{in}}{OSNR}\frac{\Delta\lambda_F}{1\text{ nm}} \tag{3.48}$$

where + refers to input ports $3'$, 2, and $4'$, and − refers to port 1. The result from (3.48) enters into the boundary conditions of the relevant SOAs in (3.35) and (3.39). Notice that the ASE power launched into the device is assumed homogeneously distributed over the noise bandwidth $\Delta\lambda$. This is not expected to have any impact when the noise is launched into ports $3'$ and $4'$, but for input port 2 the situation is different, since this noise is in-band to the switched signal. Thus, if $\Delta\lambda_F < \Delta\lambda$, which is the case in practice, since $\Delta\lambda = 10$ nm is typically used in the simulations, the OSNR calculated at the output of port 1 will be overestimated. As a consequence, $\Delta\lambda_F$ is set equal to $\Delta\lambda$ for signals of finite OSNR launched into ports 1 and 2.

A flow chart of the algorithm, as well as specific details about the implementation, is given in Appendix C.

3.2 Two-dimensional signal propagation

If the dimensions of the waveguide cross-section is large enough that the waveguide is multi-moded, an incident field may excite a subset of the eigenmodes. This leads to beating between the excited modes, which cannot be described without a transverse dimension. Even if the incident field only excites a single eigenmode, the photon density may no longer be considered constant in the core of the waveguide, which leads to an inhomogeneous carrier density. This cannot be accounted for with the one-dimensional model presented in section 3.1. In the following, the two-dimensional Fresnel equation, governing field propagation in two dimensions, will be derived and cast in a form suitable for discretization. The equation will be solved on a transversal, longitudinal, temporal $(x, z, t)-$ grid using a two dimensional FD-BPM, while simultaneously solving the carrier rate equation to account for the time-dependent nonlinearities experienced by the field.

Since a two-dimensional BPM calculation is very time consuming compared to the one-dimensional counterpart, a simple material gain model is used, assuming

linearity in the carrier density

$$g(N) = (\partial g/\partial N)\,(N - N_{tr}) \tag{3.49}$$

where the differential gain $\partial g/\partial N$ is independent of λ and N, and N_{tr} is the carrier density corresponding to transparency, i.e. zero material gain. Moreover, ASE is excluded, which is a reasonable assumption for high optical input power, where the contribution to gain saturation from ASE may be neglected. This argument may not hold in all cases, and in section 6.4 it will be argued that ASE may aid in reducing beating-induced cross-talk in a DOMO wavelength converter.

The starting point is the same as in the one-dimensional case, namely the definition of the field. For simplicity, the complex conjugate term in (3.2) is omitted in the following, reducing the electrical field to

$$\overrightarrow{E}(x,y,z,t) = E(x,y,z,t)\overrightarrow{e_x} = F(x,y,z,t)e^{j(\beta z-\omega_0 t)}\overrightarrow{e_x} \tag{3.50}$$

where $F(x,y,z,t)$ is the complex slowly varying field envelope. As explained in section 3.1 the SVEA is valid for signals with a small bandwidth compared to the carrier angular frequency ω_0. However, the approximation also includes the paraxial approximation, since the factoring of $e^{j(\beta z-\omega_0 t)}$ implies that the phase only evolves along the $z-$axis. This approximation holds for a small beam divergence angle, which is guaranteed in the present context, since the Fresnel equation is used to simulate long, narrow, dual-moded waveguides. The field is assumed separable in x and y

$$F(x,y) = \psi(x)\varphi(y) \tag{3.51}$$

where $\varphi(y)$ is single-moded, while $\psi(x)$ may be multi-moded. Moreover, $\varphi(y)$ is considered constant across the core, so that the inhomogeneity of the photon density occurs solely along the x direction. In the one-dimensional model the field was considered a plane wave with a finite power and a confinement factor governing the overlap with the fictitious waveguide. In this case the $y-$direction is collapsed in the same way by calculating a confinement factor Γ_y for $\varphi(y)$, and normalizing $\psi(x)$ so the instantaneous power is given by $P(z,t) = \int |\psi(x,z,t)|^2\,dx$. An expression for Γ_y is given in Appendix E. The integrand thus represents the power density, in units of $(W/m)^{\frac{1}{2}}$. With the collapsed y dimension the field envelope can be expressed

$$E(x,z,t) = \psi(x,z,t)e^{j(\beta_{ref} z-\omega_0 t)} \tag{3.52}$$

Here, $\beta_{ref} = n_0 k_0$ is a reference propagation constant, which is a convenient definition, since there is not a *single* propagation constant if $\psi(x,z,t)$ consists of a superposition of eigenmodes, as opposed to a single-moded waveguide (see

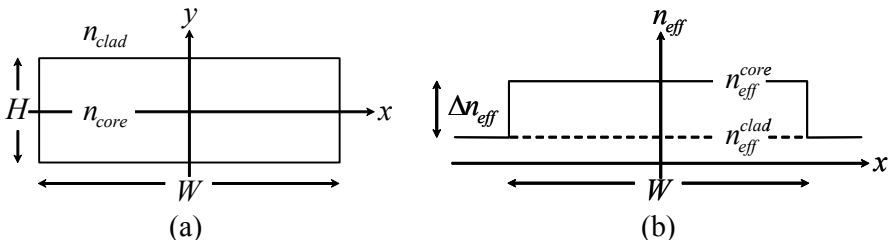

Figure 3.5: (a) Cross-section of waveguide with dimensions (W, H). (b) 1D Effective-index representation, where effect of lateral dimension is included through effective index.

(3.2)). This is clarified by expanding $\psi(x)$ in the eigenmodes $\Psi_i(x)$

$$\begin{aligned} E(x,z) &= \sum c_i \Psi_i(x) e^{j\beta_i z} \\ &= \left[\sum c_i \Psi_i(x) e^{j(\beta_i - \beta_{ref})z}\right] e^{j\beta_{ref} z} \\ &= \psi(x,z) e^{j\beta_{ref} z} \end{aligned} \tag{3.53}$$

where c_i are the field excitation coefficients, and β_i are the eigenmode propagation constants. From (3.53) it is clear that the introduction of the reference propagation constant simply adds a constant phase shift to the eigenmodes, and in return allows the term $e^{j\beta_{ref} z}$ to be factored outside $\psi(x,z)$, which proves convenient in the following. In principle, the reference index can be chosen arbitrarily. However, the beating frequencies $\beta_i - \beta_{ref}$ in (3.53) scale linearly with the difference between the mode indices and the reference index, and since a higher frequency content requires a smaller grid-spacing in the $z-$direction, the reference index should remain between the core and cladding indices to minimize the CPU time.

Fig. 3.5 (a) shows the cross section of a rectangular waveguide of width W, height H, core index n_{core}, and cladding index n_{clad}. In Fig. 3.5 (b) the $y-$ direction is collapsed, i.e. the two-dimensional cross section is reduced to a single dimension, using the EIM, which assigns an effective index n_{eff} to each value of x. This procedure is detailed in Appendix E. In the EIM the derivatives of the relative permittivities across the core-cladding boundaries are neglected, which means that the mode profile has a continuous slope at all the boundaries, regardless of the polarization of the field. This reduces the wave equation to the scalar wave equation introduced in (3.5), only in this case the $x-$ direction is included in the Laplacian

$$\left(\frac{\partial^2}{\partial x^2} + \frac{\partial^2}{\partial z^2}\right)\psi(x,z,\omega) + k_0^2\left(n_{eff}^2(x) + \chi_{NL}(x)\right)\psi(x,z,\omega) = 0 \tag{3.54}$$

Inside the core, i.e. $|x| \leq W/2$, n_{eff} equals the effective core index n_{eff}^{core}, whereas the effective index in the cladding is simply given by the cladding index, i.e. $n_{eff}^{clad} = n_{clad}$. Eq. (3.52) must satisfy the scalar wave equation, and analogous to

(3.8), the effective index is Taylor expanded to the first order around $\omega = \omega_0$

$$k_0^2 n_{eff}^2 \simeq \frac{\omega_0^2}{c_0^2}\, n_{eff}^2\big|_{\omega_0} + \frac{2\beta_{ref}}{v_g}(\omega - \omega_0) \tag{3.55}$$

where the group velocity is defined as

$$v_g^{-1} = \left[n_{eff}^2/n_0 + \omega\,(n_{eff}/n_0)\,(\partial n_{eff}/\partial\omega)\right]_{\omega_0}/c_0 \tag{3.56}$$

Inserting the Fourier transform of (3.52), $\psi(x,z,\omega)$, into (3.54) along with (3.6) and (3.55), and adding the internal scattering loss, a_l, which is assumed constant in the 2D model, the solution to (3.54) may be expressed

$$\begin{aligned}\frac{\partial\psi(x,z,\omega)}{\partial z} &= j\frac{1}{2\beta_{ref}}\frac{\partial^2\psi(x,z,\omega)}{\partial x^2} + jk_0\left[\frac{n_{eff}^2 - n_0^2}{2n_0} - \frac{\Gamma_y\alpha g(N)}{2k_0}\right]\psi(x,z,\omega) \\ &\quad + \frac{1}{2}\left(\Gamma_y g(N) - \alpha_l\right)\psi(x,z,\omega) + j\frac{\omega-\omega_0}{v_g}\psi(x,z,\omega)\end{aligned} \tag{3.57}$$

where α is the linewidth enhancement factor introduced in (3.7).

Reverting to the time domain, using (3.9), and employing a retarded reference frame t', which moves with the signal at the group velocity v_g

$$t' = t - z/v_g \tag{3.58}$$

the Fresnel equation for an active semiconductor waveguide may be expressed

$$\begin{aligned}\frac{\partial\psi(x,z,t)}{\partial z} &= j\frac{1}{2\beta_{ref}}\frac{\partial^2\psi(x,z,t)}{\partial x^2} + jk_0\left[\frac{n_{eff}^2 - n_0^2}{2n_0} - \frac{\Gamma_y\alpha g(N)}{2k_0}\right]\psi(x,z,t) \\ &\quad + \frac{1}{2}\left(\Gamma_y g(N) - \alpha_l\right)\psi(x,z,t)\end{aligned} \tag{3.59}$$

where the prime in t' is omitted for clarity. Using the retarded reference frame simplifies the implementation, but it requires all signals to propagate in the same direction, i.e. co-propagate.

3.2.1 Finite-Difference Beam Propagation Method

The Fresnel equation (3.59) may be solved in several ways, but the most efficient approach is the so-called Beam-Propagation Method (BPM) [109]. The traditional BPM employs the Fourier transform, and will thus be referred to as the FFT-BPM. The strong point of this approach is the ease of implementation, as it requires little more than a Fast-Fourier Transform algorithm. Alternatively, the BPM may be implemented using Finite-Difference (FD) approximations for the second order derivative in (3.59). This is slightly more complex, but in return the accuracy is estimated to be 5 times better than the FFT-BPM for straight

waveguides [110]. Moreover, the FFT-BPM requires an equidistant discretization in the transversal $x-$ direction, whereas an inhomogeneous grid may be employed in the FD-BPM. The latter allows for the sampling points to be distributed with a lower density in regions where the field varies on a longer scale, which reduces the number of transversal sampling points, and thus the CPU time. The FD-BPM will be outlined in the following.

In order to discretize (3.59) it is cast into the form

$$\frac{\partial \psi}{\partial z} = \mathbf{M}(z)\psi \tag{3.60}$$

where the arguments to ψ are dropped for simplicity, and $\mathbf{M}$ is an operator given by

$$\mathbf{M}(z) = \frac{j}{2n_0k_0}\left[\frac{\partial^2}{\partial x^2} + k_0^2\left(n_e^2 - n_0^2\right) - n_0k_0\Gamma_y\alpha g(N) - jn_0k_0\left(\Gamma_y g(N) - \alpha_l\right)\right] \tag{3.61}$$

The formal solution to (3.60), in the section from $z = z_k$ to $z = z_{k+1} = z_k + \Delta z$, is

$$\begin{aligned}\psi(z_{k+1}) &\approx e^{\mathbf{M}(z)\mathbf{\Delta} z}\psi(z_k) \\ &= \exp\left[\mathbf{P}(z_k)\Delta z\right]\exp\left[\mathbf{D}\Delta z\right]\psi(z_k)\end{aligned} \tag{3.62}$$

where $\mathbf{M}(z)$, $\mathbf{D}$, and $\mathbf{P}$(z) are considered constant within the section, and $\mathbf{D}$ and $\mathbf{P}$(z) are given by

$$\mathbf{D} = \frac{j}{2n_0k_0}\frac{\partial^2}{\partial x^2} \tag{3.63}$$

$$\mathbf{P}(z) = \frac{j}{2n_0}\left[k_0\left(n_e^2 - n_0^2\right) - n_0\Gamma_y\alpha g(N) - jn_0\left(\Gamma_y g(N) - \alpha_l\right)\right] \tag{3.64}$$

The two operators $\mathbf{D}$ and $\mathbf{P}$ are responsible for diffracting and propagating the optical beam, respectively. The operation $e^{\mathbf{D}\Delta z}\psi$ is difficult to evaluate, but by Taylor expanding the operator to the first order in Δz, it may be expressed $e^{\mathbf{D}\Delta z} \approx 1 + j\Delta z/(2n_0k_0)(\partial^2/\partial x^2)$. However, this operator is not Hermitian, and consequently does not conserve energy [111]. Considering instead the Hermitian operator $\mathbf{\Lambda}$ [112]

$$\mathbf{\Lambda} = \mathbf{\Lambda}^+\left[\mathbf{\Lambda}^-\right]^{-1} = \left[1 + j\frac{\Delta z}{4n_0k_0}\frac{\partial^2}{\partial z^2}\right]\left[1 - j\frac{\Delta z}{4n_0k_0}\frac{\partial^2}{\partial z^2}\right]^{-1} \tag{3.65}$$

it is readily shown that the first order expansion of $\mathbf{\Lambda}$ equals

$$\Lambda \approx 1 + j\Delta z/(2n_0k_0)(\partial^2/\partial x^2) \tag{3.66}$$

which means that $e^{\mathbf{D}(z)\Delta z}$ may be approximated by Λ, if Δz is sufficiently small that the first-order approximation is valid. Thus, (3.62) may be expressed

$$\psi(z_{k+1}) \approx \mathbf{M}_P\mathbf{\Lambda}^+\left[\mathbf{\Lambda}^-\right]^{-1}\psi(z_k) \tag{3.67}$$

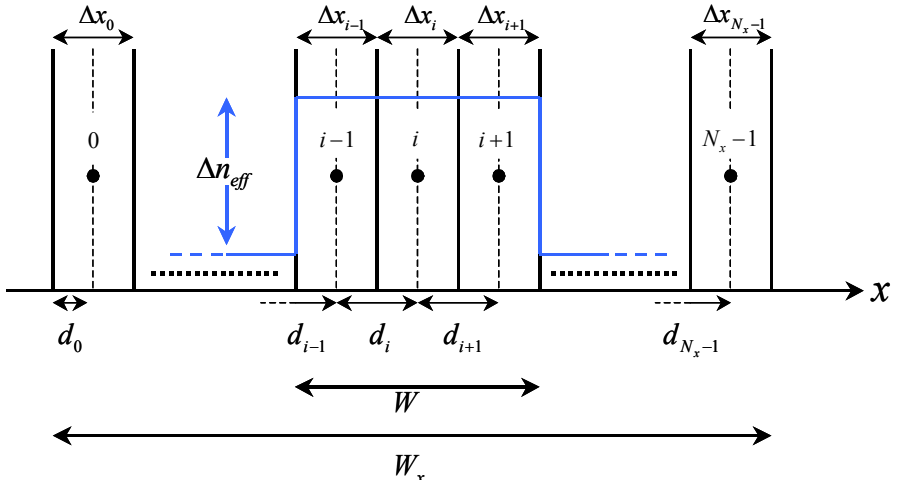

Figure 3.6: Definition of inhomogeneous transversal grid.

where $\mathbf{M}_P = \exp(\mathbf{P}(z)\Delta z)$. The field $\psi(x,z)$ is sampled on the inhomogeneous $x-$ grid shown in Fig. 3.6 and is represented by the vector $\underline{\underline{\psi}}$. The grid is made up of N_x points numbered from 0 to $N_x - 1$, distributed over the width W_x of the computation window, and each point being the center of a section of width Δx_i. The spacing between the sampling points $i-1$ and i is denoted d_i and given by $\frac{1}{2}(\Delta x_{i-1} + \Delta x_i)$, except for the special case of $i = 0$ at the left boundary of the calculation window, where $d_0 = \frac{1}{2}\Delta x_0$. Fig. 3.6 also illustrates the refractive step-index profile. The second order derivatives in Λ^+ and Λ^- are approximated by the finite-difference equivalents [113]

$$\begin{aligned}
\left(\frac{\partial\psi}{\partial x}\right)_i &= \psi_i' = \frac{\psi_{i+\frac{1}{2}} - \psi_{i-\frac{1}{2}}}{\Delta x_i} \\
\left(\frac{\partial^2\psi}{\partial x^2}\right)_i &= \frac{\psi'_{i+\frac{1}{2}} - \psi'_{i-\frac{1}{2}}}{\Delta x_i} \\
&= \frac{2}{d_i + d_{i+1}}\left[\frac{1}{d_{i+1}}\psi_{i+1} + \frac{1}{d_i}\psi_{i-1} - \left(\frac{1}{d_{i+1}} + \frac{1}{d_i}\right)\psi_i\right]
\end{aligned} \tag{3.68}$$

Inserting (3.68) into (3.64) and (3.65), the finite-difference approximations to $\mathbf{M}_P$, $\mathbf{\Lambda}^+$ and $\mathbf{\Lambda}^-$ may be expressed in terms of the $N_x - 1 \times N_x - 1$ matrices

$$\underline{\underline{\mathbf{\Lambda}}}^{\pm} = \begin{bmatrix}
d_0^{\pm} & b_0^{\pm} & 0 & 0 & 0 \\
a_1^{\pm} & d_1^{\pm} & b_1^{\pm} & \ddots & 0 \\
0 & \ddots & \ddots & \ddots & 0 \\
0 & \ddots & a_{N_x-2}^{\pm} & d_{N_x-2}^{\pm} & b_{N_x-2}^{\pm} \\
0 & 0 & 0 & a_{N_x-1}^{\pm} & d_{N_x-1}^{\pm}
\end{bmatrix} \tag{3.69}$$

where the diagonal elements $d_i^{\pm}$ and off-diagonal elements $a_i^{\pm}$ and $b_i^{\pm}$ are given by

$$d_i^{\pm} = 1 \mp j\frac{\Delta z}{2n_0 k_0 d_i d_{i+1}} \tag{3.70}$$

$$a_i^{\pm} = \pm j\frac{\Delta z}{2n_0 k_0 d_i \left(d_i + d_{i+1}\right)} \tag{3.71}$$

$$b_i^{\pm} = \pm j\frac{\Delta z}{2n_0 k_0 d_{i+1} \left(d_i + d_{i+1}\right)} \tag{3.72}$$

Notice that the matrix formulation in (3.69) implies that the field is zero outside the computation window, since ψ_{i-1} and ψ_{i+1} are ignored for $i = 0$ and $i = N_x - 1$, respectively. This is referred to as the Dirichlet boundary condition [110], and the consequences of using this condition will be discussed later.

The elements p_i of the diagonal propagation matrix $\underline{\underline{\mathbf{M}}}_P$ are expressed

$$p_i = \frac{j}{2n_0}\left[k_0\left(n_{e,i}^2 - n_0^2\right) - n_0\Gamma_y\alpha g(N_{i,k}) - jn_0\left(\Gamma_y g(N_{i,k}) - \alpha_l\right)\right] \tag{3.73}$$

where $n_{e,i}$ and $N_{i,k}$ are the effective index profile and transversal carrier density profile at $z = z_k$. The waveguide is considered straight, and thus $n_{e,i}$ is independent of z.

Since the matrices are sparse, it is advantageous to evaluate $\left[\underline{\underline{\mathbf{\Lambda}}}^-\right]^{-1}\psi(z)$ through Gauss elimination, i.e. by solving the equation

$$\left[\underline{\underline{\mathbf{\Lambda}}}^- \middle| \underline{\psi}\right] \tag{3.74}$$

Similarly, the multiplications by $\underline{\underline{\mathbf{\Lambda}}}^+$ and $\underline{\underline{\mathbf{M}}}_P$ can be evaluated significantly faster by taking advantage of the sparsity. Propagation from input to output is obtained by repeating (3.67) N_z times, where N_z is the number of sampling points in the $z-$ direction.

The grid spacing is allowed to be inhomogeneous in order to optimize the distribution of sampling points. According to the wave equation the eigenmodes are oscillating along the transversal $x-$ axis inside the core of the waveguide, and decay exponentially in the cladding. Consequently, a higher density of sampling points is needed in the core to resolve the oscillations, compared to the monotonous decay in the cladding. In this work the grid spacing assumes the form [114]

$$d_i = \begin{cases} d_{core}(1 + r_{grid})^{-(i - i_L)} & i \le i_L \\ d_{core} & i_L < i < i_H \\ d_{core}(1 + r_{grid})^{i - i_H} & i \ge i_H \end{cases} \tag{3.75}$$

where d_{core} is the spacing in the core, i_L and i_H are the indices corresponding to the lower and upper boundary of a range containing the core, as illustrated

in Fig. 3.7. r_{grid} is the relative increase of the grid spacing per step, which is related to the maximum spacing $d_{\max} = d_{core} R_{\max}$ through

$$R_{\max} = (1 + r_{grid})^{\max(N_x - i_H - 1, i_L)} \tag{3.76}$$

If the core is centered in the calculation window, $N_x - i_H - 1$ and i_L are equal, in which case the exponent in (3.76) may be replaced by i_L. The indices i_L and i_H define a range slightly larger than the core, in order to allow the field to decay from the values at the boundary, before the grid spacing is increased.

The input field will inevitably excite non-guided cladding modes. This is the case even if the input field is an eigenmode of the waveguide, due to the discretization. The cladding modes radiate into the cladding, which prompts the need for boundary conditions. As mentioned previously, the very simple zero-field or Dirichlet conditions are employed at the boundaries of the computation window. Setting the field equal to zero is equivalent to placing reflecting surfaces at the boundaries, and this is generally a problem because the reflection re-enters the waveguide and interferes with the guided field. A solution to this problem may be obtained by placing an absorbing region at the boundary, thereby effectively suppressing the radiated and reflected field. However, the position of these regions and the magnitude of the absorption are critical parameters that make this approach non-trivial [110]. Generally, the absorbing regions must be placed as far away from the core as possible, in order to avoid absorption of the guided modes, implying a large computation window. In this regime, a comparison between periodic boundary conditions[3] including absorbing regions and the Dirichlet condition has been carried out [110], and the performance was found to be comparable in terms of accuracy. Moreover, using an inhomogeneous grid the computation window may be increased significantly at the expense of a relatively modest increase of N_x. In conclusion, Dirichlet conditions are sufficient as long as $W_x >> W$. In the present case, the field in the core of the waveguide experiences gain, while the field in the cladding observes the constant absorption a_l, which corresponds to an extreme case of absorbing boundaries. This relaxes the requirement to the size of the computation window, and thus reduces CPU time.

3.2.2 The 2D carrier rate equation

In the carrier rate equation introduced in section 3.1 diffusion of carriers was neglected, since the carrier density was assumed constant in each cross-section of the active region. This assumption does not hold for wide waveguides, and the

[3] Field leaving left boundary enters at right boundary, and vice versa.

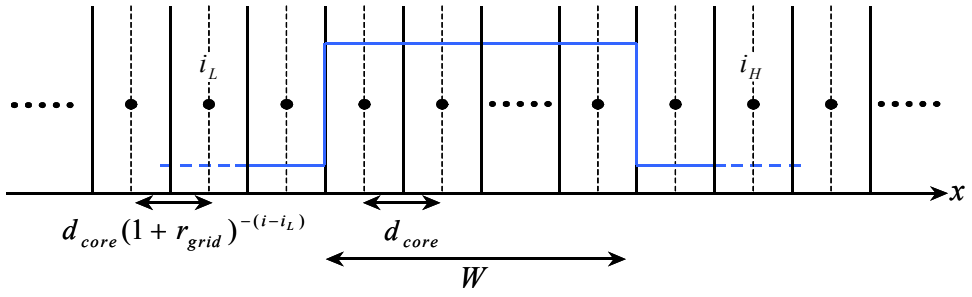

Figure 3.7: Assignment of inhomogeneous grid sizes.

diffusion term is thus included

$$\frac{\partial N_{i,k}}{\partial t} = \frac{I}{eHWL} - R(N_{i,k}) - \frac{1}{hc_0 H}\left|\sum_{signals,s}\sqrt{g(N_{i,k})\lambda_s}\psi_s(x_i,z_j,t)\right|^2 + D_x\frac{\partial^2 N_{i,k}}{\partial x^2} \tag{3.77}$$

where i identifies the sampling point on the $x-$ axis, and D_x is the transversal diffusion coefficient. Diffusion along the $z-$ direction is neglected, since the diffusion length $L_D = \sqrt{D_z\tau_e}$ is much smaller than L [103, 115], where τ_e is the effective carrier lifetime, introduced formally in Chapter 4. Since ASE is neglected, the term responsible for ASE induced carrier depletion in (3.27) is excluded. The sum accounts for the beating between the signals, which gives rise to an oscillating term in the rate equation. Assuming that two real field distributions, $\psi_0(x)$ and $\psi_1(x)$, are launched into the waveguide, and $\psi_1(x)$ is detuned by $\Delta\omega = \omega_1 - \omega_0$ compared to $\psi_0(x)$, the absolute square of the sum in (3.77) at $z = z_k$ becomes

$$\begin{aligned}&\left|\sqrt{g_0\lambda_0}\psi_0(x)e^{j\beta_0 z_k} + \sqrt{g_1\lambda_1}\psi_1(x)e^{j(\beta_1 z_k+\Delta\omega t)}\right|^2 \\ = \;& g_0\lambda_0\left|\psi_0(x)\right|^2 + g_1\lambda_1\left|\psi_1(x)\right|^2 \\ &+2\sqrt{g_0 g_1\lambda_0\lambda_1}\psi_0(x)\psi_1(x)\cos\left[\left(\beta_0-\beta_1\right)z_k - \Delta\omega t\right]\end{aligned} \tag{3.78}$$

where β_0 and β_1 are the propagation constants of the two fields. If the frequency detuning $\Delta\omega/(2\pi)$ exceeds the carrier modulation frequency the last term in (3.78) may be neglected. However, for smaller detunings the carrier density will be modulated at the frequency $\Delta\omega$, and generate four-wave mixing (FWM) products at $2\omega_1 - \omega_0$ and $2\omega_0 - \omega_1$ [116]. Moreover, if $\psi_0(x)$ and $\psi_1(x)$ are of opposite symmetry, i.e. even and odd, respectively, the transversal carrier density distribution will oscillate between antisymmetric states at the frequency $\Delta\omega$. The impact of these oscillations and the interaction with carrier diffusion will be investigated in section 6.4.

The grid spacing Δz in the longitudinal direction must be significantly smaller (typically a factor of 20) in the two-dimensional model compared to the one-dimensional case. This is because Δz must be able to resolve the potentially

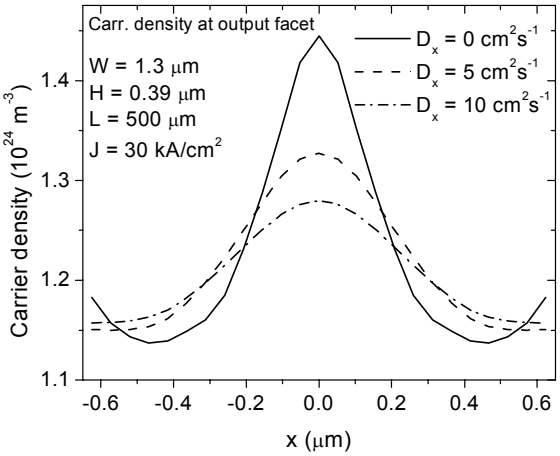

Figure 3.8: Transverse carrier density profile for different values of the diffusion coefficient D_x.

high spatial beat frequencies between the fundamental mode and higher-order cladding modes. More detail of how to estimate the necessary grid spacing is given in appendix C. The small longitudinal section width means that the section gain is very close to 1, and thus the average power in a given section may be approximated by the power at the input of the section. This corresponds to approximating $(G-1)/\ln(G)$ in (3.30) by 1.

The second order derivative of the carrier density in (3.77) is approximated by (3.68), thereby relating the carrier density in a specific transversal grid point i to the carrier density in the neighboring points $i-1$ and $i+1$. Analogous to the field a set of boundary conditions must be defined for the carrier density at the core-cladding interfaces. The carrier density will generally be significantly lower in the cladding, compared to the active core, and thus a large carrier density gradient is expected. However, the intrinsic core of the SOA is surrounded by a p and $n-$ doped layer to form a $p-i-n$ heterostructure, which gives rise to bandgap discontinuities at the interfaces [117]. The discontinuities increase the carrier confinement, which inhibits diffusion across the interface. Here, it will be assumed that the carrier densities associated with the grid points just *outside* the core are equal to the densities just *inside* the core. This corresponds to setting $N_{i-1} = N_i$ at the left boundary, and $N_{i+1} = N_i$ at the right boundary, which clearly corresponds to a gradient of zero at the boundaries. This is illustrated in Fig. 3.8, where the carrier density distribution at the output of a 500 μm long dual-moded SOA is shown for different transversal diffusion parameters. The dimensions of the SOA waveguide are $(W, H, L) = (1.3, 0.39, 500)$ μm, it is pumped with a current density of $J = I/(WL) = 30$ kA/cm^2, and excited by the first-order eigenmode, containing 0 dBm of power. The 'smoothing' effect of diffusion, as well as the vanishing gradient at the boundary (for $D_x \neq 0$) is clearly observed.

A flow chart of the propagation algorithm is given in Appendix C.

3.3 Summary

Two models, capable of describing field propagation in single-moded and multi-moded forward biased semiconductor waveguides are presented in this Chapter.

For the one-dimensional model, propagation of the complex field envelope and the ASE power in both directions is thoroughly treated. The interaction between the optical intensities and the gain is governed by the carrier rate equation, which together with the boundary conditions for the signal and ASE powers forms a self-consistent solution. Between 2 and 6 independent SOAs may be arranged in a MZI structure, where signal fields and ASE intensities travel bidirectionally through the entire interferometer.

The two-dimensional model consists of a finite-difference beam-propagation solution to the Fresnel equation, combined with the two-dimensional carrier rate equation to form a self-consistent set of equations. ASE is not included in the 2D-model to keep the computation time at a level, which allows for optimizations.

Chapter 4

Carrier dynamics

In this Chapter the effects governing the optical modulation bandwidth of an SOA will be identified and illustrated through simulations.

Taking one step back and simplifying the detailed SOA model introduced in section 3.1 by e.g. neglecting ASE, the response of the probe signal, in the presence of a modulated pump, is investigated in the small-signal regime for co- and counter propagating signals. This allows for setting forth very general guidelines for how the modulation bandwidth can be enhanced by optimizing the operating conditions and waveguide design. The conclusions drawn on the basis of the small-signal analysis are shown to be valid for large-signal modulation as well.

The detrimental patterning effects, caused by the finite response time of the SOA, are grouped into two categories: *linear* and *nonlinear* patterning, and schemes for alleviating them are discussed.

4.1 Small-signal analysis

Fig. 4.1 shows a simulation of the carrier density (upper row), probe power (center row), and control signal power (bottom row) at the input (left column), in the middle (center column), and at the output (right column) of a 1000 μm long SOA with a finite waveguide loss, defined by the parameters in Appendix D. The control input signal is a single 5 ps (FWHM) wide Gaussian pulse, as shown in Fig 4.1 (g), whereas the input probe signal is a 3 dBm CW beam. The SOA is biased at a current density of 30 kA/cm^2, and the cross-section of the active region is $(W, H) = (0.7, 0.5)$ μm, with an index step giving rise to a confinement factor of $\Gamma = 0.60$. All other simulation parameters are given in appendix D. Several important facts may be extracted from Fig. 4.1. First, the recovery of the carrier density after depletion by the control pulse is slow in the front of the SOA ($\approx$ 400 ps), but becomes increasingly faster as the pulse propagates, and is reduced to $\approx$ 20 ps at the output. Secondly, the carrier density, probe and control signal

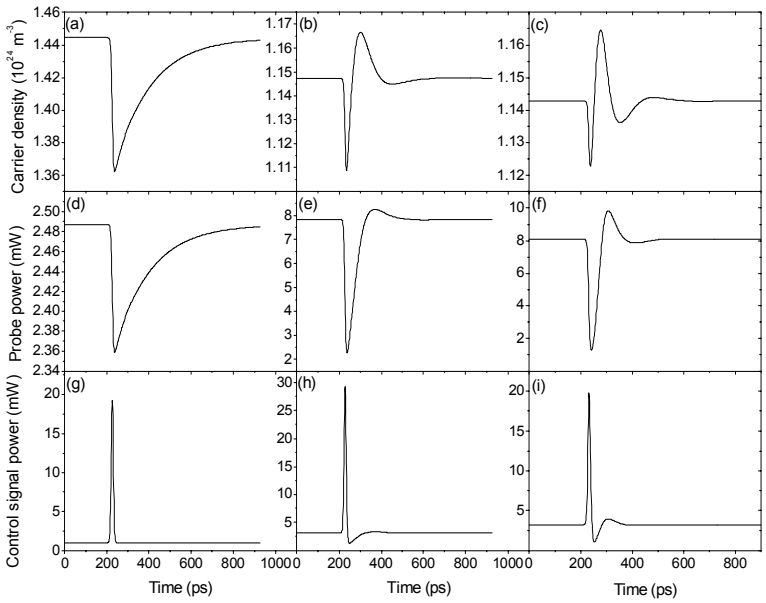

Figure 4.1: Evolution of carrier density (upper row), probe power (middle row), and control pulse power (bottom row) from the front of the SOA (left column), the middle of the SOA (middle column), and at the output (right column). Both signal wavelengths are 1550 nm, and waveguide loss is included.

powers go through a temporal overshoot, which grows with propagation distance. Both phenomena are due to the so-called travelling-wave effects or propagation effects, and are described conveniently in the small-signal modulation regime. In particular, the overshoot can be ascribed to the finite waveguide loss.

In this section, the expressions for the small-signal response of a cross-gain modulated probe signal will be reviewed, using the results of [107] and [118]. The response depends qualitatively on the relative orientation of the control and probe signals, and the scenario where signals counter-propagate through the SOA will therefore be investigated separately from co-propagation.

4.1.1 Co-propagation

The control and probe modal signal powers, $P_C(t)$ and $P_P(t)$ are defined as harmonic perturbations to a steady-state powers

$$P_i(t) = \overline{P}_i + p_i(\Omega)e^{-j\Omega t} + p_i^*(\Omega)e^{j\Omega t} \tag{4.1}$$

where $i = C, P$. $\overline{P}_i$ is the steady-state value of $P_i(t)$ and $p_i(\Omega)$ is the complex small-signal modulation amplitude corresponding to the modulation frequency $\Omega/(2\pi)$. Co-propagation of $P_C(t)$ and $P_P(t)$ is described in the retarded reference frame (3.58), which transforms the propagation equation (3.15) into

$$\frac{dP_i}{dz} = (\Gamma g - \alpha_l)\, P_i \tag{4.2}$$

Here, the material gain g is linearized in N as shown in (3.49). To maintain clarity, the carrier rate equation used in the small-signal analysis is simplified compared to (3.27) by linearizing the spontaneous recombinations rate, $R(N) = N/\tau_{sp}$, where τ_{sp}^{-1} is given by dR/dN, evaluated at the average carrier density in the SOA. Moreover, ASE is neglected, which means the steady state input powers must be high enough that the saturation from ASE may be neglected. Since $P_i(t)$ represents the modal power, the rate equation becomes

$$\frac{\partial N}{\partial t} = \frac{I}{eHWL} - \frac{N}{\tau_{sp}} - \frac{\Gamma\lambda g}{hc_0 HW} P_T(t) \tag{4.3}$$

where $P_T(t) = P_C(t) + P_P(t)$ and both signals are assumed to be at the same wavelength λ. Expanding the carrier density $N(t)$ to the first order in Ω

$$N(t) = \overline{N} + \Delta N(\Omega) e^{-j\Omega t} + \Delta N^*(\Omega) e^{j\Omega t} \tag{4.4}$$

and inserting it into (4.3) gives the following expression for the small-signal perturbation of the carrier density

$$\Delta N(\Omega) = -\frac{(\overline{N} - N_{tr})/P_{sat}}{1 + \overline{P}_T/P_{sat} - j\Omega\tau_{sp}} p_T(\Omega) \tag{4.5}$$

where $\overline{P}_T = \overline{P}_C + \overline{P}_P$, $p_T(\Omega) = p_C(\Omega) + p_P(\Omega)$, and P_{sat} is the saturation power defined as $P_{sat} = HWhc_0/\left[\lambda(\partial g/\partial N)\Gamma\tau_{sp}\right]$. Although it is not explicit in (4.5), $\Delta N(\Omega)$ depends on z through $\overline{N}$, $\overline{P}_T$, and $p_T(\Omega)$. Inserting (4.1) into (4.2), and using (4.5), the propagation equations for the steady state powers and modulation amplitudes may be expressed

$$\frac{\partial \overline{P}_i}{\partial z} = (\Gamma g - \alpha_l)\,\overline{P}_i \tag{4.6}$$

$$\frac{\partial p_i}{\partial z} = (\Gamma g - \alpha_l) p_i(z,\Omega) - \frac{\Gamma g \overline{P}_i(z)/P_{sat}}{1 + \overline{P}_T(z)/P_{sat} - j\Omega\tau_{sp}} p_T(z,\Omega) \tag{4.7}$$

After some algebra the solution to (4.7) may be expressed [118]

$$p_i(z,\Omega) = G(z)\left\{ p_i(0,\Omega) - \frac{\overline{P}_i(0) p_T(0,\Omega)}{\overline{P}_T(0)} \left(1 - \exp\left[-K(z,\Omega)\right]\right) \right\} \tag{4.8}$$

Assuming that the input probe signal is CW, i.e. $p_P(0,\Omega) = 0$, the total modulation at the input becomes $p_T(0,\Omega) = p_C(0,\Omega)$. The function $K(z,\Omega)$ is given by

$$K(z,\Omega) = \int_0^z \frac{\Gamma g(\widetilde{z}) P_T(\widetilde{z})}{P_{sat} + P_T(\widetilde{z}) - j\Omega\tau_{sp} P_{sat}} d\widetilde{z} \tag{4.9}$$

$$= \frac{1}{1 - j\Omega\tau_{sp}\xi}\left\{ \xi \ln\frac{G_0(z)}{G(z)} - \ln\left[1 - \frac{(G(z)-1)\overline{P}_T(0)/P_{sat}}{1 + G(z)\overline{P}_T(0)/P_{sat} - j\Omega\tau_{sp}}\right]\right\}$$

where ξ is the normalized waveguide loss $\xi = \alpha_l/(\Gamma g_0)$, and $G_0(z)$ and $G(z)$ are the unsaturated and saturated gains given by $G_0(z) = \exp[\Gamma g_0(1-\xi)z]$ and $G(z) = \overline{P}_T(z)/\overline{P}_T(0)$, respectively. The unsaturated material gain coefficient g_0 is given by $g_0 = (\partial g/\partial N)[\tau_{sp} I/(eHWL) - N_{tr}]$, which is readily seen from (4.3) by setting $P_T(t) = 0$. Similarly, (4.3) leads to the well-known relationship between the saturated and unsaturated gain coefficients [118]

$$g = g_0/(1 + \overline{P}_T/P_{sat}) \tag{4.10}$$

Inserting (4.10) in (4.6), with $i = T$, and integrating from $z' = 0$ to $z' = z$, $G(z)$ may be obtained implicitly through the equation [118]

$$\ln \frac{1 - \xi\left(1 + \overline{P}_T(0)/P_{sat}\right)}{1 - \xi\left(1 + G(z)\overline{P}_T(0)/P_{sat}\right)} = \xi \ln \frac{G_0(z)}{G(z)} \tag{4.11}$$

Combining (4.8), (4.9) and (4.10), the spatial evolution of the frequency responses $p_C(z,\Omega)$ and $p_P(z,\Omega)$ is obtained.

Before going into details about the effect of waveguide loss, the expression for the probe response in the loss-less case ($\xi = 0$) is considered. In this limit $p_P(L,\Omega)$ is reduced to

$$p_P(L,\Omega) = -\frac{G(L)(G(L)-1)\overline{P}_P(0)\tau_e(L)/(P_{sat}\tau_{sp})}{-j\Omega\tau_e + 1} p_C(0,\Omega) \tag{4.12}$$

where $G(L)$ is calculated from the loss-less equivalent of (4.11), which is reduced to $(G(z)-1)P_T(0)/P_{sat} = \ln(G_0(z)/G(z))$. The parameter τ_e is the effective carrier lifetime, mentioned in section 3.2, and formally defined as

$$\begin{aligned} \tau_e^{-1}(z) &= \tau_{sp}^{-1} + \frac{\Gamma\lambda(\partial g/\partial N)P_T(z)}{hc_0 HW} \\ &= \tau_{sp}^{-1} + \frac{P_T(z)}{P_{sat}\tau_{sp}} \end{aligned} \tag{4.13}$$

The probe amplitude response at the output of the SOA, $p_P(L,\Omega)$, describes the impact on a probe signal of the carrier density modulation imposed by a small-signal modulated control signal, and will in the following be referred to as the carrier density response (CDR). The normalized CDR, evaluated at $z = L$, is given by

$$\begin{aligned} T_N^{CDR}(L,\Omega) &= p_P(L,\Omega)/p_P(L,0) \\ &= \frac{1}{-j\Omega\tau_e(L) + 1} \end{aligned} \tag{4.14}$$

which is a low-pass function with a -3 dB bandwidth of

$$\Omega_{3dB} = \sqrt{3}\tau_e^{-1}(L) \tag{4.15}$$

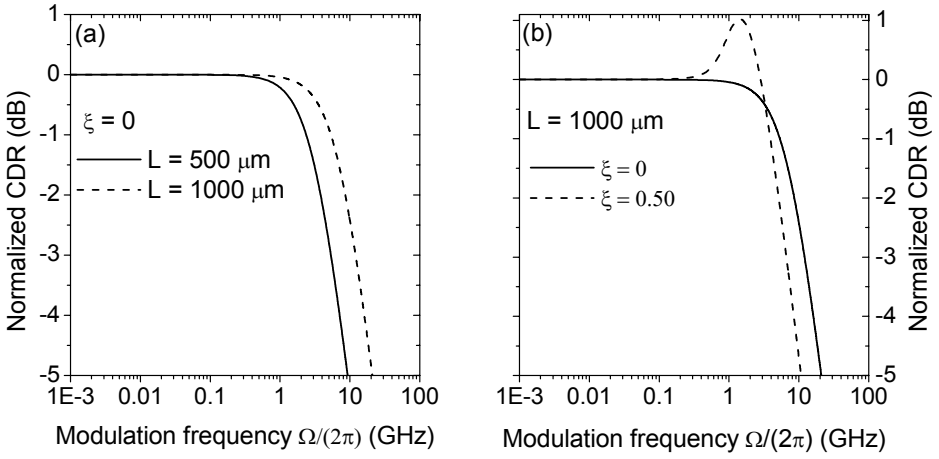

Figure 4.2: (a) Normalized CDR in the loss-less case for $L = 500$ μm (solid) and $L = 1$ mm (dashed). (b) Comparison of CDR with (dashed) and without loss (solid) for $L = 1$ mm. SOA dimensions same as in Fig. 4.1, $P_T(0) = 1$ mW, $\partial g/\partial N = 5 \cdot 10^{-20}$ m^2, $N_{tr} = 1 \cdot 10^{24}$ m^{-3}, and $\tau_{sp} = 500$ ps.

and a high frequency slope of -10 dB/decade. The second term of (4.13) accounts for the contribution to τ_e^{-1} from stimulated emission, which is observed to increase with z, as long as the gain increases with length. This effect is commonly referred to as the travelling-wave effect or simply the propagation effect, and explains the decrease of the recovery time in Fig. 4.1 (d-f) as the probe signal propagates through the SOA. Fig. 4.2 (a) shows the normalized amplitude of the CDR in the loss-less case for $L = 500$ and 1000 μm, and as expected the response is a low pass function, and the -3 dB bandwidth is larger for $L = 1000$ μm.

Taking the finite waveguide loss into account the CDR cannot be expressed analytically, but must be solved numerically. This has been done for $L = 1000$ μm and a normalized loss of $\xi = 0$ and $\xi = 0.5$, and the results are shown in Fig. 4.2 (b). As a direct consequence of the loss the response displays a resonance and the bandwidth is decreased. Although it has not been verified analytically, extensive modeling has shown complete correspondence between a resonance in the CDR and an overshoot in the large signal probe response. This observation is supported by [107,118,119]. Based on this finding, the overshoot in Fig. (4.1) (e-f) is expected to vanish for $\alpha_l = 0$.

This is verified in Fig. 4.3 (a) where the simulation in Fig. 4.1 (f) is plotted along with the corresponding temporal probe response for $\alpha_l = 0$. According to (4.13) and (4.15) the bandwidth increases linearly with the gain for $\xi = 0$

$$\Omega_{3dB} = \frac{\sqrt{3}}{\tau_{sp}} \left(\frac{P_T(0)}{P_{sat}} G + 1 \right) \tag{4.16}$$

After the first part of the SOA, corresponding to positions $z > z'$, the carrier density attains an almost constant value $\overline{N}'$ close to the transparency value N_{tr}. This is clearly seen in Fig. 4.3 (b), which shows the carrier density vs. z for $\xi = 0$

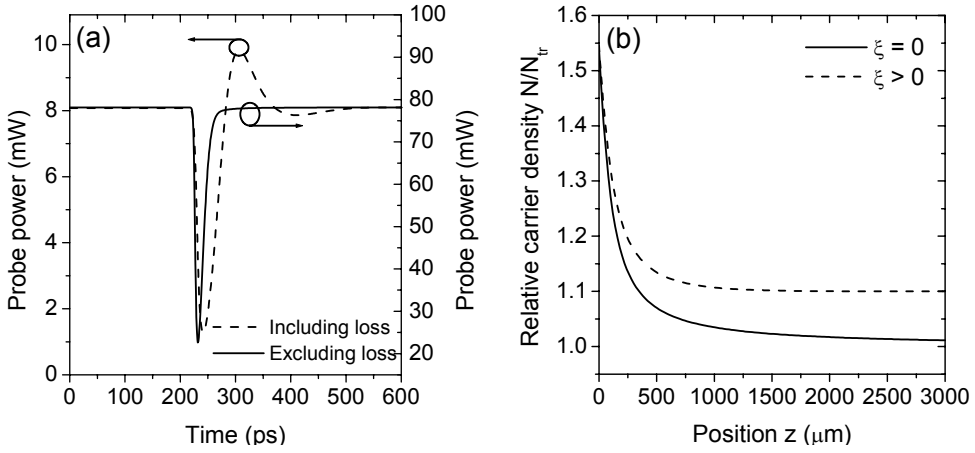

Figure 4.3: (a) Comparison of probe response from Fig. 4.1 (f) (dashed) with the corresponding response without loss (solid). Both curves are calculated with detailed model from section 3.1. (b) Spacial variation of carrier density through SOA with loss (dashed, $\xi = 0.5$) and without loss (solid). Both curves obtained with simpler model presented in this section. Parameters are the same as in Fig. 4.2.

and $\xi > 0$. Since g is small, the gain $\Delta G(z)$ of this part of the SOA may be expressed

$$\begin{aligned} \Delta G(z) &= G(z)/G(z') = \exp(\Gamma g(z - z')) \\ &\approx 1 + \Gamma g(z - z') \end{aligned} \tag{4.17}$$

where $g = (\partial g/\partial N)(\overline{N}' - N_{tr})$. Thus, $G(L)$ increases linearly with L for long amplifiers, leading to the small-signal bandwidth Ω_{3dB} increasing linearly with the slope

$$\frac{\partial \Omega_{3dB}}{\partial z} = \frac{\sqrt{3}}{\tau_{sp}} \frac{\Gamma g G(z') P_T(0)}{P_{sat}} \tag{4.18}$$

The linear dependence of gain and bandwidth with SOA length for $\xi = 0$ is verified in Fig. 4.4, which shows the gain and effective carrier lifetime (a) and small-signal bandwidth $\Omega_{3dB}/(2\pi)$ (b) as a function of SOA length for $\xi = 0$, 0.2, and 0.5, using a constant current density of $J = 30$ kA/cm^2. As observed in Fig. 4.4 (a), the gain approaches a fixed value in the long-length limit for a finite waveguide loss. This is because, as shown in Fig. 4.3 (b), the carrier density attains a level after z' at which the gain balances the loss, and in this limit $\Delta G = 1$. Correspondingly, the effective carrier lifetimes for $\xi > 0$ approach finite values in the long-length limit.

Based on the explanation for the linear bandwidth increase for $\xi = 0$ in (4.18) it may seem surprising that the bandwidth also increases linearly with z for $\xi > 0$, since the gain is limited. However, for $z > z'$ the gain g is constant, and from (4.8) the total modulation $p_T(z, \Omega)$ is found to evolve as

$$p_T(z, \Omega) = G(z) p_C(0, \Omega) e^{-K(z,\Omega)} \tag{4.19}$$

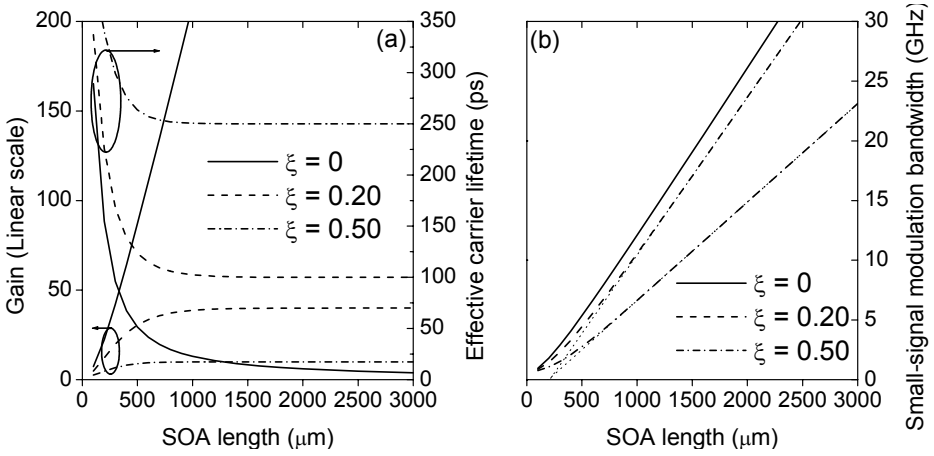

Figure 4.4: (a) Gain (left axis) and effective carrier lifetime (right axis) vs. SOA length for $\xi = 0$, 0.2, and 0.5. (b) -3 dB small-signal modulation bandwidth vs. SOA length for $\xi = 0$, 0.2, and 0.5, including linear approximations. $\partial g/\partial N = 5 \cdot 10^{-20}$ m^2, $N_{tr} = 1 \cdot 10^{24} m^{-3}$

where $K(z,\Omega)$, according to the first line in (4.9), is now linear in z

$$K(z,\Omega) = \frac{\Gamma g G P_T(0) z}{P_{sat} + G P_T(0) - j\Omega\tau_{sp} P_{sat}} + K^{'}(z',\Omega) \tag{4.20}$$

where $K^{'}(z',\Omega)$ is a high-pass function with an equal number of poles and zeros and a small contrast ratio between the high and low frequency limits. Thus, for $z > z'$, the first term of (4.20) dominates, and $K^{'}(z',\Omega)$ may be regarded as a constant, i.e. $K^{'}(z',\Omega) = K^{'}$. Since for $\Omega >> \tau_e^{-1}$, the first term of (4.20) may be expressed

$$\frac{dK(z,\Omega)}{dz} z = j\Gamma g G P_T(0) z/(\Omega\tau_{sp} P_{sat}) \tag{4.21}$$

and for $\Omega \to 0$,

$$\frac{dK(z)}{dz} z = \Gamma g G P_T(0) z/(P_{sat} + G P_T(0)) \tag{4.22}$$

Inserting (4.20) with the high or low frequency limits (4.21) or (4.22) into (4.19), the total modulation $p_T(z,\Omega)$ is readily shown to be a high-pass function with an equal number of poles and zeros. The high-pass characteristic is a general property of all amplifiers: gain saturation cancels the modulation at modulation frequencies low enough that the carrier density is able to follow the signal perturbation. At frequencies higher than the carrier modulation bandwidth the SOA becomes transparent to the input modulation, which only experiences the steady-state gain G.

As the modulation propagates, the corner frequency at which $|p_T(z,\Omega)|$ attains a value halfway between the low and high frequency limits increases with z. According to (4.8) the probe response may be expressed

$$p_P(z,\Omega) = -\frac{G\overline{P}_P(0) p_C(0,\Omega)}{\overline{P}_T(0)} \left[1 - e^{-K(z,\Omega)}\right] \tag{4.23}$$

Since the function $\left|e^{-K(z,\Omega)}\right|$ is a high pass function with a corner frequency increasing with z, the probe amplitude response $|p_P(z,\Omega)|$ is a low pass function with a corner frequency also increasing with z. The effect responsible for the bandwidth increase has been referred to as the *self-filtering effect* [23], due to the evolution of $K(z,\Omega)$ through the SOA.

Assuming that the -3 dB bandwidth of $|p_P(z,\Omega)|$, Ω_{3dB}, satisfies $\Omega_{3dB} >> \tau_e^{-1}$, which will be the case for long amplifiers, since τ_e is constant for $z > z'$, $K(L,\Omega_{3dB})$ may be approximated by the high frequency limit. Since $\left|e^{-K(z,\Omega)}\right|$ vanishes in the low frequency limit, the magnitude of the normalized carrier density response may be approximated by the following expression, which is valid for $z > z'$

$$\left|T_N^{CDR}(L,\Omega)\right| \approx \sqrt{2\left(1-\cos\left(\frac{\Gamma g G P_T(0) z}{\Omega \tau_{sp} P_{sat}}\right)\right)} \tag{4.24}$$

Solving the equation $\left|T_N^{CDR}(L,\Omega_{3dB})\right| = \frac{1}{2}$, while noting that in the transparency limit where $\Delta G = 1$, the modal gain coefficient is zero, i.e. $\Gamma g = \alpha_l = \Gamma g_0 \xi$, the bandwidth becomes

$$\Omega_{3dB} \approx \frac{\Gamma g_0 \xi G P_T(0) z}{\tau_{sp} P_{sat} \cos^{-1}(7/8)} \tag{4.25}$$

Consequently, the -3 dB small-signal modulation bandwidth is shown to increase linearly with the SOA length, with the slope

$$\frac{d\Omega_{3dB}}{dz} = \frac{\Gamma g_0 \xi G P_T(0)}{\tau_{sp} P_{sat} \cos^{-1}(7/8)} \tag{4.26a}$$

even in the presence of waveguide loss. This linear approximation is shown to be in perfect agreement with the analytical solution in Fig. 4.4 (b) for $L > 500\ \mu m$.

A similar analysis is presented in [119]. However, the gain is assumed constant throughout the SOA, which leads to an expression where the factor $GP_T(0)/P_{sat}$ is missing, thus underestimating the bandwidth slightly. The physical explanation for the underestimation of Ω_{3dB} is that the SOA is assumed transparent in [119], which does not account for the gain in the beginning of the SOA. It should be noted that the modulation bandwidth of an SOA with a finite waveguide loss is not inversely proportional to the effective carrier lifetime τ_e at the output, as it is the case for a loss-less SOA. However, regardless of the loss the bandwidth increases with Γ, I (through g_0 and G), $P_T(0)$, L, and P_{sat}^{-1}. The latter leads to the requirement that the so-called optical area $A_{opt} = HW/\Gamma$ must be minimized. This makes the dimensions of the cross section important optimization parameters, and this will be demonstrated in section 6.4 in connection with the DOMO wavelength converter.

The analysis in this section assumes that ASE can be neglected, that the differential gain is constant, that the spontaneous recombination rate is linear in the carrier density, and that the loss coefficient is constant. In reality however,

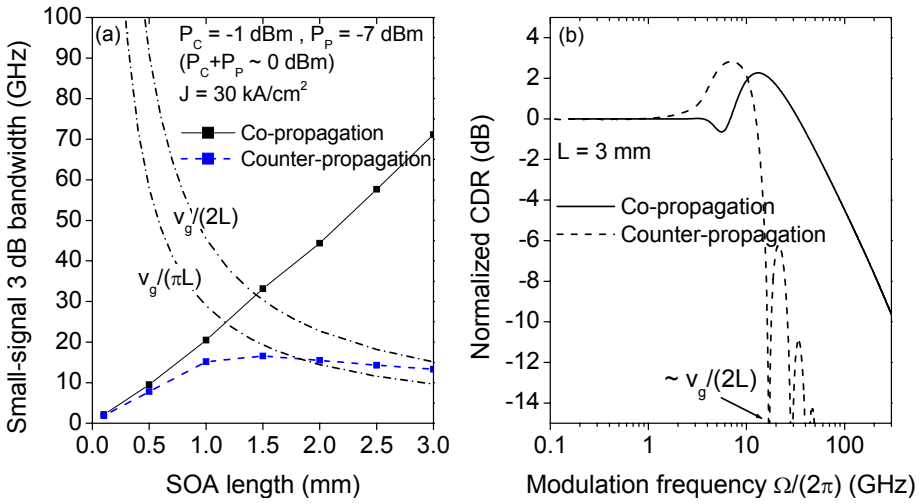

Figure 4.5: (a) −3 dB small-signal modulation bandwidth for co- and counter-propagation, calculated with large-signal model incl. ASE. (b) Comparison of normalized CDR for co- and counter-propagation. SOA length is 3 mm.

ASE can not be neglected for long SOAs, the differential gain increases as the signal propagates through the amplifier, the spontaneous recombination rate is generally approximated by the third-order polynomial in (3.28), and finally the loss coefficient was modeled in section 3.1 as being dependent on the carrier density as well as the total amplifier length. The consequences of including these effects may be investigated using the time-domain model introduced in section 3.1 by launching a single, narrow pulse $P_C(0,t)$ of width δT into the SOA along with a CW probe signal. The narrow pulse may be expressed as a Fourier series with components of almost identical magnitude over a bandwidth of $\approx 1/\delta T$

$$\begin{aligned} P_C(0,t) &= \overline{P}_C(0) + \delta P_C(0,t) \\ &= \overline{P}_C(0) + \sum_{-\infty}^{\infty} p_C(0,\Omega) e^{-j\Omega t} \end{aligned} \tag{4.27}$$

By choosing $|\delta P_C(t)| << \overline{P}_C(0)$ and $\pi/\delta T >> \Omega_{3dB}$ the complex small-signal modulation amplitude of the probe may be calculated as the Fourier components of the temporal output probe signal. This has been done for SOAs of various lengths, all biased at $J = 30$ kA/cm^2, with equal control and probe wavelengths given by the gain peak at each SOA length. The result is shown in Fig. 4.5 (a) for co-propagating control and probe signal, as treated above, and for counter-propagation, which will be explained in the following.

It is clear from Fig. 4.5 (a) that the introduction of ASE and a more detailed description of the gain, recombination rate, and loss does not give rise to qualitative changes for co-propagation. This is not surprising, since, as shown in Fig. 4.3 (b), the carrier density approaches a constant value. This is independent of the

presence of ASE, which merely changes the constant value of the carrier density through the gain. The slope of the co-propagation curve in Fig. 4.5 (a) is higher than that of the curves in Fig. 4.4 (b), but this is mainly due to the fact that $\partial g/\partial N$ for low N is larger in the detailed model, than the value used in Fig. 4.4 (b), and according to (4.25), the slope scales with $\partial g/\partial N$.

For counter-propagation, shown in the dashed, blue curve in Fig. 4.5 (a), the bandwidth peaks around $L = 1.5$ mm, and is limited by the function $v_g/(2L)$. This is due to the so-called *transit-time effect* or *phase-mismatch effect*. Fig. 4.5 (b) shows a comparison of the normalized response functions for co-propagation and counter-propagation. The counter-propagation response displays equidistant nodes at multiples of $\Omega/(2\pi) = v_g/(2L)$, which explains the bandwidth reduction. In the following the origin of the nodes will be detailed.

4.1.2 Counter-propagation

The semi-analytical expressions given in 4.1 were derived assuming a retarded time frame following the signals, which is only applicable to co-propagating control and probe signals. Considering counter-propagation in the loss-less case in a coordinate system $(z', t') = (z, t - z/v_g)$ following the probe signal $P_P(z', t')$, the probe gain may be expressed by integrating (4.2)

$$G(L, t') = \exp\left[\Gamma \int_0^L g(z', t' + z/v_g) dz'\right] \tag{4.28}$$

where the change of the material gain $g(z, t)$ is assumed linear in control pulse energy [120]

$$\begin{aligned} g(z,t) &= g_0 - a\,(h \otimes P_C)\,(t) \\ &\quad g_0 - a \int_{-\infty}^{\infty} h(t - t'') P_C(z, t'') dt'' \end{aligned} \tag{4.29}$$

Here, $\otimes$ denotes convolution, a is a constant governing the maximum gain change, $h(t)$ is the linear response function for the gain, and $P_C(z, t)$ is the backwards travelling control pulse entering the SOA at $t = 0$, and exiting at $t = L/v_g$.

Neglecting the gain experienced by the control pulse, or assuming that it is included in the constant a, $P_C(z, t)$ may be expressed

$$P_C(z, t) = P_C(t) = P_0 F_C(t + \frac{z - L}{v_g}) \tag{4.30}$$

where F_C is the backwards travelling control pulse shape. Inserting (4.29) and (4.30) into (4.28), and using the substitution $\widetilde{t} = t'' + (z' - L)/v_g$ the gain is given

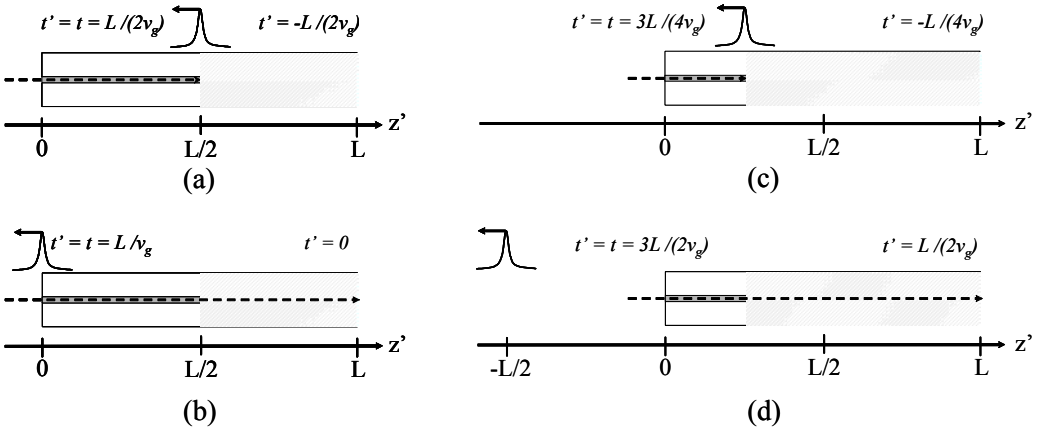

Figure 4.6: Explanation of integration limits in (4.34). Probe signal leaving right facet at retarded output time $t' = 0$ (b) has interacted with control pulse in hatched area from $L/2$ to L (a). Similarly, the probe signal leaving the SOA at $t' = L/(2v_g)$ (d) has interacted with the control signal from $L/4$ to L (c).

by [121]

$$\begin{aligned} G(L,t') &= \exp(\Gamma g_0 L)\exp\left[-\Gamma a P_0 \int_0^L \int_{-\infty}^{\infty} h(t'-\widetilde{t}+(2z'-L)/v_g) F_C(\widetilde{t}) d\widetilde{t} dz'\right] \\ &= G_0 \exp\left[-\Gamma a P_0 \int_{-\infty}^{\infty} R(t'-\widetilde{t}) F_C(\widetilde{t}) d\widetilde{t}\right] \\ &= G_0 \exp\left[-\Gamma a P_0 \left(R \otimes F_C\right)(t')\right] \end{aligned} \tag{4.31}$$

with

$$R(t') = \int_0^L h(t'+(2z'-L)/v_g) dz' \tag{4.32}$$

being the counter-propagation response function.

Assuming now that the response $h(t)$ may be described by

$$h(t) = \theta(t) e^{-t/\tau_e} \tag{4.33}$$

where the unity step function $\theta(t)$ ensures the causality of $h(t)$, eq. (4.32) is evaluated, using the substitution $z' = \widetilde{z} + L/2$

$$R(t') = e^{-t'/\tau_e} \int_{\max\{-L/2, -v_g t'/2\}}^{L/2} e^{-2\widetilde{z}/(v_g \tau_e)} d\widetilde{z} \quad ; t' > -L/v_g \tag{4.34}$$

The requirement $t' > -L/v_g$ corresponds to $t > 0$ for $z' = L$, and consequently ensures causality. The integration limits are explained in Fig. 4.6, which illustrates how the response $R(t')$ at the retarded output times $t' = 0$ (a-b) and $t' = L/(2v_g)$ (c-d) is obtained[1]. The CW probe signal, shown in Fig. 4.6 (b)

[1]Notice that retarded time only makes sense when a spatial coordinate is given.

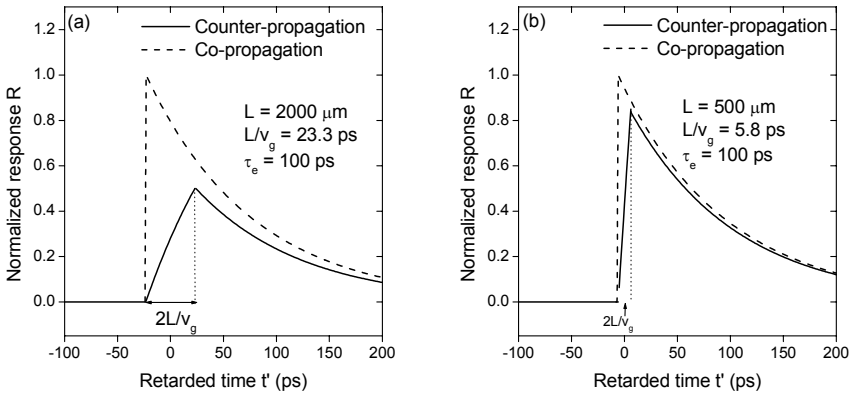

Figure 4.7: Normalized response for co-propagation (4.36) and counter-propagation (4.35) for an SOA length of (a) 2000 μm and (b) 500 μm. Parameters: $\tau_e = 100$ ps, $n_g = 3.5$.

as a dashed arrow, arriving at the output ($z = L$) at $t' = 0$, collided with the control pulse at $z' = L/2$ at the retarded output time $t' = -L/(2v_g)$, as shown in Fig. 4.6 (a). Thus, the probe leaving the SOA at $t' = 0$ has interacted with the counter-propagating control signal in the hatched part of the SOA, ranging from $L/2$ to L, which corresponds to the integration limits in (4.34) for $t' = 0$. Fig. 4.6 (c-d) shows the equivalent case for a probe signal leaving the amplifier at $t' = L/(2v_g)$. A probe signal colliding with the control pulse at $z' = 0$ reaches the output at $t' = L/v_g$, which means that the signals interact over a total time span of $2L/v_g$, during which $R(t')$ increases, corresponding to a decrease of the gain $G(L, t')$.

This becomes clear when solving (4.34)

$$R(t') = \frac{v_g \tau_e}{2} \begin{cases} 0 & ; t' \leq -L/v_g \\ 1 - e^{-\frac{t'+L/v_g}{\tau_e}} & ; -L/v_g < t' \leq L/v_g \\ e^{-t'/\tau_e} \left[e^{L/(v_g \tau_e)} - e^{-L/(v_g \tau_e)} \right] & ; t' > L/v_g \end{cases} \tag{4.35}$$

From (4.35) it is clear that $R(t')$ increases for $-L/v_g < t' \leq L/v_g$ and decreases for $t' > L/v_g$. The solution is shown in Fig. 4.7 along with the equivalent solution for co-propagation, which is given by

$$R_{co}(t') = L\theta(t')e^{-t'/\tau_e} \tag{4.36}$$

In Fig. 4.7 (a) the response functions are shown for a 2000 μm long SOA, and the rising edge of the response amounts to 46.6 ps. As a comparison, the results are shown for a 500 μm long SOA in Fig. 4.7 (b), and as expected the counter-propagation response approaches the co-propagation response in the limit $L \to 0$.

The assumption in (4.29) that the gain change is linear in the control signal energy implies that the small-signal gain response may be obtained by considering the limit $P_0 \to 0$ in (4.30). Assuming that $F_C(t')$ is a delta-function, the Fourier

transform of the gain becomes

$$\begin{aligned} G(L,\Omega) &= \mathbf{F}\left[G(L,t')\right] \\ &= G_0\left(\delta(\Omega) - \Gamma a P_0 R(\Omega)\right) \ ;\text{for } P_0 \to 0 \end{aligned} \tag{4.37}$$

where $R(\Omega)$ is the Fourier transform of $R(t')$. Consequently, the normalized probe amplitude response $T_{N,cnt}^{CDR}(\Omega)$ may be expressed

$$\begin{aligned} T_{N,cnt}^{CDR}(\Omega) &= \frac{R(\Omega)}{R(0)} \\ &= \mathrm{sinc}\left(\frac{\Omega L}{v_g}\right)\frac{1}{-j\Omega\tau_e + 1} \\ &= T_N^{CNT}(\Omega, L) T_N^{CDR}(\Omega) \end{aligned} \tag{4.38}$$

In the second line, (4.34) is Fourier transformed, which allows the introduction of a counter-propagation envelope function $T_N^{CNT}(\Omega, L)$ given by the simple sinc-function $\sin(x)/x$, which goes through zero at integer multiples of $\Omega = v_g\pi/L$, and has a -3 dB angular frequency bandwidth of $\Omega_{\mathrm{sinc}} \approx 1.9 v_g/L$. The decrease of Ω_{sinc} with L explains the increased normalized amplitude of $R(t')$ from Fig. 4.7 (a) to Fig. 4.7 (b). Eq (4.38) states that the normalized small-signal frequency response for counter-propagation is obtained from the co-propagation response by multiplication with the sinc envelope function, which represents the transit-time effect in the frequency-domain. The sinc-function is an approximation, since the spatial inhomogeneity of the carrier density, as well as travelling wave effects, are neglected in the present analysis. A more detailed analysis reveals that the response displays a resonance, regardless of the presence of waveguide loss, due to spatial inhomogeneity of the carrier density, and thus the effective carrier lifetime [p1]. The resonance increases the bandwidth, and explains why the -3 dB bandwidth for counter propagation in Fig. 4.5 (a) exceeds the high frequency limit $1.9v_g/(2\pi L) \approx v_g/(\pi L)$. Moreover, this analysis assumes that the signals interact over the entire length of the SOA. However, as explained in [119], the modulation efficiency at the end of the SOA (where the control signal enters) is very small, since the average power of the probe dominates the saturation. As a consequence, this part of the SOA can be considered transparent with respect to transfer of modulation, and may be excluded be defining an effective amplifier length $L_{eff} < L$. The effective length depends on the ratio of control to probe power, the SOA gain, etc, and will also tend to increase the bandwidth beyond the before-mentioned high frequency limit.

4.2 Large-signal comparison: XGM

In the small-signal analysis above, it was concluded that the bandwidth increases with SOA length when control and probe signals are co-propagating. Moreover,

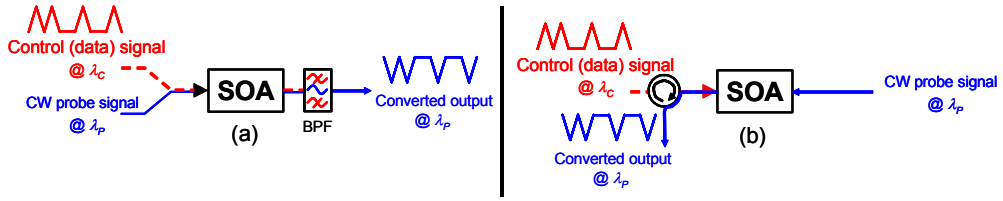

Figure 4.8: XGM in an SOA. (a) Co-propagation scheme, (b) counter-propagation scheme.

for a given length (4.25) predicts that the bandwidth can be extended further by minimizing the optical area, and increasing the current density and optical input power. For counter-propagation, small-signal theory predicts that the bandwidth is limited by the long leading edge of the response, which gives rise to an optimum SOA length for a given bitrate. In this section the small-signal predictions will be investigated in the large-signal domain using the model described in 3.1. The large-signal equivalent of the small-signal modulation amplitude is the extinction ratio (ER) of a cross-gain modulated probe signal. However, as it will be shown in the following, the ER is not representative of the signal quality for long SOAs, as the ASE power attains a level where it contributes to the closing of the eye diagram. Thus, the Q-factor presented in Appendix A.3 will be employed as a figure of merit, and used to calculate the receiver power penalty.

Fig. 4.8 (a) shows the classic co-propagation XGM setup, where the data signal at the wavelength λ_C (shown as RZ signal) and CW probe at λ_P are merged in a 3 dB coupler and launched into the SOA. Here, the data signal modulates the probe gain through the carrier density, and at the output the wavelength converted probe signal may be observed after suppression of the data signal, using a band-pass filter (BPF). Similarly, Fig. 4.8 (b) shows the counter-propagation setup, in which the two signals are injected from opposite facets. The wavelength converted probe signal is distinguished from the input data signal by direction of propagation using an optical circulator, and thus eliminating the need for a filter. This is considered a major advantage since an expensive, non-integratable component is saved, and it is an enabling solution for switching in packet switching applications [11], since filters with fast (ns) tuning are not available.

As in the small-signal simulations, the data and probe wavelengths are identical and equal to the gain peak position in the large-signal calculations. This is clearly not physical for co-propagating signals, as the modulated probe cannot be distinguished from the data signal if the wavelengths are identical. However, this choice of wavelengths eliminates the effect of wavelength detuning, which is critical, but nonetheless predictable, as the differential gain $\partial g/\partial N$ decreases with wavelength as a consequence of the bandfilling effect [23]. Thus, the XGM efficiency is larger when λ_P is on the blue side of λ_C, and analogously decreases when λ_P is moved to the red side of λ_C. Choosing $\lambda_P = \lambda_C$ represents a compromise in terms of performance.

In the small-signal analysis, the bandwidth is independent of the ratio of power in the control and probe signals. This is not the case in the large-signal domain: if the probe input power is 10 dB higher than the average control signal power the latter may be unable to provide the gain modulation required for XGM, as the input saturation power is determined by the probe power. On the other hand, if the control signal power is 10 dB higher than the probe power the gain will be efficiently modulated, but the low probe power will give rise to a high effective carrier lifetime between control pulses, which will slow down the recovery of the probe power. Moreover, the output OSNR of the probe signal scales with the input probe power, thereby setting a lower limit. As a result of this trade-off the input data[2] and probe powers are swept over the ranges $0 \rightarrow 20$ dBm and $-10 \rightarrow 30$ dBm, respectively, in order to determine the best operating conditions for each SOA length, in terms of receiver sensitivity. In all cases the current density is fixed at $J = 30$ kA/cm^2.

4.2.1 Co-propagation

Cross-gain modulation with co-propagating signals is investigated at 80 Gb/s, using long, highly confining SOAs with a cross section of $(W, H) = (0.7, 0.5)$ μm and a confinement factor of 0.6. For each amplifier length in the range $1 - 5$ mm, the input powers have been optimized to obtain the smallest possible power penalty[3] at a bit-error rate (BER) of 10^{-9}. The input data signal is a Pseudo Random Bit Sequence (PRBS) signal of length $2^5 - 1$ with an ER of 13 dB, and consisting of 3 ps (FWHM) wide Gaussian pulses. Fig. 4.9 (a) shows the minimum power penalty vs. SOA length: for $L = 1$ mm to $L = 3.5$ mm the penalty decreases as a result of the self-filtering effect explained in section 4.1. However, for $L > 3.5$ mm the penalty increases again because the amount of ASE in the signal band inevitably increases with the amplifier length. The exact length at which the penalty minimum occurs depends on receiver parameters, and also on the transmission distance before detection. Here, the wavelength converted probe signal is detected at the output of the SOA, neglecting the effect of the chirp on the transmission properties. Detecting the signal after a transmission span may change the result in Fig. 4.9 significantly, because the amount of chirp imposed on the probe signal also depends on the SOA length. The solid curves in Fig. 4.9 (b) show the ER (left axis) and OSNR (right axis) vs. SOA length, corresponding to the minimum penalties in Fig. 4.9 (a). As a comparison, the dashed and dotted curves show the maximum ER and OSNR that may be obtained by optimizing the input powers with only these figures of merit in mind.

The combination of ER and OSNR leading to the minimum penalty at a particular length are lower than the figures that may be obtained through in-

[2]The terms "data signal" and "control signal" are used interchangeably.

[3]Power penalty: ratio of receiver sensitivities after Device Under Test (DUT) and before DUT at specific bit error-rate, typically 10^{-9}.

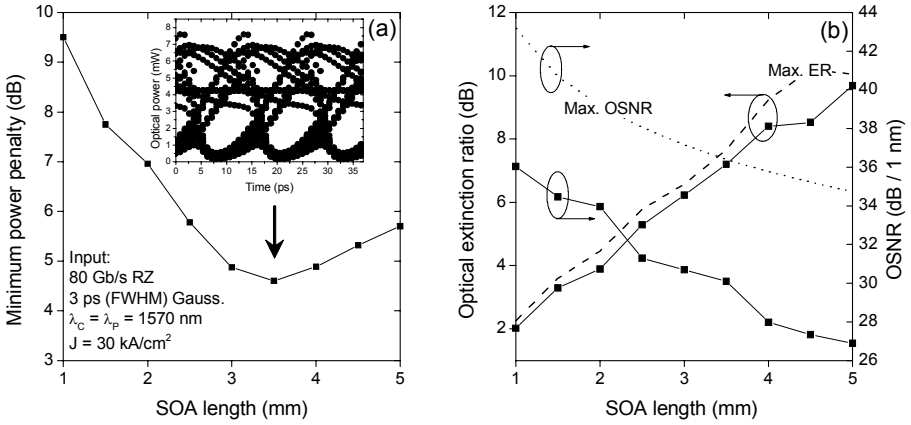

Figure 4.9: (a) Minimum power penalty of co-propagation XGM'ed probe at 80 Gb/s vs. SOA length L. Inset shows eye diagram corresponding to $L = 3.5$ mm. (b) Extinction ratio (left axis) and OSNR (right axis) vs. L. Solid curves: optimized for minimum penalty. Dashed/dotted curves: optimized for maximum extinction ratio/OSNR, respectively.

dividual optimizations of ER and OSNR, and this illustrates the clear trade-off between speed and noise. It should be noticed that by considering only the ER, i.e. by neglecting the influence of ASE on the receiver sensitivity, the performance increases for $L > 3.5$ mm as predicted by the small-signal analysis. The reduction in ER observed from $L = 4.5$ mm to $L = 5$ mm is because the data power attains the upper limit of 30 dBm at $L = 5$ mm, which is sub-optimal. The before-mentioned trade-off is also illustrated in Fig. 4.10 (a), which shows the power penalty (left axis) and the ER and OSNR (right axis) vs. data signal power with the probe input (CW) power as a parameter for a 4 mm long SOA. For the low probe power of 0 dBm the OSNR decreases to a critical level before the ER reaches its maximum, causing the penalty to go through a minimum at a sub-optimal ER. Increasing the probe power to 14 dBm increases the OSNR, but at the same time moves the ER-curve towards higher average data powers, as the probe increases the level of saturation. This is equivalent to increasing the length of the SOA, since the increased length gives rise to a higher output ASE power, which must be compensated for by increasing the input probe power. Consequently, the "sweet spot" in terms of input power increases with the length, and sets a practical limit to the amplifier length.

The upper limit of the average data power of 30 dBm in this example represents a conservative estimate of the limit of commercially available Erbium-Doped Fiber-Amplifiers (EDFAs). At power levels of this magnitude, and a large total injection current, heating of the SOA becomes an issue, which is not accounted for in the model. If heat cannot be removed from the chip sufficiently fast, the temperature will stabilize at a level above the optimum, which changes the Fermi distributions (B.6) and reduces the available gain, requiring an additional increase of the input powers to compensate for the reduced gain.

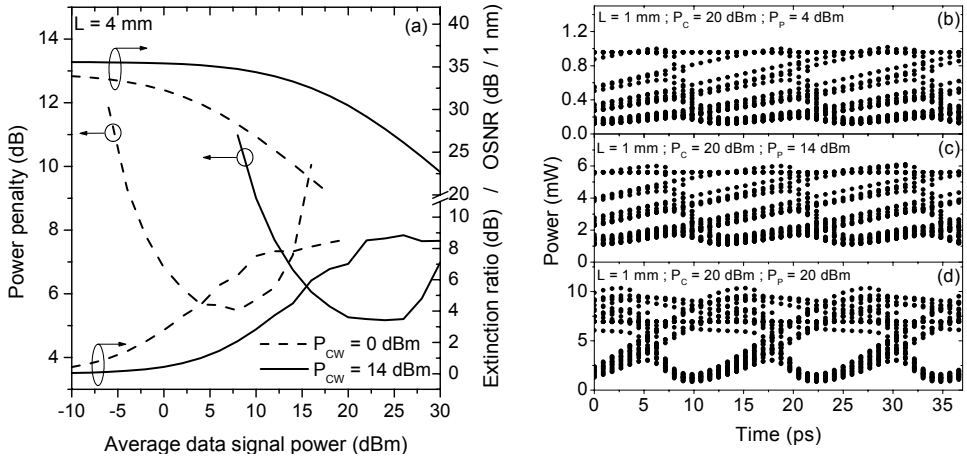

Figure 4.10: (a) Power penalty (left axis) and ER/OSNR (right axis) vs. average data power for CW probe powers of 0 dBm and 14 dBm, obtained with an SOA length of $L = 4$ mm. (b-d) Eye diagrams for $L = 1$ mm for CW probe powers of 4, 14, and 20 dBm. The average data power is fixed at 20 dBm.

Eq. (4.25) predicts that the small-signal bandwidth increases with the total input power. As explained already, the ratio of data to probe power is critical for large-signal modulation. Moreover, as recovery of the carrier density takes place in the time spans in-between excitation by data pulses, the recovery time is determined solely by the spontaneous lifetime and the contribution to the stimulated lifetime from the probe signal. Thus, in order to speed-up the gain recovery the input probe power must be increased. This is illustrated in Fig. 4.10 (b-d), which shows eye diagrams for the XGM probe signal at 80 Gb/s, obtained using a 1 mm long SOA with an average input data power of 20 dBm and a probe input power of (b) 4 dBm, (c) 14 dBm, and (d) 20 dBm. The principle of reducing the gain recovery time by increasing the input probe power is a so-called *holding beam* technique. The literature contains several investigations of these techniques, including the exploitation of the holding beam effect without injecting additional signals, as illustrated in Fig. 4.10 (b-d), the use of separate holding beams, either CW [45,122] or modulated beams [123]. Employing holding beams reduces *patterning effects*, i.e. the deterministic variation of the logic levels caused by the preceding data sequence. Patterning effects are discussed in detail in section 4.3, where the effect on a XGM probe signal will also be addressed.

According to Fig. 4.9 wavelength conversion at 80 Gb/s is possible using XGM. However, since the slope of the probe gain with respect to the control power does not exceed -10 dB/decade, except for conversion towards lower wavelengths, the ER of the wavelength converted probe signal will generally be smaller than the ER of the input signal, which inevitably limits the cascadability [124, 125]. Another drawback is the fact that the large gain modulation required for successful XGM operation is accompanied by a significant phase modulation. The XPM is beneficial in many cases, as described later in this chapter. However,

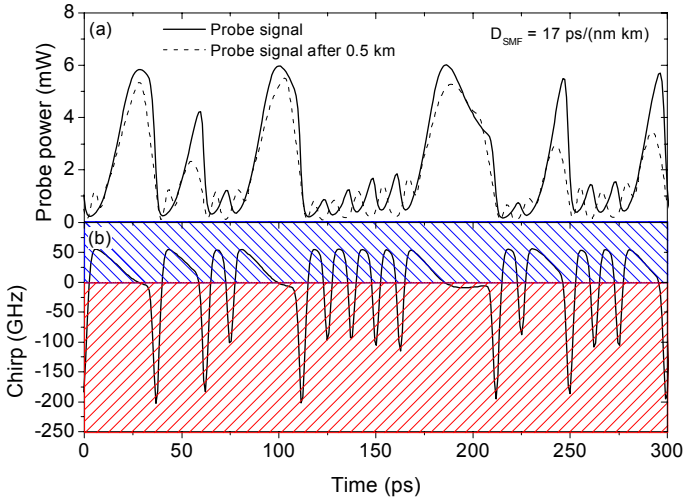

Figure 4.11: (a) Waveform of co-propagation XGM'ed before (solid) and after (dashed) transmission on 0.5 km of SMF. (b) Corresponding chirp of XGM'ed signal before transmission. SOA length is $L = 3.5$ mm, and data/probe average input powers are 28/20 dBm.

for standard[4] XGM the XPM-induced chirp and the resulting spectral broadening makes the wavelength converted signal more sensitive towards the anomalous dispersion of SMF. This is illustrated in Fig. 4.11, which shows the power (a) and chirp (b) of the converted probe signal corresponding to the best case in Fig. 4.9 (a), i.e. $L = 3.5$ mm with average data and probe input powers of 28 dBm and 20 dBm. According to (3.20), the phase increases when the carrier density is suppressed and vice versa. This leads to a negative frequency chirp (red shift) at the leading edges, and a positive chirp (blue shift) on the trailing edges of the inverted probe pulses. On SMF with anomalous dispersion the blue-shifted edges propagate faster than the red-shifted edges, which accelerates the pulse broadening. This is shown in Fig. 4.11 (a), where a part of the converted waveform right after the SOA (solid curve) is compared to the waveform after transmission of only 0.5 km on SMF with a dispersion of $D_{SMF} = 17$ ps/(nm km). It is clear that the red-shifted edges of the pulses at $t \approx 50$ ps and $t \approx 250$ ps have broken up and reduced the peak power significantly, at the expense of the ER.

4.2.2 Counter-propagation

According to the small-signal results in Fig. 4.5 (a), the modulation bandwidth is almost constant, and equal to 15 GHz, in the range 1 mm $< L <$ 3 mm, which suggests that operation at 20 Gb/s is possible using SOA lengths in this range, and that the performance will be almost invariant to the length. This has been investigated at 20 Gb/s and 40 Gb/s, using 12 ps and 6 ps wide RZ data pulses,

[4]Standard XGM: Without pulse shaping using optical filtering, corresponding to using a filter with a bandwidth much larger than the bitrate, centered on the carrier wavelength.

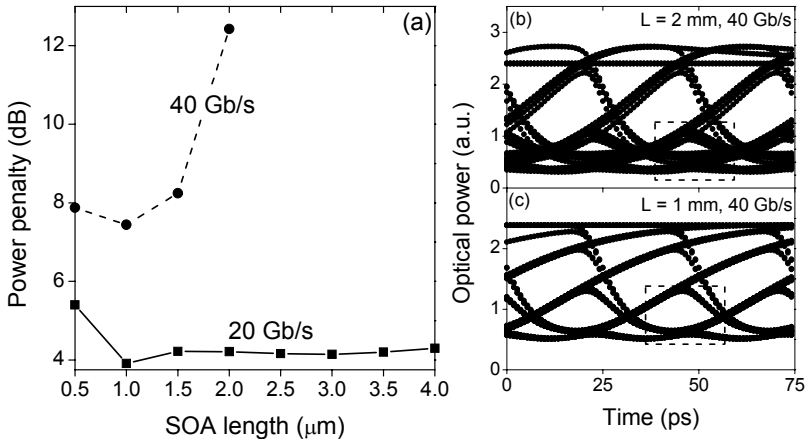

Figure 4.12: (a) Power penalty vs. SOA length L for XGM in counter-propagation. Comparison of bitrates 20 Gb/s and 40 Gb/s. (b-c) 40 Gb/s eye diagram for $L = 2$ mm and $L = 1$ mm, respectively. Dashewd boxes indicate eye opening.

respectively, and the result is shown in Fig. 4.12 (a) in terms of the power penalty at $BER = 10^{-9}$. For 20 Gb/s, the penalty drops from 0.5 mm to 1 mm due to the self-filtering advantage, but for $L > 1$ mm the penalty remains almost constant at 4 dB, as predicted by the small-signal analysis. The performance is not degraded by the decreasing OSNR as in Fig. 4.9, since the receiver is 4 times less sensitive to noise at 20 Gb/s, compared to 80 Gb/s. At 40 Gb/s, the transit-time effect becomes critical, and the penalty is observed to increase rapidly with length for $L > 1$ mm.

The 40 Gb/s eye diagrams in Fig. 4.12 (b) and (c) correspond to SOA lengths of 2 mm and 1 mm, respectively. Whereas the eye, indicated by the dashed box, is still open for $L = 1$ mm (c), it is almost completely closed for $L = 2$ mm (b). This is a direct consequence of the fact that the duration of the "1" $\rightarrow$ "0" transition increases with SOA length, and far exceeds the 25 ps timeslot for $L = 2$ mm.

4.3 Patterning effects

Ideally, the phase and amplitude modulation of the probe at the output of the SOA should follow the control signal at the input. However, due to patterning effects and ASE, the logic "0" and "1" levels of the probe may vary between timeslots. In most scenarios involving SOA-based switches operated with a pseudo-random control signal at high bitrates, patterning is the most serious source of eye-closure, since variations due to noise can usually be made insignificant by injecting a sufficiently strong probe, thereby ensuring a large OSNR at the output. As explained above, this is not necessarily the case for very long SOAs in excess of ≈ 3 mm, and clearly, in the absence of patterning effects noise will ultimately

limit the performance.

Using the retarded-frame propagation equation (4.2) for $\alpha_l = 0$, without applying the small-signal assumption in (4.1), the time dependent large-signal gain $G(t)$ and the corresponding phase shift $\phi(t)$ of the data and probe signal may be expressed

$$G(t) = \exp\left[\Gamma(\partial g/\partial N)\left(\sigma(t) - N_{tr}L\right)\right] \tag{4.39}$$

$$\phi(t) = -\frac{\alpha}{2}\Gamma(\partial g/\partial N)\left[\sigma(t) - N_{tr}L\right] \tag{4.40}$$

where α is the linewidth enhancement factor (3.7), and $\sigma(t)$ is the carrier density integrated over the length of the SOA

$$\sigma(t) = \int_0^L N(z,t)dz \tag{4.41}$$

which satisfies the integrated rate equation [107]

$$\frac{d\sigma}{dt} = -\frac{\sigma(t) - \sigma_0}{\tau_{sp}} - \lambda\frac{\exp\left[\Gamma\left(\partial g/\partial N\right)\left(\sigma(t) - N_{tr}L\right)\right] - 1}{hc_0A}\left[\overline{P}_P(0) + P_C(0,t)\right] \tag{4.42}$$

The constant σ_0 is the steady-state value of $\sigma(t)$ in the absence of any optical input signals, $\overline{P}_P$ is the probe input power, assumed to be CW, and $P_C(0,t)$ is the instantaneous control input power. Eq. (4.42) may be expanded into a steady-state and time-dependent large-signal part by expressing $\sigma(t)$ and $P_C(0,t)$ like $\sigma(t) = \overline{\sigma} + \Delta\sigma(t)$, and $P_C(0,t) = \overline{P}_C(0) + \Delta P_C(t)$

$$\frac{d\Delta\sigma}{dt} = -\frac{\Delta\sigma(t)}{\tau_e} - \frac{\lambda}{hc_0HW}\left(\overline{G} - 1\right)\Delta P_C(t) - \frac{\lambda}{hc_0HW}\Gamma\left(\partial g/\partial N\right)\overline{G}\Delta\sigma(t)\Delta P_C(t) \tag{4.43}$$

where τ_e is the effective carrier lifetime at the output of the SOA, and $\overline{G} = \exp\left[\Gamma\left(\partial g/\partial N\right)\left(\overline{\sigma} - N_{tr}L\right)\right]$ is the steady-state gain.

The last two terms in (4.43) contain the temporal variation of the control signal, $\Delta P_C(t)$, and are consequently the driving terms of the equation, responsible for modulating the carrier population. These are the sources of patterning effects. However, there is an important difference between the two terms: the first term is a *linear* function of $\Delta P_C(t)$, since the pre-factor $\left(\overline{G} - 1\right)\lambda/(hc_0HW)$ is time-independent, whereas the second term is a *nonlinear* function of $\Delta P_C(t)$, as the pre-factor $\Gamma\lambda\left(\partial g/\partial N\right)\overline{G}\Delta\sigma(t)/(hc_0HW)$ contains the instantaneous value of $\sigma(t)$. For a string of control input pulses, the linear term causes the same change of σ for every pulse, whereas the nonlinear term gives rise to a change of σ, which depends on the degree of gain saturation in the SOA. The patterning effects inflicted by the linear and nonlinear terms will be referred to as *linear patterning* and *nonlinear patterning* [p2], respectively.

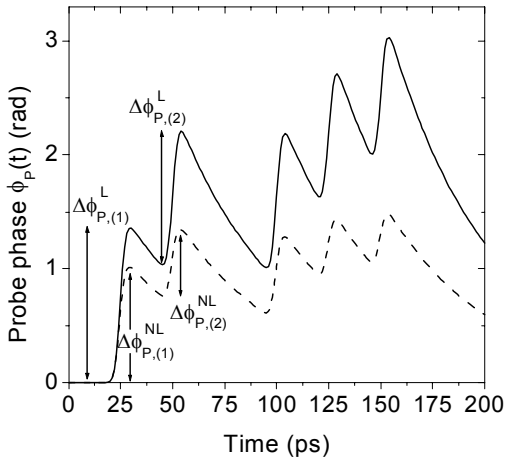

Figure 4.13: Temporal evolution of the probe phase including the nonlinear term of rate equation (4.43) (dashed curve), and without the nonlinear term (solid curve). Simulation parameters: $\overline{P}_p = 1$ mW, $L = 500\ \mu m$, $A = 0.7\mu m \times 0.5\mu m$, $\Gamma = 0.6$, $I = 70$ mA (20 kA/cm^2), $dg/dN = 5 \cdot 10^{-20}$ m^2, $N_{tr} = 1 \cdot 10^{24}$ m^{-3}, $\tau_{sp} = 0.5$ ns, $\alpha = 5$, and $\hbar\omega = 0.8$ eV.

Fig. 4.13 illustrates the difference between linear and nonlinear patterning for a specific 40 Gb/s input data sequence (110111): the dashed curve shows the evolution of the probe phase $\phi_P^{NL}(t)$ obtained by solving (4.40)-(4.43) including both the linear and nonlinear term. In contrast, the solid curve represents the probe phase $\phi_P^{L}(t)$ in the case where only the linear term is included. The input data signal $P_C(t)$ used in the simulation consists of 5 ps wide (FWHM) Gaussian pulses with an infinite extinction ratio and a peak power of 10 mW. The remaining parameters are listed in the caption of Fig. 4.13. The nonlinear term effectively reduces the phase shift $\Delta\phi_P^{NL}$ imposed on the probe by succeeding control pulses, i.e. the phase shift $\Delta\phi_{P,(2)}^{NL}$ introduced by the second data pulse is smaller than the phase shift $\Delta\phi_{P,(1)}^{NL}$ caused by the first pulse, etc. On the other hand, the linear term causes identical phase shifts $\Delta\phi_P^{L}$ for each input pulse. By neglecting the nonlinear term in (4.43), thus including only linear patterning, the dynamics of σ is described by

$$\frac{d\Delta\sigma}{dt} = -\frac{\Delta\sigma(t)}{\tau_e} - \frac{\lambda}{hc_0HW}\left(\overline{G} - 1\right)\Delta P_c(t) \tag{4.44}$$

From this rate equation it is clear that linear patterning can be described exclusively by the effective carrier lifetime τ_e, which determines the rate of recovery of $\sigma(t)$ and ultimately the modulation bandwidth of the gain and phase through (4.39)-(4.40).

Returning to the limit in which $\Delta P_C(t)$ is a small-signal perturbation to $\overline{P}_C$, $\Delta\sigma(t)$ and $\Delta P_C(t)$ can be expressed as $\Delta\sigma(t) = \sigma(\Omega)e^{-j\Omega t} + c.c.$ and $\Delta P_C(t) = p_C(\Omega)e^{-j\Omega t} + c.c.$, where $\sigma(\Omega)$ and $p_C(\Omega)$ are the complex small-signal modulation amplitudes at the modulation angular frequency Ω. Inserting these expansions

into (4.43), it is clear that the nonlinear term is second-order, and thus vanishes in a small-signal analysis. Correspondingly, the exact rate equation for $\Delta\sigma$ in (4.43) is reduced to (4.44) by assuming that the control signal is small-signal modulated, and thus it may be concluded that a small-signal analysis only takes linear patterning into account.

Not surprisingly, predictions of performance, based on a small-signal analysis, are accurate in schemes where nonlinear patterning is not the limiting factor. The consequences of nonlinear patterning effects depend on the scheme, in which the SOA is employed. For a simple switch based on XGM, the effect responsible for nonlinear patterning, namely gain saturation, is beneficial, as it reduces the patterning in the zero-level of the probe signal. This is observed in Fig. 4.13, by noting that the gain and phase are subject to the same patterning effects, as described by (4.39)-(4.40). Thus, for XGM the modulation bandwidth is primarily limited by linear patterning, defined by the effective carrier lifetime τ_e. This is illustrated in Fig. 4.10 (b-d), where the zero-level is well-defined, unlike the one-level, due to an insufficiently fast gain recovery. In other words the performance of XGM is not limited by the fact that some data pulses experience a higher gain than others, but rather by the rate of recovery. As already verified in section 4.2, the large-signal performance of a switch based on XGM may thus be estimated from a small-signal analysis with reasonable accuracy.

Other examples of this correlation are found in the literature, where e.g. operation guidelines derived from small-signal analysis are verified in the large-signal regime [23], and error-free XGM wavelength conversion at bitrates close to the predicted small-signal bandwidth is demonstrated [126]. In section 5.3 it will be shown that, by employing SOAs in the so-called differential mode of operation, linear patterning effects can be completely compensated for. Consequently, the performance of switches based on this scheme is ultimately limited by nonlinear patterning.

The bitrate at which nonlinear patterning effects become detrimental can be increased by applying holding-beam techniques, which involves launching an additional signal into the SOA, either CW or modulated [45,122,123]. The effect of these schemes is two-fold: first, they speed-up the recovery of the carrier density by lowering τ_e, thereby reducing linear as well as nonlinear patterning by limiting the timeslot-to-timeslot variation of $\Delta\sigma(t)$. Secondly, the holding beam limits the excursion of the probe gain and phase, by reducing the carrier density available to the probe during a long string of zeros in the data control signal. This translates into an effective suppression of nonlinear patterning. It should be stressed that linear and nonlinear patterning effects are by no means independent, since nonlinear patterning vanishes if the carrier recovery is fast enough that linear patterning may be neglected.

Simulation studies suggest that a modulated holding beam with an inverted polarity compared to the data signal is more effective than the CW counterpart in reducing nonlinear patterning [123],[p3]. The basic idea of this scheme, which is

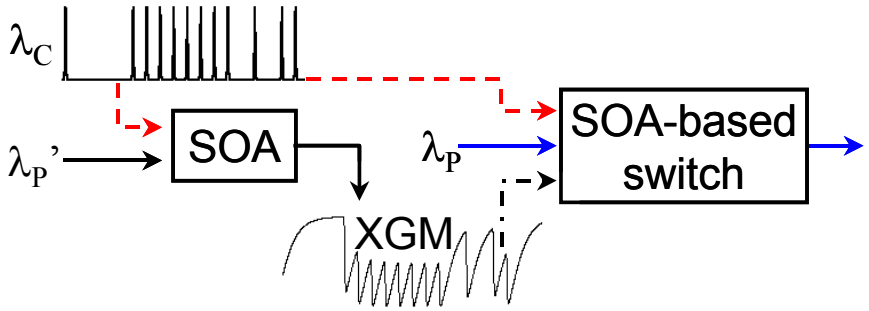

Figure 4.14: Modulated holding-beam approach for reducing nonlinear patterning. Figure courtesy of S. Bischoff.

illustrated in Fig. 4.14, is to equalize the total power into the SOA-based switch, and thereby limit the gain difference experienced by succeeding data pulses. In Fig. 4.14 the inverted holding signal is generated by co-propagating XGM in an SOA. In a practical implementation it would be more convenient to generate the holding signal in counter-propagation, in order to eliminate the filter (not shown). This is possible at significant bitrates, since the scheme works even for a moderate modulation depth of the holding signal [p3].

As discussed briefly in section 4.2, the benefits of a holding beam, without the inconvenience of an additional input signal, can be obtained by simply increasing the input probe power to the SOA. Apart from lowering the effective carrier lifetime and reducing the carrier density excursion, as explained above, it also increases the optical signal to noise ratio at the output. However, as the bitrate is increased, so does the necessary data average power, assuming a constant data pulse energy, and this brings on an increased carrier density variation. This may be compensated for by increasing the probe power, but at some point the available carrier density will be too low for the data pulses to facilitate a phase shift sufficient to switch the probe signal. Thus, employing a holding-beam technique does not eliminate nonlinear patterning, but merely increases the bitrate at which nonlinear patterning limits the performance, and at the same time expands the frequency range in which a small-signal analysis may be considered accurate.

4.4 Summary

Transfer of modulation from a control signal to a CW probe signal was investigated in the small-signal regime for co- and counter propagating signals, using already published approaches. Using a simplified SOA model without ASE, the dependence on waveguide loss of the probe response for co-propagating signals was explained, and an analytical expression for the bandwidth as a function of SOA length was given. For counter-propagation, an even simpler model lead to a convenient description of the probe response as the product of the co-propagation

response and a simple sinc-shaped bandwidth-limiting transfer function. The simple small-signal models were verified by operating the large-signal model, including ASE, in the small-signal regime.

The small-signal analysis concluded that the bandwidth increases with length for co-propagation. This was verified by the large-signal model at 80 Gb/s, but for lengths exceeding 3.5 mm the increasing amount of ASE added to the signal degraded the performance in terms of receiver sensitivity, and the existence of an optimum length was demonstrated. For counter-propagation the correspondence between the small and large-signal models is also excellent. Operation at 20 Gb/s was demonstrated with a power penalty of 4 dB, and at 40 Gb/s the transit-time effect makes wavelength conversion prohibitive.

Patterning effects were introduced and divided into two groups: linear and nonlinear patterning. The alleviating effect of the differential control scheme and holding beam techniques on linear and nonlinear patterning, respectively, was discussed.

Chapter 5

SOA-based switch configurations

A generic XPM-based switch, illustrated in Fig. 5.1, consists of a nonlinear element (NLE), in this context an SOA, in combination with a phase modulation (PM) to amplitude modulation (AM) converter such as an interferometer or filter. The control signal modulates the phase of the probe signal, which is turned into amplitude modulation through the PM-to-AM conversion. In this chapter, three types of switches, falling under the definition above, are investigated: the *standard-mode* XPM switch, the *differential-mode* XPM switch, and the *filtering-assisted* XPM switch. Significant overlap exists between the three categories, especially between differential-mode and filtering-assisted switches, where the former may, in some cases, be considered a special case of the latter. The advantages and disadvantages of interferometric switches compared to the simple XGM switch are explained and studied numerically. The differential control scheme is investigated through a detailed analysis of the MZI operated in the differential-mode and the so-called DISC, with special attention to alleviation of linear patterning effects, and the influence on the system margin.

Finally, the effect of placing an optical filter after a single SOA is analyzed

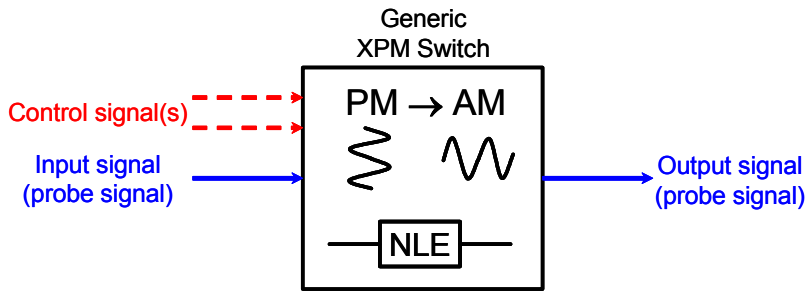

Figure 5.1: Schematic of generic cross-phase modulation switch, with one or more control signal determining the state of the switch. NLE: nonlinear element

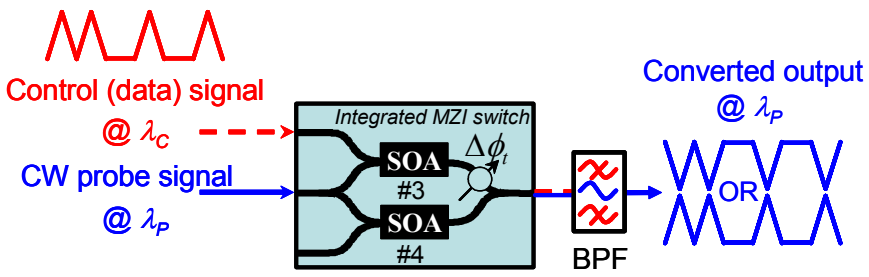

Figure 5.2: Schematic of MZI operated in the standard-mode configuration. The choice of signal polarity is indicated.

in the small-signal regime. A general method for carrying out a small-signal analysis is presented, based directly on the analysis of the modulated field envelope. Treating the signals in the optical frequency domain, as opposed to a traditional analysis, where the modulation of power and phase is investigated separately, proves very convenient for analyzing the Small-Signal Frequency Response (SSFR) of an SOA followed by an arbitrary filter. The approach leads to a simple and general criterion for the filter transfer function, in order to obtain a flat SSFR. Analytical expressions for the small-signal bandwidth that may be obtained using different types of filters are provided, and the effect of the filter phase response is analyzed.

5.1 Standard-Mode Cross-Phase Modulation

The term *standard-mode* XPM (SM-XPM) refers to the operation of interferometric switches, for which *only one* of the interfering signals is modulated. This mode of operation can be realized in a Mach-Zehnder interferometer (MZI) configuration, as shown in Fig. 5.2 for co-propagation, and in a Michelson interferometer (MI) [67], but not in e.g. a Sagnac interferometer, which will be explained further in section 5.2.

Since most of the experimental work has been carried out with MZIs, the principle of operation will be explained using the MZI as an example: the probe signal, which can be CW or pulsed, depending on the application, is launched into the common arm of the interferometer, and recombines at the output after traversing the SOAs in the interferometer arms. If the MZI is made up of a $1x2$ and a $2x1$ coupler, which do not introduce phase shifts, the phase difference between the interfering parts of the probe signal, in the absence of a control input signal, is defined exclusively by the SOA bias currents and the passive phase shift $\Delta\phi_t$. Depending on the desired polarity of the switched probe signal, the currents and/or the passive phase shift are adjusted to obtain constructive or destructive interference at the output, in the absence of a control input, corresponding to a logic zero. When the control input power goes from low to high and introduces a phase shift on the probe signal traveling in the upper arm, the probe signal

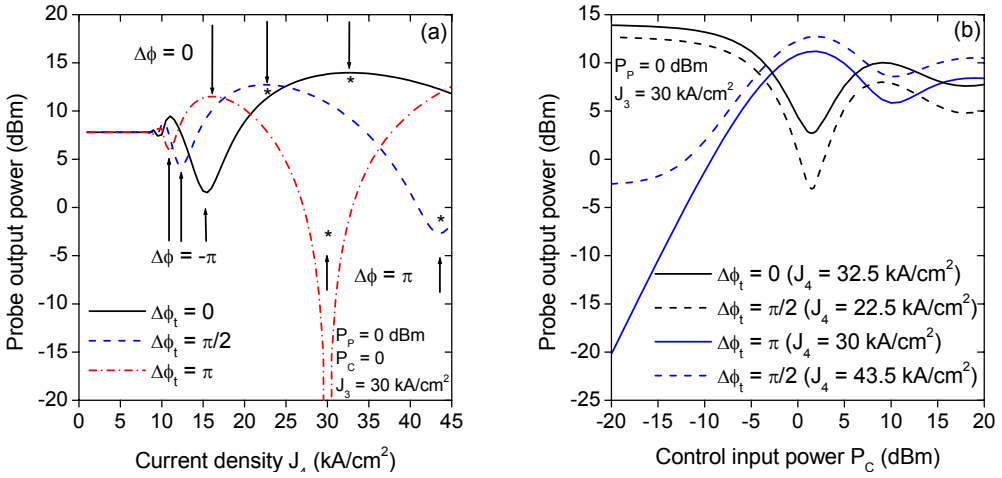

Figure 5.3: Static MZI transfer funtions. (a) Probe output power vs. current density through SOA #4 (J_4) for fixed $J_3 = 30$ kA/cm^2. The passive phase shift $\Delta\phi_t$ is a parameter. (b) Probe output power vs. control input power for configurations indicated by asterisks in (a).

is switched, as constructive interference is turned into destructive interference, giving rise to a polarity-inverted probe signal, or vice versa. Polarity-inversion and polarity-preservation is also often referred to as *out-of-phase* (OOP) and *in-phase* (IP), respectively. A full π phase shift is needed to switch from constructive to destructive interference, or vice versa, but in practice a smaller phase shift may be optimal, since a larger phase modulation requires a larger carrier modulation, which increases the level of nonlinear patterning effects and chirp. Moreover, a π phase shift may not be achieved at very-high repetition frequencies [127]. The MZI operated in standard-mode (SM-MZI) is transparent towards the data format, which means that it may be switched by an RZ or NRZ control signal without modifying the operating conditions. This is important from a systems perspective, and represents an advantage over differential-mode switches, for which the operating conditions are different for RZ and NRZ.

Fig. 5.3 (a) shows the output probe power vs. the current density J_4 through the lower arm (SOA 4) for $J_3 = 30$ kA/cm^2, $P_P = 0$ dBm, and $P_C = 0$ W, with the passive phase shift in the upper arm as a parameter. According to the sign convention in (3.20) the phase change $\phi_{T,4}$ observed by the probe signal traversing SOA 4 decreases with an increase of J_4. Thus, a phase difference between the interferometer arms of $\Delta\phi = \phi_{T,3} - \phi_{T,4} + \Delta\phi_t = 0$, corresponding to constructive interference, is obtained at decreasing values of J_4 as the passive phase shift is increased. Similarly, the minima corresponding to $\Delta\phi = -\pi$ and $\Delta\phi = \pi$ also move towards lower values of J_4 for increasing $\Delta\phi_t$. This is important, since it means that $\Delta\phi = \pi$ can be satisfied, while ensuring that the gains in the two SOAs are equal, i.e. $G_{T,3} = G_{T,4}$. When both requirements are fulfilled, which is the case for $J_4 = J_3$ and $\Delta\phi_t = \pi$, as observed in Fig. 5.3 (a), complete destructive interference is obtained, which gives rise to an in-phase operating

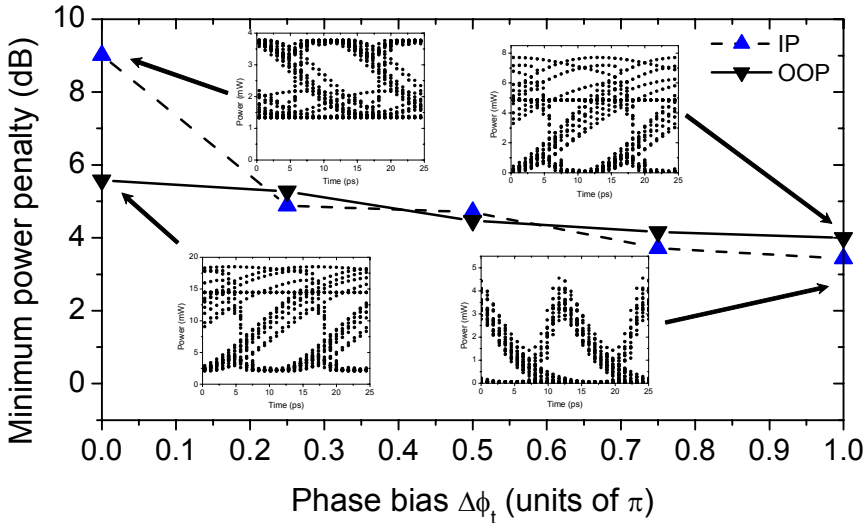

Figure 5.4: Minimum power penalty for 80 Gb/s standard-mode switching vs. passive phase shift $\Delta\phi_t$, for in-phase (IP) and out-of-phase (OOP) operation.

condition with a highly nonlinear transfer function. This condition may also be obtained without the passive phase shifter by constructing the MZI from $2x2$ couplers, which introduce a $\pi/2$ phase shift for the cross-output, compared to the bar-output. In that case the two probe outputs are referred to as *conjugate signals*[1] [120].

Fig. 5.3 (b) shows static transfer functions corresponding to the points marked by asterisks in Fig. 5.3 (a), and several important facts can be deduced from the characteristics: the range of the control input power for which the slope magnitude of a transfer function is larger than 10 dB/decade, is larger for the *in-phase* operating points. This has a major impact on the so-called *input power dynamic range* (IPDR), which defines the range of the control input power for which the excess power penalty is less than 1 dB. Moreover, a nonlinear transfer function is able to *reshape* the input data signal by improving the extinction ratio and potentially suppress amplitude fluctuations if the transfer function is flat around the logic "0" and "1" levels. This reshaping is often referred to as 2R regeneration in combination with (re)amplification, and will be detailed in chapter 7. Finally, a significantly smaller pulse energy is required to facilitate a π phase shift, compared to suppressing the gain. This reduces the switching energy, and thus the power consumption, of interferometric switches, and due to a decreased carrier modulation the chirp is potentially reduced.

The analysis made in section 4.2.1 predicted an optimum SOA length of $L = 3.5$ mm for XGM, and the result for SM-XPM is expected to be similar. However, for the large-signal analysis of SM-XPM, the SOAs in the arms of the

[1]Not to be confused with the conjugate signal in a Four-Wave Mixing (FWM) process

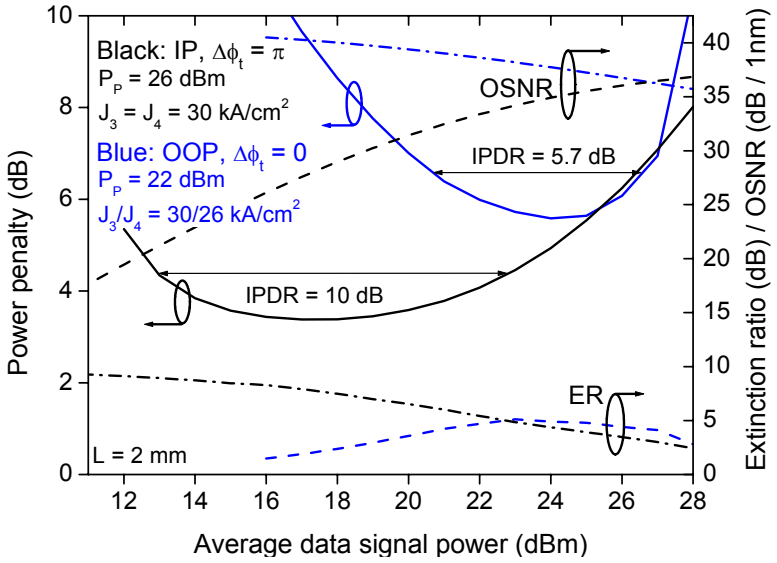

Figure 5.5: Power penalty (left axis) and Extinction ratio/OSNR (right axis) at 80 Gb/s vs. average data signal power for in-phase and out-of phase operating conditions, with indication of IPDR.

MZI assume lengths of $L = 2$ mm, as this is compatible with devices that have been available for experimental studies. The cross-section of the SOAs in the MZI model is identical to the SOA used so far, and the input data signal is still an 80 Gb/s PRBS of word length $2^5 - 1$, consisting of 3 ps wide Gaussian pulses with an ER of 13 dB.

The MZI is assumed to be of the active-passive (A-P) variant, i.e. only the interferometer arms are active. This is opposed to the all-active (A-A) devices used in many of the experiments presented in this thesis, where the entire interferometer is active. As illustrated in Fig. 5.2, the data signal is launched into the upper arm (SOA #3), which is biased at $J_3 = 30$ kA/cm^2, and for each value of the phase bias $\Delta\phi_t$ in the set 0, $\pi/4$, $\pi/2$, $3\pi/4$, π, the current density J_4, and the probe and data signal powers are varied to determine the set of parameters giving rise to the lowest power penalty for both the in-phase and out-of-phase condition.

Fig. 5.4 shows an overview of the effect of the phase bias. The performance of the out-of-phase operating point is almost invariant towards $\Delta\phi_t$, which is expected from the static transfer functions in Fig. 5.3 (b). The reason for the slight improvement of performance for high values of $\Delta\phi_t$ is that the optimum current density J_4 decreases with an increase of $\Delta\phi_t$. Thus, $G_{T,4}$ decreases and approaches the value of $G_{T,3}$ at the input power corresponding to a π phase shift, which gives a better extinction. For the in-phase condition however, a phase bias close to π is favored, since as mentioned, this gives rise to a highly nonlinear transfer function, and thus a high ER of the wavelength converted signal, and suppression of nonlinear patterning, since the transfer function goes through a

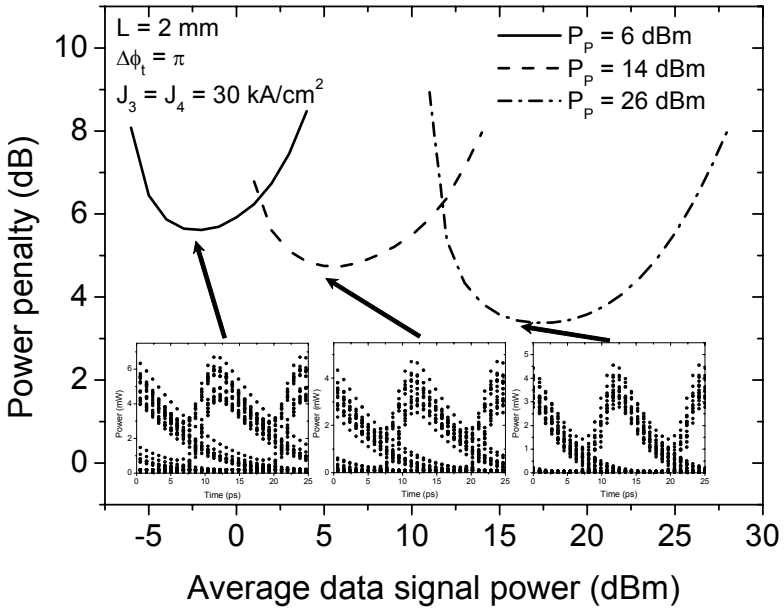

Figure 5.6: Power penalty at 80 Gb/s for standard-mode, in-phase operation of MZI vs. average data signal power, with the input probe power as a parameter.

maximum in Fig. 5.3 (b). The latter is clearly observed in the lower, right inserted eye diagram. For $\Delta\phi_t = 0$, the minimum transmission is quite high (> 0 dBm in Fig. 5.3 (a)), which corresponds to a very poor ER for the in-phase operating point. This explains the high in-phase penalty observed for $\Delta\phi_t = 0$ in Fig. 5.4.

From the inserted eye diagrams in Fig. 5.4 it is clear that the performance is limited by an insufficiently fast recovery of the phase response, which causes intersymbol interference - in other words linear patterning. This is not surprising, since this was also the conclusion for XGM, and the only effect on the patterning of inserting the SOA in a MZI is the nonlinear transfer function, which actually reduces the saturation-induced, i.e. nonlinear, patterning.

Fig. 5.5 shows the power penalty, ER, and OSNR vs. average data signal input power for an in-phase and out-of-phase operating point, and reveals some fundamental differences between the two cases. First, the input power dynamic range (IPDR) is observed to be higher for in-phase operation. As mentioned briefly, this is because the in-phase transfer function is super-linear for low data input powers, which ensures a large ER. When the average input power is increased the ER decreases with a moderate slope, while the OSNR increases. These effects tend to balance each other over a large range of data powers, resulting in a large IPDR. Notice that the minimum penalty is obtained as a trade-off between the ER and OSNR. As it may be seen from the out-of-phase transfer functions in Fig. 5.3 (b), a large negative slope magnitude, and thus ER, can only be maintained in a relatively small range of the input data power. The low modulation depth means that the OSNR only decreases moderately as the data power in-

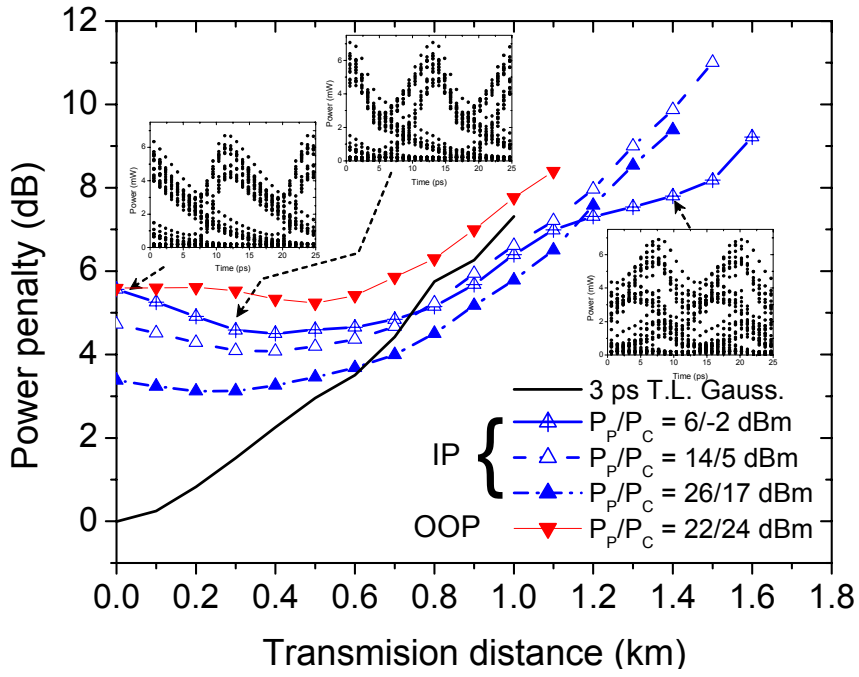

Figure 5.7: Power penalty at 80 Gb/s for IP and OOP conditions of MZI operated in standard-mode vs. transmission distance on SMF.

creases, and since the OSNR is very high, the power penalty is governed almost exclusively by the ER.

For the in-phase operating point in Fig. 5.5 a large CW probe power of 26 dBm was used, corresponding to 20 dBm coupled into the common arm (SOA #2). Fig. 5.6 shows the effect of reducing it: the minimum penalty increases, because the effective carrier lifetime increases. The inserted eye diagrams clearly show that the trailing edges of the converted pulses become longer as the probe power is decreased, leading to intersymbol interference and a decreased ER. In other words, decreasing the CW probe power brings increased linear patterning.

It is worth pointing out that the smallest power penalty achieved with XGM in a 2 mm long SOA was about 7 dB (see Fig. 4.9 (a)), which was obtained using $P_P/P_C = 18/24$ dBm. According to Fig. 5.6, a penalty below 6 dB can be obtained with $P_P/P_C = 6/-2$ dBm, by putting the same SOA in a MZI.

The transmission properties of the three "sweet spots" in Fig. 5.6 are compared in Fig. 5.7, which shows the power penalty as a function of transmission distance on standard SMF with a dispersion of $D_{SMF} = 17$ ps/(nm km). As mentioned in section 4.2.1, the blue-shifted parts of the signal travel faster than the red-shifted parts, which means that pulses of a wavelength converted probe signal with in-phase polarity are expected to narrow initially upon propagation. This is shown to be the case in Fig. 5.7 by comparing the eye diagrams corresponding to $L = 0$ and $L = 0.3$ km, respectively. The slight pulse compression leads to

reduced intersymbol interference and consequently an increased ER, which gives rise to a sensitivity improvement. Comparing the transmission properties of the three in-phase signals from Fig. 5.6, the signal with the highest penalty at $L = 0$ is the one with the lowest penalty at $L > 1.2$ km. Since all three signals are similarly chirped, the superior transmission properties of the signal obtained with $P_P = 6$ dBm, is primarily due to the larger pulse width at $L = 0$, corresponding to a narrower spectrum, which is less sensitive towards dispersion. This shows that the operating conditions of SOA-based switches should ideally be optimized for a specific link, and not right at the output. Fig. 5.7 also shows the penalty curve for the out-of-phase operating point in Fig. 5.5. An out-of-phase signal is expected to disperse faster than an in-phase counterpart, and this should show in the evolution of the penalty. However, as it turns out, the penalty goes through an unexpected minimum before it increases, and an error-floor is reached after 1.1 km. The reason for the initial improvement is that field components of pulses broaden into neighboring timeslots containing logic zeros. Here, the fields may interfere destructively, which reduces the power in the zero-level, thereby increasing the ER and decreasing the penalty.

Finally, Fig. 5.7 shows the penalty curve for the input data signal consisting of transform limited, 3 ps wide Gaussian pulses. Due to the significantly wider spectrum, the pulses of the input data disperse much faster than the converted signal, and after only 1 km the signal can no longer be detected.

5.2 Differential-Mode Cross-Phase Modulation

The analysis in section 5.1 showed that standard-mode XPM in a MZI gives rise to performance enhancements over XGM, but that linear patterning effects, characterized by the relatively slow carrier recovery, still remains the limiting factor. During the last decade, a new type of fast, all-optical switch, which alleviates some of the consequences of the long carrier lifetime, has been developed and demonstrated at bitrates exceeding 100 Gb/s. This new type of switch takes advantage of the fact that the switching characteristic of an interferometer is governed exclusively by the phase difference between its two arms. This allows operation in a so-called *differential-mode* of operation, enabling the generation of a narrow switching window.

The history of the differential-mode concept started with the demonstration of the TOAD by Sokoloff et al. in 1993 [71]. Shortly thereafter, still in 1993, the first integratable switch-configuration exploiting a differential phase shift was suggested by Tajima [128], and is based on a MZI with SOAs in both interferometer arms. This configuration will in the following be referred to as the differential-mode MZI (DM-MZI). A widely used SOA/fiber hybrid differential-mode switch, referred to as the *Ultrafast Nonlinear Interferometer* (UNI), containing a single SOA and two short spans of PM fiber, was proposed by Patel et al. in 1996 [69], and has been dubbed the *Polarization Discriminating MZI* (PD-MZI) by some

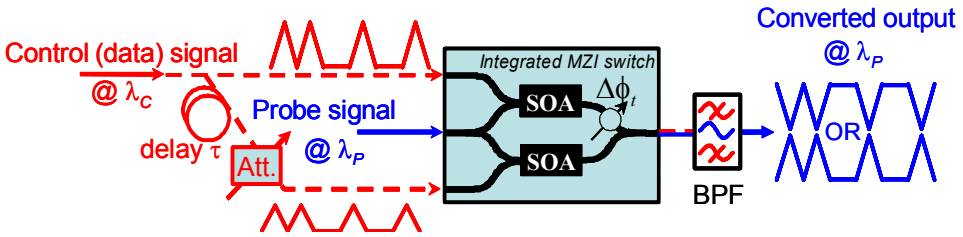

Figure 5.8: Schematic of differential-mode operation of MZI. Choice of signal polarity is indicated.

authors [70]. Finally, the Delayed-Interference Signal Converter (DISC), which is a simplified and integratable version of the UNI, and based on a single SOA and a passive, asymmetric MZI filter, was proposed by Ueno et al. in 1998.

In the following, the principle of operation of all four switch configurations will be explained, with the emphasis on the DM-MZI and the DISC, which are analyzed and compared in great detail.

5.2.1 Differential-mode MZI

The DM-MZI configuration is shown in Fig. 5.8, and the principle of operation is as follows: by exciting both SOAs with the same RZ control signal, with one signal delayed by τ with respect to the other, the phase difference between the arms of the MZI, observed by a probe signal travelling through the interferometer, effectively cancels-out the slow recovery of the carrier density. The result is a switching window, with a width limited solely by the width of the control pulses and not by the carrier lifetime. This has been exploited to extract the individual 10.5 Gb/s tributaries from a 336 Gb/s OTDM data stream, by passing the 336 Gb/s data signal through the MZI, and switching a single tributary by means of two 10.5 GHz clock signals, with a relative delay of one 3 ps timeslot [129]. The periodic excitation of the SOAs, which is needed for demultiplexing, leads to a pseudo steady-state, in which the carrier density varies periodically, and gives rise to identical switching windows in each period of the clock signal. The latter corresponds to eliminating patterning effects. In contrast, it was explained in section 4.3 that when the transmission of the switch is controlled by a random data signal, as needed for wavelength conversion and regeneration, the probe transmittance may depend on the data sequence prior to the bit to be switched.

Fig. 5.9 (a) shows a simulation of the probe phases $\phi_{T,3}^{NL}(t)$ and $\phi_{T,4}^{NL}(t)$ vs. time at the output of the two SOAs in the MZI, using the simple model in section 4.3 with the same parameters as in Fig. 4.13 and a differential delay of $\tau = 5$ ps. Again, the superscript "NL" denotes that both the linear and nonlinear terms of the rate equation (4.43) are included. The amplitude of $\phi_{T,4}(t)$ is reduced slightly compared to that of $\phi_{T,3}(t)$ in order to satisfy $\phi_{T,4}(t) \approx \phi_{T,3}(t)$ during phase recovery.

As shown in (3.43), the transmission of the MZI is determined by the phase

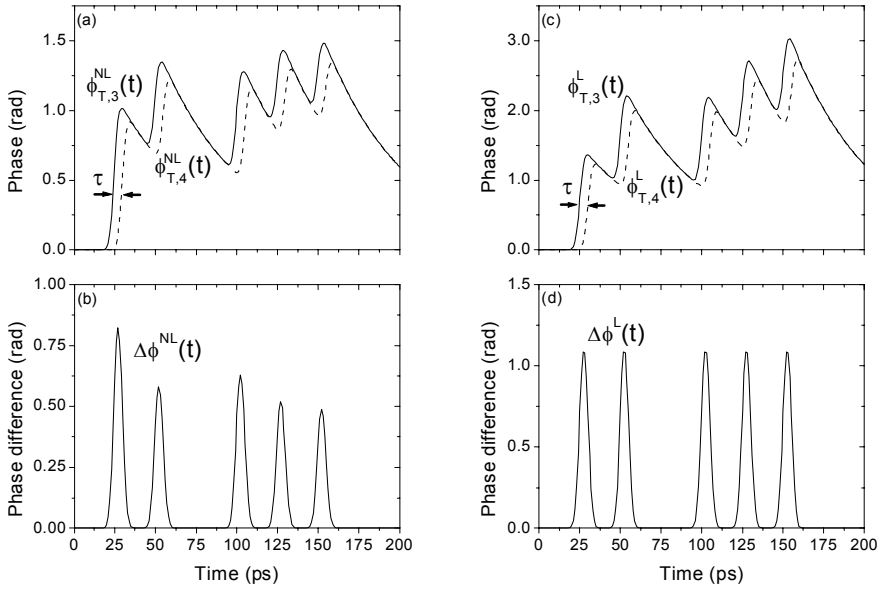

Figure 5.9: Switching windowd obtained with DM-MZI with and without nonlinear saturation term of eq. (4.43). (a) Phase of probe signal in individual interferometer arms, including nonlinear term. (b) Corresponding phase difference. (c) Equivalent to (a), but without nonlinear term. (d) Corresponding phase difference.

difference between the two components of the probe signal. Consequently, the probe signal reaching the output first, in this case the signal in the upper arm, switches the transmission of the MZI from low to high. When the probe signal from the lower arm arrives at the output, the phase difference is reset to the original level, and thereby effectively cancels the long recovery of $\phi_{T,3}^{NL}(t)$. The slight reduction of $\phi_{T,4}(t)$ in Fig. 5.9 is obtained "artificially" by simple multiplying it by an appropriate factor. In reality, an attenuation of the data signal, as illustrated in Fig. 5.8, is necessary to obtain the same effect. Fig. 5.9 (b) shows how the resulting phase difference $\Delta\phi^{NL}(t) = \phi_{T,3}^{NL}(t) - \phi_{T,4}^{NL}(t)$ opens a switching window with a width determined by τ, in this case 5 ps. Figs. 5.9 (c-d) are equivalent to (a-b), the only difference being that the nonlinear term in the rate equation (4.43) is neglected. Comparing Figs. 5.9 (b) and (d), the effect on the carrier density induced patterning effects of applying the differential-mode of operation to the MZI becomes clear: linear patterning effects are completely compensated for, since the long recovery of the carrier density cancels out. However, the nonlinear patterning effects persist, and manifest as a decrease of the phase difference $\Delta\phi^{NL}$ for successive excitations of the SOA by control pulses, which translates into an equivalent peak pulse power variation for the output probe signal. The peak probe power ultimately reaches a steady-state-like minimum level after a time span given by the effective carrier lifetime, which corresponds to a large number of timeslots at high bitrates. Nonlinear patterning is likely to be the reason why the DM-MZI has been demonstrated at a maximum bitrate of

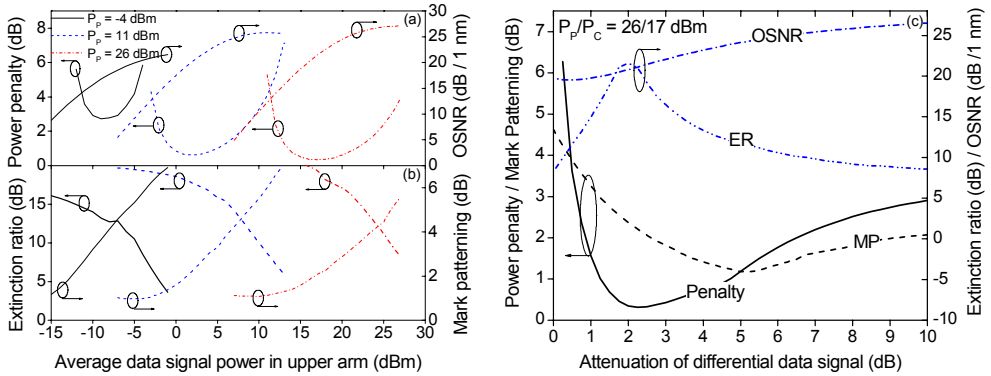

Figure 5.10: (a) Power penalty (left axis) and OSNR (right axis) vs. average data power in upper arm of MZI with input probe power as a parameter. Power in lower arm of MZI is optimized in each case. (b) ER (left axis) and MP (right axis) vs. data power to upper arm. (c) Power penalty/MP (left axis) and ER/OSNR (right axis) vs. attenuation of data signal to lower arm for $P_P/P_C = 26/17$ dBm.

84 Gb/s [93], which is modest compared to the demultiplexing experiments.

The performance of the DM-MZI is investigated numerically at 80 Gb/s, using a MZI configuration with a differential delay $\tau = 3$ ps, and a phase bias of $\Delta\phi_t = \pi$, which was shown in Fig. 5.4 to be the best choice for the SM-MZI. There is no reason to believe that the optimum phase bias is different for the DM-MZI, since as mentioned, the effect of launching a copy of the data signal into the lower arm, is simply to cancel the long phase recovery. Thus, all the results presented in the following are obtained with $J_3 = J_4 = 30$ kA/cm^2, which was found to be the optimum bias condition for $\Delta\phi_t = \pi$.

Before discussing the results, a quantity referred to as *Mark patterning* (MP) is introduced, and defined as the ratio of the highest to the lowest logic one-level. Fig. 5.10 (a) and (b) show the power penalty, OSNR, ER, and the newly defined MP as a function of the average data signal power into the upper arm for the CW probe powers $P_P = -4$, 11, and 26 dBm. Notice that due to the 6 dB splitting loss, the probe power entering each of the two SOAs is in fact only -10, 5, and 20 dBm. In each case the attenuation of the data signal launched into the other (in this case, the lower) data input, has been optimized to obtain the smallest possible power penalty. For $P_P = 26$ dBm the minimum penalty is reduced to about 0.34 dB, which is about 3 dB better than the smallest penalty obtained with the standard-mode configuration.

As the data power in the upper arm is increased the ER decreases, while the MP increases. The latter is a consequence of the increased level of saturation, and will be addressed further in the following. The degradation of the ER, however, is simply due to fact that the MZI transfer function for $\Delta\phi_t = \pi$ becomes less nonlinear as the average input data power increased, cf. Fig. 5.3 (b). It is also noticed that the IPDR for $P_P = 26$ dBm is approximately the same as for the SM-MZI configuration. When the probe power is decreased, the power penalty increases, similar to the SM-MZI as shown in Fig. 5.6. However, whereas the

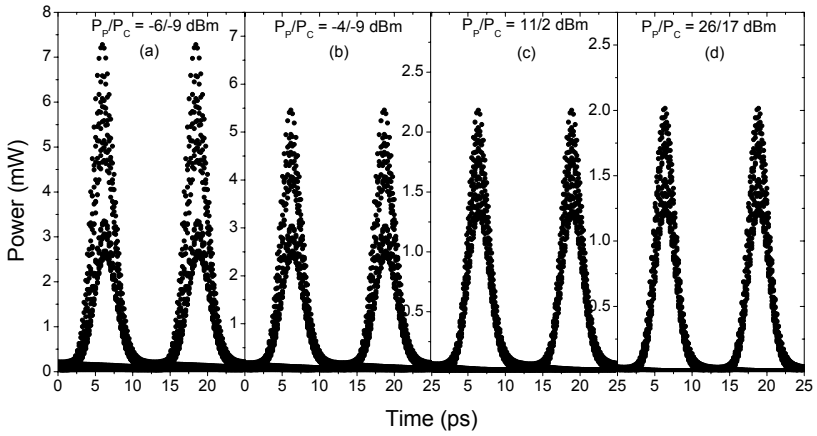

Figure 5.11: Eye diagrams corresponding to the minimum power penalty for increasing input probe powers: (a) −6 dBm, (b) −4 dBm, (c) 11 dBm, and (d) 26 dBm.

degradation for the SM-MZI configuration was due to linear patterning, leading to intersymbol interference, the increase of the penalty in Fig. 5.10 (a) is caused by an increase of the mark patterning, which is a nonlinear patterning effect. This is illustrated in Fig. 5.11, where the eye diagrams corresponding to the minimum power penalties for $P_P = -6$, -4, 11, and 26 dBm are shown. All four eye diagrams are clearly open and symmetrical, but the level of power fluctuation above the detectable eye diagram increases as the probe power is lowered. Since these fluctuations represent useless power to the receiver, they give rise to an increased power penalty. The dependence of the MP on the probe power was already addressed in section 4.3, and can be attributed the holding-beam effect of the probe signal.

Fig. 5.10 (c) shows the power penalty, ER, OSNR, and MP as a function of the attenuation of the data signal in the lower arm for the optimum combination $P_P/P_C = 26/17$ dBm, where P_C represents the average data power into the upper arm. Increasing the attenuation to infinity, i.e. turning the power to the lower arm off, is clearly equivalent to the SM-MZI configuration. Thus, Fig. 5.10 (c) is helpful in illustrating the effect on the different figures of merit of applying the differential scheme of operation.

When the attenuation is decreased, the penalty drops and goes through a minimum at an attenuation of $Att = 2.25$ dB, primarily due to the large increase of the ER, which attains its maximum at approximately the same attenuation. The OSNR decreases slightly as the attenuation is lowered, because applying the differential data signal prevents the phase difference $\Delta\phi(t)$ between the interferometer arms to reach the maximum, thus reducing the output power. This is also clearly illustrated in Fig. 5.9. Finally, the mark patterning is observed to go through a minimum at 5.25 dB, and attains a level at $Att = 2.25$ dB very similar to the level obtained with the SM-MZI ($Att \to \infty$).

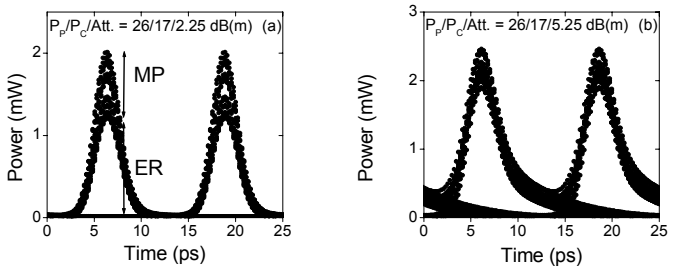

Figure 5.12: Eye diagrams corresponding to minimum power penalty (a) and minimum mark patterning (b) in Fig. 5.10 (c)

The eye diagrams corresponding to $Att = 2.25$ dB (minimum penalty) and $Att = 5.25$ dB (minimum MP), are illustrated in Fig. 5.12 (a) and (b), respectively. From these eye diagrams it is seen that for $Att = 5.25$ dB the switch is operated in a *partial* differential-mode, since the switched pulses are symmetrized, but still with clear evidence of the slow phase recovery, which is not properly cancelled by the differential data signal. The construction of the two signals is detailed in Fig. 5.13, which shows the probe phases $\phi_{T,3}(t)$ and $\phi_{T,4}(t)$, the phase difference, and the switched probe output for $Att = 2.25$ dB (a-c) and $Att = 5.25$ (d-f). For $Att = 2.25$ dB, the trailing edges of the phase response are completely cancelled out, giving rise to short, symmetric pulses with a high extinction. The first pulse in the string of five causes a slightly larger phase difference (see (b)) than the following, due to saturation, i.e. nonlinear patterning. This effect is enhanced by XGM, which reduces the amount of probe power available after the first data pulse in the string of five. For $Att = 5.25$ dB, the differential signal only partially cancels the trailing edge, resulting in sharpened pulses with remaining, though reduced, trailing edges. More importantly, since the differential signal is so weak that the peaks of $\phi_{T,4}(t)$ are lower than the valleys of $\phi_{T,3}(t)$, the peaks of the phase difference $\phi_{T,3}(t) - \phi_{T,4}(t)$ are determined primarily by $\phi_{T,3}(t)$. Accordingly, the phase difference displays a patterning similar to that of $\phi_{T,3}(t)$, which is noticeably smaller than for $Att = 2.25$ dB. Moreover, the partial differential-mode operation in Fig. 5.13 (d-f) is slightly less degraded by XGM, since the probe power modulation in SOA #4 is also reduced. All in all, the switched probe output in Fig. 5.13 (f) displays about 1 dB ($\approx 25\%$) less mark patterning compared to the output in Fig. 5.13 (c), at the expense of a reduced ER.

The reduced patterning of the phase difference is an important property of the DM-MZI, which makes it fundamentally different from differential-mode switches that do not allow control of the individual phase shifts, such as e.g. the UNI and the DISC.

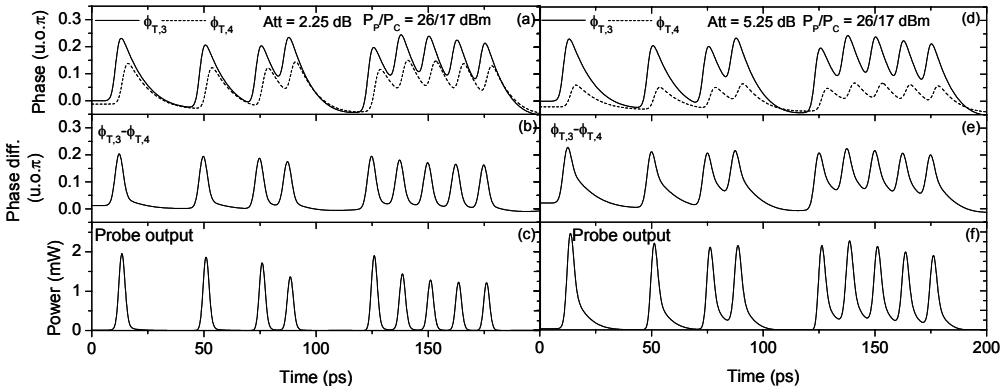

Figure 5.13: Detailed comparison of conditions leading to minimum penalty (a-c), and minimum MP (d-f). Individual probe phases in the two interferometer (a,d) cause the phase differences depicted in (b,e), and ultimately the different output pulse patterns in (c,f).

5.2.2 The TOAD Switch

As mentioned already, the differential control scheme was initially proposed with the introduction of the TOAD, shown in Fig. 5.14 configured as a wavelength converter. The TOAD is a Sagnac interferometer with an SOA displaced Δx compared to the center of the loop. In the absence of a control signal the clockwise and counter-clockwise propagating parts of the probe signal acquire the same phase shift, and the output transmission may be tuned by means of the polarization controller (P.C.), which plays the role of the passive phase bias in the MZI in Fig. 5.8. For in-phase operation the phase bias is adjusted to give destructive interference at the output, corresponding to a full reflection of the probe signal. In the presence of the data signal the probe component travelling in the clockwise direction co-propagates with the data signal through the SOA, giving rise to a power and phase modulation of the probe. The counter-clockwise travelling component reaches the SOA at a time $\approx 2\Delta x/v_g$ later. When the two probe components interfere at the output of the 3 dB 2x2 coupler, the phase shift acquired by the clockwise travelling component opens up a switching window which is closed by the phase shift of the delayed counter-clockwise travelling part.

The principle of operation is identical to that of the MZI in differential mode, but the performance is inferior, since the duration of the trailing edge of the switching window is determined by the length of the SOA, whereas the duration of the leading edge is governed by the stimulated lifetime. This gives rise to an asymmetric switching window, corresponding to asymmetric wavelength converted pulses in the configuration in Fig. 5.14, and a maximum bitrate limited by $\approx v_g/(2L)$, as explained in section 4.1.2.

Although the TOAD has been integrated and demonstrated at 10 Gb/s [68], most published demonstrations of the TOAD switch have been realized in SOA/

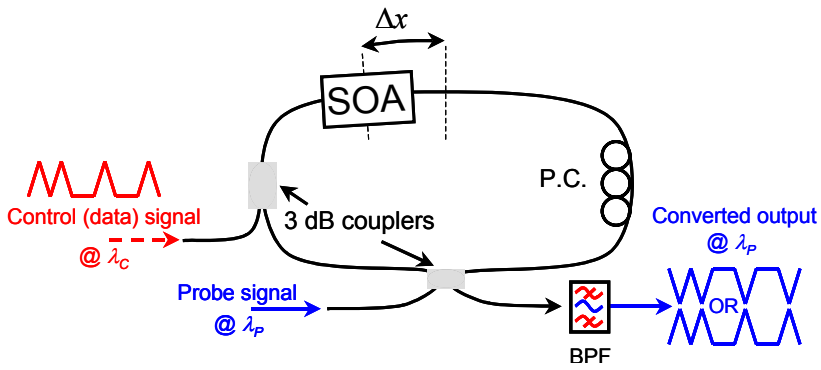

Figure 5.14: Schematic of the Terahertz Optical Asymmetric Demultiplexer (TOAD) switch. P.C. polarization controller.

fiber hybrid setups, using 2 fiber couplers and an SOA. Compared to the MZI the TOAD is much more stable in a hybrid setup, since the interfering components in the TOAD share the same physical medium. Mechanical instabilities and thermal fluctuations are thus experienced by both components and tend to average out. This is not the case in a MZI, where the interferometer arms are physically separated, and will consequently experience independent perturbations.

5.2.3 The UNI Switch

The UNI, which is shown in Fig. 5.15, is also referred to as the PD-MZI, which makes sense, since the UNI may be interpreted as in in-line implementation of a MZI operated in the differential mode. The clocked probe signal is launched into a birefringent fiber (BRF) at an angle of 45° compared to the principal axes of polarization, thereby exciting the two polarization states equally. At the output of the BRF each clock pulse is split into two orthogonally polarized pulses of equal energy with a temporal separation of τ, corresponding to the group delay between the fast and slow axis of the BRF. This signal is injected into an SOA along with the control signal, in this case a random data signal, with a relative timing such that the data pulses arrive at the input facet of the SOA between the two orthogonal probe pulses.

In the presence of a control pulse inducing a π phase shift, the probe signal at the output of the SOA looks like Fig. 5.16 (a), where the phase relaxation is depicted as a linear function for simplicity. The separated probe pulses are re-aligned by launching the signal into an identical piece of BRF, at an angle of $-45°$ such that the leading (white) and trailing (grey) probe pulses are aligned to the slow and fast axes, respectively. At the output of the BRF the probe signal looks like Fig. 5.16 (b): the probe pulses are aligned, but the phase modulation $\phi(t)$ is displaced.

Fig. 5.16 (c) explains the switching principle: for $\Delta\phi = \phi(t) - \phi(t-\tau) = 0$, corresponding to times before the switching window opens, the total field is

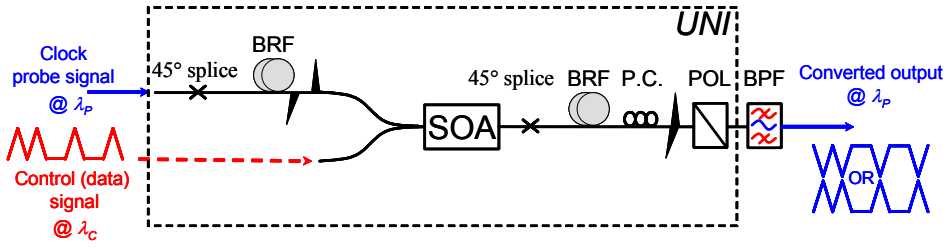

Figure 5.15: Schematic of the Ultrafast Nonlinear Interferometer (UNI). BRF: Birefringent fiber, POL: polarizer, P.C: polarization controller.

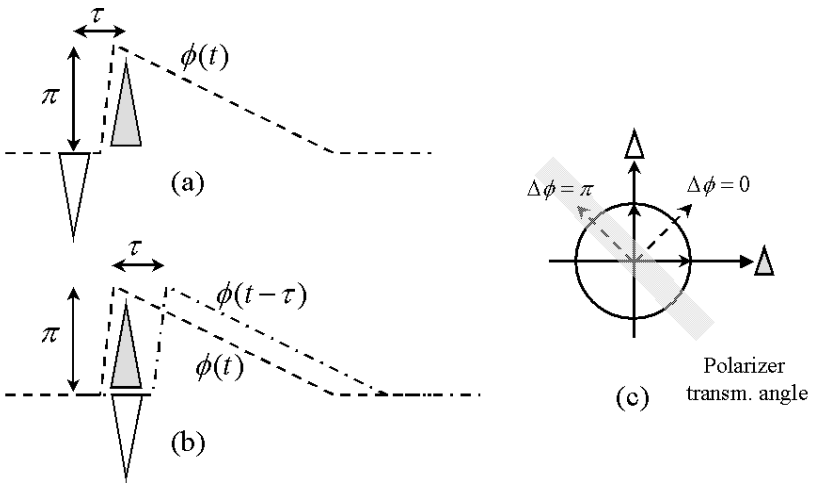

Figure 5.16: Principle of operation of UNI switch. (a) Phase shift induced on the trailing pulse, and (b) differential phase shift obtained when pulses are temporally re-aligned. (c) transmision angle of polarizer set to 135° compared to angle of trailing pulse.

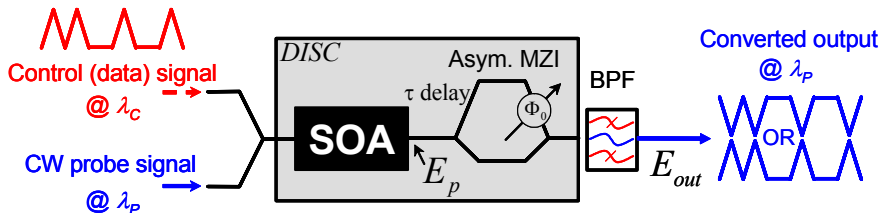

Figure 5.17: Schematic of Delayed-Interference Signal Converter (DISC), with a delay of τ and a phase shift Φ_0 in the upper arm of the asymmetric MZI filter.

polarized at an angle of 45° compared to the angle of the grey pulse. At the onset of the phase modulation of the grey pulse, we have $\phi(t) = \pi$, corresponding to a 90° counter-clockwise rotation of the polarization angle, and finally, when the delayed phase response $\phi(t-\tau)$ increases from 0 to π, the polarization state returns to the 45° angle. By aligning the full-transmission axis of the polarizer (POL) to $\approx 135°$ the UNI will only transmit the probe signal within the window of width τ. As sketched in Fig. 5.16 (b), $\phi(t-\tau)$ is not completely equal to $\phi(t)$ during phase recovery, which means the polarization angle settles at a value $v_{\min}$ larger than 45°. This gives rise to a finite, and potentially bad extinction during this time interval. To some extent this may be compensated for by tuning the zero-transmission angle of the polarizer to $v_{\min}$ at the expense of a reduced peak transmission, and a degraded extinction for $\phi(t) = \phi(t-\tau) = 0$. In other words the P.C in front of the polarizer is an important optimization parameter.

The UNI can potentially be integrated by using TE-TM splitting couplers instead of BRF, and rotating the polarization of one of the two separated probe pulses by 90° before interference [70]. The latter may be obtained using a half-wave plate and ensures that the re-aligned probe pulses are in the same polarization state. Due to the complexity of integrating polarization discriminating elements the two-SOA MZI in differential mode, shown in Fig. 5.8, is more suitable for integration. For hybrid implementations, however, the UNI is the configuration-of-choice due to the high-speed potential, relative insensitivity to environmental disturbances, and ease of implementation.

5.2.4 The DISC Switch

The UNI implementation shown in Fig. 5.15 employs a clocked input probe signal. This is necessary however, only if the data signal requires re-timing, and the clock signal is dispensable if the switch is intended for wavelength conversion only. In this case the clock may be replaced by a CW probe, and the polarization splitting differential delay before the SOA is unnecessary. So is the polarizer at the output, as the polarization of the signal is intended to maintain its state from input to output. The simplified differential-mode wavelength converter is referred to as the *delayed interference signal converter* (DISC). The DISC has been demonstrated at bitrates up to 168 Gb/s using a hybrid implementation [74], and up to 100 Gb/s

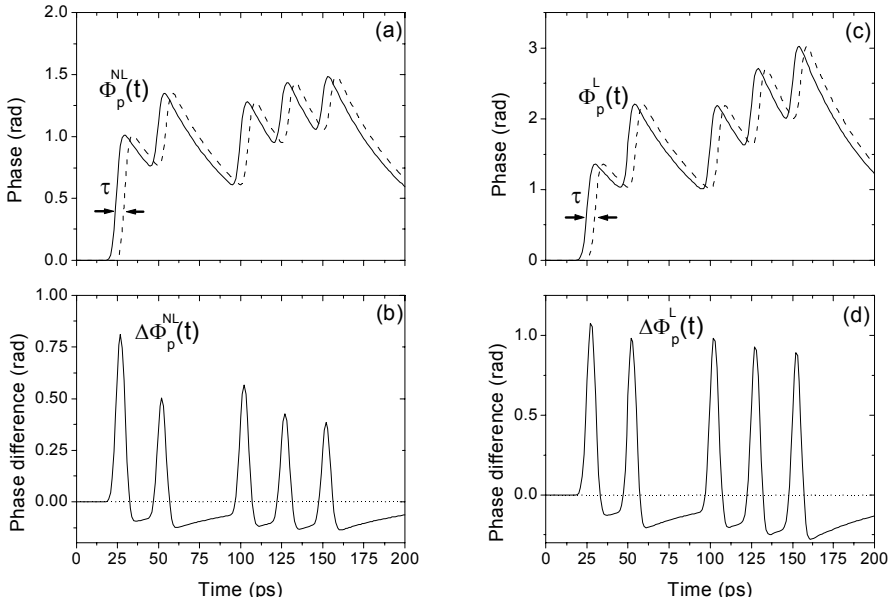

Figure 5.18: Nonlinear patterning persists, whereas linear patterning is eliminated by the DISC. The figure is equivalent to Fig. 5.9. Differential delay $\tau = 5$ ps.

with a monolithically integrated device [75]. It consists of a single SOA followed by a passive, asymmetric MZI (AMZI), which determines the differential delay.

The device is shown schematically in Fig. 5.17, with the relative delay τ and phase shift Φ_0 situated in the upper arm of the asymmetric MZI. The data and probe signals are launched into the SOA, where the amplitude and phase of the probe signal are modulated according to the bit-pattern of the data signal. In the AMZI the signals are split in two, and the part travelling in the upper arm acquires a delay of τ relative to the signal in the lower arm.

This is illustrated in Fig. 5.18 (a), which shows the simulated probe phase $\Phi_p^{NL}(t)$ vs. time at the output of the two arms of the asymmetric MZI, using the same parameters as in Fig. 4.13 and Fig. 5.9 with a differential delay of $\tau = 5$ ps, and including both the linear and nonlinear terms in (4.43). The principle of operation is the same as for the MZI operated in differential-mode: assuming that the phase offset Φ_0 is adjusted to in-phase operation, the signal in the lower arm arrives at the output first, and switches the transmission of the MZI from low to high. At the arrival of the probe signal from the delayed arm, the phase difference is reset, thereby effectively cancelling the slow recovery of $\Phi_p^{NL}(t)$.

Fig. 5.18 (b) shows how the resulting phase difference $\Delta\Phi_p^{NL}(t) = \Phi_p^{NL}(t) - \Phi_p^{NL}(t-\tau)$ opens a switching window of width τ, in this case 5 ps. Unlike for the differential-mode operation of the MZI, the DISC configuration does not provide any means of equalizing the phase responses, i.e. ensuring $\Phi_p(t) \approx \Phi_p(t-\tau)$, during phase recovery. This causes the negative phase difference between data pulses observed in Fig. 5.18 (b), and as explained for the UNI, this makes the

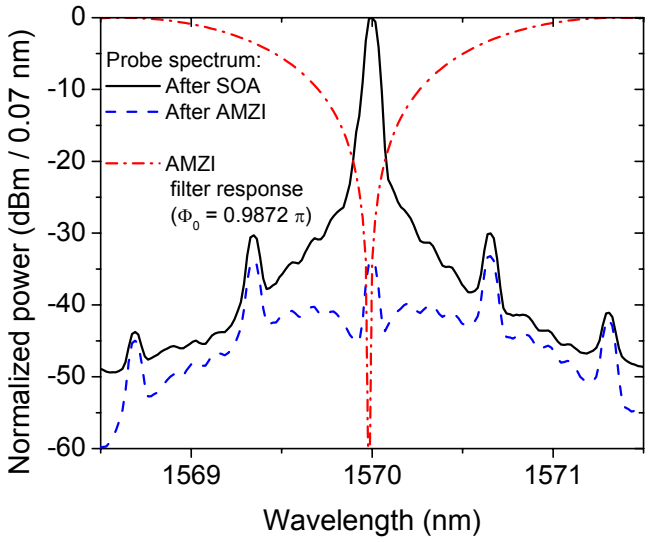

Figure 5.19: Example of simulated power spectra in 0.07 nm resolution. Spectrum after SOA (solid), after AMZI (dashed). Power transfer function of AMZI (dash-dotted).

phase bias Φ_0 subject to optimization. As it will be shown in the following, the undershoot of $\Delta\Phi_p^{NL}(t)$ gives rise to trailing "satellite pulses", and in order to minimize the amplitude of these pulses the phase bias Φ_0 must be smaller than π.

The nonlinear term in the rate equation (4.43) is neglected in Figs. 5.18 (c-d), and by comparison with Figs. 5.18 (b) and (d) the effect of the asymmetric MZI on the patterning effects is illustrated. Not surprisingly, the conclusion is the same as for the DM-MZI: linear patterning is compensated for, whereas nonlinear patterning persists.

In the following the DISC configuration is simulated by passing the cross-gain and cross-phase modulated probe waveforms calculated in section 4.2.1 with the detailed large-signal model through an AMZI with a differential delay of $\tau = 3$ ps. As it will be shown in section 5.3, the AMZI has a field transfer function given by

$$H_{AMZ}(\omega) = \frac{E_{out}(\omega)}{E_p(\omega)} = \frac{1}{2}\left(1 + e^{j(\omega\tau+\Phi_0)}\right) \tag{5.1}$$

where $E_{out}(\omega)$ and $E_p(\omega)$ are the Fourier transforms of the field envelopes $E_{out}(t)$ and $E_p(t)$, respectively (see Fig. 5.17). Thus, a convenient way of including the effect of the AMZI is by Fourier transforming the complex probe field envelope $E_p(t)$ at the output of the SOA, and multiplying it by $H_{AMZ}(\omega)$, before inverse Fourier transforming the result.

Fig. 5.19 shows a probe power spectrum in a 0.07 nm resolution[2] before and

[2]Spectra obtained by convoluting Fourier transforms by response function, measured with spectrum analyzer resolution at 0.07 nm.

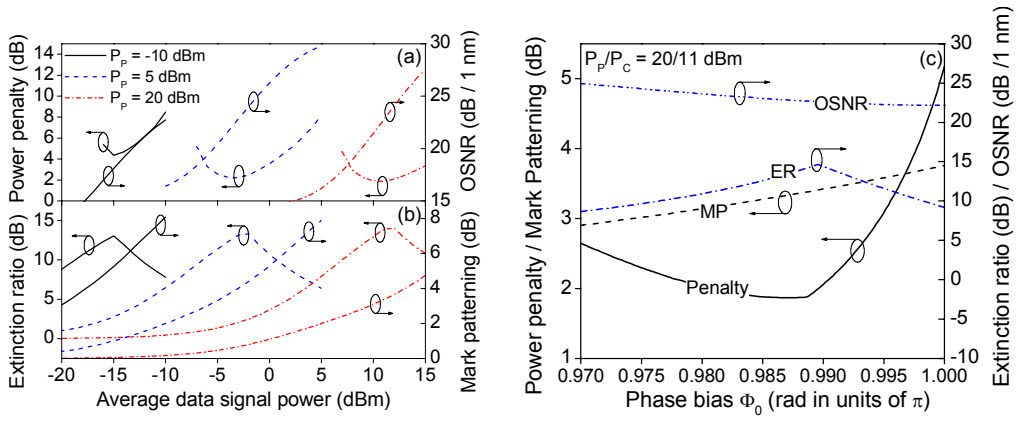

Figure 5.20: (a) Power penalty (left axis) and OSNR (right) axis vs. average data power with the probe input power as a parameter. (b) ER (left axis) and MP (right axis) vs. average data power. (c) Power penalty/MP (left axis) and ER/OSNR (right axis) vs. phase bias Φ_0 for $P_P/P_C = 20/11$ dBm

after the AMZI, as well as a part of the power transfer function of the AMZI, for which $\Phi_0 = 0.9939\pi$. Notice that the envelope of the spectrum is broadened considerably, corresponding to a reduction of the pulse width. Moreover, the switched output power is significantly decreased, which indicates that the phase difference $\Delta\Phi_p(t)$ is far below π.

For each SOA length in the range $1 - 5$ mm the phase bias Φ_0 and CW and data signal input powers are optimized to obtain the smallest possible power penalty. It turns out that for a bitrate of 80 Gb/s the performance does not improve by increasing the SOA length beyond 2 mm. Thus, to minimize the amount of data, and to facilitate comparison with the DM-MZI, the SOA length is fixed at $L = 2$ mm in the following.

Fig. 5.20 (a-b) shows the power penalty, ER, OSNR, and MP vs. the average data signal power P_C for CW input probe powers P_P of -10, 5, and 20 dBm, which are identical to the probe powers entering each of the two SOAs in the DM-MZI (see Fig. 5.10 (a-b)). For each probe power the phase bias Φ_0 is optimized to obtain the smallest possible power penalty, and this value of Φ_0 is used in the calculation of the ER, OSNR, and MP. As for the DM-MZI switch the MP increases with the average data power, but in this case the ER goes through a maximum. The latter is related to the fact that the phase difference $\Delta\Phi_p(t)$ changes sign between the data pulses. The transmission of the steady-state zero-level, corresponding to $\Delta\Phi_p(t) = 0$ in Fig. 5.18 (b), is determined by Φ_0, and for a given choice of Φ_0, a data power on the low side of the optimum induces a smaller phase shift, which gives rise to a smaller switched peak power, and thus a decrease of the ER. On the high-power side of the optimum, the satellite pulses generated by the negative phase difference overlap with the succeeding timeslots, which causes a decrease of the ER.

This is illustrated in Fig. 5.21, which shows eye diagrams for $P_P = 5$ dBm,

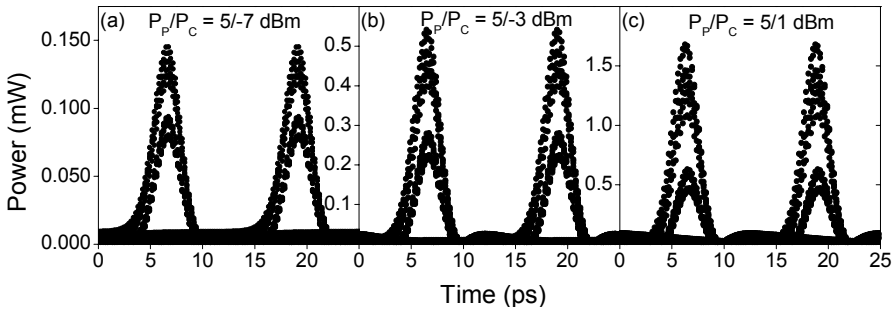

Figure 5.21: 80 Gb/s eye diagrams obtained with the DISC for an input probe power of 5 dBm, and an average data input power of (a) −7 dBm, (b) -3 dBm, and (c) 1 dBm, where the optimum is −3 dBm.

and data powers of (a) $P_C = -7$ dBm, (b) $P_C = -3$ dBm, and (c) $P_C = 1$ dBm, where −3 dBm corresponds to the optimum, cf. Fig. 5.20 (a). Notice the creation and enhancement of the satellite pulses as the data power is increased.

Fig. 5.20 (c) shows the power penalty, ER, OSNR, and MP as a function of the phase bias Φ_0 for the combination of input powers $P_P/P_C = 20/11$ dBm, giving rise to the smallest possible power penalty. The power penalty is observed to go through a minimum, which is primarily due to the fact that the ER goes through a maximum. As explained above, the phase bias Φ_0 determines the transmission of the steady-state zero-level. As Φ_0 approaches π, the steady-state zero-level is decreased, while the amplitude of the satellite pulses increases. Consequently, an optimum exists at an intermediate value of Φ_0. The minimum penalty is around 1.87 dB, which is $\approx$ 1.5 dB higher than for the DM-MZI. More importantly, the MP does not go through a minimum, which means that there is no way of decreasing the patterning without severely sacrificing the sensitivity.

Although the principle of operation of the DM-MZI and DISC switches is the same, there are several important differences in terms of ASE noise and patterning, which have a non-trivial impact on the performance. In the following section the main differences will be explained.

5.2.5 DM-MZI vs DISC

The operating conditions leading to the smallest power penalty for the DM-MZI and DISC configurations are quite different. For a CW probe power of 20 dBm into the single SOA of the DISC and each SOA of the DM-MZI (the latter corresponds to an input power of 26 dBm), the optimum data signal power is 17 dBm in the upper arm of the DM-MZI (corresponding to 14 dBm into the SOA), and 2.25 dB less in the lower arm, whereas the optimum is obtained with only 11 dBm for the DISC. There are two reasons for this. First, as explained above, the DISC generates detrimental satellite pulses if the input data power is too large.

This is illustrated further in Fig. 5.22, which shows the phases of the interfering signals, as well as the phase difference, for the DM-MZI (a-b) and the DISC

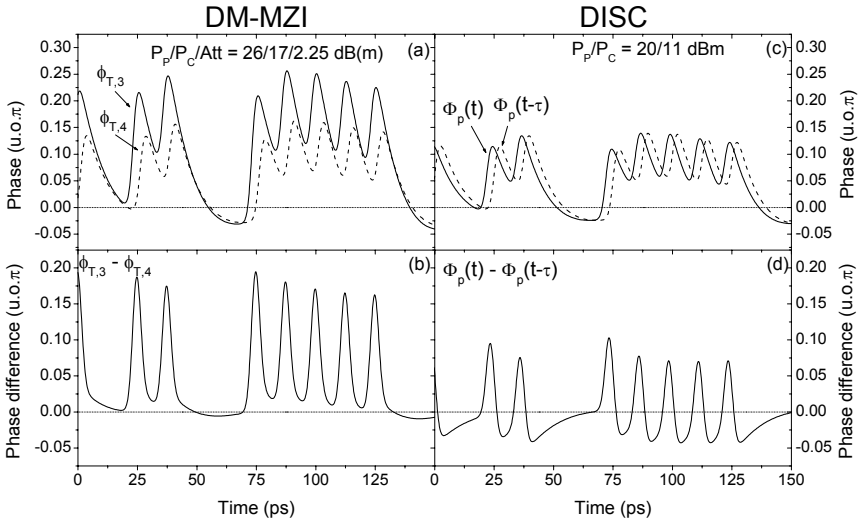

Figure 5.22: Comparison of DM-MZI and DISC for equal probe power of 20 dBm in to the SOA(s), and with data power corresponding to the minimum power penalty. (a,c) show the individual phases, and (b,d) illustrate the phase differences.

(c-d), using parameters corresponding to the minimum penalty in both cases. Focusing on the DISC, i.e. Fig. 5.22 (c-d), it is clear that the undershoot of the phase difference, which causes the satellite pulses, scales with the peak of the phase shift $\Phi_p(t)$. Consequently, the input data power is limited to a level which introduces a sufficiently large phase shift to switch the CW probe, without degrading the ER by generating significant satellite pulses.

The small phase shift inevitably gives rise to a small output power, which is also clearly seen in the eye diagrams of Fig. 5.21. An obvious question would be: why does the low output power *not* result in a proportionately low OSNR? According to Fig. 5.20 (a), the OSNR is above 25 dB/1 nm for $P_P = 20$ dBm. The answer to this question is related to the way the interferometers filter spontaneous emission noise. Denoting the spectral density of the average ASE power generated in the single SOA of the DISC by $\widetilde{P}_{SOA}(\lambda)$, the spectral density at the output of the AMZI filter, $\widetilde{P}_{DISC}(\lambda)$ is given by

$$\widetilde{P}_{DISC}(\lambda) = \widetilde{P}_{SOA}(\lambda)\,|H_{AMZ}(\lambda)|^2 \tag{5.2}$$

Fig. 5.23 (a) shows the normalized spectral density at the output of the SOA (solid line), which is assumed independent of λ within the 2 nm span considered, and the power transfer function $|H_{AMZ}(\lambda)|^2$ (dashed curve) that was found to be optimum for $P_P/P_C = 20/11$ dBm. Assuming that the AMZI is followed by a 1 nm wide BPF, approximated by a rectangular shape, the ASE power emerging from the DISC is represented by the hatched area in Fig. 5.23 (a). From (5.1), the power transfer function of the AMZI may be shown to be sinusoidal

$$|H_{AMZ}(\omega)|^2 = \frac{1}{2}\left(1 + \cos(\omega\tau + \Phi_0)\right) \tag{5.3}$$

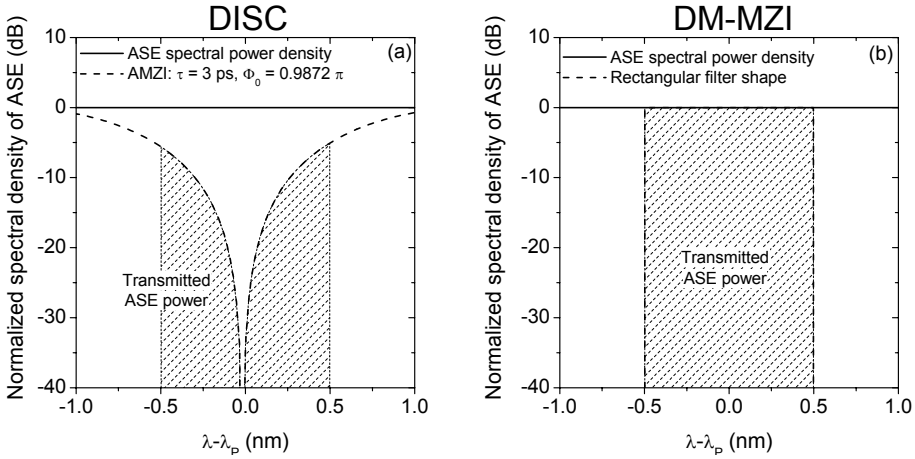

Figure 5.23: (a) Normalized spectral density of ASE after the SOA (solid), and after the AMZI filter of the DISC (dashed). (b) Normalized ASE spectral density after MZI (solid), and after a rectangular, 1 nm wide BPF. The hatched areas represent the transmitted ASE power for the two switches.

with a free-spectral (frequency) range (FSR) of τ^{-1}.

Integrating (5.3) over the bandwidth of the BPF, which is centered on the carrier wavelength λ_P of the probe and spans $\Delta\lambda_F$, the total ASE power, P_{ASE}^{DISC}, within $\Delta\lambda_F$ becomes

$$P_{ASE}^{DISC} = \widetilde{P}_{SOA}(\lambda_P)\frac{\Delta\lambda_F}{2}\left[1+\cos(\Phi_0)\mathrm{sinc}\left(\frac{\pi c\tau\Delta\lambda_F}{\lambda_P^2}\right)\right] \tag{5.4}$$

The ASE power within $\Delta\lambda_F$ before the AMZI is simply given by $P_{ASE}^{SOA} = \widetilde{P}_{SOA}(\lambda_P)\Delta\lambda_F$, which means the AMZI reduces the transmitted ASE power by a factor of

$$R_{DISC} = \frac{P_{ASE}^{SOA}}{P_{ASE}^{DISC}} = 2\left[1+\cos(\Phi_0)\mathrm{sinc}\left(\frac{\pi c\tau\Delta\lambda_F}{\lambda^2}\right)\right]^{-1} \tag{5.5}$$

which attains a value of $R_{DISC} = 9.9$ dB for $\Delta\lambda_F = 1$ nm and $\lambda_P = 1570$ nm. Consequently, the low output power from the DISC does not give rise to a low OSNR because the ASE power is dramatically reduced by the AMZI. Notice that R_{DISC} is bitrate independent, since the differential delay τ and the necessary optical bandwidth $\Delta\lambda_F$ (may be interpreted as the optical bandwidth of the receiver) are inverse proportional, and R_{DISC} depends very little on Φ_0, for $\Phi_0 \approx \pi$.

As mentioned in the description of boundary conditions in section 3.1 of Chapter 3, ASE generated in different SOAs cannot interfere because there is no phase correlation between the ASE sources. The spectral density at the output of the DM-MZI, $\widetilde{P}_{DM}$, is therefore given by

$$\widetilde{P}_{DM} = \frac{\widetilde{P}_{SOA}+\widetilde{P}_{SOA}}{2} = \widetilde{P}_{SOA} \tag{5.6}$$

As illustrated in Fig. 5.23 (b), the ASE power transmitted through the BPF following the DM-MZI is given simply by P_{ASE}^{SOA}. Since this quantity is a factor of R_{DISC} larger than P_{ASE}^{DISC}, it is clear that the switched probe power must be larger for the DM-MZI, in order to enhance the OSNR and thereby reduce the noise-induced sensitivity degradation. The larger probe power is obtained by increasing the data power, and this is the second reason for the difference in required data power.

Fig. 5.10 (a) clarifies the trade-off for the DM-MZI: as the data power is increased, the ER decreases while the OSNR is enhanced, and the minimum penalty is obtained for an intermediate data power.

By comparing the phase response for the DM-MZI and DISC in Fig. 5.22 it is observed that the patterning is noticeably smaller for the DM-MZI. The reason for this may understood by focusing on the phase modulation induced by the string of five data pulses. For the DISC, the peak of the phase difference induced by each data pulse is given by a fraction of the phase shift induced by the individual pulses, where the fraction is governed by the differential delay τ. Since the first data pulse in the string of five induces a larger phase shift than the following, the peak phase difference, and thus the peak output power, becomes higher for the first pulse. For the DM-MZI, the situation is similar to the DISC for the first pulse. However, since the modulation depth of $\phi_{T,4}(t)$ is smaller than that of $\phi_{T,3}(t)$, the valleys of $\phi_{T,4}(t)$ are below the valleys of $\phi_{T,3}(t)$, which means that the phase *difference* induced by the second data pulse is *larger* than the corresponding phase shift, and consequently larger than the phase difference that would have been induced by a DISC. This leads to the conclusion that the DM-MZI is able to operate with lower mark patterning than the DISC.

Fig. 5.24 shows the minimum power penalty (a), and the corresponding MP (b), average probe output power and OSNR (c), as a function of the CW input probe power launched into the SOA(s) of the DM-MZI and DISC[3]. Over the entire range of input probe powers in Fig. 5.24 the ER remains above 13 dB, which means it contributes only very little to the sensitivity degradation that follows from decreasing the input probe power.

The figure summarizes the results of the comparison between the two switch configurations. The DM-MZI is overall superior in terms of power penalty. This is mainly due to the lower mark patterning, since for a fixed average power, an increased mark patterning corresponds to a smaller eye opening, which prompts a larger BER in the presence of noise. Thus, if the OSNR is low, the BER performance becomes increasingly sensitive to MP. Fig. 5.24 (c) shows the average output probe power, P_{out}, on the left axis, and the OSNR on the right axis. It is observed that P_{out} is about 8 dB higher for the DM-MZI compared to the DISC, over the entire range of input probe powers, and the reason for this has already been established. On the other hand, the OSNR is $1.6 - 1.7$ dB higher for the

[3]E.g., 26 dBm of probe power into the DM-MZI is shown as 20 dBm.

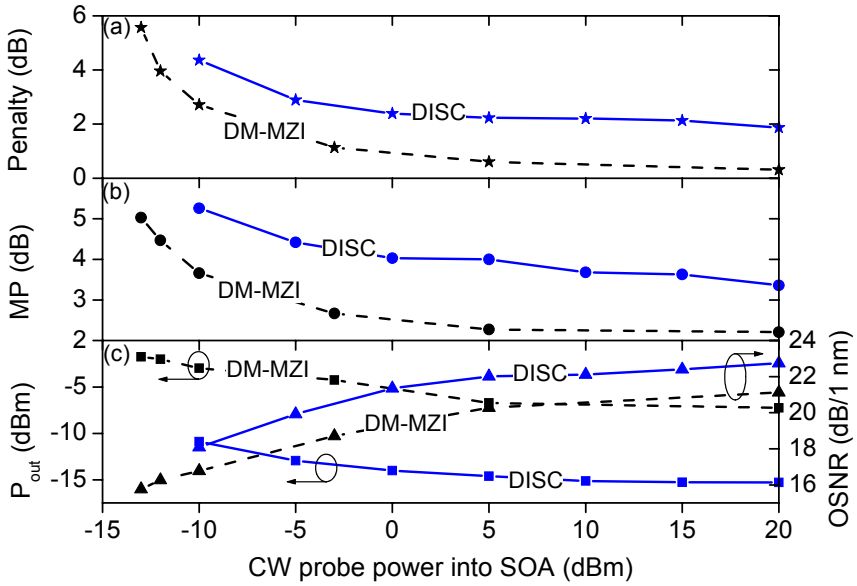

Figure 5.24: Comparison of (a) power penalty, (b) MP, and (c) average probe output power (left axis) and OSNR (right axis) for the DISC and DM-MZI switches vs. CW probe input power.

DISC, and this is a direct result of the DISC transmitting a factor of R_{DISC} less ASE power compared to the DM-MZI. Without the enhanced ASE suppression, the OSNR at the output of the DISC would drop by a factor of approximately R_{DISC}, which would make the performance much more sensitive to MP.

Paradoxically, the average output probe power is observed to *decrease* as the input probe power *increases*. The reason is that the MP-level is high for low input probe powers, due to the high effective carrier lifetime. To minimize the impact on the receiver sensitivity the output probe power must be high, and this is obtained through a relatively high input data power. An example of this may be seen in Fig. 5.11, where the ratio P_P/P_C increases from 3 dB to 9 dB as P_P is increased from −6 dBm to 26 dBm. Fig. 5.11 also shows that the eye opening is almost constant and the difference in average power is mainly due to patterning.

Speed potential of DISC/DM-MZI

To investigate the speed potential, and the problems that may arise at ultra-high bitrates, simulations on the DM-MZI and DISC are carried out at 160 Gb/s, using 1.5 ps wide (FWHM) Gaussian pulses, forming a PRB sequence of length 2^5-1. According to (3.1), pulses as short as 1.5 ps excite intraband dynamic effects, which are not included in the model. However, interband effects are still expected to be dominant, and since the situation is the same for both the DM-MZI and the DISC, a qualitative comparison between the two switches at 160 Gb/s is justified.

Fig. 5.25 shows the power penalty, mark patterning, extinction ratio, and

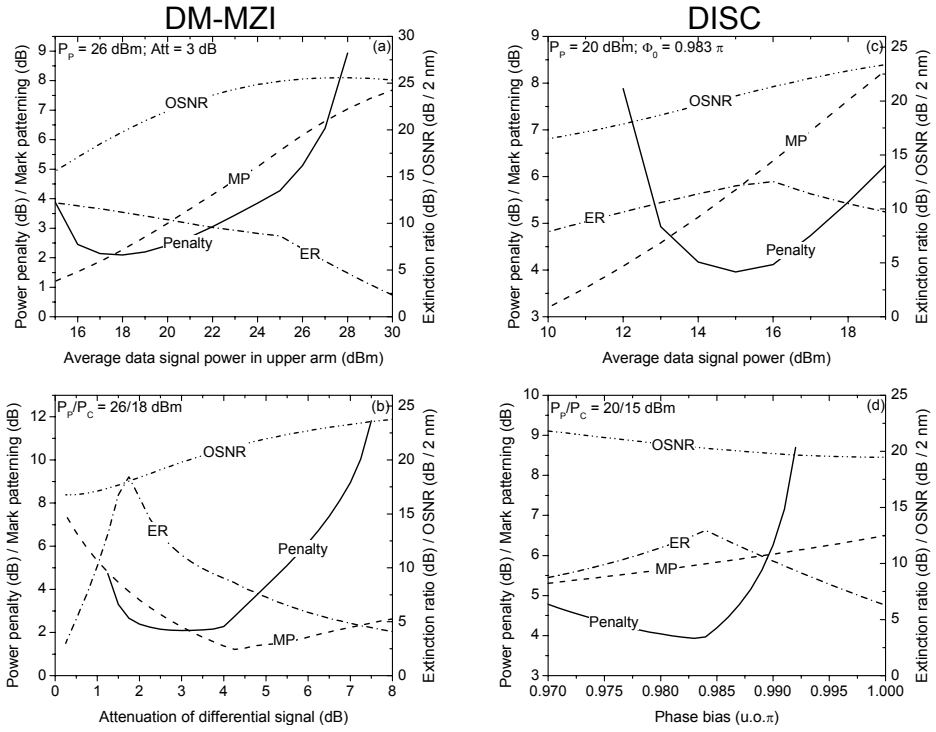

Figure 5.25: Comparison of power penalty/MP/ER/OSNR for DM-MZI (a,b) and DISC (c,d) at 160 Gb/s. (a) and (c) show the figures of merite vs. average data power for optimized attenuation to the lower arm and optimized phase bias Φ_0, respectively. In (b) and (d) the data powers are optimized, and the attenuation and phase bias, respectively, are varied.

OSNR vs. the average data power, for the DM-MZI (a) and the DISC (c). In both cases the differential delay τ is reduced to 1.5 ps, the probe power is 20 dBm into the SOA(s), and the attenuation *Att* of the differential signal, and the phase bias Φ_0, respectively, have been optimized to obtain a minimum power penalty.

At 80 Gb/s the optical bandwidth $\Delta\lambda$ of the BPF was set, somewhat arbitrarily, to 1 nm. When the bitrate is increased to 160 Gb/s, the required optical bandwidth doubles, and is thus set to 2 nm in this case. Other things being equal, this inevitable reduces the OSNR by 3 dB for both switches, as R_{DISC} is bitrate independent for a constant $\Delta\lambda\tau$. At the same time, the carrier density recovers less between excitations by data pulses, which brings an increased level of mark patterning.

As explained, MP may be reduced by lowering the data power, but this reduces the output probe power and thereby the OSNR. For the DM-MZI, this trade-off leads to an optimum data power of 18 dBm, corresponding to a lower pulse energy than the 17 dBm at 80 Gb/s. However, the lower phase phase shift is compensated by a reduction of the power in the differential signal, which allows for a higher phase difference (see e.g. Fig. 5.13).

This is illustrated in 5.25 (b), where the minimum penalty is obtained at an

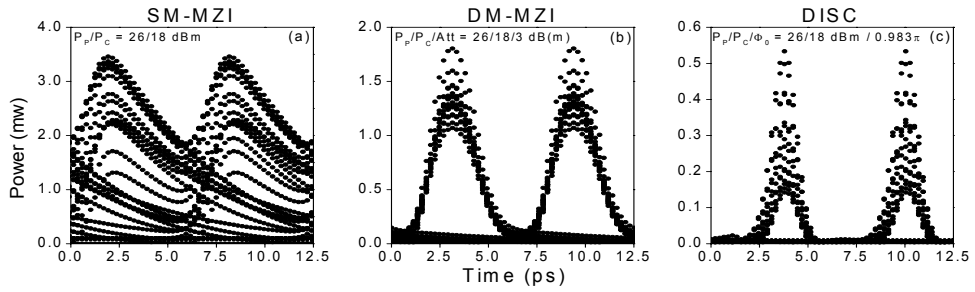

Figure 5.26: Eye diagrams at 160 Gb/s optimized for minimum power penalty. (a) SM-MZI, (b) DM-MZI, (c) DISC.

attenuation of 3 dB (2 dB at 80 Gb/s), which increases the OSNR at the expense of the ER. Decreasing the power in the differential signal also reduces the MP, which, along with the lower data pulse energy, counteracts the increase of the MP caused by halving the timeslot. With the DISC it is not possible to reduce the mark patterning by reducing the data power, without compromising the OSNR, since the delayed phase shift cannot be decreased independently. As a result, the trade-off between OSNR and ER on one side, and MP on the other, leads to an optimum data power of 15 dBm, which is 4 dB higher than at 80 Gb/s. Fig. 5.25 (d) shows the figures of merit as a function of the phase bias Φ_0, and at the value corresponding to a minimum penalty, the ER and OSNR are very similar to what was obtained with the DM-MZI. However, due to lack of means to reduce the patterning, Fig. 5.25 (d) shows an MP level of 5.7 dB, compared to 2.27 dB for the DM-MZI.

The large difference in the level of patterning is illustrated in Fig. 5.26, which shows the 160 Gb/s eye diagrams obtained with (a) the SM-MZI configuration, (b) the DM-MZI, and (c) the DISC, all optimized for the lowest power penalty. Comparing Fig. 5.26 (a) and (b), it is clear that a bitrate of 160 Gb/s is far beyond the limit of standard-mode operation; the eye diagram in Fig. 5.26 (a) is completely closed and the signal not detectable. According to Fig. 5.25 (b), an attenuation of the differential signal above ≈ 7.5 dB results in an error-floor. The eye diagram corresponding to the DM-MZI in Fig. 5.26 (b) is clearly observed to have a sub-optimum ER, which was the price for the increased OSNR and low patterning. Fig. 5.26 (c) illustrates the large patterning of the signal switched by the DISC. Comparing Fig. 5.26 (b) and (c), it is also clear that the reduced power in the differential signal leads to a significantly larger pulse width for the DM-MZI.

In all the large-signal simulations so far, a PRBS of word length $2^5 - 1$ has been used as the control signal. For a bitrate of 80 Gb/s this is a sufficiently long sequence, since the string of five data pulses is long enough that the peak of the phase difference reaches a steady state, which means that level of patterning is accounted for. Fig. 5.27 (a) shows a part of the pulse pattern that corresponds to

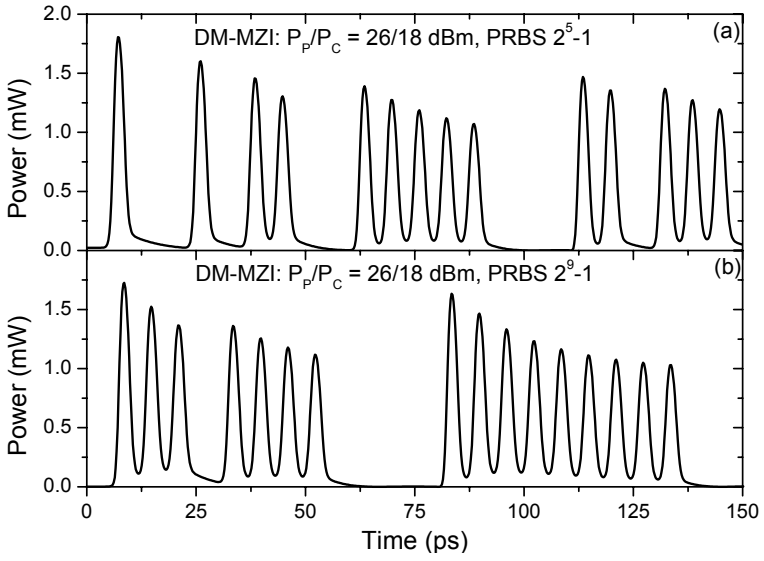

Figure 5.27: Word length dependence of DM-MZI. (a) optimized output for PRBS $2^5 - 1$, and (b) optimized output for PRBS $2^9 - 1$.

the eye diagram in Fig. 5.26 (b), and it seems as if a word length of $2^5 - 1$ is not long enough to account for the worst case patterning at 160 Gb/s. Fig. 5.27 (b) shows the DM-MZI output pattern for an input PRB sequence of word length $2^9 - 1$, using the same average input powers. As observed, the peak pulse power in the string of nine pulses only decreases marginally after the first five pulses, which means that the word length dependence of the mark patterning increases only very moderately for a PRBS word length above $2^5 - 1$. Quantitatively, the MP level increases from 2.27 dB for $2^5 - 1$ to 2.56 dB for $2^9 - 1$.

Experimental results have shown that the DISC is indeed able to operate at 160 Gb/s[4] [74] without significant patterning. This could in principle be due to an extremely fast carrier recovery, but no published results are available to suggest this. However, there are other ways of reducing the patterning. Since the first pulses in a long string are chirped more than the following, the larger peak power of the first pulses may be reduced by an appropriate filter. This technique is successfully employed in a 100 Gb/s experiment [75]. The demonstration at 168 Gb/s [74] was carried out with a hybrid, in-line implementation of the DISC, using the polarization domain to split and delay the cross-phase modulated probe signal. This provides an additional optimization parameter, namely the relative polarization state of the two probe signals upon interference. Due to the carrier density dependent birefringence of the SOA [130, 131], the polarization state, represented by the polarization angle, is rotated more for the first pulse(s) of the string. By properly adjusting the relative polarization to allow maximum transmission of the last, and thus least rotated, pulses, the peak pulse powers are

[4] 168 Gb/s, actually

expected to be equalized.

The analysis presented in this section has focused exclusively on RZ input data, since NRZ Pulse Pattern Generators (PPGs) are not available at bitrates above 50 Gb/s. However, recent results demonstrate that the DM-MZI is able to operate with NRZ input data from 2.5 Gb/s to 42 Gb/s without changing the operating conditions, such as bias currents and differential delay [132]. Thus, the DM-MZI switch is bitrate transparent to beyond 40 Gb/s for the NRZ data format, but not for the RZ format, since the differential delay τ and attenuation *Att* need to be optimized if the bitrate changes.

5.3 Bandwidth enhancement by optical filtering

It has been established that a small-signal analysis is only capable of accounting for linear patterning, and consequently a small-signal analysis of a switch operating in differential-mode neglects nonlinear patterning, and represents a theoretical best-case scenario. However, an analytical small-signal approach is able to provide better insight into the role of different parameters and the interplay between them. In the following, the DISC will be analyzed in the small-signal regime, and a detailed account for the effect of the asymmetric MZI will be given. The DISC is chosen over the DM-MZI due to its simplicity, and because it may be considered as an SOA followed by a filter. A spectral formalism is introduced, which relates the small-signal response to the optical spectrum. This provides a convenient way of analyzing the effect of an arbitrary filter after an SOA. The contents of this section is based on [p2].

5.3.1 Traditional small-signal analysis of DISC

In this section a traditional analysis of the SSFR of the DISC is undertaken. In this context, *traditional* means that the modulation of the power and the phase are analyzed separately. The electric field of the probe signal at the output of the asymmetric MZI, $E_{out}(t)$, is represented by its slowly varying envelope, and may be related to the input probe field envelope $E_p(t)$ in the following way (cf. Fig. 5.17)

$$\begin{aligned} E_{out}(t) &= \frac{1}{2}\left(E_p(t) + E_p(t-\tau)e^{j\Phi_0}\right) \\ &= \frac{1}{2}\left(\sqrt{P_p(t)}e^{j\Phi_p(t)} + \sqrt{P_p(t-\tau)}e^{j\Phi_p(t-\tau)}e^{j\Phi_0}\right) \end{aligned} \tag{5.7}$$

where $P_p(t)$ and $\Phi_p(t)$ are the power and phase of the cross-gain and cross-phase modulated probe signal at the output of the SOA, entering the asymmetric MZI.

The output power is given by

$$\begin{aligned} P_{out}(t) &= |E_{out}(t)|^2 = \frac{1}{4}\Big(P_p(t) + P_p(t-\tau) + 2\sqrt{P_p(t)}\sqrt{P_p(t-\tau)} \\ &\quad \times \cos\left(\Phi_p(t) - \Phi_p(t-\tau) - \Phi_0\right)\Big) \end{aligned} \tag{5.8}$$

To investigate the SSFR of the DISC, all time-dependent parameters in (5.8) are expanded to the first harmonic

$$X(t) = \overline{X} + \Delta X(t) = \overline{X} + x(\Omega)e^{-j\Omega t} + x^*(\Omega)e^{j\Omega t} \tag{5.9}$$

where $\overline{X}$ represents the steady state value of X, and x is the complex small-signal modulation amplitude corresponding to the modulation angular frequency Ω ($\Omega > 0$). In (5.9), X and x should be substituted with P_{out}, P_p, Φ_p and p_{out}, p_p, ϕ_p, respectively.

To obtain an expression for the modulation amplitude, $p_{out}(\Omega)$, at the output of the DISC the output power $P_{out}(t)$ is expanded to the first order in $\Delta P_p(t)$ and $\Delta\Phi_p(t)$

$$\begin{aligned} P_{out}(t) &= \overline{P}_{out} + \Delta P_{out}(t) \\ &= \frac{\overline{P}_p}{2}\left(1+\cos(\Phi_0)\right) + \frac{1}{4}\left(1+\cos(\Phi_0)\right)\left[\Delta P_p(t) + \Delta P_p(t-\tau)\right] \\ &\quad + \frac{1}{2}\overline{P}_p \sin(\Phi_0)\left[\Delta\phi_p(t) - \Delta\phi_p(t-\tau)\right] \end{aligned} \tag{5.10}$$

The DC and modulated terms can now be identified

$$\overline{P}_{out} = \frac{\overline{P}_p}{2}\left(1+\cos(\Phi_0)\right) \tag{5.11}$$

$$\begin{aligned} \Delta P_{out}(t) &= \frac{1}{4}\left(1+\cos(\Phi_0)\right)\left[\Delta P_p(t) + \Delta P_p(t-\tau)\right] \\ &\quad + \frac{1}{2}\overline{P}_p \sin(\Phi_0)\left[\Delta\Phi_p(t) - \Delta\Phi_p(t-\tau)\right] \end{aligned} \tag{5.12}$$

$$\begin{aligned} &= \frac{1}{4}\left(1+\cos(\Phi_0)\right)\left[p_p(\Omega)\left(1+e^{j\Omega\tau}\right)e^{-j\Omega t} + c.c.\right] \\ &\quad + \frac{1}{2}\overline{P}_p \sin(\Phi_0)\left[\phi_p(\Omega)\left(1-e^{j\Omega\tau}\right)e^{-j\Omega t} + c.c.\right] \end{aligned}$$

where $p_p(\Omega)$ and $\phi_p(\Omega)$ are the Fourier transforms of $\Delta P_p(t)$ and $\Delta\Phi_p(t)$, respectively, evaluated at the angular frequency Ω.

Comparing (5.9) and (5.12), the following expression for the small-signal modulation amplitude at the output of the DISC is obtained

$$\begin{aligned} p_{out}(\Omega) &= \frac{1}{4}\left(1+\cos(\Phi_0)\right)p_p(\Omega)\left(1+e^{j\Omega\tau}\right) \\ &\quad + \frac{1}{2}\overline{P}_p \sin(\Phi_0)\phi_p(\Omega)\left(1-e^{j\Omega\tau}\right) \end{aligned} \tag{5.13}$$

5.3.2 Compensation for carrier density response

The analysis presented above is very general, in the sense that it is independent of the model used to describe the SOA preceding the asymmetric MZI filter. All artifacts of the SOA are contained in $\overline{P}_p$, $p_p(\Omega)$, and $\phi_p(\Omega)$, which depend not only on material properties like e.g. linewidth enhancement factor and gain, but also on the relative orientation of data signal and probe signals, as explained in section 4.1. Here, the focus will be on the co-propagation case, where the input data signal and the CW probe are launched into the SOA from the same facet, since this gives rise to the largest modulation bandwidth [119]. Scattering loss inside the SOA as well as ASE and intraband carrier dynamics is neglected, since this enables expressing $p_p(\Omega)$ and $\phi_p(\Omega)$ analytically. As established in section 4.1, loss does have an impact on the SSFR of the modulated probe signal. In particular, loss was shown to be responsible for a resonance in the SSFR [118],[p1]. To include this artifact in the present analysis would require a numerical approach, and the additional accuracy obtained would be at the expense of clarity. ASE can also give rise to resonant behavior [133], but only in the case where the SOA is saturated primarily by ASE, which is the case only for very low input probe powers. In a practical scenario the SOA will be operated with an input probe power large enough to ensure a large OSNR at the output, and to reduce the stimulated carrier lifetime [45], and in this case gain saturation by ASE can be neglected. Intraband dynamic effects could be included using the theory of Ref. [134], but is again excluded in order to maintain clarity.

If the SOA is assumed to have zero scattering loss, $p_p(\Omega)$ may be expressed by (4.12), and using (4.40), $\phi_p(\Omega)$ can be related to $p_p(\Omega)$ [107] through

$$\phi_p(\Omega) = -\frac{\alpha}{2\overline{P}_p} p_p(\Omega) \tag{5.14}$$

Inserting (4.12) and (5.14) into (5.13), the SSFR of the DISC can be expressed

$$\begin{aligned} T(\Omega) &= \frac{p_{out}(\Omega)}{p_c(\Omega)} \\ &= \frac{p_p(\Omega)}{4p_c(\Omega)} \left[(\cos(\Phi_0)+1)\left(1+e^{j\Omega\tau}\right) - \alpha\sin(\Phi_0)(1-e^{j\Omega\tau}) \right] \end{aligned} \tag{5.15}$$

In a normalized form, (5.15) becomes

$$T_N^{AMZ}(\Omega) = \frac{T(\Omega)}{T(0)} = T_N^{CDR}(\Omega) T_{AMZ}(\Omega) \tag{5.16}$$

where $T_N^{CDR}(\Omega) = p_p(\Omega)/p_p(0)$ is the normalized CDR, introduced in (4.14). The function $T_{AMZ}(\Omega)$, which will be referred to as the equalizer function for the asymmetric MZI, accounts for the action of the asymmetric MZI filter on the

small-signal modulated probe

$$\begin{aligned} T_{AMZ}(\Omega) &= \frac{1}{2}\left[\left(1+e^{j\Omega\tau}\right) - \frac{\alpha\sin(\Phi_0)}{1+\cos(\Phi_0)}\left(1-e^{j\Omega\tau}\right)\right] \\ &= \frac{1}{2}\left[T_{AMZ}^{XGM}(\Omega) + T_{AMZ}^{XPM}(\Omega)\right] \end{aligned} \tag{5.17}$$

From (5.13) it is clear that the first term in $T_{AMZ}(\Omega)$ can be attributed to XGM, while the second term is due to XPM. Consequently, the two terms will be referred to as the XGM and XPM *filter functions*, $T_{AMZ}^{XGM}(\Omega)$ and $T_{AMZ}^{XPM}(\Omega)$, respectively. Choosing τ and Φ_0 properly, $T_{AMZ}(\Omega)$ can compensate for, or *equalize*, the roll-of of the CDR in a frequency range up to $\Omega = 2\pi/\tau$, where $T_{AMZ}(\Omega)$ has the first local minimum.

Introducing a characteristic parameter γ

$$\gamma = \frac{\alpha\sin(\Phi_0)}{1+\cos(\Phi_0)} = \alpha\tan\left(\frac{\Phi_0}{2}\right) \tag{5.18}$$

and noting that the phase difference between the XGM and XPM filter functions is $\pm\pi/2$, the magnitude of $T_N^{AMZ}(\Omega)$ can be expressed

$$\begin{aligned} \left|T_N^{AMZ}(\Omega)\right| &= \left|T_N^{CDR}(\Omega)\right| \left|T_{AMZ}(\Omega)\right| \\ &= \left|T_N^{CDR}(\Omega)\right| \sqrt{\frac{1+\gamma^2-(\gamma^2-1)\cos(\Omega\tau)}{2}} \end{aligned} \tag{5.19}$$

The parameter γ will be referred to as the *bandwidth enhancement factor* for reasons that will become clear in the following. The parameter has the property

$$\gamma^2 \to \infty \quad \text{for} \quad \Phi_0 \to \pi \tag{5.20}$$

From (5.17) it is clear that the XPM filter function vanishes for $\Omega \to 0$, regardless of the size of γ. This is physically clear, since XPM does not lead to any frequency shift for $\Omega \to 0$. Outside this limit, (5.20) states that for Φ_0 approaching π, i.e. $\gamma \to \infty$, the XPM filter function dominates over the XGM filter function.

Fig. 5.28 (a) shows $\left|T_N^{CDR}(\Omega)\right|$ for $\tau_e = 50$ ps, $\left|T_{AMZ}^{XGM}(\Omega)\right|$ and $\left|T_{AMZ}^{XPM}(\Omega)\right|$ for $\tau = 5$ ps, and the resulting $|T_{AMZ}(\Omega)|$ for $\gamma = 10$, 20, and 40. For a specific γ, the magnitude of the XPM filter function peaks at a value which is a factor of $|\gamma|$ higher than the DC value of the XGM filter function. When the filter functions are added according to (5.17), $|T_{AMZ}(\Omega)|$, which is a high-pass characteristic for $\Omega < \pi/\tau$, peaks at the value $|\gamma|$ (10, 13, and 16 dB for $\gamma = 10$, 20, and 40). The corner frequency of $T_{AMZ}(\Omega)$, i.e. the frequency at which $T_{AMZ}(\Omega)$ starts compensating for the decreasing CDR, is observed to decrease as $|\gamma|$ is increased, and vice versa. Thus, to maintain a flat, normalized amplitude response, $\left|T_N^{AMZ}(\Omega)\right|$, γ must be carefully optimized to ensure that the increase of $|T_{AMZ}(\Omega)|$ exactly balances the decrease of $\left|T_N^{CDR}(\Omega)\right|$.

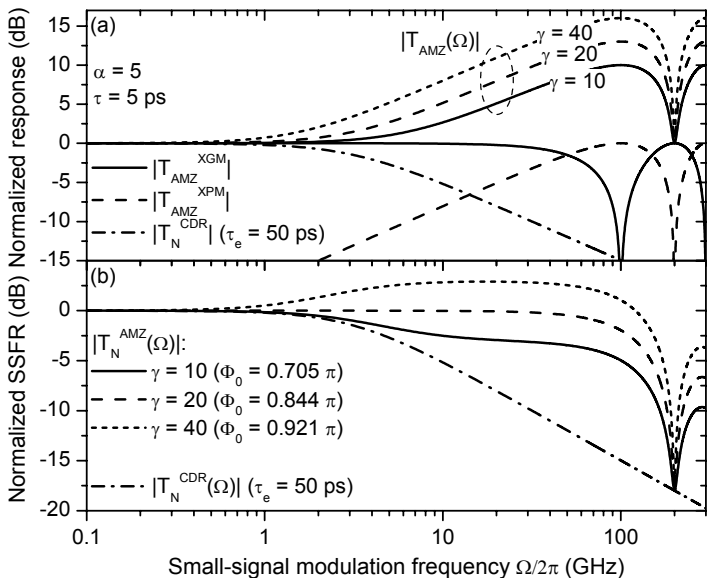

Figure 5.28: (a) The magnitude of the XGM (solid) and XPM (dashed) filter functions, and the resulting magnitude of the equalizer function for $\gamma = 10$, 20, and 40. The normalized carrier density response (CDR) is shown as a reference (dash-dotted). (b) The normalized SSFR corresponsing to the three equalizer functions in (a): $\gamma = 10$ (solid), $\gamma = 20$ (dashed), and $\gamma = 40$ (dotted), with the normalized CDR for $\tau_e = 50$ ps as reference (dash-dotted). $\alpha = 5$ and $\tau = 5$ ps in both plots.

This is illustrated in Fig. 5.28 (b): when the slope magnitude of $\log|T_{AMZ}(\Omega)|$ surpasses the slope magnitude of $\log\left|T_N^{CDR}(\Omega)\right|$, where log is the base-10 logarithm, the overall SSFR of the DISC displays an overshoot. For $\gamma = 20$, the SSFR is observed to be flat for frequencies up to around 100 GHz, whereas an overshoot exists for $\gamma > 20$.

Fig. 5.29 shows the relationship between γ and the phase bias Φ_0 for an $\alpha-$parameter of 3 and 5. The effect of the relative delay τ is straightforward: since $|T_{AMZ}(\Omega)|$ peaks at $\Omega = \pi/\tau$, the entire high-pass characteristic moves towards higher frequencies when τ is decreased, which leads to an increased bandwidth of $\left|T_N^{AMZ}(\Omega)\right|$.

A criterion for obtaining a flat SSFR can be derived by Taylor expanding the Cosine in (5.19) to the second order in Ω around $\Omega = 0$ and requiring $\left|T_N^{AMZ}(\Omega)\right| = 1$. The required value for the γ-factor, γ_f, becomes

$$\gamma_f = \sqrt{4\tau_e^2\tau^{-2} + 1} \approx 2\tau_e\tau^{-1} \tag{5.21}$$

The validity of (5.21) is limited only by the Taylor expansion $\cos(\Omega\tau) \approx 1 - \frac{1}{2}\Omega^2\tau^2$, and since the deviation is less than 8 percent at $\Omega\tau = 1$, the overall SSFR for $\gamma = \gamma_f$ can be regarded as flat for $\Omega\tau < 1$. For $\tau = 5$ ps and $\tau_e = 50$ ps, (5.21) predicts a flat SSFR for $\gamma = \gamma_f = 20$, which is in agreement with Fig. 5.28 (b). Considering the normalized SSFR at $\Omega\tau = \pi$, corresponding to the first peak of

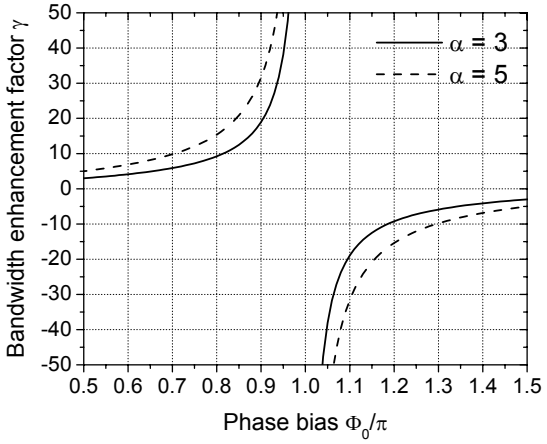

Figure 5.29: The bandwidth enhancement factor γ as a function of the phase bias Φ_0 of the asymmetric MZI, with the linewidth enhancement factor as a parameter: $\alpha = 3$ (solid), $\alpha = 5$ (dashed).

$|T_{AMZ}(\Omega)|$, it is found that

$$\begin{aligned} \left|T_N^{AMZ}(\Omega = \pi/\tau)\right| &= \gamma_f \left|T_N^{CDR}(\Omega = \pi/\tau)\right| \\ &= \frac{\gamma_f}{\sqrt{1 + (\pi\tau_e/\tau)^2}} \approx \frac{2}{\pi} = -1.96\ dB \end{aligned} \tag{5.22}$$

where it is assumed that $4\tau_e^2\tau^{-2} >> 1$, such that $\gamma_f \approx 2\tau_e\tau^{-1}$, cf. (5.21). Equation (5.22) states that the -2 dB bandwidth of $\left|T_N^{AMZ}(\Omega)\right|$, using the flat response criterion in (5.21), is given by $\Omega_{2dB} = \pi/\tau$. Using $\gamma_f \approx 2\tau_e\tau^{-1}$ and $\Omega_{3dB}^{CDR} = \sqrt{3}/\tau_e$, the following relationship between the -2 dB small-signal modulation bandwidth of the DISC and the -3 dB modulation bandwidth Ω_{3dB}^{CDR} of the CDR is found

$$\Omega_{2dB} \approx \frac{\pi}{2\sqrt{3}}\gamma_f\Omega_{3dB}^{CDR} \approx 0.9\gamma_f\Omega_{3dB}^{CDR} \tag{5.23}$$

This relationship justifies referring to γ as the bandwidth enhancement factor.

5.3.3 Optical spectrum approach

The mathematics leading up to equation (5.13) is a traditional small-signal analysis, and similar to the work of Marcenac and Mecozzi [107,118] it is based on the analysis of the modulation of the probe *power* and *phase* and not directly in the corresponding field envelope. However, by considering a small-signal modulated field envelope, and regarding the asymmetric MZI as an optical filter operating on the field in the *optical* frequency domain ω, a relationship between the optical spectrum and the SSFR may be obtained. This relationship applies not only to the asymmetric MZI, but to any filter, which makes this so-called optical spectrum approach much more powerful than the traditional small-signal analysis presented above.

From (5.7) it is readily shown that the asymmetric MZI can be considered an optical filter with the field transfer function $H_{AMZ}(\omega)$ given by (5.1). Since $E_p(t)$ describes the slowly varying field envelope, the angular frequency ω is defined as $\omega = \omega_a - \omega_0$, where ω_a is the actual angular frequency, and ω_0 is the angular frequency of the optical carrier. Using (5.7) and (5.9) the small-signal modulated probe field envelope at the input of the asymmetric MZI can be expressed

$$E_p(t) = \sqrt{\overline{P}_p + (p_p(\Omega)e^{-j\Omega t} + c.c.)}e^{j\left((\overline{\Phi}_p + \left(\phi_p(\Omega)e^{-j\Omega t} + c.c.\right)\right)} \tag{5.24}$$

Noting that, per definition, $\left|\frac{p_p(\Omega)}{\overline{P}_p}\right| \ll 1$ and $\left|\phi_p(\Omega)\right| << 1$, (5.24) can be expanded to first order in p_p and ϕ_p.

$$E_p(t) = \sqrt{\overline{P}_p}e^{j\overline{\Phi}_p}\left[1 + \left(j\phi_p^*(\Omega) + \frac{p_p^*(\Omega)}{2\overline{P}_p}\right)e^{j\Omega t} + \left(j\phi_p(\Omega) + \frac{p_p(\Omega)}{2\overline{P}_p}\right)e^{-j\Omega t}\right] \tag{5.25}$$

From (5.25), the optical small-signal probe spectrum is identified as

$$E_p(\omega) = E_{p,0}\delta(\omega) + E_{p,-1}\delta(\omega + \Omega) + E_{p,1}\delta(\omega - \Omega) \tag{5.26}$$

and by employing (5.14) the spectral components are given by

$$\left\{\begin{array}{l} E_{p,0} \\ E_{p,-1} \\ E_{p,+1} \end{array}\right\} = \sqrt{\overline{P}_p}e^{j\overline{\Phi}_p}\left\{\begin{array}{l} 1 \\ \frac{1-j\alpha}{2\overline{P}_p}p_p^*(\Omega) \\ \frac{1-j\alpha}{2\overline{P}_p}p_p(\Omega) \end{array}\right\} \tag{5.27}$$

The contribution to the sidebands $E_{p,\pm1}$ from XGM is readily identified by setting $\alpha = 0$. Analogously, the contribution from XPM is obtained by replacing $1 - j\alpha$ by $-j\alpha$.

The action of the asymmetric MZI can now be imposed on the field by a simple multiplication

$$\begin{aligned} E_{out}(\omega) &= H_{AMZ}(\omega)E_p(\omega) \\ &= E_0\delta(\omega) + E_{-1}\delta(\omega + \Omega) + E_1\delta(\omega - \Omega) \end{aligned} \tag{5.28}$$

where E_0, E_{-1}, and E_1 are the spectral components of the probe after the filter, given by

$$\left\{\begin{array}{l} E_0 \\ E_{-1} \\ E_{+1} \end{array}\right\} = \frac{1}{2}\left\{\begin{array}{l} E_{p,0}\left(1 + e^{j\Phi_0}\right) \\ E_{p,-1}\left(1 + e^{j(-\Omega\tau + \Phi_0)}\right) \\ E_{p,+1}\left(1 + e^{j(\Omega\tau + \Phi_0)}\right) \end{array}\right\} \tag{5.29}$$

Reverting to the time domain, the small-signal field envelope is expressed as

$$E_{out}(t) = E_0 + E_{-1}e^{j\Omega t} + E_{+1}e^{-j\Omega t} \tag{5.30}$$

Squaring the magnitude of $E_{out}(t)$, and again discarding second harmonic terms, $p_{out}(\Omega)$ may be obtained as

$$p_{out}(\Omega) = E_0 E_{-1}^* + E_{+1} E_0^* \tag{5.31}$$

which, by inserting the spectral components from (5.29), can be transformed into (5.12). Consequently, the optical spectrum approach is equivalent to the traditional small-signal analysis.

5.3.4 Applications of optical filtering approach

A small-signal analysis based directly on the optical field has the advantage that the effect of an arbitrary filter transfer function, $H(\omega)$, on the overall SSFR can be investigated merely by replacing $H_{AMZ}(\omega)$ by $H(\omega)$ in (5.28), and identifying the small-signal modulation amplitude as (5.31). In other words, a change of filter can be accomplished through simple multiplications in (5.28) and (5.31). This should be compared to the traditional small-signal analysis, where the procedure outlined in (5.7)-(5.12) must be repeated for each change of filter. At best this procedure is cumbersome, as it requires an expression for the filter impulse response.

Optimum filter response

If the optical spectrum is known at the input side of a filter, it is possible to calculate the filter response required to transform the spectrum into a desired output spectrum. Such a response will be referred to as an *optimum filter*, regardless of whether it is physically realizable or not. The formal definition of the optimum filter is given by

$$E_{out}(\omega) = H_{opt}(\omega) E_p(\omega) \tag{5.32}$$

where $E_{out}(\omega)$ is the Fourier transform of the desired output signal, $E_{out}(t)$, $H_{opt}(\omega)$ is the optimum filter response, and $E_p(\omega)$ is the probe spectrum at the input of the filter. If no constraints are put on the phase of $E_{out}(t)$, an infinite number of filters will satisfy (5.32), each one resulting in the same signal power $P_{out}(t)$, but with different chirp. By requiring a chirp-free output, $E_{out}(\omega)$ becomes unique, and (5.32) only has a single solution. This approach has been used by Leuthold et al. [44] to design an optimum filter, transforming the wavelength converted probe output from an SOA into a signal with a well-defined pulse shape and width.

In the small-signal limit the desired output power $P_{out}(t) = |E_{out}(t)|^2$ will be defined as a sinusoid with an amplitude independent of the modulation frequency. In other words, the optimum filter $H_{opt}(\omega)$ satisfies the flat-response criterion for all modulation frequencies Ω. Using (5.27) and (5.31) the normalized SSFR can be expressed generally as a function of the optical spectrum at the output of an

arbitrary filter

$$\begin{aligned} T_N^H(\Omega) &= \frac{p_{out}(\Omega)}{p_{out}(0)} && (5.33)\\ &= \frac{\overline{P}_p}{p_p(0)}\left(\frac{E_{-1}^*}{E_0^*}+\frac{E_{+1}}{E_0}\right) && (5.34)\\ &= T_N^{CDR}(\Omega)T_H(\Omega) \end{aligned}$$

where the function $T_H(\Omega)$ is the equalizer function for an arbitrary filter $H(\omega)$

$$T_H(\Omega)=\frac{1}{2}\left[(1+j\alpha)\frac{H^*(-\Omega)}{H^*(0)}+(1-j\alpha)\frac{H(\Omega)}{H(0)}\right] \tag{5.35}$$

It follows that for $H(\omega)=H_{opt}(\omega)$ the equalizer function satisfies

$$\begin{aligned} |T_H(\Omega)| &= \left|T_H^{opt}(\Omega)\right| && (5.36)\\ &= \left|T_N^{CDR}(\Omega)\right|^{-1}=\sqrt{1+\Omega^2\tau_e^2} \end{aligned}$$

Notice that the phase of the field is not constrained by this definition of the optimum filter, and thus an infinite number of filters may satisfy (5.36). However, the monotonous increase of $\left|T_H^{opt}(\Omega)\right|$ can only be accommodated by a filter $H(\omega)$ for which $|H(\omega)|\to\infty$ for $\omega\to\infty$ and/or $\omega\to-\infty$. This is not physically realizable, since a passive filter must satisfy $0\le|H(\omega)|\le 1$, and consequently there is an upper limit, $\Omega_{\max}$, to the modulation frequencies for which realizable filters can satisfy, or approximate (5.36). It follows from (5.33) and (5.36) that $\Omega_{\max}$ may be used as a loose definition of the bandwidth of the overall SSFR.

In the following the optimum filter criterion in (5.36) will be used as a general version of the flat response criterion, which was stated for the asymmetric MZI in (5.21).

Influence of filter phase response

Replacing $1\pm j\alpha$ by $\pm j\alpha$ in (5.35), the equalizer function is reduced to the XPM filter function for $H(\omega)$, introduced in (5.17) for the asymmetric MZI filter. Analogously, substituting $1\pm j\alpha$ by 1, transforms the equalizer function into the corresponding XGM filter function.

In order to analyze the influence of the filter's phase response, (5.35) is expressed as

$$\begin{aligned} T_H(\Omega) &= \frac{1}{2\,|H(0)|}\Big[(1+j\alpha)\,|H(-\Omega)|\,e^{-j(\psi(-\Omega)-\psi(0))} && (5.37)\\ &\quad +(1-j\alpha)\,|H(\Omega)|\,e^{j(\psi(\Omega)-\psi(0))}\Big] \end{aligned}$$

where it is used that $H(\omega) = |H(\omega)|\, e^{j\psi(\omega)}$, with $\psi(\omega)$ being the phase of $H(\omega)$. The two terms in (5.37) represent the effect of the lower and upper sidebands of $H(\omega)$, which may interfere destructively or constructively, depending on $\psi(\Omega)$.

Two different types of phase response that give rise to either destructive or constructive interference between the contribution from the lower and upper sidebands to the XPM filter function are now considered.

$$\text{Destructive:} \qquad \psi(\Omega) + \psi(-\Omega) - 2\psi(0) = 0 \tag{5.38}$$

$$\text{Constructive:} \qquad \psi(+\Omega) + \psi(-\Omega) - 2\psi(0) = \pm\pi \tag{5.39}$$

Inserting (5.38) and (5.39) into (5.37) yields

$$\begin{aligned} T_H(\Omega) \;=\; & \frac{e^{-j(\psi(-\Omega)-\psi(0))}}{2\,|H(0)|}\,[|H(-\Omega)| \pm |H(\Omega)| \\ & +j\alpha\,(|H(-\Omega)| \mp |H(\Omega)|)] \end{aligned} \tag{5.40}$$

where the upper and lower signs correspond to (5.38) and (5.39), respectively. The second term of (5.40), proportional to α, represents the XPM filter function, which must dominate for $\Omega > \Omega_{3dB}^{CDR}$ if $T_H(\Omega)$ is to compensate for the roll-off of $T_N^{CDR}(\Omega)$ in (5.33). For a continuous, antisymmetric phase response (5.38), the contributions from the two sidebands to the XPM filter function interfere destructively, whereas they interfere constructively for a corresponding discontinuous phase response (5.39).

Two important conclusions can be drawn from (5.40). First, if the sidebands of the probe spectrum are transmitted equally by the filter, i.e. if $|H(-\Omega)|$ and $|H(\Omega)|$ are comparable, as may be the case for the asymmetric MZI, the phase response must have a discontinuity, as specified in (5.39), to avoid cancellation of the XPM filter function. Secondly, if the filter has an antisymmetric, continuous phase response as in (5.38), the filter should be detuned to suppress one of the sidebands, i.e. $|H(-\Omega)| \ll |H(\Omega)|$, or $|H(-\Omega)| \gg |H(\Omega)|$, in order to prevent cancellation of the XPM filter function. The latter is a special case of a much more general observation, since according to (5.37), suppressing one of the sidebands leads to a $|T_H(\Omega)|$, which is independent of the filter phase response. Thus, by selecting a single sideband, cancellation of the XPM filter functions can be avoided, regardless of the filter phase response.

This mode of operation has been investigated using band-pass filters (BPFs), and demonstrated experimentally at 10 Gb/s [135] and at 40 Gb/s [136], selecting the lower (red-shifted) sideband, and at 40 Gb/s [p4], by selecting the upper (blue-shifted) sideband. In all demonstrations the performance was improved significantly, in terms of response time, extinction ratio, and power consumption, by detuning the filter.

The solid curve in Fig. 5.30 shows the phase response, $\psi_{AMZ}(\omega)$, of the asymmetric MZI in the frequency range from $\omega = -2\pi/\tau$ to $\omega = 2\pi/\tau$, corresponding to a range of 2 times the FSR. The phase is derived from (5.1) for $\tau = 5$ ps and

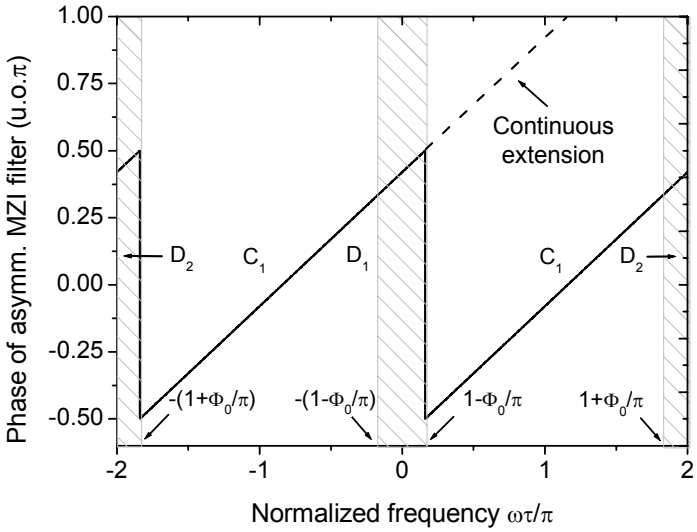

Figure 5.30: Phase of the asymmetric MZI filter (solid) as a function of normalized frequency $\omega\tau/\pi$. In the frequency ranges D_1 and D_2 equation (5.38) is satisfied, whereas (5.39) is satisfied in C_1. The dashed line is a continuous extension of the phase.

$\Phi_0 = 0.84\pi$, satisfying the flat response criterion (5.21). By close inspection of Fig. 5.30, $\psi_{AMZ}(\omega)$ is observed to satisfy (5.38) in the ranges $\Omega \leq (\pi - \Phi_0)/\tau$ and $(\pi + \Phi_0)/\tau < \Omega < 2\pi/\tau$, which are referred to as D_1 and D_2, respectively. On the other hand, (5.39) is satisfied in $(\pi - \Phi_0)/\tau < \Omega \leq (\pi + \Phi_0)/\tau$, which is labeled C_1. According to (5.22) this phase response causes $|T_{AMZ}(\Omega)|$ to approximate $\left|T_H^{opt}(\Omega)\right|$ for $\Omega < \Omega_{2dB} = \pi/\tau$. However, without the phase discontinuity, i.e. assuming a continuous phase response as in (5.38) over the entire spectrum, as indicated by the dashed line in Fig. 5.30, $|T_{AMZ}(\Omega)|$ starts to deviate from $\left|T_H^{opt}(\Omega)\right|$ at a significantly lower modulation angular frequency $\Omega_{\max}^{DEST}$. This may be shown by noting that for $\Omega > \Omega_{3dB}^{CDR}$, the XGM filter function in (5.40) may be neglected, thereby reducing $|T_{AMZ}(\Omega)|$ to

$$\left|T_{AMZ}^{DEST}(\Omega)\right| \approx \frac{\alpha}{2\sqrt{1+\cos(\Phi_0)}}\left[\sqrt{1+\cos(-\Omega\tau+\Phi_0)} - \sqrt{1+\cos(\Omega\tau+\Phi_0)}\right] \tag{5.41}$$

where "DEST" underlines that this expression assumes destructive interference between the two sidebands contributing to the XPM filter function, i.e. the upper signs in (5.40). By inspection, (5.41) is observed to reach a maximum at $\Omega_{\max}^{DEST} = (\pi - \Phi_0)/\tau$, and decrease for $\Omega > \Omega_{\max}^{DEST}$, with a slope magnitude much less than 10 dB/decade. As already mentioned, the asymmetric MZI satisfies (5.38) for $\Omega \leq \Omega_{\max}^{DEST}$, and thus the assumption of a continuous phase response only has implications for $\Omega_{\max}^{DEST} < \Omega < (\pi + \Phi_0)/\tau$, which is the range referred to as C_1 in Fig. 5.30. Assuming that the relative amplitude response $\left|T_N^{DEST}(\Omega)\right| =$

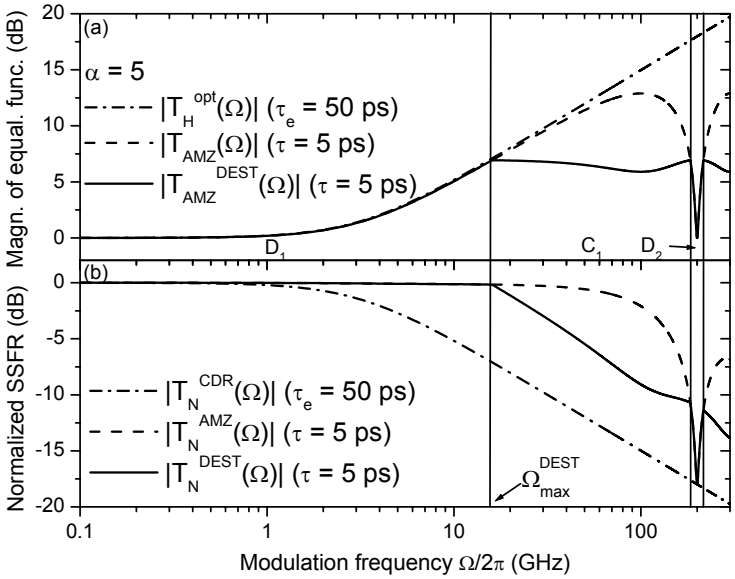

Figure 5.31: (a) Magnitude of the equalizer functions of the asymmetric MZI filter, assuming a continuous phase response (solid), the physical MZI filter (dashed), and the optimum filter (dash-dotted) as a reference. (b) The normalized SSFRs corresponding to the asymmetric MZI filter with continuous phase response (solid), and the physical MZI filter (dashed). The normalized CDR for $\tau_e = 50$ ps is shown as a reference. $\alpha = 5$ and $\tau = 5$ in both plots, and the frequency ranges D_1, D_2, and C_1 are indicated.

$\left|T_N^{CDR}(\Omega)\right| \left|T_{AMZ}^{DEST}(\Omega)\right|$ is completely flat for $\Omega < \Omega_{\max}^{DEST}$, and has a slope of -10 dB/decade for $\Omega > \Omega_{\max}^{DEST}$, the -3 dB bandwidth may be estimated by

$$\begin{aligned} \Omega_{3dB}^{DEST} &\approx 2\Omega_{\max}^{DEST} = 2\frac{\pi - \Phi_0}{\tau} \\ &= 2\frac{\pi - 2\arctan(\gamma_f/\alpha)}{\tau} \end{aligned} \tag{5.42}$$

Fig. 5.31 (a) compares $\left|T_{AMZ}^{DEST}(\Omega)\right|$ to $|T_{AMZ}(\Omega)|$ and $\left|T_H^{opt}(\Omega)\right|$ for $\tau = 5$ ps, $\tau_e = 50$ ps, and $\alpha = 5$, and Fig. 5.31 (b) shows the corresponding normalized SSFRs. The assumption that $\left|T_N^{DEST}(\Omega)\right|$ is flat for $\Omega < \Omega_{\max}^{DEST}$ is equivalent to assuming the same for $\left|T_N^{AMZ}(\Omega)\right|$, as the two are identical for $\Omega < \Omega_{\max}^{DEST}$. As already established, $\left|T_N^{AMZ}(\Omega)\right|$ is flat for $\Omega < 1/\tau$ if Φ_0 satisfies (5.21). Thus, by applying (5.21) with $4\tau_e^2\tau^{-2} >> 1$, the assumption is valid if

$$\begin{aligned} \Omega_{\max}^{DEST} &< 1/\tau \\ &\Rightarrow \frac{\tau_e}{\alpha\tau} > \frac{1}{2}\tan\left(\frac{\pi - 1}{2}\right) \approx 0.92 \end{aligned} \tag{5.43}$$

This is clearly fulfilled in Fig. 5.31, as $\tau_e/(\alpha\tau) = 2$. As predicted, the slope magnitude of $\left|T_{AMZ}^{DEST}(\Omega)\right|$ in C_1 is observed to be significantly smaller than 10 dB/decade, which justifies the assumption that $\left|T_N^{DEST}(\Omega)\right|$ has a slope of -10

dB/decade for $\Omega > \Omega_{\max}^{DEST}$. Consequently, the estimate presented in (5.42) is accurate, as long as (5.43) is satisfied.

With the present choice of parameters, the -3 dB bandwidth predicted by (5.42) amounts to $\Omega_{3dB}^{DEST}/(2\pi) \approx 31$ GHz, which is significantly smaller than the -2 dB bandwidth, Ω_{2dB}, of the real asymmetric MZI (5.23), including the phase discontinuity, which reaches $\Omega_{2dB}/(2\pi) = 1/(2\tau) = 100$ GHz. Finally it should be noticed that for $\tau \to 0$, $\Omega_{2dB} \to \infty$, whereas it may be shown that

$$\Omega_{3dB}^{DEST} \to 2\alpha/\tau_e = \frac{2\alpha}{\sqrt{3}}\Omega_{3dB}^{CDR} \quad ; \ \tau \to 0 \tag{5.44}$$

by Taylor expanding (5.42) and applying (5.21). In other words, assuming that a notch filter, with an amplitude response identical to the asymmetric MZI, has a continuous phase response across the notch, leads to a bandwidth, which is limited to $\Omega_{3dB}^{DEST}/(2\pi) = \alpha/(\tau_e\pi) \approx 31.8$ GHz. This is a factor of $2\alpha/\sqrt{3} \approx 1.15\alpha$ larger than the CDR bandwidth, but, according to (5.23), a factor $\approx 4\alpha/(\pi\gamma_f)$ smaller than $\Omega_{2dB}/(2\pi)$. The importance of the phase discontinuity has also been addressed by Ueno et al. [137] through large-signal simulations.

Comparison of filter types

Comparing the magnitude of the equalizer function $|T_H(\Omega)|$ to $\left|T_H^{opt}(\Omega)\right|$ graphically is a convenient way of assessing the performance of different filters, qualitatively and quantitatively. This is done in Fig. 5.32 (a) for the asymmetric MZI filters with $\tau = 5$ ps and $\tau = 10$ ps, and a Lorentzian band pass filter given by

$$H_L(\omega) = \frac{\Delta\omega}{\Delta\omega + 2j(\omega - \omega_m)} \tag{5.45}$$

where $\Delta\omega = 2\pi\Delta f$ is the full width at half (power) maximum bandwidth and $\omega_m = 2\pi f_m$ is the peak angular frequency. The equalizer function corresponding to $H_L(\omega)$ is referred to as $T_L(\Omega)$. The Lorentzian is used as an example of a BPF, which is interesting from an applications point-of-view, since BPFs are commercially available in a large variety of shapes and widths. Fig. 5.32 (b) shows the overall SSFR magnitudes, $\left|T_N^{AMZ}(\Omega)\right|$ and $\left|T_N^{L}(\Omega)\right|$, corresponding to the equalizer functions in Fig. 5.32 (a). The asymmetric MZI filters satisfy the flat-response criterion (5.21). For the Lorentzian BPF, the filter bandwidth Δf and the peak position f_m have been adjusted to minimize the discrepancy between $|T_L(\Omega)|$ and $\left|T_H^{opt}(\Omega)\right|$ over the largest possible bandwidth.

Centering the filter on the lower sideband, i.e. choosing $f_m < 0$, the optimum combination of $(\Delta f,\ f_m)$ is found to be approximately $(18, -13)$ GHz. As shown in Fig. 5.32 (b), the Lorentzian BPF gives rise to a significant enhancement of the CDR, but is sub-optimal compared to the asymmetric MZI filters of $\tau = 5$ ps and 10 ps. Choosing the upper sideband instead of the lower, i.e. $(\Delta f,\ f_m) = (18, 13)$

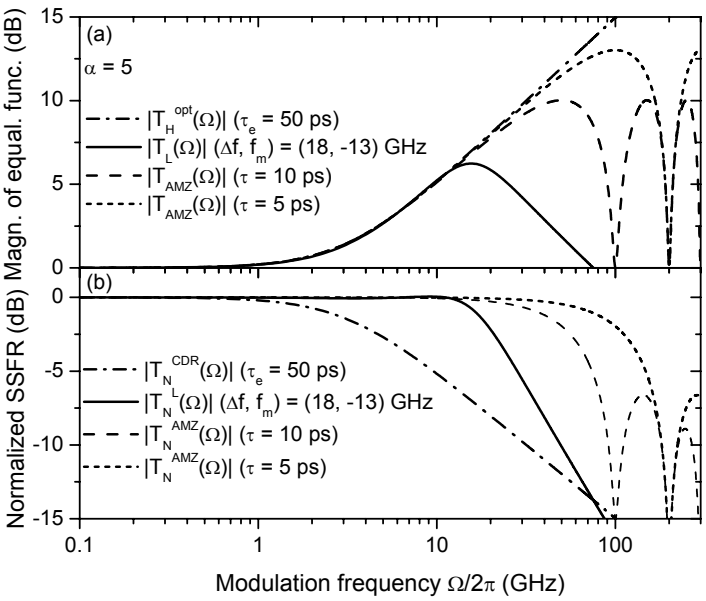

Figure 5.32: (a) Magnitude of the equalizer functions of the Lorentzian BPF (solid), the asymmetric MZI with $\tau = 5$ ps (short dashed) and $\tau = 10$ ps (dashed), and the optimum filter (dash-dotted). (b) the normalized SSFRs corresponding to the Lorentzian BPF (solid), the asymmetric MZI filter with $\tau = 5$ ps (short dashed) and $\tau = 10$ ps (dashed), and the normalized CDR for $\tau_e = 50$ ps. $\alpha = 5$ in both plots.

GHz, changes $|T_L(\Omega)|$ slightly. This is because the Lorentzian BPF does not completely suppress the other sideband, which leads to a dependence of $|T_L(\Omega)|$ on the filter phase response, as discussed above. The phase of the Lorentzian, $\psi_L(\omega)$, is antisymmetric around $\omega = \omega_m$, while the amplitude response $|H_L(\omega)|$ is symmetrical, which by careful analysis of (5.37) may be shown to cause the slight difference between the SSFRs obtained from the two sidebands. It should be mentioned that for large signal modulation the probe spectrum at the output of the SOA is asymmetric, due to the fact that the red-shift is caused by fast, stimulated recombinations, whereas the relatively slow carrier density recovery is responsible for the blue-shift. This asymmetry gives rise to a difference between the sidebands, regardless of the filter phase response.

Fig. 5.33 shows the transmission characteristics for the three filters giving rise to flat SSFRs in Fig. 5.32 (b). As indicated by the straight, parallel lines the filters have one thing in common, namely that their slopes coincide at $\omega = 0$. In the following it will be shown that this is a general consequence of the flat response criterion, and thus a general property of a filter approximating an optimum filter.

The starting point is a Taylor expansion of the arbitrary filter magnitude $|H(\omega)|$ and phase $\psi(\omega)$ to the first order around $\omega = 0$

$$|H(\omega)| \approx K\omega + |H(0)| \tag{5.46}$$

$$\psi(\omega) \approx K_\psi \omega + \psi(0) \tag{5.47}$$

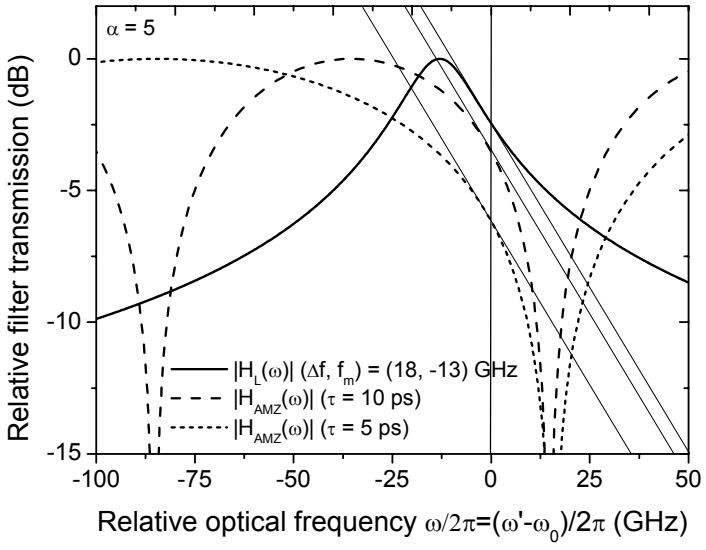

Figure 5.33: Comparison of amplitude responses for different filters giving rise to a flat overall SSFR: Lorentzian BPF (solid) and asymmetric MZI filters with $\tau = 10$ ps (dashed) and $\tau = 5$ ps (shot dashed). The straight lines indicate that all three filters have equal slopes at $\omega = 0$.

Just as in (5.38), the phase is assumed continuous around $\omega = 0$ in (5.47), which is correct if the filter does not have a notch at $\omega = 0$. K and K_ψ are the slopes of the amplitude and phase responses at $\omega = 0$, respectively. Physically, K_ψ can be interpreted as the filter's group delay at $\omega = 0$. Inserting (5.46) into (5.35), the magnitude of the equalizer function can be approximated by

$$\begin{aligned} |T_H(\Omega)| &\approx \frac{1}{2}\left|2e^{jK_\psi\omega}\left[1 - j\alpha\frac{K\Omega}{|H(0)|}\right]\right| \\ &= \sqrt{1 + \frac{\alpha^2 K^2\Omega^2}{|H(0)|^2}} \end{aligned} \tag{5.48}$$

which, by comparison with the optimum equalizer function (5.36), gives the following requirement to K

$$K = \pm\frac{\tau_e\,|H(0)|}{\alpha} \tag{5.49}$$

where $+/-$ corresponds to positioning the transmission peak of the filter at the upper/lower sideband. The corresponding slope on a logarithmic scale becomes

$$\left.\frac{d\log|H(\omega)|}{d\omega}\right|_{\omega=0} = \frac{K}{\ln(10)\,|H(0)|} = \pm\frac{\tau_e}{\ln(10)\alpha} \tag{5.50}$$

which is a constant and independent of filter parameters. Using (5.21) in (5.1) it is readily verified that $H_{AMZ}(\omega)$ satisfies (5.50).

Eq. (5.50) provides valuable insight into the effect of τ_e and α on the the small-signal response. It is clear from Fig. 5.32 (a) and (b) that the small-signal

bandwidth is closely related to the filter detuning of a BPF, when the flat response criterion, expressed e.g. as (5.50), is satisfied. Considering the Lorentzian BPF in Fig. 5.33 it is observed that a decrease of the slope requirement in (5.50) would enable a larger filter detuning, and consequently larger bandwidth, while maintaining the flat response. This may be obtained through a decrease of τ_e and/or an increase of α, i.e. by using an SOA with a faster response and/or a larger phase-amplitude coupling. Moreover, it follows that a BPF with steeper slopes, such as e.g. a cascade of Lorentzian filters, can satisfy (5.50) for a larger filter detuning, thereby increasing the bandwidth.

According to (5.30), the average power transmitted through the filter is given by $\overline{P} = |E_0|^2$ in the small-signal regime, which means that the average power decreases with the detuning of a BPF. Although this simple relationship is not valid in the large-signal regime, where the power in the sidebands can not be neglected, the conclusion remains the same [p4]. As a consequence, a large detuning of a BPF is not beneficial for the OSNR of the probe signal, and in general the optimum detuning will be a trade-off between bandwidth and OSNR. For the asymmetric MZI, a decrease of τ_e and/or an increase of α demands a decrease of the detuning (decrease of Φ_0) according to (5.50), which gives rise to an increased average output power. The bandwidth is unaffected, since it depends exclusively on τ.

Fixed-slope filter

Since filters leading to a flat SSFR share the property that the slope at $\omega = 0$ satisfies (5.49), it would be natural to investigate a filter $H_{LIN}(\omega)$ defined by (5.46) and (5.47), with the slope K given by (5.49), in the entire dynamic range, for which $0 \leq |H_{LIN}(\omega)| \leq 1$.

For $K > 0$ and $K < 0$, the dynamic range is defined as -$\omega' \leq \omega \leq \omega''$ and $-\omega'' \leq \omega \leq \omega'$, respectively, with the limits given by

$$\begin{aligned} \omega' &= |H_{LIN}(0)| \,/\, |K| \\ \omega'' &= (1 - |H_{LIN}(0)|) \,/\, |K| \end{aligned} \tag{5.51}$$

Outside the dynamic range, the amplitude response $|H_{LIN}(\omega)|$ is fixed to 0 or 1, as shown in Fig. 5.34. For $|\omega| \leq \min(\omega', \omega'')$, the amplitude and phase of $H_{LIN}(\omega)$ are linear functions of ω, described completely by (5.46) and (5.47). Substituting (5.46) and (5.47) into (5.37), the equalizer function $T_{LIN}(\omega)$ for the transfer function $H_{LIN}(\omega)$, can be reduced to

$$T_{LIN}(\Omega) = e^{jK_\psi \Omega} \left(1 - j\alpha K \Omega / |H_{LIN}(0)|\right) \tag{5.52}$$

Inserting the expression (5.49) for K into (5.52), it is found that $|T_{LIN}(\Omega)| = \left|T_H^{opt}(\Omega)\right|$, which means that $H_{LIN}(\omega)$ is an optimum filter, giving rise to a flat

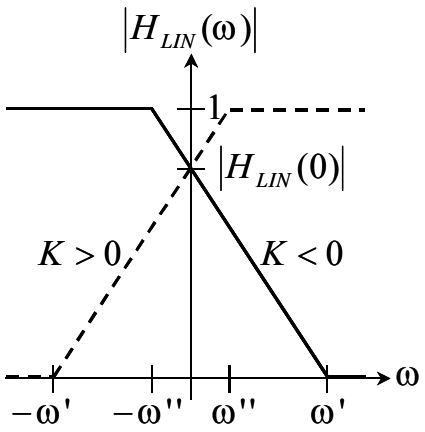

Figure 5.34: Sketch of amplitude response with a constant slope K given by (5.49) in the entire dynamic range. $K < 0$ (solid), $K > 0$ (dashed), and ω' and ω'' indicate the boundaries of the dynamic range.

SSFR in the frequency range $\Omega \leq \min(\omega', \omega'')$, which may be expressed

$$\Omega \leq \min\left(\omega', \omega''\right) = \frac{\alpha}{\tau_e \left|H_{LIN}(0)\right|}\left(\frac{1}{2} - \left|\left|H_{LIN}(0)\right| - \frac{1}{2}\right|\right) \tag{5.53}$$

Eq. (5.53), which can be derived from (5.51), defines the modulation frequency at which the magnitude of the overall SSFR, $\left|T_N^{LIN}(\Omega)\right|$, starts decreasing from its low-frequency value. The function $\min(\omega', \omega'')$ attains its maximum $\Omega_{\max}^{LIN} = \alpha/\tau_e$ for $|H_{LIN}(0)| = \frac{1}{2}$, corresponding to $\omega' = \omega'' = 1/(2\,|K|)$, and in this case it is readily shown from (5.35) that $T_{LIN}(\Omega) = 1 \mp j\alpha$ for $\Omega > \Omega_{\max}^{LIN}$, where $\mp$ corresponds to $K \gtrless 0$. Since $|T_{LIN}(\Omega)| = \sqrt{1+\alpha^2}$, the -3 dB bandwidth, Ω_{3dB}^{LIN}, of $\left|T_N^{LIN}(\Omega)\right|$ can be obtained in the following way

$$\begin{array}{rcl} \left|T_N^{LIN}(\Omega_{3dB}^{LIN})\right| = & \left|T_N^{CDR}(\Omega_{3dB}^{LIN})\right| \left|T_{LIN}(\Omega_{3dB}^{LIN})\right| = \frac{1}{2} \\ \Longrightarrow \quad \Omega_{3dB}^{LIN} = & \frac{1}{\tau_e}\sqrt{4\alpha^2+3} \\ \approx & \frac{2\alpha}{\tau_e} = \frac{2\alpha}{\sqrt{3}}\Omega_{3dB}^{CDR} \approx 1.15\alpha\Omega_{3dB}^{CDR} \end{array} \tag{5.54}$$

Comparing (5.54) to (5.44) it is observed that the linear filter gives rise to the same bandwidth as an asymmetric MZI with an assumed continuous phase response, in the limit $\tau \to 0$. Thus, the conclusions are the same: the asymmetric MZI provides a bandwidth enhancement, which is approximately a factor of $\pi\gamma_f/(4\alpha)$ larger than the linear filter. Since γ can be increased simply by decreasing τ, the asymmetric MZI is the superior equalizing filter. Yu et al. [138], have investigated, both theoretically and experimentally, the effect of an FBG at the output of an SOA in the small-signal limit. The amplitude response of the FBG was approximated by a linear function as in (5.46), whereas the phase was neglected, corresponding to $K_\psi = 0$. Using somewhat different arguments they arrive at the same conclusion, namely that the small-signal bandwidth scales with α.

A large-signal verification of the bandwidth enhancement resulting from shaping the probe signal by a sharp, detuned BPF is given in Chapter 6, numerically and experimentally.

5.4 Summary

Three types of all-optical switches, the MZI operated in standard-mode (SM-MZI), differential-mode (DM-MZI), and the delayed-interference signal converter (DISC) have been investigated numerically, using the detailed time-domain model. Moreover, a class of switches based on a single SOA and an arbitrary optical filter was analyzed in the small-signal regime.

Compared to the XGM switch, the SM-MZI represents a significant improvement at 80 Gb/s, as the minimum power penalty obtained with a 2 mm long SOA was reduced from 7 dB to 3.5 dB, due to the nonlinear transfer function, which gives rise to an enhancement of the extinction ratio. The limiting factor for the SM-MZI switch is the linear patterning effects, which manifest as intersymbol interference. The polarity-preserving in-phase operating condition is compared to the polarity-inverting out-of-phase condition, and in terms of extinction ratio and input power dynamic range, the former is superior.

Launching a delayed and attenuated replica of the data signal into the other interferometer arm (differential scheme), the trailing edge of the phase response may be cancelled out, thus eliminating the linear patterning effects. The performance is limited primarily by the remaining nonlinear patterning, which are expressed through fluctuations of the mark-level. As it is the case with the SM-MZI, the probe act as a holding-beam, and increasing the input probe power reduces the patterning.

The DISC works by the same principle as the DM-MZI, but several fundamental differences have been identified and quantified. Since the phase responses in the arms of the asymmetric MZI are equal, the trailing edge cannot be fully cancelled and a satellite pulse after each switched pulse is introduced. Limiting the modulation depth of the phase difference reduces the amplitude of the satellite pulses at the expense of the output power. This is to a great extent compensated by a very effective suppression of the ASE power compared to the DM-MZI, which provides an acceptable optical signal-to-noise ratio in spite of the low output power. An analytical expression for the ratio of transmitted ASE power for the DM-MZI and DISC switches is presented, and amounts to around 10 dB independently of the bitrate.

At 160 Gb/s, nonlinear patterning severely degrades the performance of the DISC, whereas the DM-MZI still performs well, since the patterning may be reduced by lowering the data pulse energy, and compensate for the inherent drop of output power by reducing the phase modulation in the differential arm. The PRBS word length dependence was investigated at 160 Gb/s, and only a slight increase of the mark patterning level was observed from $2^5 - 1$ to $2^9 - 1$.

Using the DISC as an example, analytical formulas relating the parameters of the SOA and the asymmetric MZI to the obtainable small-signal bandwidth are derived. A bandwidth enhancement factor was defined, governing the increase of modulation bandwidth brought about by the asymmetric MZI. A new approach to small-signal analysis, based on the analysis of the field envelope, has been presented and applied to all-optical switches based on a single SOA and an optical filter. The new approach provides a convenient means of analyzing the effect of an arbitrary filter on the small-signal frequency response (SSFR). In particular, the importance of the filter phase response is demonstrated by showing that the bandwidth enhancement effect of the asymmetric MZI filter relies on a discontinuous phase shift of π. Moreover, for a filter with a continuous phase response, such as e.g. a band-pass filter (BPF), it is shown that the highest bandwidth is obtained by suppressing one of the sidebands. This explains recently published experimental results. An optimum filter, which completely counter-balances the carrier density response of the SOA, and thus gives rise to an infinite bandwidth, is introduced as a reference. Comparison of this response with those of physically realizable filters provides a convenient way of visualizing the performance of specific filters. It is shown that all filters giving rise to a flat SSFR have identical slope magnitudes at the optical carrier frequency, and the slope is expressed analytically.

The only figure of merit used in the small-signal analysis is the modulation bandwidth. This leads to the conclusion that the bandwidth of the DISC can be increased indefinitely, simply by reducing the differential delay in the asymmetric MZI, since this increases the bandwidth enhancement factor. However, whereas linear patterning can be eliminated by equalizing the SOA response with an appropriate filter, nonlinear patterning persists, which was also clearly demonstrated through the large-signal simulations. Therefore, modulation bandwidths predicted by the small-signal analysis should be regarded as upper limits. Also, the degradation of the OSNR that follows from detuning a filter at the output of an SOA is not included in the small-signal analysis. However, a clear trade-off between modulation bandwidth and OSNR exists.

Chapter 6

All-Optical Wavelength Conversion

As pointed out in Chapter 2, the ability to shift the wavelength of WDM channels is expected to be a key functionality in future transparent optical networks. This is likely to be the reason why several companies and numerous research institutions are devoting resources for research of techniques and technologies for high-speed wavelength conversion, although indications from service providers hardly suggest an immediate implementation of wavelength conversion in the networks.

This chapter contains a series of experiments demonstrating wavelength conversion with SOA-based devices. It will be shown that the majority of the requirements to converters listed in Chapter 2 may be fulfilled by these implementations. Simulations similar to those in Chapter 5 are used here to support and explain the experimental data, where needed. The experimental demonstrations include a wavelength converter consisting of a single SOA and a band-pass filter, operating at 40 Gb/s with a record-low data pulse switching energy, two experiments at 40 Gb/s with an active/passive MZI and an all-active MZI, both operated in standard-mode, a demonstration of 80 Gb/s standard-mode conversion with an all-active MZI, enabled by filtering-induced pulse shaping, and an example of an all-active MZI wavelength converter used as a $2x20$ Gb/s to 40 Gb/s WDM-to-OTDM translator. The final section of the chapter contains a simulation-study of the DOMO wavelength converter.

6.1 Filtering-assisted wavelength conversion

This section picks up the analysis from section 5.3, and shows the results of a large-signal experiment at 40 Gb/s, supported by simulations. Parts of the contents of the section are based on [p4].

As it should be clear from Chapter 5, the DISC and MZI configurations rely

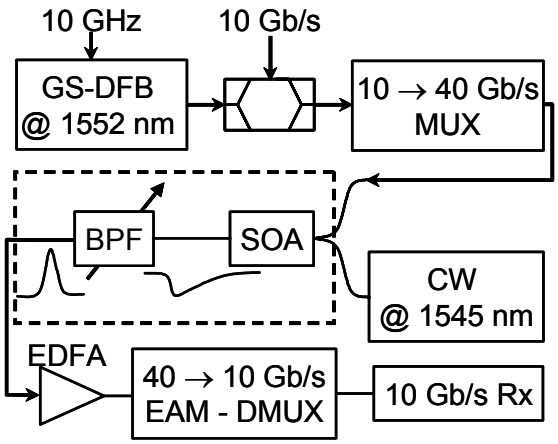

Figure 6.1: Setup for 40 Gb/s filtering-assisted wavelength conversion experiment.

on the control of at least two bias currents (SOA bias or phase tuning currents) for optimizing the operating conditions. Moreover, to compensate for the inherently low input power dynamic range (IPDR) of these interferometers, an additional SOA may be needed at the data signal input [p7]. This adds up to at least three currents, which need to be tuned to accommodate changes of wavelength, input signal power and quality, etc.

Here, a very simple all-optical wavelength converter, based on a single SOA and a BPF is analyzed. The converter operates at 40 Gb/s, preserves the data polarity and RZ format, and does not introduce patterning effects. A single bias current allows for very simple control and stable operation, and in a recent report of a wavelength converter using the same principle of operation [44], an open-loop IPDR (i.e. no feedback control) of 11 dB indicates that control of input power variations may not be necessary.

6.1.1 Principle and experimental setup

The principle of operation of the wavelength converter can be understood from the experimental setup in Fig. 6.1: a gain-switched DFB laser (GS-DFB) emits a 10 GHz train of ≈ 7 ps wide pulses at a wavelength of 1552 nm, which is then modulated with a PRB sequence of word-length $2^{31}-1$ before being multiplexed to 40 Gb/s in a passive fiber-based interleaver. The 40 Gb/s RZ data signal is combined with a CW probe at 1545.08 nm, and launched into the 800 μm long SOA, which is realized in a buried ridge structure (BRS) with a tensile-strained, polarization independent bulk InGaAsP double heterostructure. The cross-section of the SOA has been optimized to give a minimum optical area A/Γ, which as explained in section 4.1, minimizes the saturation power and enhances the modulation bandwidth [66]. The result is an SOA with a cross-section of 0.7 x 0.5 μm and $\Gamma = 0.6$, which is biased at 300 mA. Notice that these parameters are

identical to those chosen in the large-signal simulations in the previous chapters.

Measured at the SOA input, after the 3 dB coupler, the data and probe average powers are −12.25 dBm (≈ 3 fJ/data pulse) and −3.0 dBm, respectively. Inside the SOA the probe is cross-gain modulated and thus polarity-inverted, as well as cross-phase modulated, by the data signal. The leading edge of the modulated probe is shifted towards lower frequencies (red-shifted), whereas the trailing edge is shifted towards higher frequencies (blue-shifted). Due to the low data-to-probe power ratio of −9.25 dB, XGM is quite inefficient. However, this is not the case for XPM, due to a significant α-parameter, and thus a significant broadening of the probe spectrum can be observed. At the output of the SOA, a commercially available tunable grating filter with a bandwidth (FWHM) of 0.22 nm is centred at 1544.58 nm, i.e. detuned 0.5 nm to the blue side of the probe carrier wavelength. The filter selects the blue-shifted sideband of the probe, converting the phase modulation into amplitude modulation, while efficiently suppressing the CW carrier wavelength, which according to Fig. 5.32 (a) corresponds to suppressing the DC content of the polarity-inverted probe waveform. As indicated in Fig. 6.1, this restores the non-inverted polarity of the converted signal, which is important for obtaining good transmission properties [23], as explained in section 4.2.1. The wavelength converted signal is amplified in an EDFA, and demultiplexed into the four 10 Gb/s tributaries using an EAM, before detection[1] and BER measurements.

A scheme exploiting the same mechanism has been used to demonstrate wavelength conversion at 40 Gb/s, using a re-configurable MEMS-based filter at the output of a 2 mm long SOA [44]. To obtain polarity-preserving operation the filter was configured as a notch, transmitting both sidebands of the probe spectrum with a suitable group delay between them. This is clearly different from the approach presented here, where only the blue-shifted sideband is transmitted. From the analysis and discussion in section 5.3.4 about the influence of the filter phase response, it is clear that the present scheme is significantly simpler, since the performance of this scheme does not depend on the phase response of the filter, as opposed to the design in [44]. The best BER performance in [44] for polarity-preserving conversion was obtained for an average data input power of 2 dBm, measured at the SOA input. Analogous approaches have been taken to realize NLF-based wavelength converters exploiting ultra-fast, but very power-inefficient, fibre nonlinearities, at 40 Gb/s [139], and 80 Gb/s [21].

6.1.2 Experimental and modeling results

The amount of spectral broadening induced by XPM is seen in Fig. 6.2 (a) by comparing the probe spectra before filtering, with and without the data signal turned on. Significant spectral broadening is introduced by the low average data

[1] The receiver used in this experiment is not pre-amplified, like it is the case in most of the experiments presented in this thesis.

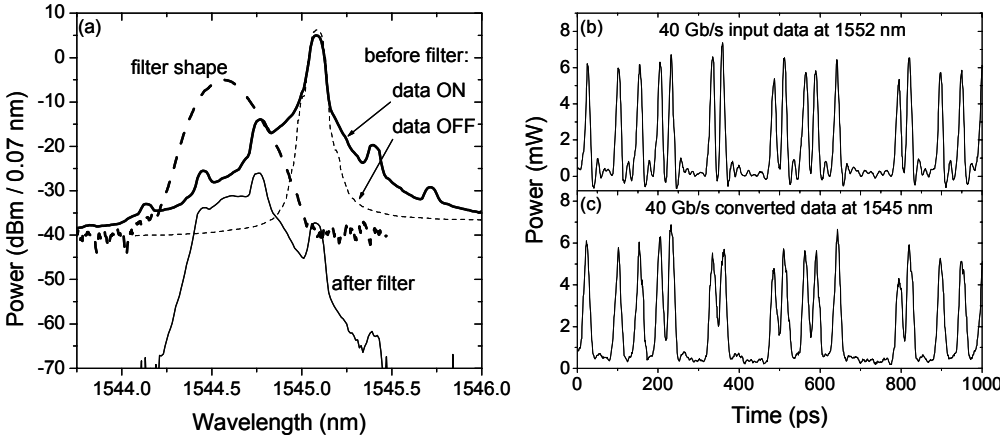

Figure 6.2: (a) Optical probe spectra and filter shape (resolution: 0.07 nm). Thin, dashed: before BPF, data signal off. Thick, solid: before BPF, data signal on (-12.25 dBm). Thin, solid: after BPF. Thick, dashed: BPF characteristic. (b,c) Comparison of input and output data patterns.

power of -12.25 dBm, while the modulation of the gain is kept at a minimum. Fig. 6.2 (a) also shows the BPF characteristic, and the corresponding probe spectrum after filtering. The probe power after the filter is only -21 dBm, measured in a large optical bandwidth. As explained in 5.3.4 a low output power is inherent to the scheme because most of the power is contained in the 'carrier peak'.

In the discussion of (5.50) it was concluded that a faster SOA and/or an SOA with a higher $\alpha-$parameter, would allow for an increase of the filter detuning, an consequently the bandwidth, while maintaining a flat SSFR. Care should be taken in extending all conclusions from the small-signal analysis to the large-signal domain, since the filter position giving rise to a flat SSFR does not necessarily provide a large ER. Nonetheless, the slope of the filter (field) amplitude response at the probe carrier wavelength is estimated from Fig. 6.2 (a) to $5.4 \cdot 10^9$ m^{-1}, which should be compared to $3.43 \cdot 10^9$ m^{-1}, obtained from (5.50) with $\tau_e = 50$ ps and $\alpha = 5$. In other words, the small-signal analysis provides a very good estimate of the optimum filter detuning found experimentally. It is not clear whether this will be the case for all filters, but regardless, the conclusions from the small-signal analysis still hold in the large-signal regime. An increased $\alpha-$parameter gives rise to increased spectral broadening and a general enhancement of the power at a given frequency in the sidebands. Thus, the slope magnitude, which governs the phase-to-amplitude conversion efficiency, may be reduced by increasing the detuning of the BPF, while maintaining the equalization of the CDR roll-off at low frequencies (see e.g. Fig. 5.33). The larger detuning enhances the equalization at higher frequencies, and consequently the modulation bandwidth increases. As explained in section 5.3, a decrease of the effective carrier lifetime τ_e has the same effect, see e.g. (5.27). There is an additional reason why an increased $\alpha-$parameter is beneficial, which is not covered by the small-signal analysis,

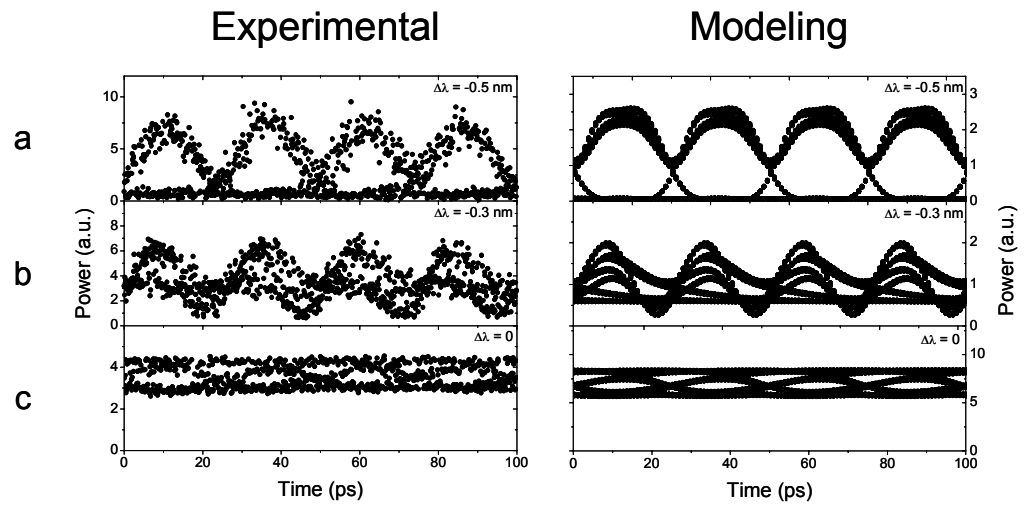

Figure 6.3: Comparison of 40 Gb/s eye diagrams obtained experimentally (left coloumn) and through modeling (right column). The filter detuning is (a) -0.5 nm, (b) -0.3 nm, (c) 0 nm.

namely the fact that the enhanced spectral broadening enables a larger filter detuning for a constant OSNR, which enables operation at higher bitrates.

Fig. 6.2 (b,c) shows a comparison between the input signal at 1552 nm and the wavelength converted output at 1545 nm, respectively, both measured with a 50 GHz photodiode. Notice that the bit-polarity is preserved, and that the probe pulses are symmetric and only slightly broadened compared to the input data pulses. The extinction ratio for both input and output is estimated at 15 dB. The mark patterning observed in Fig. 6.2 (b,c) is exaggerated by the sampling oscilloscope - a phenomenon commonly observed with short pulses, which is believed to be due to the limited number of sampling points used in the measurement. The patterning is assessed more accurately from an eye diagram, as it will be clear from the following.

Extensive modelling, using the detailed large-signal model, has been carried out. The physical input parameters to the model, such as SOA dimensions, optical confinement factor, bias current, input powers, filter shape, etc., are identical to the experimental parameters. Fig. 6.3 (a-c) shows a comparison between experimental (left column), and simulated (right column) eye diagrams of the converted signal. The upper (a), middle (b), and bottom (c) rows correspond to filter detunings of -0.5 nm, -0.3 nm, and 0 nm, respectively. As observed, the agreement is very good. For the optimum filter detuning of -0.5 nm, the extinction ratio is ≈ 15 dB, and the data polarity and the RZ format is clearly preserved. Notice that the modulation depth for $\Delta\lambda = 0$ is very small. This is because the only contribution to the modulation comes from XGM, which is very inefficient due to the low data to probe power ratio.

Attempts were also made to use the red-shifted part of the probe spectrum, and this is illustrated in Fig. 6.4 (a-c). The pattern effects seem more pronounced

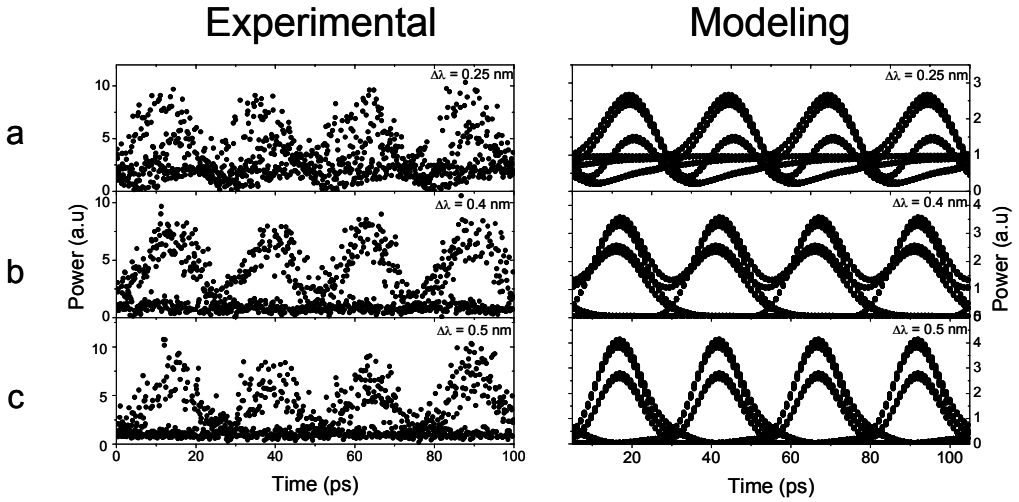

Figure 6.4: Comparison of 40 Gb/s eye diagrams obtained experimentally (left coloumn) and through modeling (right column). The filter detuning is (a) 0.25 nm, (b) 0.4 nm, (c) 0.5 nm.

than in Fig. 6.3, particularly in the modeling results. It is observed in Fig. 6.2 (a) that the probe spectrum has broadened more on the blue side than the red side. This is discussed in some detail below, but here it should just be noted that the reduced amount of power in the red sideband, compared to blue, gives rise to a corresponding reduction of the OSNR, which is clearly observed in Fig. 6.4 as an increased level of noise as the detuning is increased.

A physical explanation for the larger patterning observed when filtering on the red side of the carrier, is apparent from Fig. 4.11 (b), which shows the chirp vs. time for a probe signal cross-gain/phase modulated by an 80 Gb/s data signal. Here, it is clearly observed that the patterning on the blue-chirped part is almost nonexistent, whereas it is pronounced for the red-chirped part. The reason is that the red-chirp occurs during carrier depletion, and in this scenario the carrier density available to the first pulse, in a string of several pulses, is larger than for the succeeding pulses, which results in nonlinear patterning, as explained in section 4.3. On the other hand, the blue-chirp occurs during recovery of the carrier density, which takes place immediately after depletion. Due to saturation, the carrier density available to the probe signal after carrier depletion varies only slightly with the data pattern, and consequently the blue-shift exhibits very little patterning. This is verified experimentally in [136].

Fig. 6.5 (a) shows the BER performance of all four 10 Gb/s tributaries of the input data signal at 1552 nm and the wavelength converted signal at 1545 nm. The power penalty at BER = 10^{-9} ranges between 1.7 and 2.8 dB for the best and worst tributary, respectively, and is believed to be primarily due to ASE noise added by the EDFA after the BPF.

The dependence of the ER and OSNR (in dB/0.23 nm) on the filter position has been investigated numerically, using parameters identical to those of the

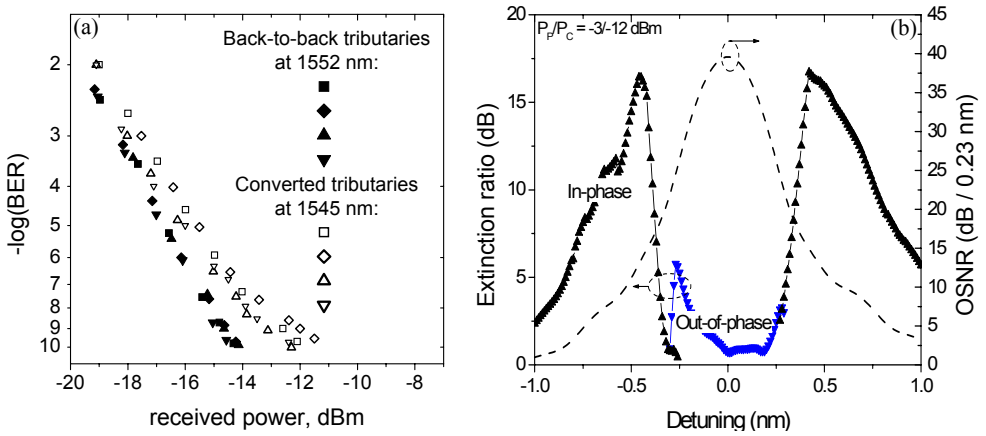

Figure 6.5: (a) BER curves. Solid symbols: back-to-back at 1552 nm, hollow symbols: wavelength converted at 1545 nm. (b) Simulation of ER (left axis) and OSNR (right axis) vs. filter detuning. The ER is given for In-phase (up-triangle) as well as out-of-phase (down-triangle) polarity.

experiment, and the results are illustrated in Fig. 6.5 (b). For polarity-preserving operation, the highest ER of 16.5 dB is obtained for filter detunings of -0.46 nm and $+0.42$ nm. Comparing this with the experimental eye diagrams in Figs. 6.3 and 6.4, the agreement is observed to excellent. The optimum detuning depends on the suppression ratio of the filter, defined as the ratio of the peak to the background transmission, and observed to be $35 - 40$ dB in Fig. 6.2 (a). For detunings large enough that the carrier experiences the background transmission of the filter, an increase of the detuning gives rise to a *decrease* of the sideband-to-carrier (StC) ratio, which translates directly into a decrease of the ER. In Fig. 6.5 (b) the suppression ratio is set to 40 dB, and it has been verified that an increased suppression ratio results in an increased optimum detuning, as well as an increased maximum ER.

For a small filter detuning towards the blue side of the probe carrier, the ER of the polarity-inverted probe signal is significantly increased. This is well-documented [138], and may be explained in the following way: the enhancement of the blue-shifted parts of the signal, and the simultaneous suppression of the carrier, results in a reduced steady-state mark-level and an enhancement of the power during carrier recovery. This combination of effects leads to an increased extinction ratio. Fig. 6.5 (b) also shows the variation of the OSNR with the filter detuning, and as already stressed in section 5.3, there is a trade-off between the ER and OSNR as long as the ER increases.

Using a higher input data power enhances the spectral broadening, and consequently the power that may be transmitted by the detuned filter. However, the shape and width of the present filter was ill-suited for a larger phase modulation. This is readily explained from the concept of the optimum filter in section 5.3.4, since the optimum filter shape depends on the shape of the probe spectrum at the output of the SOA, which in turn depends strongly on the phase modulation.

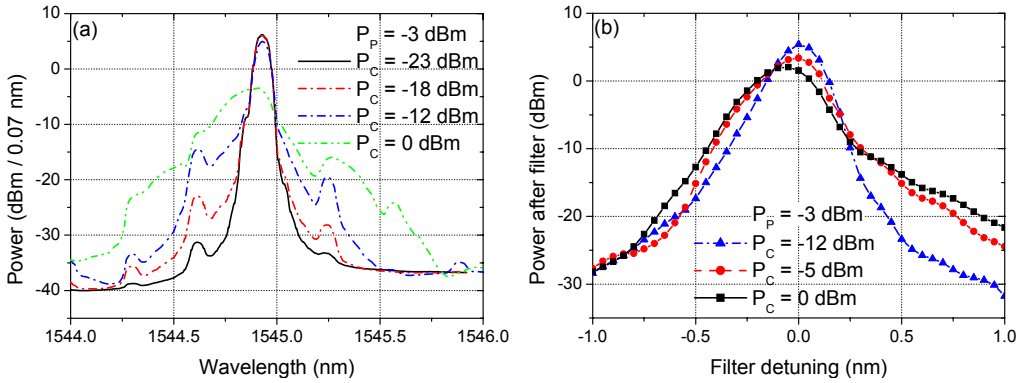

Figure 6.6: (a) Experimental probe spectra (res: 0.07 nm) for $P_P = -3$ dBm and with the the average data power P_C as a parameter. (b) Average probe power transmitted by the filter vs. filter center wavelength with P_C as a parameter.

6.1.3 Spectral discrepancies

When a single saturating signal propagates through an SOA it modulates the carrier density, which gives rise to SPM and consequently spectral broadening. The red-shifting carrier depletion occurs during the presence of signal pulses, i.e. when the power is high. Carrier recovery takes place between the signal pulses, where the power is significantly smaller than the pulse peak power, and thus the power in the blue-shifted part of the optical spectrum is low compared to the red-shifted part. This phenomenon is well-described in literature [103], and may be exploited to construct e.g. intensity dependent gates (2R regenerators) [p5],[p6].

The situation is more complex when considering a CW probe, which is cross-phase modulated by a data signal. If XGM is neglected, corresponding to assuming a constant probe output power, the spectrum becomes a pure XPM spectrum. This is a good approximation in the present case, as observed in Fig. 6.3 (c), where only very little power variation is observed. As observed in Fig. 4.11 (b) the red-shift is significantly larger than the blue-shift, since the rate of stimulated recombination generally far exceeds the rate of carrier recovery. However, Fig. 4.11 (b) clearly illustrates that the slower recovery results in a significantly longer duration of the blue-shift, compared to the red-shift. Since a large peak chirp and a large chirp duration both tend to increase the power in the sidebands, see (3.3), it is impossible to conclude unambiguously that the spectrum should be broader on the red side or the blue side of the carrier wavelength.

Fig. 6.6 (a) shows the probe spectrum for average data powers of -23, -18, -12, and 0 dBm. For the three lowest data powers the spectral broadening is clearly more pronounced on the blue side, whereas the trend is less clear for the highest data power of 0 dBm. However, considering the peaks corresponding to the first harmonics, i.e. ± 40 GHz, the blue-shifted peak is generally higher than the red-shifted counterpart. Fig. 6.6 (b) shows the power transmitted through

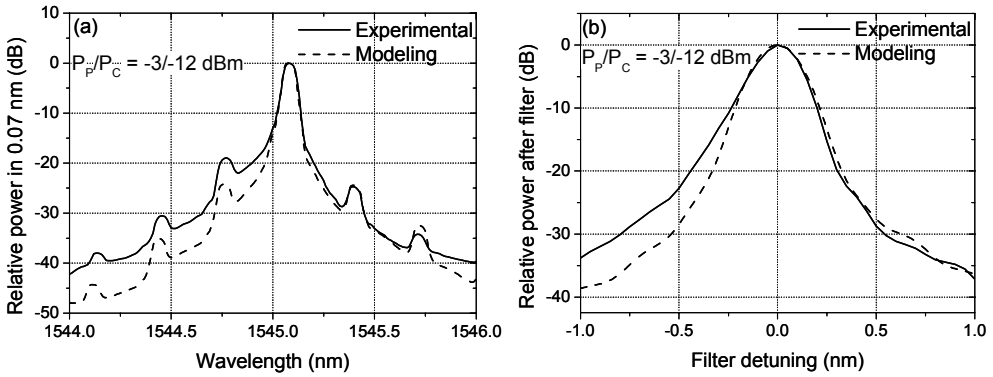

Figure 6.7: (a) Comparison of experimental (solid) and calculated (dashed) probe output spectra and (b) the corresponding average (normalized) probe power transmitted by the filter vs. filter peak transmission wavelength. $P_P/P_C = -3/-12$ dBm in both cases.

the 0.23 nm wide BPF vs. the spectral detuning of the filter's peak transmission relative to 1545 nm for average data powers of -12, -5, and 0 dBm. For -12 dBm, more power is clearly transmitted from the blue sideband, but as the power - and with that the stimulated recombination rate - is increased, the power in the red sideband increases. For large detunings, e.g. 1 nm, more power is actually transmitted from the red side of the spectrum.

Fig. 6.7 (a) shows a comparison between the experimental and calculated probe spectrum for an average data power of -12 dBm. The model predicts the spectrum very well on the red side of the carrier, but clearly underestimates the broadening on the blue side. In Fig. 6.7 (b) the power transmitted through the BPF is calculated and illustrated as a function of the filter detuning. At a detuning of -0.5 nm the calculated and measured powers deviate by as much as 5 dBm. Moreover, focusing again on the first harmonics, the model predicts slightly higher peaks on the *red side* of the carrier, i.e. the *opposite* of what was concluded from the experimental data. Consequently, the model predicts a slightly higher OSNR on the red side.

Since the discrepancy is primarily on the blue side it would be obvious to conclude that the carrier recovery is inaccurately modeled. To test this hypothesis, all simulation parameters with an influence on the rate of carrier recovery have been varied, including the coefficients A, B, and C of the spontaneous recombination rate. Unfortunately, the parameter sweep was unable to explain the discrepancy. Ultra-fast dynamics was introduced via the nonlinear gain-suppression parameter introduced in (3.1), using the formulation of [102], but this had little effect on the spectrum as well. At present the source of discrepancy is yet to be identified, but it is believed to be caused by a physical effect not currently included in the model. It should be noted, though, that the underestimated spectral broadening on the blue side of the carrier influences primarily the power level, since the agreement with experiments in terms of pulse shape and width, extinction ratio,

optimum detuning, etc, is satisfactory.

It should be noted that if the random data signal is replaced by a clock signal consisting of very short pulses, the XPM spectrum may be expressed analytically. This is shown in [127], where it leads to an important relation between the phase modulation depth and the ratio between the specific harmonics in the probe power spectrum. The model presented in this report verifies the analytical expression given in [127]. An analysis of the effect of the input data pattern on the probe spectrum showed that the spectra corresponding to excitation by a clock signal and a data signal are qualitatively different, whereas the influence of the PRBS word length is very small. In other words, the conclusions of [127] apply to excitation by a clock signal only, and should not be extrapolated to random data. Finally, it is worth mentioning that the numerical model presented in [127] also underestimates the spectral content on the blue side of the probe carrier.

6.2 Standard-mode operation of MZIs

As explained in Chapter 5, the performance may also be improved by employing an SOA in an interferometric structure, since this enhances the ER and reduces nonlinear patterning. Here, the standard-mode operation of MZIs is investigated, and it is shown that the filtering technique from section 6.1 also applies to the output of an interferometer.

MZIs fabricated using two different integration technologies, all-active and active-passive, have been available for testing. All-active devices require a minimum number of fabrication steps, and are thus suitable for mass production. Moreover, the active input and output sections, shown in Fig. 3.2, provide a means of controlling the input and output power level, where the former is particularly useful in increasing the IPDR [p7],[p8]. On the other hand, an all-active device inherently emits more ASE, and has a higher electrical power consumption, since the active waveguides must be pumped to at least transparency in order to reduce the propagation loss. Modular, active-passive integrated MZIs, where only the interferometer arms, and optionally one or both of the data input waveguides ($3'$ and $4'$ in Fig. 3.2), are active, address the disadvantages of the all-active design. Active-passive integration allows devices to be designed and optimized for a more specific application, since active input and output sections may be included if necessary, or otherwise left out, thereby saving power and increasing the OSNR. Two different technologies are currently used to obtain coupling between active and passive waveguides: the butt-coupling and the evanescent - or leaky - coupling.

The butt-coupling, which is illustrated in Fig. 6.8 (a), is a direct coupling. It requires additional fabrication steps compared to the all-active device [140], and due to the difference in refractive index between the active and passive regions, light is reflected in the interface. However, if the interface is angled, the reflections may effectively be reduced to a tolerable level [141,142]. The evanescent coupling

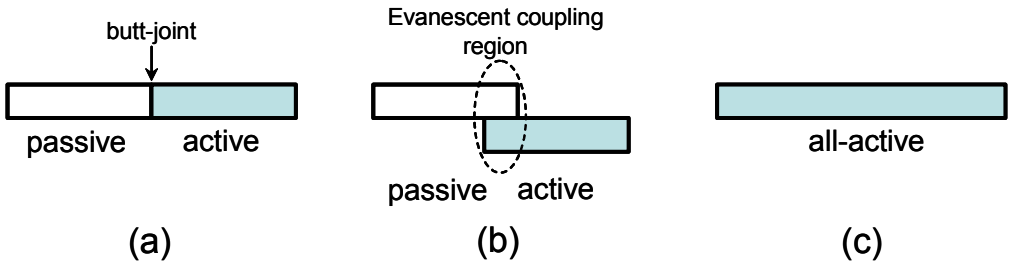

Figure 6.8: Sketch of (a) active-passive butt-joint, (b) evanescent active-passive coupling, and (c) all-active "coupling".

is sketched in Fig. 6.8 (b). Light from the passive waveguide leaks into the active waveguide along the transition region. The fabrication process is very similar to that of the all-active device, with the added advantage of modularity [p7]. However, calculations have shown that the butt-joint improves the coupling by a factor of $2-3$ times compared to an evanescent coupling [140]. This figure may be reduced by using a well-defined, optimized coupling length. Good coupling is not easily obtained for a relatively thick active layer, needed for high optical confinement [143], which makes the active-passive evanescent coupling generally more lossy than the butt-coupling. Consequently, the choice of technology is not obvious.

6.2.1 Operation at 40 Gb/s

In this section, results from two standard-mode wavelength conversion experiments at 40 Gb/s are presented. In the first experiment, an active-passive MZI with SOAs only in the two interferometer arms is used, whereas an all-active MZI is used in the second experiment. The active layers of the two devices are identical (BRS with a tensile-strained, polarization independent bulk InGaAsP double heterostructure) with active region dimensions of $0.7\ x\ 0.5\ \mu m$, giving rise to a confinement factor of $\Gamma = 0.6$. The length of the active interferometer arms is 2 mm in both cases.

Active-passive MZI

The experimental setup is identical to the setup in Fig. 6.1, used in the filtering-assisted wavelength conversion, except for the wavelength converter, which now consists of an evanescent coupling active-passive MZI operated in the standard-mode. In addition, the narrow grating filter is replaced by a 0.8 nm wide (FWHM) BPF. The filter suppresses the data signal, but does not shape the converted probe signal significantly, since it is relatively broad compared to the signal bandwidth.

Fig. 6.9 (a) shows the BER performance of a random 10 Gb/s tributary for conversion from 1552 nm to 1540 nm and 1556 nm, corresponding to down and

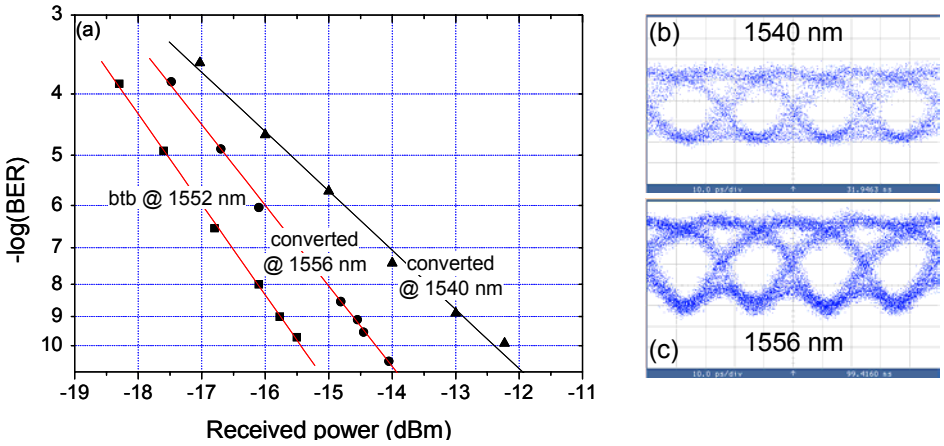

Figure 6.9: (a) BER curves of back-to-back signal at 1552 nm, and wavelength converted signals at 1540 nm and 1556 nm. (b,c) Eye diagrams at 1540 nm and 1556 nm, respectively.

up-conversion, respectively. The BER curve for 1540 nm is not parallel to the back-to-back curve, which means that the BER-floor is higher for the converted signal. A power penalty of 2.8 dB is observed, and as shown in Fig. 6.9 (b), the eye diagram of the converted signal has NRZ characteristics. The latter is likely to be the reason for the small slope of the BER curve, as the receiver inflicts a power penalty on NRZ-like signal due to the reduced peak power. In both cases the bias currents to the interferometer arms are $I_3/I_4 = 765/204$ mA, and the obtained ERs and OSNR are $\approx$ 10 dB and 24 dB/1 nm, respectively, for both probe wavelengths. As it may be seen from the eye diagrams in Fig. 6.9 (b,c), the device is operated in OOP mode. It was not possible to operate in IP mode and preserve the polarity, and this is evidence that the optical path length difference between the interferometer arms is close to zero. In the terminology of Chapter 5, this corresponds to $\Delta\phi_t \approx 0$. The average data and probe signal powers in the fibers at the input of the chip were $P_C/P_P = 2.9/14.3$ dBm. The high input probe power is believed to be due to a large loss in the coupler right after the probe input. Up-conversion makes the unwanted effect of XGM less significant, due to the wavelength dependence of the differential gain. This may be the reason why the performance is improved for conversion to 1556 nm, as shown in Fig. 6.9 (a). The BER curve for the converted signal is parallel to the back-to-back curve, and the power penalty is reduced to 1.2 dB. Moreover, the eye diagram in Fig. 6.9 (c) reveals a faster response than for conversion to 1540 nm, since the format of the converted signal has RZ characteristics. The optical power consumption for conversion to 1556 nm was $P_C/P_P = 7.4/14.3$ dBm, which represents an increase of the necessary data signal power. Again, this may be related to the wavelength dependence of the differential gain, since a large signal power enhances XGM - particularly for down-conversion. It is therefore expected that for up-conversion, the data power may be used to increase the

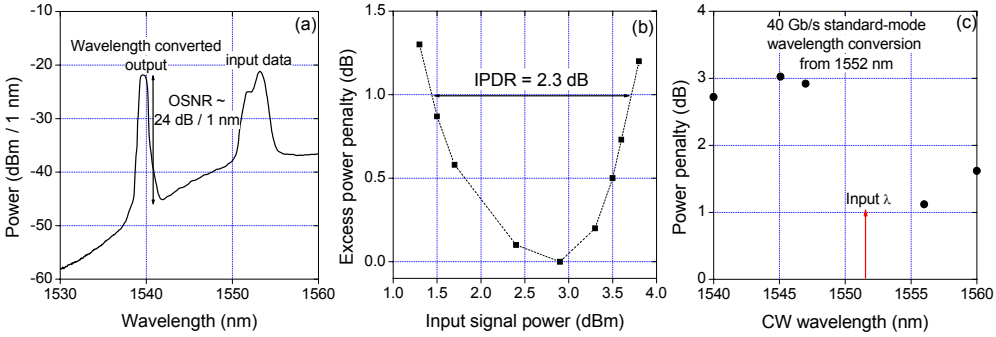

Figure 6.10: (a) Output spectrum (res: 1 nm). (b) Excess power penalty vs. average input signal power, with an indication of the IPDR. (c) Power penalty vs. CW probe wavelength. Data signal wavelength is fixed at 1552 nm.

phase modulation, without simultaneously adding significant distortion from the gain modulation.

The spectrum in Fig. 6.10 (a) is an example of an output spectrum in the case of conversion from 1552 nm to 1540 nm. Notice the large red-shift (> 1 nm) of the input data signal, which is evidence of strong saturation. The IPDR was measured for conversion to 1540 nm, and as shown in Fig. 6.10 (b) the result at 1 dB excess power penalty is 2.3 dB. This relatively small tolerance towards fluctuations in the input data power illustrates the need for an external control of the input power. This may be accomplished by employing a MZI design with an active data input section (corresponding to activating SOA # $3'$ in Fig. 3.2), and modifying the bias current I_3' to compensate for variations of the input power. Using a device identical to the one presented here[2], except for the addition of 400 μm long active input sections, this technique was shown in [p7] to increase the IPDR to 8 dB at 40 Gb/s, for an input-SOA current variation of only 15 mA.

The dependence of the target wavelength on the BER performance was investigated at 40 Gb/s, and although the measured performance is better for conversion to higher wavelengths, the power penalty variation of the converted signal, which is shown in Fig. 6.10 (c), is within 2 dB from 1540 nm to 1560 nm.

All-active MZI

In this section, the results of an all-optical wavelength conversion experiment, using an all-active MZI, are given. The presentation is partly based on [p9], which represents the first demonstration of power penalty-free 40 Gb/s standard-mode operation of a MZI. An all-active Michelson interferometer (MI) has previously been used to demonstrate standard-mode operation at 40 Gb/s, where conversion was accompanied by RZ $\rightarrow$ NRZ format conversion, due to insufficient modulation bandwidth of the device [67], and a power penalty of 1.7 dB.

[2] The devices are from the same wafer.

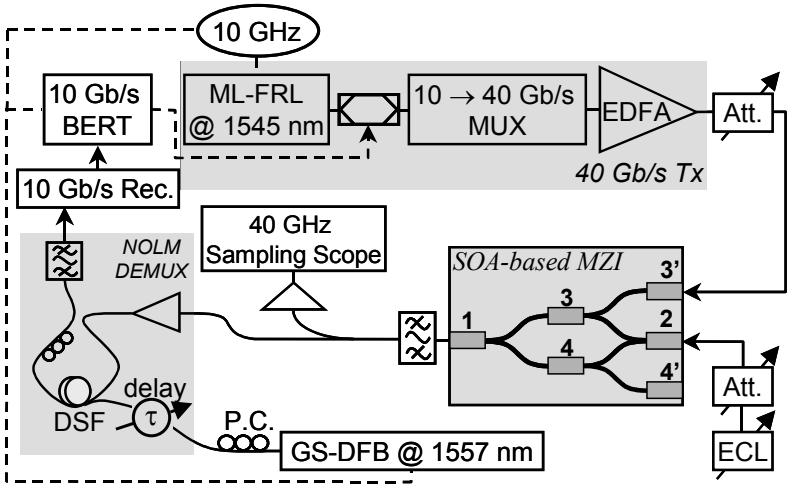

Figure 6.11: Setup for 40 Gb/s wavelength conversion experiment with all-active MZI. BERT: Bit error-rate test set.

The experimental setup is shown in Fig. 6.11: a mode-locked fibre ring-laser (ML-FRL) emits a 10 GHz train of ≈ 2 ps wide, transform-limited pulses at 1545 nm, which is subsequently modulated with a 10 Gb/s PRB-sequence of word-length $2^{31} - 1$. Following passive $10 \rightarrow 40$ Gb/s multiplexing in a fibre-based interleaver, the data signal is amplified in an EDFA, and finally launched into the MZI at section 3'. At this point the data pulses are $\approx 4 - 5$ ps wide due to narrow-band ASE filtering (not shown in Fig. 6.11). CW light from a tunable external-cavity laser (ECL) at the target wavelength is coupled into section 2 of the MZI, and at the output a sharp 0.3 nm wide BPF selects the wavelength converted signal. As it will be shown in detail below, the BPF is slightly detuned towards the blue side of the probe spectrum.

A NOLM is used to demultiplex the converted signal from 40 to $4x10$ Gb/s. The nonlinear element in the NOLM is 3 km DSF with zero-dispersion wavelength at 1555 nm, dispersion slope of 0.06 psnm^{-2}km^{-1}, and a nonlinear coefficient of 2.6 W^{-1}km^{-1} [53]. The 10 GHz control pulses are generated by a GS-DFB laser at 1557 nm, compressed to ≈ 8 ps in a DSF, and then launched into the NOLM. A variable optical delay line is used to synchronize the control pulses to one of the 10 Gb/s tributaries traversing the NOLM clockwise. The control pulses are suppressed in a 1.3 nm wide BPF before entering a 10 Gb/s pre-amplified receiver. Finally, the performance, in terms of BER, is evaluated.

Fig. 6.12 (a) shows eye diagrams of the input signal at 1545 nm, as well as the wavelength converted signal at 1540, 1550, and 1560 nm, all detected with a 40 GHz photo diode. The converted eye diagrams are all clear and open, the polarity and RZ format are preserved, and the converted pulses are very symmetric. The latter indicates a very fast carrier recovery of <14 ps (1/e), which is shown in the next section to be fast enough for standard-mode conversion with RZ $\rightarrow$ NRZ

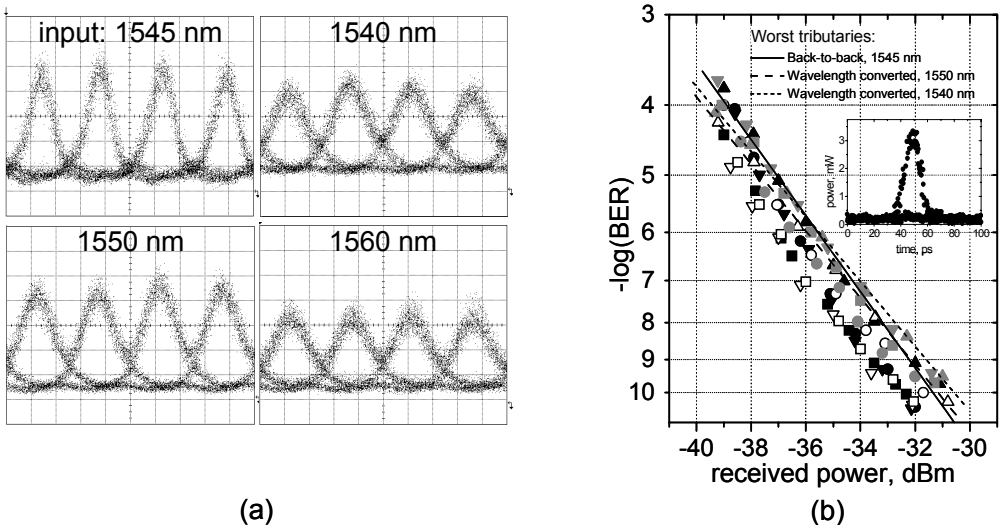

Figure 6.12: (a) Eye diagrams at 40 Gb/s. Top row: input at 1545 nm and output at 1540 nm. Bottom row: Outputs at 1550 and 1560 nm. (b) BER curves for $4x10$ Gb/s tributaries of back-to-back and wavelength converted signals. Black: back-to-back at 1545 nm. Gray: wavelength converted at 1540 nm. White: wavelength converted at 1550 nm. Inset shows demultiplexed eye diagram at 1550 nm.

format conversion at 80 Gb/s. Fig. 6.12 (b) shows the BER performance for all 4 10 Gb/s tributaries of the wavelength converted signals at 1540 and 1550 nm, compared to the back-to-back signal at 1545 nm.

The lines in Fig. 6.12 (b) represent the worst tributary for each signal, and by comparison wavelength conversion is observed to be penalty-free at 1550 nm, and suffering a small penalty of 0.6 dB at 1540 nm. No indications of error-floors are observed. It was not possible to measure BERs at 1560 nm, because this wavelength is too close to the control pulse wavelength in the demultiplexer. However, the quality of the eye diagram is very similar to that at 1540 nm, and consequently similar BER performance is expected. The device was insensitive towards the polarization state of the input data signal, with a receiver sensitivity variation < 0.5 dB.

The applied currents are (see Fig. 6.11) $I_1/I_2/I_3\prime/I_3/I_4\prime/I_4 = 120/70/30/600/0/200$ mA, giving a total applied current of 1.02 A, which is only slightly higher than the total current applied to the 2 active sections of the active-passive MZI. The optical input powers, measured in the fiber, are $\approx$ 12 dBm for the signal, and $\approx$ 9 dBm for the CW light. The high signal power is a direct consequence of the low current through the peripheral section $I_3\prime$, which the signal enters. The low $I_3\prime$, which makes the input section transparent, is believed to be necessary to prevent saturation-induced pulse distortion, which increases the fall-time of the signal pulses entering the interferometer arm [103].

Another example of the fast response of the device is given in Fig. 6.13, which shows a part of the input pattern (ripple in zero-level due to limited detector bandwidth), and the wavelength converted in-phase and out-of-phase patterns at

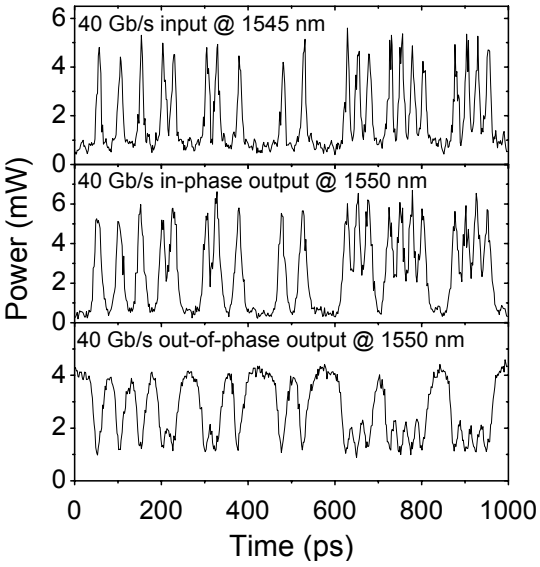

Figure 6.13: 40 Gb/s data patterns. Up: input at 1545 nm, middle: IP output at 1550 nm, down: OOP output at 1550 nm.

1550 nm. The only observable difference between the input and in-phase patterns is the pulse width, which has increased to about 12 ps (measured with a 40 GHz photo diode). Pulse amplitudes are observed to be independent of the preceding pulse pattern, which is also apparent from the eye diagrams in Fig. 6.12 (a). In other words, the patterning effect is negligible. The out-of-phase pattern in Fig. 6.13 is obtained with the same bias currents and input powers as in-phase, except that I_4 is reduced from 200 mA to 160 mA, and that the BPF detuning is reduced considerably.

The effect of reducing I_4 on the probe spectrum is illustrated in Fig. 6.14 (a-b), where the spectra corresponding to the out-of-phase (a) and in-phase (b) signal are shown before filtering (dashed) and after filtering (solid). The only major difference between the spectra before filtering is a 3.5 dB enhancement of the carrier peak for the out-of-phase case. Remembering the discussion from section 6.1.2 about the relationship between the sideband-to-carrier (StC) ratio and the ER, it makes sense that the optimum in-phase condition corresponds to the larger StC ratio, since this allows for a sufficiently large suppression of the carrier peak with a moderate filter detuning. For out-of-phase operation the filter is detuned very little, approximately -0.06 nm, in order to maintain a high output power, whereas the in-phase optimum is obtained for a detuning of -0.33 nm. The reason this value is lower than for the single-SOA experiment in section 6.1.2 is primarily due to the enhancement of the StC ratio obtained by changing the interferometer bias.

It is difficult to assess the OSNR from the very high-resolution spectra in Fig. 6.14. In a 1 nm resolution bandwidth, the OSNR is measured to 27 dB

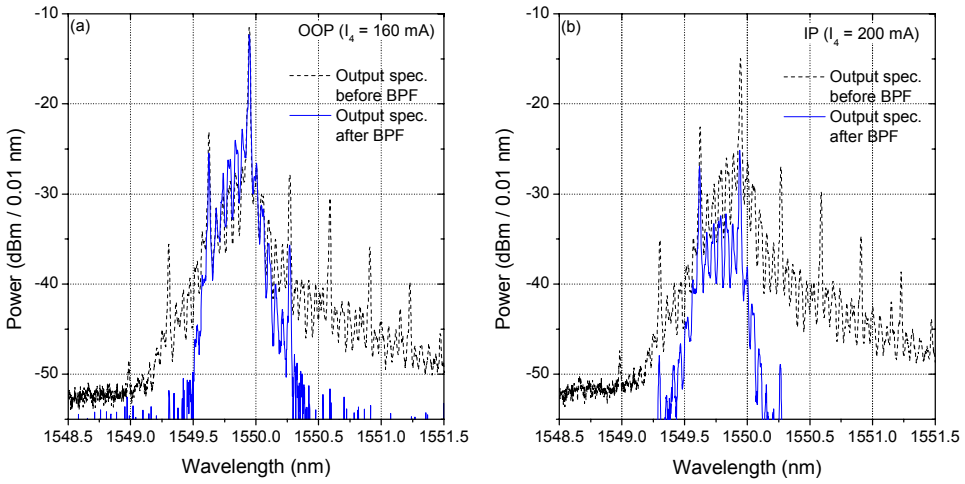

Figure 6.14: Probe spectra corresponding to (a) OOP and (b) IP. Dashed curves: before BPF, solid curves: after BPF.

before the BPF. The OSNR of the out-of-phase signal is close to this figure, due to the small detuning, whereas the OSNR for the in-phase signal is smaller.

6.2.2 Operation at 80 Gb/s

The all-active MZI used for the 40 Gb/s experiment in the previous section unfortunately stopped working before the speed potential could be properly investigated. However, an identical device from the same wafer was available, and this was investigated in the standard-mode configuration at a bitrate of 80 Gb/s, still using the sharp 0.3 nm filter as a pulse shaper at the output. Some of the results shown in this section were presented in [p10].

The experimental setup is identical to Fig. 6.11, except that the data signal and CW probe wavelengths were 1555 nm and 1560 nm, respectively, and that the data signal was passively multiplexed to 80 Gb/s, instead of 40 Gb/s. The fiber-interleaver used in the experiment is commercially available[3], and was made of polarization maintaining (PM) fiber exclusively, including tunable PM couplers and delay lines, which enabled perfect alignment of the interleaved timeslots and a homogeneous peak pulse power.

Operating conditions were strikingly similar to those mentioned in the previous section, except that CW probe power was increased to 15 dBm, which was the maximum power available after an EDFA, followed by ASE filtering and a polarization controller. The current through the conversion SOA (I_3) was 640 mA, and the total current consumption was just above 1 A.

Fig. 6.15 (a) shows a comparison of the back-to-back and wavelength converted eye diagrams, and Fig. 6.15 (b) shows the corresponding pulse patterns.

[3]Made available by PriTel, inc.

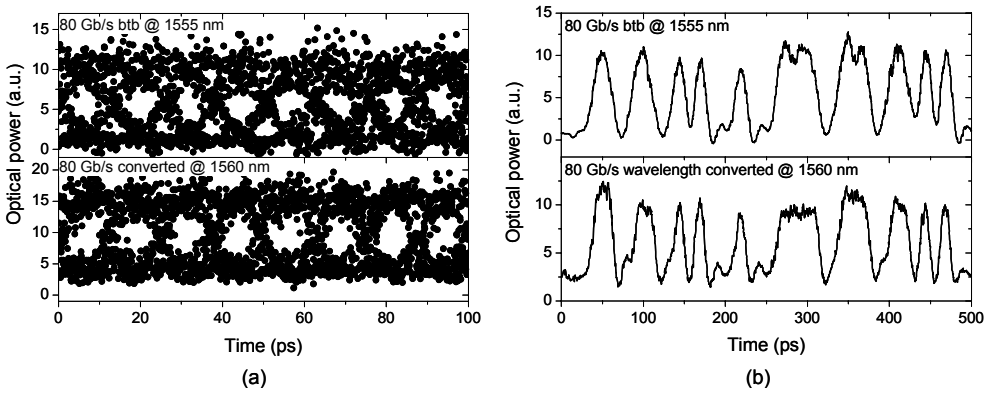

Figure 6.15: (a) Eye diagrams of 80 Gb/s back-to-back (1555 nm) and wavelength converted (1560 nm) signal. (b) Corresponding pulse patterns.

The bandwidth of the photo diode was 50 GHz, which is the reason the back-to-back signal appears to be of NRZ format. Focusing on the pulse patterns, the pulse width does not appear to have increased by the conversion process, which can be attributed to the pulse shaping effect of the BPF. However, by comparing the series of 4 marks around $t = 300$ ps, it appears that the photo diodes response to the back-to-back signal drops in-between two of the pulses, whereas the wavelength converted pulse trace maintains the mark level during the same series of pulses. Although this is not hard evidence, it appears as if the wavelength converted signal has also been format converted from RZ to NRZ. This was predicted in [p9] based on the response of the device from the same wafer.

Despite the fast response, the extinction ratio of the converted signal is only around 6 dB. The explanation for this is two-fold: as mentioned previously the output power is decreased when the filter is detuned away from the probe carrier, which causes a trade-off, since the filter detuning must be large enough that the StC ratio becomes sufficiently high to obtain an in-phase signal with a high ER. At 80 Gb/s, the phase modulation depth is clearly smaller than at 40 Gb/s, which gives rise to a smaller amount of power in the sidebands. This prompts a larger filter detuning in order to sufficiently suppress the carrier, which in turn causes a decrease of the probe power at the output of the filter. The NOLM demultiplexer represents a significant power loss for the probe, including 9 dB (a factor of 8) from the demultiplexing itself, 3 dB coupling loss, a loss from the fact that the control signal may not introduce a full π phase shift, and filter insertion losses. All in all, a significant loss, which must be compensated for by an EDFA before the NOLM. However, if the average input power to this EDFA is too low to fully saturate it, the EDFA emits so much ASE that it may be observed on a sampling oscilloscope as a significant increase of the baseline, corresponding to a reduction of the ER. Thus, if the phase modulation depth is not sufficiently high, compensating for the slow SOA response may not be sufficient to obtain a large ER.

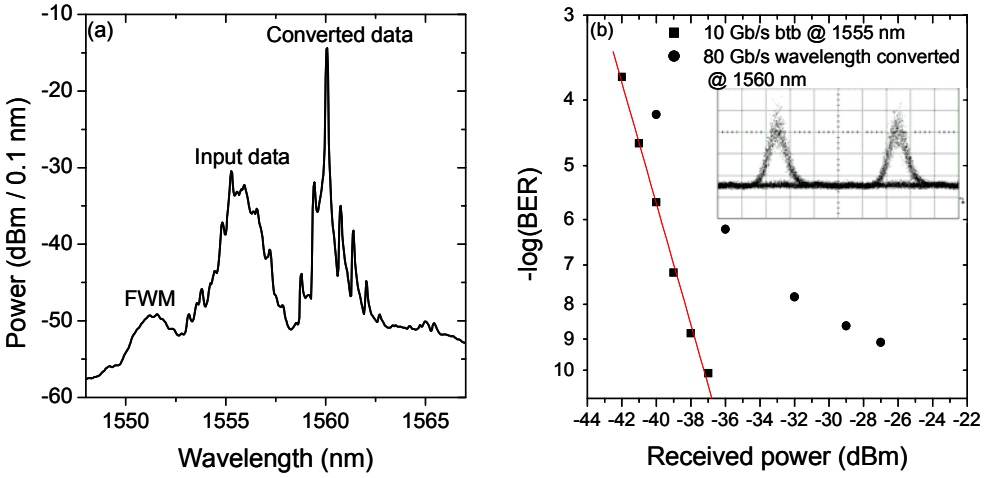

Figure 6.16: (a) Optical spectrum (res: 0.1 nm) of 80 Gb/s input and wavelength converted signals. (b) BER curves: 10 Gb/s back-to-back, and 80 Gb/s wavelength converted and demultiplexed. Inset shows demultiplexed 10 Gb/s eye diagram.

The total output spectrum is shown in Fig. 6.16 (a), and compared to Fig. 6.13 (b), it clearly observed that the smaller phase modulation leads to less spectral broadening. Unfortunately, the spectrum after the BPF was not recorded, but the detuning was ≈ -0.6 nm. The BER measurement in Fig. 6.16 (b) represents an arbitrary 10 Gb/s tributary of the wavelength converted signal. A clear error-floor is obtained at BER $\approx 10^{-10}$, and this is believed to be caused primarily by the low output power, which translates into a low ER of 6 dB after the EDFA. The inset in Fig. 6.16 (b) shows the demultiplexed 10 Gb/s eye diagram, which appears wide open. Notice however, that the zero-level offset is significant.

6.3 WDM → OTDM translator

As an illustration of the versatility of the all-active MZI wavelength converter, this section describes an experimental implementation of a $2x20$ Gb/s WDM to 40 Gb/s OTDM translator based on the device used in the 80 Gb/s experiment.

The function is shown schematically in Fig. 6.17 (a): N WDM channels centered at $\lambda_0 - \lambda_{N-1}$ containing RZ data at a (low) bitrate of B, are multiplexed and simultaneously wavelength converted to a common wavelength λ'. Applications for such a scheme could be aggregation of low-bitrate channels at the input of a high-capacity link, or simply an interface between a WDM network and an OTDM link. The wavelength conversion capability allows for adapting the wavelength to the link, which is a necessity if the link carries WDM data, in order to resolve contention. Moreover, multiplexing the WDM channels to one wavelength enables wavelength routing downstream. If the link only carries a single high-bitrate OTDM, wavelength conversion is still necessary, since a simple in-

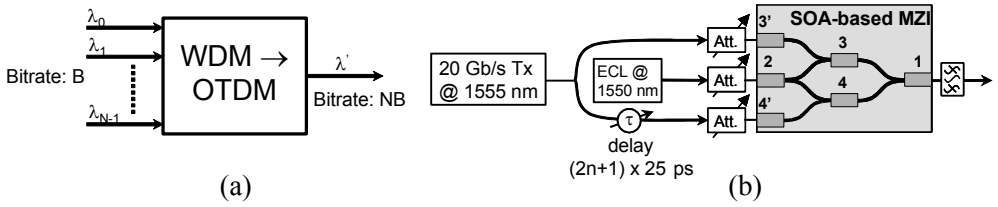

Figure 6.17: (a) Schematic of WDM-to-OTDM translator. (b) Sketch of implementation using all-active MZI.

terleaving of the N WDM channels would lead to a devastating pulse walk-off due to chromatic dispersion.

The experimental setup is identical to Fig. 6.11, except for the details illustrated in Fig. 6.17 (b). Since only a single short-pulse source was available at the time of the experiment, the two signals emulating the WDM channels are at the same wavelength of 1555 nm. This is of no importance for the proof of principle, since the peripheral SOAs may be biased to compensate for the slight wavelength dependence of the phase shift, if the signals are at different wavelengths. Before the two data signals are launched into ports $3'$ and $4'$, one of the signals is delayed an odd number of 40 Gb/s timeslots, i.e. $(2n+1)\cdot 25$ ps, in order to multiplex the two 20 Gb/s signals into a 40 Gb/s OTDM signal upon wavelength conversion. At the output of the MZI the probe at 1550 nm is selected by the 0.3 nm wide BPF, which is detuned by -0.58 nm to shape the waveform, before being observed on a 40 GHz sampling oscilloscope, and demultiplexed in the NOLM using a 10 GHz clock from the data pulse source at 1555 nm.

In a previous experiment [144], $2x10$ Gb/s WDM channels (at different wavelengths) were multiplexed in a passive fiber-based interleaver, and subsequently wavelength converted to 20 Gb/s using an all-active MZI in standard-mode of operation. The approach in [144] could potentially be combined with the scheme suggested here to allow for a larger number of channels to be multiplexed and simultaneously wavelength converted. The only restriction is that channels at the same wavelength must be launched into separate input ports to prevent interference problems.

Fig. 6.18 (a) shows the results in terms of output pulse patterns: the upper and middle traces show the converted 20 Gb/s pattern for input $4'$ and input $3'$ turned off, respectively. They represent the standard-mode wavelength converted signal using the upper and lower arm, respectively. By turning both input signals on, the two 20 Gb/s input signals are OTD multiplexed, or logic OR'ed, while wavelength converted to 1550 nm. The 40 Gb/s pattern is shown in the bottom row of Fig. 6.18 (a), and the corresponding eye diagram is depicted in Fig. 6.18 (b).

This mode of operation is more challenging for the MZI than standard-mode wavelength conversion, because some of the pulse energy may be used to cancel the phase response in the other arm, thus leaving less energy for switching. This

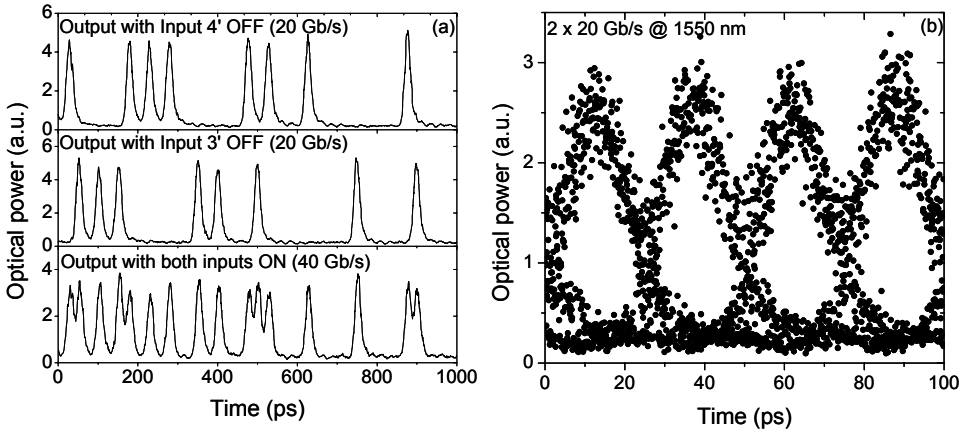

Figure 6.18: (a) Wavelength converted 20 Gb/s signals obtained with input $4'$ off (upper), and input $3'$ off (middle). Multiplexed $2x20$ Gb/s output obtained with inputs turned on. (b) Eye diagram of $2x20$ Gb/s signal.

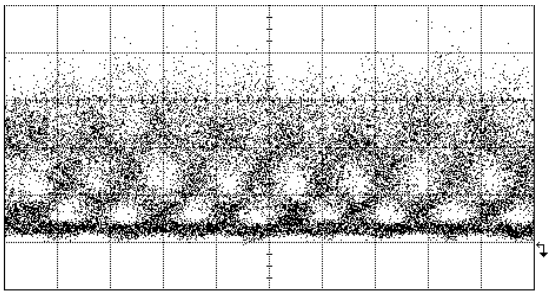

Figure 6.19: Eye diagram of $2x40$ Gb/s $\rightarrow$ 80 Gb/s multiplexing.

is only a problem when a pulse in one arm, say the upper, is immediately followed by a pulse in the lower arm. Consequently the choice of input power to a specific arm becomes a trade-off: if the pulse energy is too small the converted pulses cannot maintain the amplitude when some of the energy goes into canceling the response of a pulse in the other arm. On the other hand, if the pulse energy is too high, the amplitude of the converted pulses from this input will "overshoot" in cases where a pulse does not follow a pulse in the other arm, and all the energy goes into opening the switching window. It should be mentioned that the partial canceling of the phase response is not evident from the pulse pattern in Fig. 6.18 (a, bottom), but this is because the phase of the probe in one arm has almost completely recovered before the pulse arrives in the other arm. However, a short dip in the waveform would be expected in the transition between two immediately following excitations of the two interferometer arms. This may not be resolved, however, in a detector bandwidth of 40 GHz.

Fig. 6.19 shows an attempt at increasing the bitrate of the individual WDM channels from 20 to 40 Gb/s. The eye diagram is very noisy and distorted,

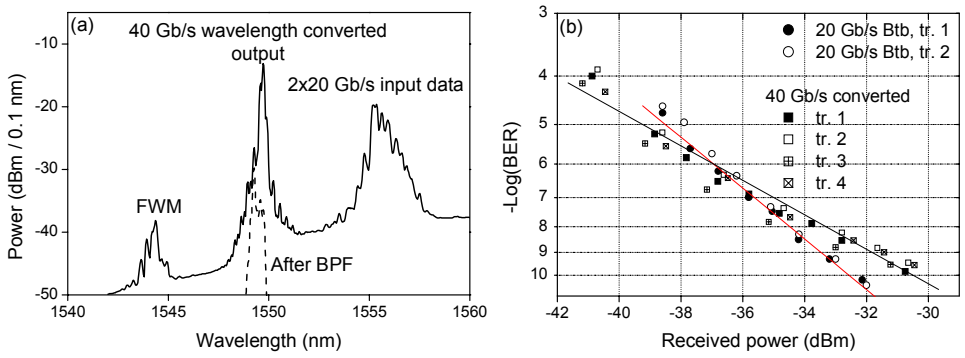

Figure 6.20: (a) Optical spectrum at output of MZI (solid) and after BPF (dashed). (b) BER curves: Back-to-back (circles), Wavelength converted and demultiplexed (squares).

which, by comparison to Fig. 6.15 (a, bottom), clearly illustrates the point that this mode of operation is more challenging than standard-mode conversion.

The best performance was obtained for very symmetrical input powers and bias currents: $P_{C,3}/P_{C,4}/P_P/I_1/I_2/I_{3'}/I_{4'}/I_3/I_4 = 6.6$ dBm/6.3 dBm/16 dBm/120 mA/220 mA/40 mA/60 mA/520 mA/520 mA, where $P_{C,3}$ and $P_{C,4}$ represent the average data signal power to the upper and lower arms, respectively. The high P_P is due to an excessive coupling loss at the coupler following the probe input.

The total output spectrum is shown in Fig. 6.20 (a), revealing an OSNR of around 29 dB/0.1 nm before filtering. As usual the output power is reduced by the filter detuning, to about -20 dBm measured in a large optical bandwidth. Fig. 6.20 (b) shows the BER curves of the two 10 Gb/s tributaries of the 20 Gb/s data signal, as well as the 4 tributaries of the multiplexed and wavelength converted 40 Gb/s signal. As observed, the latter suffers a power penalty on the order of $1.5 - 2$ dB.

6.4 Dual-Order MOde (DOMO) wavelength converter

In all the wavelength converter demonstrations of this chapter the data and probe signals have co-propagated, i.e. propagated in the same direction, through the converter. Since the wavelength converted probe as well as the amplified input data signal exit through the same waveguide, the two signals must have different wavelengths to allow discrimination by an optical filter. If wavelength *conversion* is desired this is not a problem, except that the output filter needs to be tuned whenever the probe (target) wavelength is changed. However, wavelength conversion may not be required for all WDM channels arriving at a wavelength converter array, and in order to fulfill the $\lambda_{out} \neq \lambda_{in}$ requirement, additional wavelengths must be allocated to maintain the same total throughput. Employing a dual-stage wavelength converter solves the problem at the expense of the additional hardware, which has been demonstrated at 20 Gb/s [145] and 40 Gb/s [39]. Al-

ternatively, the data and probe signals may counter-propagate through the wavelength converter, in which case the maximum bitrate is limited by the transit time of the SOA, as illustrated in Chapter 4.

A new type of MZI switch, the DOMO-MZI, where the data and probe signals co-propagate in different transverse optical modes was proposed by Leuthold et al. in 1996 [146], and demonstrated at 2.5 Gb/s in [147], 10 Gb/s [148], and 20 Gb/s [149]. The main difference between a conventional MZI and the DOMO-MZI is the use of specially designed Multi-Mode Interference (MMI) couplers, capable of creating an antisymmetric first-order mode from a symmetric fundamental mode at the input of the MZI, and physically separate the modes again at the output. In this section, the DOMO wavelength converter is investigated numerically at 10 Gb/s using the 2D FD-BPM model presented in section 3.2. In particular, a cross-talk mechanism is identified for small wavelength detunings between the data and probe signals.

The results and discussions presented here are in part based on [150] and [p11].

6.4.1 Principle of operation

The principle of operation may be explained from the schematic of the DOMO-MZI in Fig. 6.21 (a), operated in the standard-mode. The data and probe signals are launched into different ports of the mode-converter combiner MMI in the upper arm as fundamental modes, and the data signal is converted into the first-order eigenmode of the dual-moded (DOMO) SOA, whereas the probe remains a fundamental mode. The two signals co-propagate through the DOMO-SOA as orthogonal modes, and the data signal modulates the gain and phase of the probe, as in a conventional single-mode MZI. At the output of the SOA, the signals enter the mode-filter, which maps the fundamental mode to the center of the output facet, while mapping the first-order mode to the edges, where the it is guided into absorbing waveguides to minimize reflections. The probe signal, carried by the fundamental mode, merges with the probe from the lower arm, and interference takes place.

Time domain simulations of multimode devices are very time consuming [151], and a simulation of the full DOMO-MZI wavelength converter is not realistic. A clear delimitation of the device is necessary to keep the computation time down. As pointed out already, the novelty of the device lies in the use of the MMI couplers and the DOMO-SOA. For this reason it has been chosen to restrict the attention to the subsystem consisting of these three parts, also indicated by the dashed box in Fig. 6.21 (a). The considered subsystem is shown in more detail in Fig. 6.21 (b), including the outline of the MMI couplers.

The principle of the mode-converter combiner MMI is illustrated in the calculated field intensity plots in Fig. 6.22, which shows how the input field of the data signal is converted into the first-order mode of the DOMO-SOA (b), while

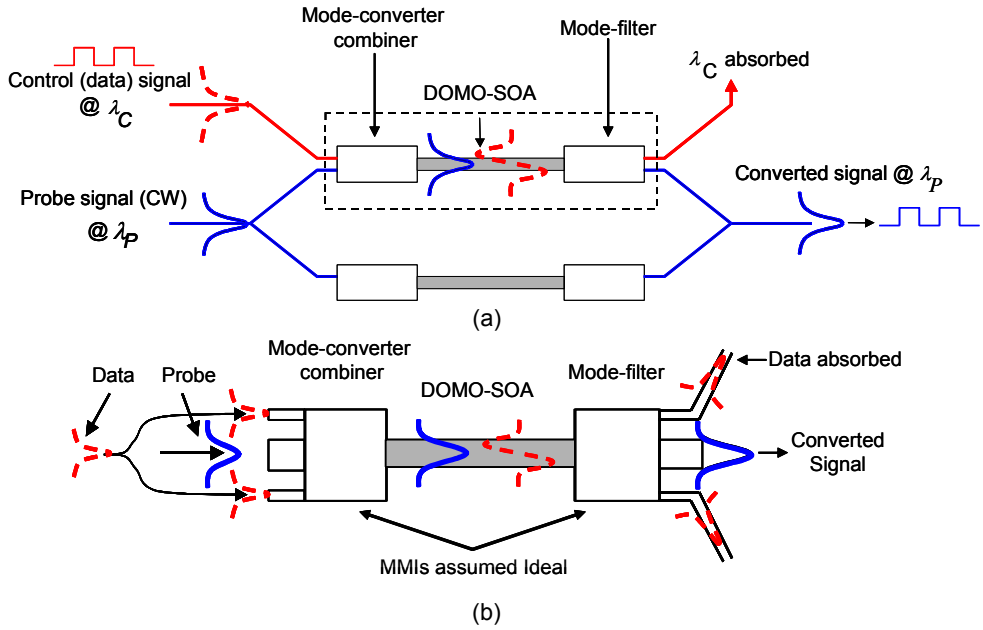

Figure 6.21: (a) Schematic of DOMO-MZI, including mode-converter combiners and mode-filters. The contents of the dashed box is detailed in (b). The figure is not to scale, as the DOMO-SOAs are much longer longer than the MMIs.

the fundamental mode passed right through the MMI (a). The plots are obtained for a passive MMI of width 9.6 μm, height 0.350 μm, length 236.8 μm, and index step 0.14. As also illustrated in Fig. 6.21 (b), the data signal is split in two and launched symmetrically into the mode-converter combiner MMI at the edges, with a π phase shift between them (not shown in Fig. 6.21 (b)). Each of the two input fields excite the eigenmodes supported by the MMI.

The eigenmodes have different propagation constants, and thus travel at slightly different speeds, which causes the modes to interfere constructively in some parts of the MMI, and destructively in others. An interesting consequence of this behavior is the waveguide's ability to reproduce single or multiple replicas, *self-images*, of the input field periodically along the propagation direction of the waveguide [152, 153]. In this case, each of the two input fields produces four self-images at the output, where two of them are right next to each other in the middle of the waveguide with a phase difference of π between them - characteristic of an antisymmetric first-order mode - and the remaining two images are at the edges. Adding the fields from both data signal inputs, the images at the edges interfere destructively and vanish, whereas the images in the center add constructively.

This is clearly observed in Fig. 6.22 (b). The probe signal is launched into the center of the mode-converter combiner as a fundamental mode of the DOMO-SOA, which may be obtained by adiabatically up-tapering the field from a single-

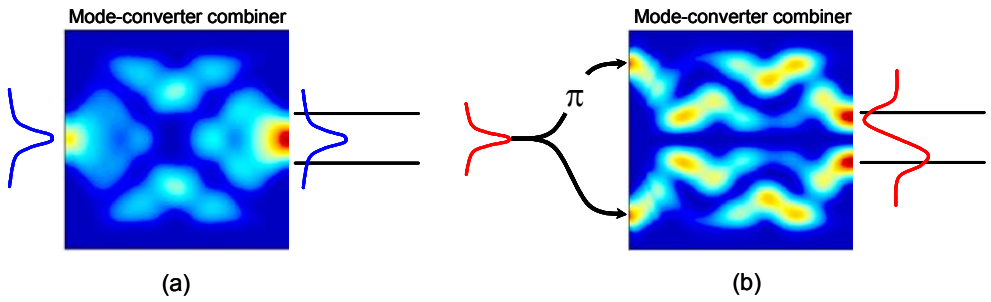

Figure 6.22: Field intensity patterns inside mode-converter combiner MMI. (a) and (b) show mode-combination and mode-conversion, respectively.

mode waveguide. Fig. 6.22 (a) shows the field intensity pattern of the probe as it travels through the MMI, and produces a self-image at the output. This implementation of the mode-converter combiner converts a fundamental mode into a first-order mode and maps a fundamental mode to itself with 100% efficiency, i.e. without loss of power. Notice that this is not the case in a traditional MZI design, where 50 % of the power is radiated out of the coupler when the two single-mode waveguides are merged into one.

The operation of the mode-filter is easily understood by considering Fig. 6.22 and interchanging the input and output: the symmetric, fundamental mode is mapped to itself in the middle of the waveguide, whereas the antisymmetric first-order mode maps to the edges of the MMI, where the images are absorbed in unpumped waveguides. A detailed review of mode-converter combiners, including the design used here, is given in [154].

6.4.2 Optimization of DOMO waveguide

As shown in section 4.1 the small-signal modulation bandwidth scales with $A_{opt}^{-1} = \Gamma/(HW)$, and the same dependence has been shown to apply to large-signal modulation [66]. For single-mode SOAs both signals propagate in the same mode, and the problem is reduced to finding the combination of H and W that minimizes A_{opt}. For dual-moded SOAs the two modes have different confinement factors, and there are two possibilities: the waveguide dimensions can be optimized to obtain the minimum A_{opt} for either the fundamental (zero-order) or first-order mode. Using the EIM the confinement factor has been calculated on a dense (W, H) grid requiring that $W > H$, and that the waveguide supports either one or two transverse modes.

Fig. 6.23 shows 2D surface plots of A_{opt} on a (W, H) grid for index contrasts $\Delta n = n_{core} - 3.17$ of 0.1, 0.2, and 0.3. In the upper row (a), the waveguide is required to be single-moded, and in the second and third row, (b) and (c), the waveguide is required to be dual-moded, and the 2D plots illustrate A_{opt} for the zero-order and first-order modes, respectively. The brighter the color

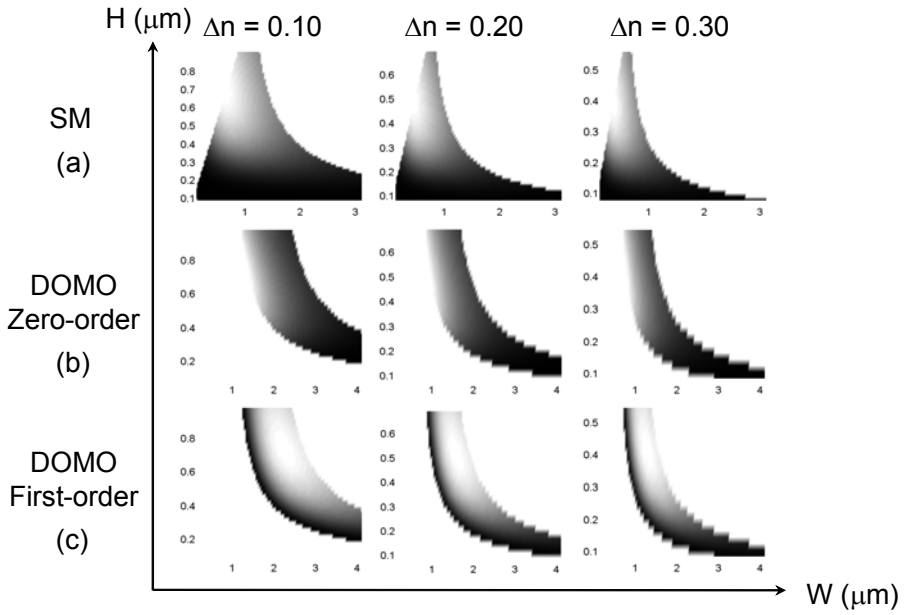

Figure 6.23: Two-dimensional surface plots of the optical area A_{opt} vs. (W, H) for $\Delta n = 0.1$ (left coloumn), $\Delta n = 0.2$ (middle coloumn), $\Delta n = 0.3$ (right coloumn). The first row corresponds to a single-mode waveguide, whereas the second and third rows show A_{opt} for the zero- and first-order modes of the DOMO waveguide,

in Fig. 6.23, the smaller the value of A_{opt}. When Δn is increased, a specific confinement factor Γ is obtained for a combination of W and H corresponding to a lower cross-section area WH. Thus, in all three cases in Fig. 6.23, an increase of Δn moves the position of the minimum closer to origo. Notice that A_{opt} for the fundamental mode of the DOMO waveguide attains its minimum on the left boundary of the dual-mode area, whereas the minimum occurs closer to the right boundary for the first-order mode. This is because the difference in confinement of the fundamental mode only changes slightly from one boundary to the other, whereas the first-order mode is significantly better confined on the right boundary.

In Fig. 6.24 (a) the minimum optical area is shown as a function of Δn for a single-mode waveguide (SM), and the fundamental mode (DM-0) and first-order mode (DM-1) of a dual-moded waveguide, optimized for both modes, as explained above. Optimizing for a minimum A_{opt} for the fundamental DOMO waveguide mode leads to a combination of W and H on the left boundary of the dual-mode area in Fig. 6.23 (b), where the first-order mode is poorly confined, thus causing a very large A_{opt} as illustrated in Fig. 6.24 (a). Alternatively, if the DOMO waveguide is optimized for the first-order mode, the corresponding A_{opt} is reduced by a factor of ≈ 10, while A_{opt} for the fundamental mode only increases slightly. In the following, this mode of optimization is used exclusively.

Notice that even though the dimensions of the DOMO waveguide are carefully optimized, the optical area for the single-mode waveguide is smaller, regardless of

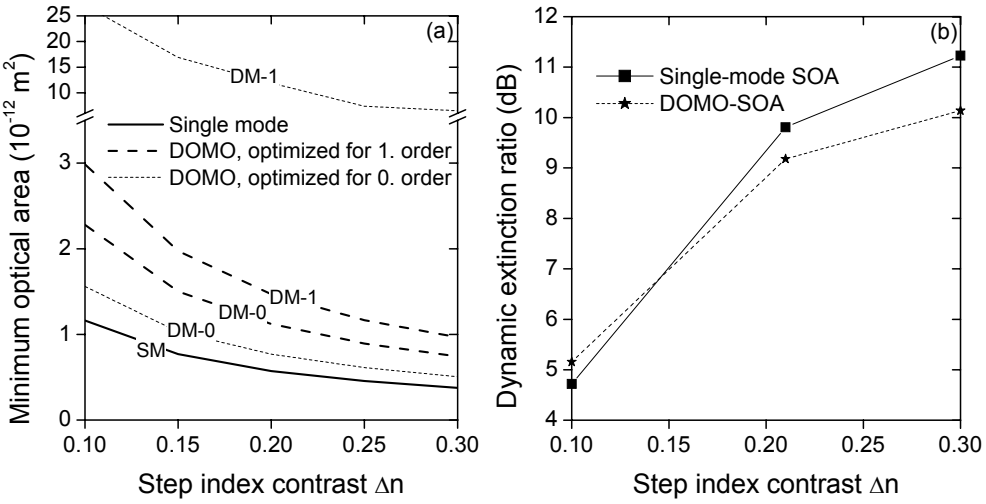

Figure 6.24: (a) Minimum optical area for single-mode waveguide (solid), DOMO waveguide optimized for zero-order mode (dotted), and DOMO optimized for first-order mode (dashed) vs. index contrast. (b) Extinction ratio (XGM) vs. index contrast for single-mode SOA (solid), adn DOMO-SOA, optimized for first-order mode

the index contrast, due to the smaller cross-section. As a result, the DOMO-SOA is expected to have a slower response than a single-mode SOA for the same index step.

This has been investigated by calculating the extinction ratio of the cross-gain modulated probe for both a single-mode and DOMO-SOA. The input data signal is a 10 Gb/s PRBS of word length $2^4 - 1$ consisting of 20 ps wide Gaussian pulses with an ER of 13 dB. In each calculation, the wavelength detuning is assumed high enough to prevent beating between the CW signal and the data signal, while the MMIs are assumed to be ideal (see below). The SOA is 1500 μm long, the linewidth enhancement factor α is 5.0, the diffusion coefficient is $D_x = 10\ \mathrm{cm}^2 s^{-1}$, the current density is $J = 30\ \mathrm{kA/cm}^2$, and the data and probe input powers are 13 dBm and -5 dBm, respectively. All other simulation parameters are given in Appendix D.

The long computation time prevents an optimization of the input powers, and thus the powers have been chosen somewhat arbitrarily. This is not expected to influence the conclusions of this section qualitatively, but as it will be discussed later, the ratio of data to probe power is expected to significantly impact the amount of cross-talk added to the wavelength converted probe signal.

Fig. 6.24 (b) shows the comparison of ER vs. Δn for the single-mode and DOMO-SOAs. For low index steps the DOMO-SOA gives a higher ER than the SM-SOA due to a higher gain, which according to (4.25) also increases the modulation bandwidth. However, as the index step is increased, the advantage of the lower A_{opt} of the SM-SOA dominates. Another advantage of the single-mode SOA is that the mode-overlap between the data-signal and CW-probe is

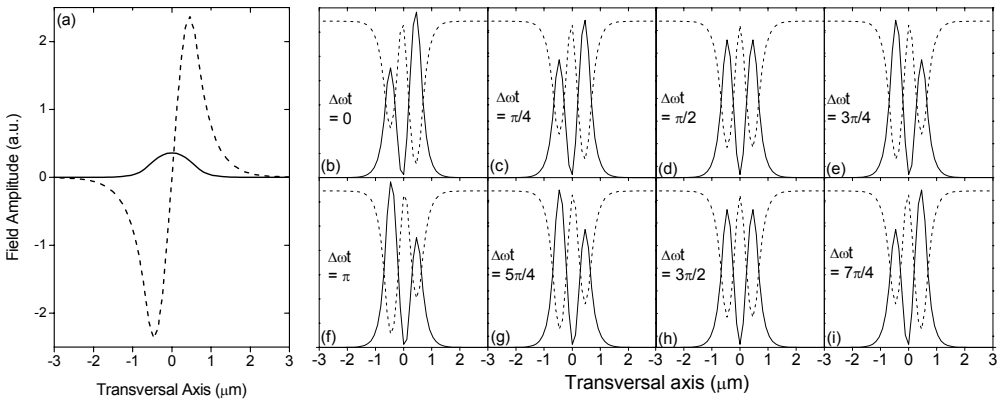

Figure 6.25: (a) Zero- and first order transverse modes of DOMO waveguide with power ratio of 18 dB. (b-i) Total transversal field intensity (solid), and corresponding carrier density profile for $\Delta\omega t = 0$ to $\Delta\omega t = 7\pi/4$, in steps of $\pi/4$.

larger than for the DOMO-SOA. Thus, a 3 dB reduction of the probe gain may be obtained with less data signal power if both signals propagate in the fundamental mode.

6.4.3 Cross-talk mechanism

For a step index contrast of $\Delta n = 0.3$, the minimum optical area for the first-order mode is obtained for $(W, H) = (1.3, 0.39)\ \mu m$. Fig. 6.25 (a) shows the two transversal eigenmodes, $\psi_0(x)$ and $\psi_1(x)$, of the waveguide for a power ratio $\int |\psi_0|^2\, dx / \int |\psi_1|^2\, dx$ of -18 dB. The two modes are assumed to carry light beams of angular frequency ω_0 and ω_1, with a difference defined as $\Delta\omega = \omega_1 - \omega_0$. As explained in section 3.2, and shown specifically in eq. (3.77), the total field intensity governs the transversal carrier density profile.

Fig. 6.25 (b-i) shows the total field intensity profile $|\psi_0(x) + \psi_1(x)|^2$ (solid curves) and the corresponding calculated carrier density profile (dashed curves) at a specific cross-section $z = z'$ in the DOMO-SOA at eight different times, spaced by $T/8$, where T is the beating period $T = 2\pi/\Delta\omega$ between the two modes. The plots are obtained by solving (3.77) in the static limit ($\partial/\partial t = 0$) with $D_x = 0$, and thus correspond to a beating period large enough that the carrier density is able to follow the variation of the total field intensity.

As illustrated in Fig. 6.25, the total field intensity, and consequently the carrier density, oscillates between two asymmetric distributions, corresponding to (b) and (f), with the total period T. If T is smaller than the effective carrier lifetime in the considered cross-section z' the carrier density will not be able to follow the intensity variations, and will instead experience the average intensity distribution, which is symmetric, and according to (3.78) simply given by $|\psi_0(x)|^2 + |\psi_1(x)|^2$. Fig. 6.26 (a) and (b) show surface plots of the carrier density distribution in the (x, z) plane for $T \to \infty$ and $T = 0$, respectively, correspond-

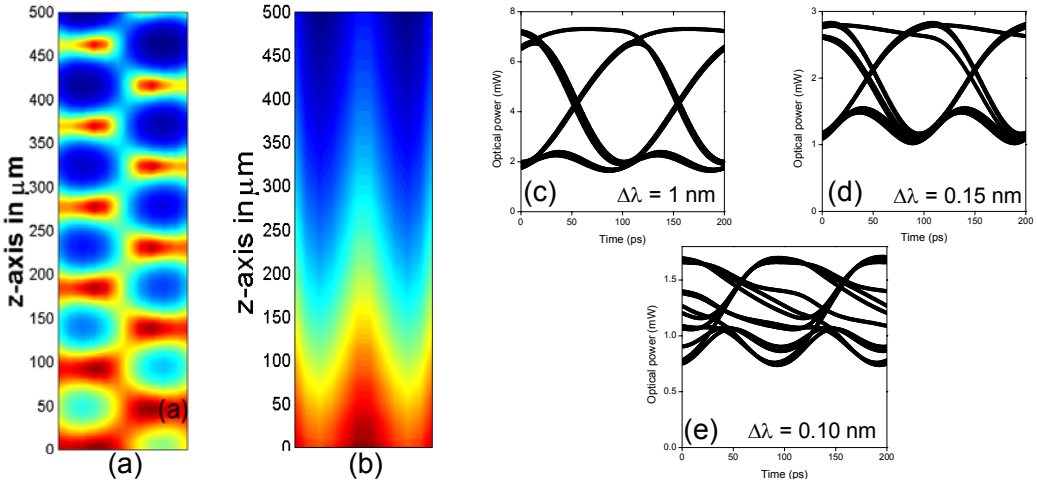

Figure 6.26: Propagation of total field intensity pattern through DOMO-SOA for (a) $\Delta\lambda = 0$ nm and (b) $\Delta\lambda >> \Delta\lambda_{crit}$. Eye diagrams of wavelength converted signal for (c) $\Delta\lambda = 1$ nm, (d) $\Delta\lambda = 0.15$ nm, and (e) $\Delta\lambda = 0.10$ nm. $L_{DOMO} = 1$ mm, $D_x = 10$ cm$^2 s^{-1}$.

ing to $\Delta\omega = 0$ and $\Delta\omega \to \infty$. For $\Delta\omega = 0$ there is no temporal mode beating, cf. Fig. 6.25, but the static, asymmetric input field distribution is reproduced periodically through the DOMO-SOA according to the self-imaging principle explained above, while being amplified due to stimulated emission. This gives rise to the increasingly deep spatial holes in the carrier density distribution, illustrated in Fig. 6.26 (a). For $\Delta\omega \to 0$, however, the carrier density distribution remains symmetric, since the mode beating occurs on a time scale too short for the carrier density to follow. In between the two extremes, the 2D carrier density plots are time dependent and cannot be illustrated by a "static" plot, but at a particular time the distribution will look similar to Fig. 6.26 (a), except that the spatial holes will become increasingly shallow as $\Delta\omega$ is increased.

An important consequence of the asymmetric carrier density distribution is that the symmetry of the data and probe signals, launched into the DOMO-SOA as perfect zero and first-order eigenmodes, is perturbed. At the output of the DOMO-SOA, the signal injected as an odd first-order mode will have acquired an even component and vice versa, because the modes have been perturbed by an asymmetric gain distribution. In the mode-filter this asymmetry is converted into cross-talk because the contents of the data field distribution with an even symmetry will be guided to the center waveguide along with the wavelength converted probe.

Since the beating period, T, is related to the wavelength detuning, $\Delta\lambda$, between the two modes as

$$T = \frac{\lambda^2}{c_0 \Delta\lambda} \tag{6.1}$$

a critical wavelength detuning, $\Delta\lambda_{crit}$, below which the transversal gain distribution becomes asymmetric, and the cross-talk mechanism sets in, can be intro-

duced as

$$\Delta\lambda_{crit} = \frac{\lambda^2}{c_0 \tau_{eff}(L)} \tag{6.2}$$

Here, $\tau_{eff}(L)$ represents the shortest effective carrier lifetime in the DOMO-SOA, which is obtained at the output facet.

Fig. 6.26 (c), (d), and (e) show calculated eye diagrams of the XGM'ed probe signal for wavelength detunings of 1 nm, 0.15 nm, and 0.1 nm, respectively, and the detrimental effect of the cross-talk mechanism is clearly observed. These results are obtained with a DOMO-SOA length of $L_{DOMO} = 1000\ \mu m$, a diffusion coefficient of $D_x = 10\ \mathrm{cm}^2 s^{-1}$, and a current density of $J = 30\ \mathrm{kA/cm}^2$. From the eye diagrams the critical detuning is estimated to be around 0.15 nm. The mode-filter is assumed to be ideal, which means it may be replaced by the following overlap integral

$$P_{zero}(t) = \frac{\left| \int E_{tot}(x, z = L, t) \psi_0^*(x) dx \right|^2}{\int |\psi_0(x)|^2 \, dx} \tag{6.3}$$

where $P_{zero}(t)$ is the power of the zero-order content of the total field $E_{tot}(x, z, t)$ at the output of the DOMO-SOA, which is exactly what the mode-filter produces. Analogously, the mode-converter combiner is also assumed ideal, and the data and probe signals are launched into the DOMO-SOA as perfect eigenmodes.

In the following the dependence of the performance, in terms of extinction ratio power penalty, on the wavelength detuning, DOMO-SOA length, and diffusion coefficient is investigated. The ER power penalty, pen_{ER}, is the power penalty suffered from a reduction of the ER in the absence of ASE, and may be expressed as [106]

$$pen_{ER} = \frac{ER + 1}{ER - 1} \frac{ER_{btb} - 1}{ER_{btb} + 1} \tag{6.4}$$

where ER_{btb} is the extinction ratio of the back-to-back signal, in this case 13 dB. In all the comparisons in the following, the average data and probe input powers are 13 dBm and -5 dBm, respectively, and the current density is 30 $\mathrm{kA/cm}^2$.

Fig. 6.27 (a) shows pen_{ER} vs. $\Delta\lambda$ for a 500 μm long DOMO-SOA with a diffusion coefficient of 10 $\mathrm{cm}^2\mathrm{s}^{-1}$. As expected the penalty increases dramatically as $\Delta\lambda$ drops below a critical detuning. On the right axis of Fig. 6.27 (a) the beating period T (6.1) is plotted as a function of $\Delta\lambda$. The effective carrier lifetime at the output has been calculated to $\tau_{eff}(L) = 81$ ps, based on the carrier and photon densities, and according to (6.2) this corresponds to a critical detuning of $\Delta\lambda_{crit} \approx 0.1$ nm. Indeed, the power penalty starts to increase for a wavelength detuning below approximately 0.1 nm, which verifies (6.2).

Fig. 6.27 (b) shows pen_{ER} vs. the DOMO-SOA length for a wavelength detuning $\Delta\lambda$ of 0.1 nm, 0.2 nm, and 1.0 nm. The effective carrier lifetime drops as the device length is increased, and this has two opposite effects on the performance: the faster gain recovery leads to an improvement of the ER, but at the same time it increases the critical wavelength detuning. As illustrated in

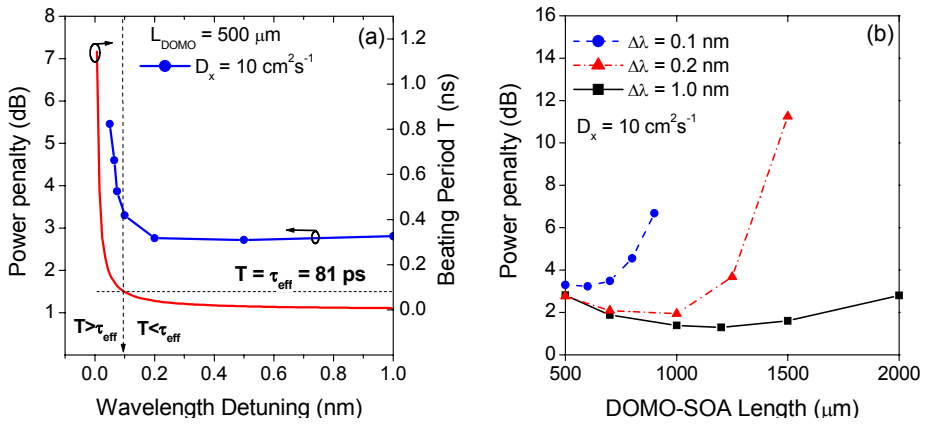

Figure 6.27: (a) Power penalty (left axis) and Beating period (right axis) vs. wavelength detuning between data and probe signals. (b) Power penalty vs. SOA length for $D_x = 10$ cm^{2}s^{-1} with $\Delta\lambda$ as a parameter.

Fig. 6.27 (b) this leads to an optimum device length, which is very dependent on the wavelength detuning. The penalty starts to increase when the reduction of the carrier lifetime makes $\Delta\lambda_{crit}$ comparable to $\Delta\lambda$. Consequently, the optimum length will be small for small detunings, and larger for larger detunings. Fig. 6.27 (b) also verifies that the critical detuning for $L_{DOMO} = 1000$ μm is between 0.1 nm and 0.2 nm, as estimated above from the appearance of the eye diagrams in Fig. 6.26.

The dependence on the diffusion coefficient is investigated in Fig. 6.28 (a) for a fixed wavelength detuning of $\Delta\lambda = 0.1$ nm. The plot shows pen_{ER} vs. L_{DOMO} for $D_x = 0, 10$, and 20 cm$^2s^{-1}$, and the trend is clear: the larger the diffusion, the smaller the cross-talk penalty. The physical explanation for this is that diffusion has an averaging effect on the carrier density distribution, which reduces the asymmetry and thus the perturbation of the mode symmetries. Fig. 6.28 (b) shows pen_{ER} vs. $\Delta\lambda$ for a fixed device length of $L_{DOMO} = 500$ μm, again with D_x as a parameter. Notice that $\Delta\lambda_{crit}$, measured as the onset of the cross-talk penalty, is unaffected by diffusion, but that the quantitative impact is reduced. ASE is not included in the simulations, but it is expected to have an influence similar to diffusion, since more/less ASE will be generated where the carrier density is high/low, which will also have an averaging effect on the carrier density distribution.

In the simulations presented here the average data input power is 18 dB higher than the average probe power, and as mentioned earlier, this is somewhat arbitrary and is clearly subject to optimization. As explained in Chapter 5, the gain recovery rate will benefit from a higher probe power, which will enable operation at higher bitrates. Moreover, for the DOMO wavelength converter an increase of the input probe power relative to the data power also has the effect of reducing the cross-talk power, since a lower data power obviously reduces

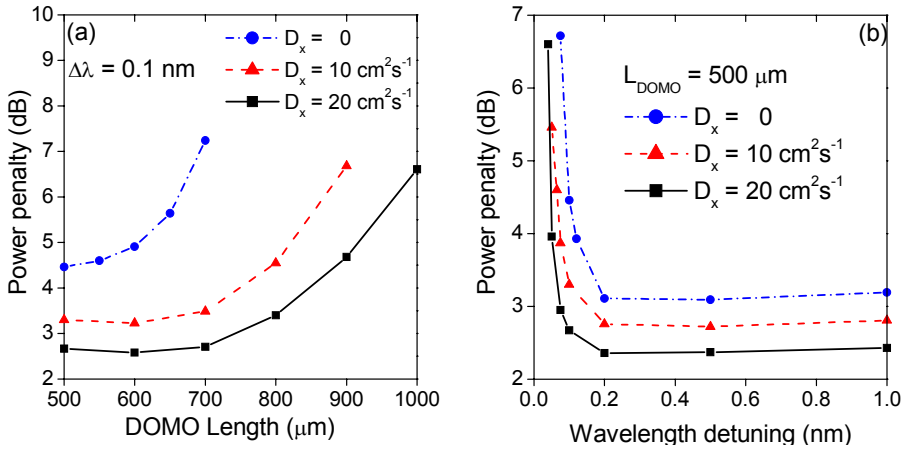

Figure 6.28: (a) Power penalty vs. DOMO-SOA length for $\Delta\lambda = 0.1$ nm and with the diffusion coefficient as a parameter. (b) Power penalty vs. wavelength detuning for $L_{DOMO} = 500\ \mu m$ and with the diffusion coefficient as a parameter.

the power converted into cross-talk. Thus, for a specific wavelength detuning, a reduced data-to-probe power ratio is expected to reduce the cross-talk power penalty.

A lower data signal power is generally needed to switch an interferometric wavelength converter compared to converters based on XGM, and so the cross-talk problem may be even less significant in a DOMO-MZI converter. In [151] it is demonstrated experimentally that if a DOMO-MZI is optimized for $\Delta\lambda = 0.1$ nm, setting $\Delta\lambda = 0$ almost completely closes the eye diagram. However, by reducing the average data power, the eye diagram re-opens at the expense of a reduced ER. The fact that the eye diagram changes from being open for $\Delta\lambda = 0.1$ nm (12.5 GHz) to being closed for $\Delta\lambda = 0$ is in [151] attributed to interferometric cross-talk in the photodiode. However, since the bandwidth of the employed photodiode is 30 GHz, interferometric cross-talk should have had an effect for $\Delta\lambda = 0.1$ nm as well. Based on the simulations presented in this section, it is believed that the dramatic performance degradation from $\Delta\lambda = 0.1$ nm to $\Delta\lambda = 0$ observed in [151] is instead caused by the hole–burning induced cross-talk mechanism introduced here.

The assumptions of ideal MMIs are not necessary, but are made to save CPU time. Simulations of the entire wavelength converter in Fig. 6.21 (b), including both MMI couplers, have been carried out, and the difference between assuming ideal MMIs, or simply passive MMIs, is very small. If the MMIs are active, the problem with asymmetric hole-burning also exists here for small wavelength detunings. However, this problem can be avoided by biasing the MMIs at 'transparency', since this will keep the carrier density approximately fixed. This correponds to making the MMIs passive. Another mechanism degrading the performance of active MMIs is the dependence of the refractive index on

carrier density, which changes with bias current and optical power level. Index changes cause the output images of the MMIs to shift slightly along the propagation direction, thereby moving them away from the output facet. This results in a de-focusing of the output fields, which manifests itself as a source of cross-talk in the mode-filter MMI [150]. This cross-talk contribution will exist independently of the wavelength detuning.

6.5 Summary

Wavelength conversion at high bitrates, using different SOA-based devices and technologies has been demonstrated experimentally and through simulations.

A simple converter based on a single SOA and a commercially available band-pass filter (BPF) was demonstrated at 40 Gb/s with only 3 fJ of data pulse energy. The experiments verify the theoretical predictions made in Chapter 5, based entirely on a small-signal analysis. Moreover, excellent agreement with the large-signal modeling tool is demonstrated. The performance of the scheme is limited by the low output power following from the filter detuning, which gives rise to a low OSNR. This problem can be addressed by optimizing the filter shape to a larger phase modulation, which provides a higher output power.

An active-passive and an all-active MZI, both operated in the standard-mode, were demonstrated at 40 Gb/s with good results in terms of fast response and large tunability. In the experiment with the all-active MZI a narrow BPF was detuned slightly towards the blue-side of the spectrum, thereby enhancing the response. The result is a very fast, pattern-effect-free response that should be fast enough for 80 Gb/s. The latter was verified, but a BER-floor at 10^{-9} was encountered due to a low extinction ratio.

The all-active MZI was also used to demonstrate $2x20$ Gb/s to 40 Gb/s WDM-to-OTDM translation and multiplexing, by delaying two 20 Gb/s data signals by one 40 Gb/s timeslot before launching them into separate interferometer arms. This is a more demanding process than standard-mode operation, and thus $2x40$ Gb/s to 80 Gb/s was not possible.

Finally, the dual-mode (DOMO) wavelength converter was investigated numerically with a 2D FD-BPM model. The waveguide dimensions were carefully optimized for high speed, but due to the inherently larger cross-section area of a dual-mode waveguide the DOMO wavelength converter is found to be slightly inferior compared to the single-mode SOA. For small wavelength detunings between the data and probe signals a mode-beating induced cross-talk mechanism has been identified, and this mechanism is able to explain previously published experimental results. Transverse carrier diffusion is found to reduce the cross-talk by averaging out asymmetries in the carrier distribution.

Chapter 7

All-Optical Regeneration

In recent years, a lot of effort has been devoted to developing all-optical solutions to regeneration, since the alternative, detecting the optical signal, regenerating it electronically, and using this signal to modulate a new optical carrier, may not be a viable solution in a future scenario with line rates exceeding 40 Gb/s and an increasing WDM channel count. However, advances in high speed electronics, such as the Decision Flip-Flop (DFF), seem to have closed the gap between optical and optoelectronic approaches at bitrates up to 40 Gb/s.

In a recent recirculating loop demonstration, an optical 40 Gb/s NRZ signal was regenerated optoelectronically 1000 times, each time followed by two 40 km spans of DSF [36]. The optoelectronic 3R regenerator was described in section 2.2, and compared to the most recent all-optical 3R regenerators implemented using SOA-based MZIs [39, 40], the tolerance towards noise is inferior after the first laps. An input OSNR of ≈ 29 dB/0.1 nm is needed to obtain a BER of 10^{-9} after the first lap, which may be accomplished with only 24.5 dB/0.1 nm with the all-optical implementation. The BER increases with each lap, primarily due to the ASE added to the signal by the EDFAs in the fiber loop, but also as a consequence of the noise added by the regenerator itself.

The main figure of merit of a regenerator is the nonlinearity of the decision gate transfer function, which determines the rate at which the BER increases with the number of concatenated regenerators, or in this case the number of laps in the recirculating loop. It turns out that although the BER for the optoelectronic 3R is higher than for the all-optical 3R after the first laps, the performance is comparable after 100 laps, which indicates that the DFF is more nonlinear than the all-optical solution in [39, 40], which is also detailed in section 7.4 of this Chapter.

Since the optoelectronic 3R represents a simplification over the all-optical 3R, in terms of the number of parameters that need to be controlled, system providers will probably not hesitate before choosing the former for a 40 Gb/s system. However, there are still a few points to consider before choosing one technology over the other, e.g. power consumption and cost. 3R regeneration is

likely to be implemented in a WDM environment, which means that regeneration must be performed on each channel separately. For a large WDM channel count a small difference in single channel regenerator power consumption may add up to a significant amount. The DFF used in [36] has a power dissipation of 1 W [38], and though the brand of the broadband modulator driver is unknown, a typical power consumption of a 40 Gb/s driver with an 8 V_{pp} output is around 1.25 W [155]. This adds up to 2.25 W, excluding the clock recovery circuit, which is needed regardless of the choice of technology. The total electrical power consumption of the SOA-based MZI 3R regenerator [39, 40] (including cooling) is estimated to be below 2.5 W, i.e. comparable to the optoelectronic approach. In other words, power dissipation may not be used as an argument for optical regeneration at 40 Gb/s.

With respect to cost, the level of integration and complexity are key issues. At present, all-semiconductor gates such as the all-optical SOA-based MZI and the PD-EAM 3R regenerators are monolithically integrated, unlike the optoelectronic implementation in [36], which is based on discrete components. However, the DFF, driver amplifier, and clock recovery circuit may all be realized using the same semiconductor substrate (GaAs or InP [64]), which makes integration a possibility, if the $LiNbO_3$ modulator is replaced by an EAM. So far, however, the component count is clearly higher for the optoelectronic approach, and this seems to be the only clear advantage of optical 3R regeneration at 40 Gb/s, which may potentially offer a cost saving.

All in all, the prospects for all-optical regeneration at 40 Gb/s do not look promising. At higher speeds of 80 or 160 Gb/s, optical approaches are still the only possibility, and consequently all-optical regeneration remains an important forward-looking research topic.

In the following, an introduction to the principle of operation of a general regenerator is given, with special attention to the nonlinearity of the decision gate. Experimental results at 10 Gb/s are presented, demonstrating 2R regeneration, i.e. (reamplification) and reshaping, in a MZI. This is followed by an analysis, documenting that the dispersion tolerance at 10 Gb/s is enhanced by 3R regenerating the signal prior to detection, and subsequently a full recirculating loop demonstration of 3R regeneration at 40 Gb/s, using a cascade of a XGM wavelength converter and a MZI is presented. An alternative 2R regenerator based on a compact all-active 2x2 MMI coupler, with a very nonlinear transfer function, is then demonstrated at 10 Gb/s, and finally an all-optical method for clock extraction from NRZ data is demonstrated at 40 Gb/s.

7.1 Regeneration: principle of operation

The aim of this section is to give an explanation of how 2R regeneration works, present key formulas that may be used to estimate the rate of BER accumulation, and to clarify what is believed to be a common misunderstanding about regen-

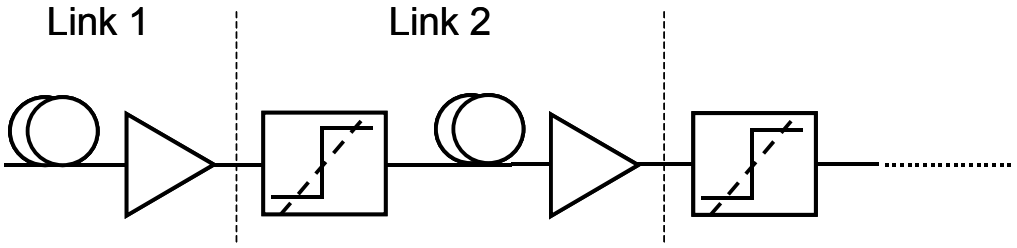

Figure 7.1: Cascade of 2R regenerators, with definition of interfaces between links.

erators. Retiming is not considered explicitly, but as mentioned in Chapter 2, it may be obtained by sampling the output of the 2R regenerator with a recovered clock signal.

Fig. 7.1 shows the considered scenario, namely a cascade of fiber links, where the loss is compensated by optical amplifiers (EDFAs). At the input of each link, starting with link number 2, the signal passes through an optical gate, characterized by the parameter γ governing the nonlinearity of its transfer function. The effect of the nonlinear gate is to redistribute the logic signal levels and the ASE added to the signal by the EDFAs, in a way that inhibits the accumulation of bit errors. This reshaping action of the gate will be referred to as 2R regeneration, even though the signal is amplified separately. The definition of 'a link' in Fig. 7.1, indicated by the vertical, dashed lines, is somewhat arbitrary, and only has significance to the numbering of regenerators in the mathematical description below.

The distribution of noise around the logic levels is described by probability density functions (pdfs), which account for the probability that the addition of noise causes the power level to attain a certain value. Fig. 7.2 (a) shows the pdfs of the "0" and "1" level at the input of a gate, centered around the average logic level $P_{in,0}$ and $P_{in,1}$. The probability of erroneously detecting a logic "0" in the input signal as a logic "1" is given by the integration of the tail of $pdf_{in,0}(P_{in})$, from the threshold power, $P_{in,D}$, to infinity, identified as the light gray area in Fig. 7.2 (a). Analogously, the probability of detecting a "1" as a "0" is calculated from the tail of $pdf_{in,1}(P_{in})$, which is identified by the darker gray area in Fig. 7.2 (a). Consequently, the total BER is given by the sum of the two contributions, graphically identified as the two gray areas.

Fig. 7.2 (b) and (c) illustrate how the pdfs are transformed through a linear gate (a piece of ideal fiber or a linear amplifier) and an ideal threshold (a step function). For the linear case, corresponding to a transfer function slope of $\gamma = 1$, it is not surprising that the pdfs at the output are identical to the functions at the input. However, for the ideal threshold, the input pdfs are transformed into delta functions, which means that the logic levels are completely defined by the power levels $P_{out,0}$ and $P_{out,1}$. This prompts an interesting question: since the BER is governed by the overlap of the pdfs of the two logic levels, does this mean

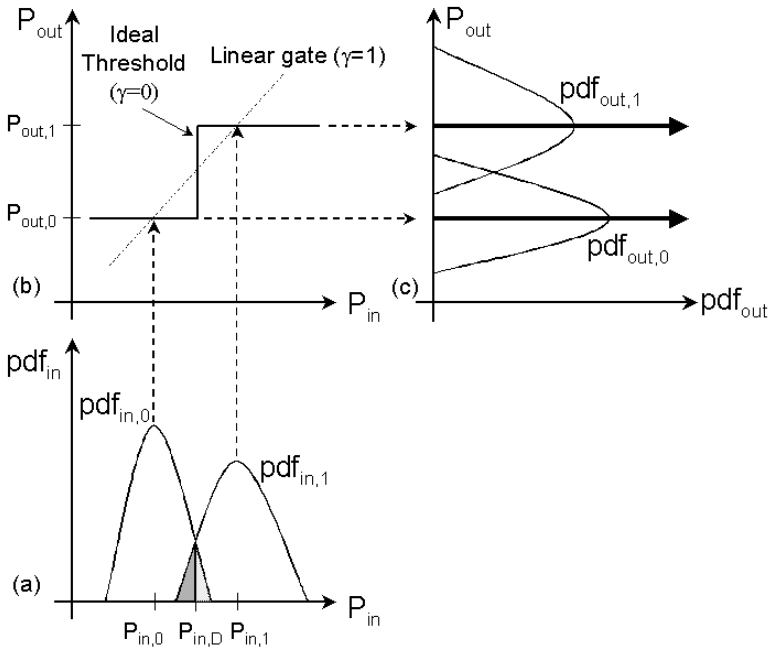

Figure 7.2: (a) Propability density functions (pdfs) of logic levels at the input of gate, (b) transfer function of nonlinear gate, (c) pdfs at output of gate.

that the signal is error-free at the output of an ideal threshold? The answer is no, because the "0"s above the threshold are included in $pdf_{out,1}$ and vice versa, which makes the errors unrecoverable. This leads to the general fact that, regardless of nonlinearity, the BER of a signal *cannot* be reduced by passing it through a nonlinear gate.

Pioneering work in describing the evolution of pdfs through a cascade of fiber links including regenerators, as illustrated in Fig. 7.1, is presented in [63]. The matrix formulation developed in [63] requires a numerical approach, which provides great accuracy, but at the expense of clarity. In a continuation of this work, approximate, analytical formulas for the evolution of the BER are developed in [156]. In the following, the main results of this reference are reviewed, as they form the basis for the further analysis.

The normalized transfer function $f_A(x)$ of the nonlinear gate is assumed stepwise linear

$$f_A(x) = \begin{cases} \gamma x & ; x < \frac{1}{2} \\ \gamma(x-1)+1 & ; x > \frac{1}{2} \end{cases} \tag{7.1}$$

where x is the normalized input power ($0 \leq x \leq 1$). Notice that γ represents the slope of the linear pieces of the transfer function. By extending the two linear parts of f_A on both sides of the decision threshold[1], $x = \frac{1}{2}$, the individual

[1]The optimum decision threshold becomes $x = \frac{1}{2}$ for an equal ratio of "0"s and "1"s and an equal noise variance in the logic levels.

pdfs maintain the shape upon transformation, although the variance is scaled according to the slope of the transfer function [156]. In other words, a Gaussian distribution remains Gaussian after the gate.

As discussed above, the tails of the pdfs crossing the discontinuity of f_A at $x = \frac{1}{2}$ represent unrecoverable errors. ASE noise added by the EDFAs in the fiber link is modeled as a convolution of the individual pdfs with a Gaussian distribution of variance σ^2_{ASE}. Assuming Gaussian pdfs, the convolution does not change the shape of the distribution, but only the variance, obtained by a simply adding σ^2_{ASE} to the variance of both pdfs before the EDFA. By assuming that the overlap of the pdfs right after the regenerator is negligible, i.e. that the errors have been fully "absorbed" in the pdfs as explained above, the BER after the n'th link (after the n'th EDFA), BER_n, can be expressed as

$$BER_n = BER_{n-1} + E(\sigma_n) \tag{7.2}$$

where $E(\sigma_n)$ is the total overlap between the pdfs, governed by the variance σ_n^2 at the output of the n'th EDFA. Since $E(\sigma_n)$ is meant to represent the addition to the BER brought about by the EDFA, a pdf overlap before the EDFA is included again, and thus leads to an overestimated BER_n. The introduced error is largest for the linear, and least interesting gate from a regeneration perspective, and vanishes for the ideal step function [156].

The approximative expression for BER_n is given by [156]

$$BER_n(\gamma) \approx \frac{1}{\sqrt{\frac{2\pi Q_0^2}{F}}} n \sqrt{\frac{1-\gamma^2}{1-\gamma^{2n}}} \exp\left(-\frac{1}{2}\frac{Q_0^2}{F}\frac{1-\gamma^2}{1-\gamma^{2n}}\right) \tag{7.3}$$

Here, Q_0 is the Q-factor (see section A.3) at the input of link number 1, and F is the EDFA noise figure. The Q value after the first amplifier is given by $Q_1 = Q_0/\sqrt{F}$ [157], and in the following Q_0 and F have been chosen such that $10 \log Q_1^2 = 17$ dB, which corresponds to a BER of approximately 10^{-12}.

Fig. 7.3 shows the accumulation of the BER as a function of the number of fiber links, with the transfer function nonlinearity as a parameter. The inset shows the step-wise linear transfer function used in the calculations. As observed, the rate of error accumulation depends significantly on the nonlinearity of the gate. This is because the higher the nonlinearity, the narrower the distributions at the output of the gates, which gives rise to a smaller pdf overlap after the noise from EDFAs is added. Notice that all the curves become linear for $n \to \infty$

$$\underset{n\to\infty}{Lim}\ BER_n(\gamma) \approx \frac{\sqrt{1-\gamma^2}}{\sqrt{\frac{2\pi Q_0^2}{F}}} n \exp\left(-\frac{1}{2}\frac{Q_0^2}{F}\left(1-\gamma^2\right)\right) \tag{7.4}$$

In addition, by defining the effective noise figure $F_\gamma = F/(1-\gamma^2)$, eq. (7.4) is reduced to

$$\underset{n\to\infty}{Lim}\ BER_n \approx \frac{1}{\sqrt{\frac{2\pi Q_0^2}{F_\gamma}}} n \exp\left(-\frac{1}{2}\frac{Q_0^2}{F_\gamma}\right) \tag{7.5}$$

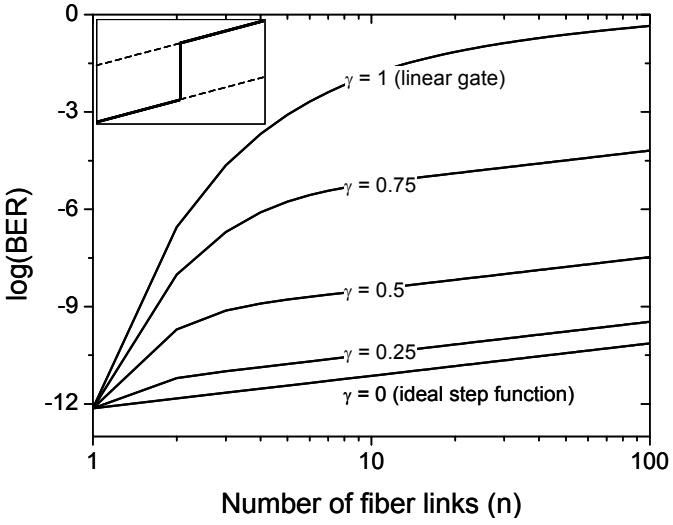

Figure 7.3: Evolution of BER vs. number of regenerated links with the nonlinearity as a parameter. The step-wise linear transfer function is shown in the inset.

which is identical to $BER_n(\gamma = 0)$, except that the EDFA noise figure is higher by a factor of $1/(1-\gamma^2)$. Thus, after a large number of links, including regenerators with nonlinearity γ, the BER evolves as if the gates had been ideal step functions ($\gamma = 0$), preceded by EDFAs with a noise figure of F_γ.

In the present analysis the BER is calculated after the EDFAs (see. Fig. 7.1), and this is an important detail when analyzing experimental results. If instead, the BER is calculated right after the regenerators, i.e. *before* the EDFAs, one finds that the BER at the output of the first regenerator is independent of the nonlinearity, simply because the regenerator itself cannot change the BER. In [13] and [88] this observation is used to make the argument that the regenerative capabilities of a regenerator cannot be assessed through a single-regenerator experiment - only through a recirculating loop experiment. However, by placing a noise source after the first regenerator, and evaluating the BER here, as shown in Fig. 7.1, the BER does indeed depend on the nonlinearity.

By applying (7.3) to the scenario in Fig. 7.4 (a), it may be shown that the BER at the output of the second EDFA becomes

$$BER_2(\gamma) = \sqrt{\frac{2F}{\pi Q_0^2(1+\gamma^2)}} \exp\left(-\frac{1}{2}\frac{Q_0^2}{F}\frac{1}{1+\gamma^2}\right) \tag{7.6}$$

In Fig. 7.4 (c), eq. (7.6) is plotted against the nonlinearity $1-\gamma$, along with corresponding results for 100 regenerators. The figure reveals that the trend is exactly the same, regardless of the number of cascaded regenerators. In most single-regenerator experiments noise is not explicitly added to the signal before reception and BER analysis. Rather, most experiments are carried out as illustrated in Fig. 7.4 (b), where the first amplifier adds ASE to the signal, which

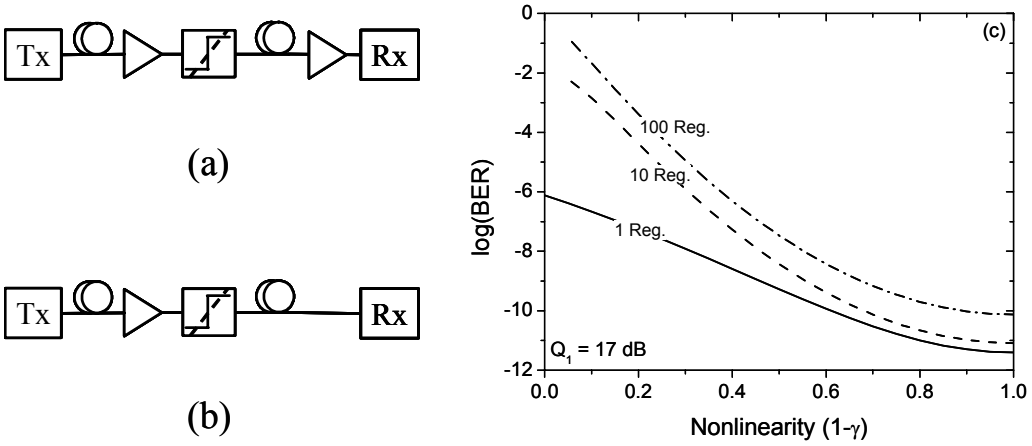

Figure 7.4: (a) Cascade as in Fig. 7.1, including two links. (b) Typical single-regenerator setup. (c) Comparison of BER after 1, 10, and 100 regenerators vs. nonlinearity for $Q_0 = 17$ dB. The trend is the same in all three cases.

is redistributed by the regenerator, and subsequently the receiver adds signal-spontaneous beat noise or thermal noise to the signal, depending on whether the receiver is optically preamplified or not [158]. Thus, the scenarios depicted in Fig. 7.4 (a) and (b) are equivalent in the sense that the pdfs at the output of the regenerator in both cases are convoluted with a noise distribution before BER analysis. The variance of the noise distribution, determined by e.g. the noise figures of electrical, and potentially optical, amplifiers in the receiver, will clearly affect the results quantitatively, but this does not change the fact that an improvement of the receiver sensitivity obtained by inserting a regenerator before the receiver, is indeed a measure of the gate's ability to redistribute the noise - or in other words a measure of the nonlinearity. It should be mentioned that when the received power attains a level high enough that the noise added by the receiver itself can be neglected, the BER is determined solely by the noise at the output of the regenerator. In this limit, where the BER has reached the floor, the predictions in [13] and [88], that a single regenerator does not change the BER[2] are expected to be correct.

7.2 2R regeneration at 10 Gb/s using MZIs

The noise redistributing capabilities of the active-passive MZI, demonstrated at 40 Gb/s in section 6.2.1, is here investigated at 10 Gb/s. The experimental setup is as depicted in Fig. 7.4 (b), except that the noise level before the regenerator is varied.

As explained in the previous section, the noise source at the output of the

[2]In the analysis the regenerator itself is assumed noise free. In reality this will not be the case, and the error-floor is thus expected to increase slightly by inserting a single regenerator.

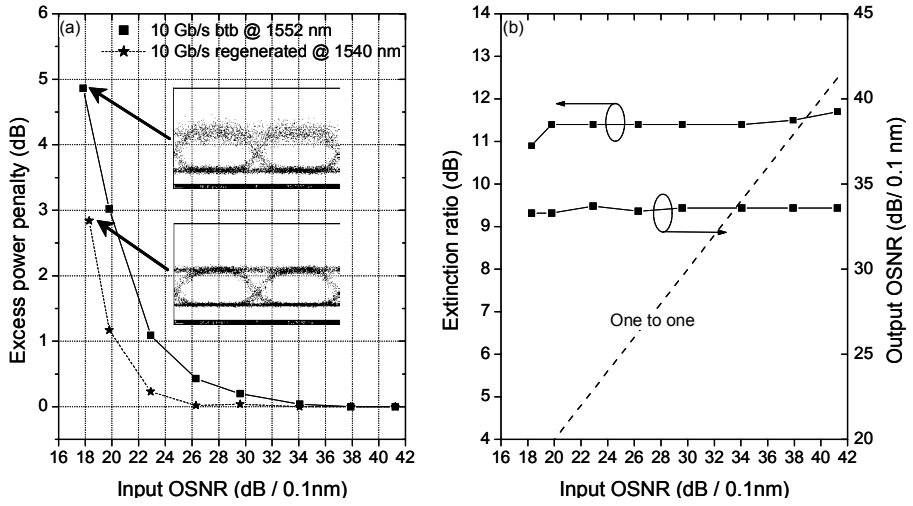

Figure 7.5: (a) Excess power penalty vs. input OSNR with (1540 nm) and without (1552 nm) 2R regeneration. Insets shows comparison of eye diagrams for input OSNR of $\approx$ 18 dB/0.1 nm. (b) Extinction ratio (left axis) and output OSNR (right axis) vs. input OSNR.

regenerator, which is necessary to assess the reshaping, consists of the receiver noise, which in the present case is dominated by thermal noise, as the receiver is not preamplified. Noise is added to the input data signal using the following scheme: ASE from an EDFA is attenuated and merged with the data signal in a 90/10 coupler, before a 50/50 coupler splits the signal evenly between the regenerator and an Optical Spectrum Analyzer (OSA), used to monitor the input OSNR. Before the noisy signal is launched into the regenerator a BPF removes out-of-band ASE, thereby simulating a WDM demultiplexer.

Fig. 7.5 (a) shows the excess power penalty as a function of the OSNR of the input signal at 1552 nm. The CW probe wavelength is 1540 nm and the probe power is 10 dBm. The bias currents remained constant at $I_3/I_4 = 650/208$ mA throughout the experiment, whereas the input data power (including the added ASE) was increased to maintain the operating point as the OSNR of the input signal was decreased. For a large input OSNR the optimum was obtained for an average input data power of -5 dBm. As mentioned in the previous section the sensitivity improvement obtained by employing the MZI as a 2R regenerator is evidence that noise redistribution has taken place. This is also evident from the eye diagrams in Fig. 7.5 (a). Notice that the error-floor in Fig. 7.5 (a) approaches 10^{-9} for the back-to-back, as well as the regenerated signal, for an input OSNR just below 18 dB/0.1 nm. This is due to negligible influence of the receiver noise at high input powers (high power penalties). Fig. 7.5 (b) illustrates the variation of the ER and OSNR of the regenerated signal vs. the input OSNR. Clearly, neither of the two parameters are representative of the BER, as they remain almost constant over the entire range. This is not surprising, since the BER is determined by the tails of the pdfs, and the ER is a measured using the

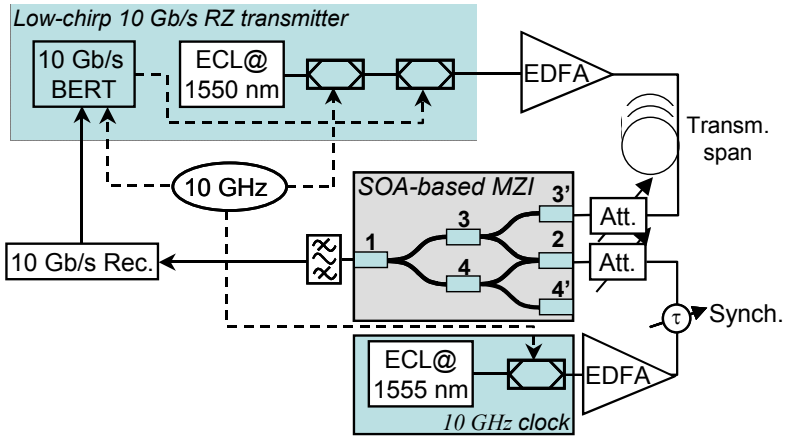

Figure 7.6: Setup for experimental evaluation of dispersion tolerance of MZI-based 3R regenerator.

mean logic levels. Likewise, the OSNR is only a measure of the average signal power compared to the noise background, which is not directly affected by noise distribution.

The large OSNR improvement is due to the fact that the noisy input signal is wavelength converted to a "clean" optical carrier. The output OSNR is determined by the amount of noise added to the probe signal by the MZI, which means that the OSNR is only improved for an input OSNR < 34 dB/0.1 nm.

7.3 Dispersion tolerance of MZI-3R at 10 Gb/s

Most demonstrations of regeneration focus on the noise redistributing property of a nonlinear gate. In this section, the ability of a 3R regenerator to reconstruct the waveform of a signal distorted by chromatic dispersion is investigated. The action of the 3R regenerator, which consists of an all-active MZI operated in out-of-phase mode, will not be referred to as *dispersion compensation*, since that implies operating on the optical field to reverse the evolution of the phase. Here, the dispersion is not compensated, but instead it is tolerated to a greater extent through reshaping and sampling.

To be able to propagate over significant transmission spans, a 10 Gb/s RZ transmitter at 1550 nm with a reasonably low chirp was implemented using two $LiNbO_3$ modulators as indicated in the setup in Fig. 7.6. The first modulator generates a 10 GHz clock, which is subsequently modulated with a PRBS of word length $2^{31} - 1$. Before the data signal is launched into port $3'$ of the MZI it is transmitted over variable lengths of SMF, in order to accumulate dispersion. The retiming 10 GHz clock was generated by modulating a CW beam at 1555 nm using a third $LiNbO_3$ modulator. Synchronization between data and clock signal was obtained by passing the clock signal through an optical delay line. At

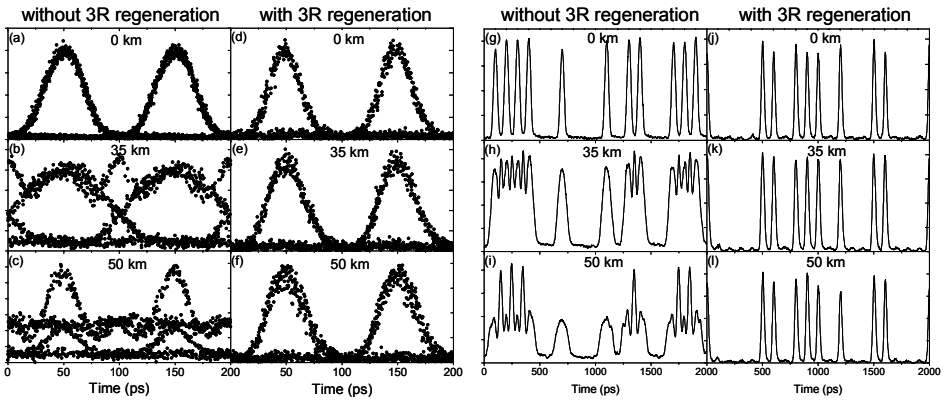

Figure 7.7: Comparison of eye diagrams with and without 3R regeneration after transmission of (a,d) 0 km, (b,e) 35 km, and (c,f) 50 km on SMF. The corresponding pulse patterns are shown in (g-l).

the output of the MZI a BPF with a bandwidth of 1.3 nm serves to suppress the input data before the regenerated signal is detected in a preamplified receiver. The all-active MZI used in this experiment has an active cross-section of $(W, H) = (1.2, 0.2)\ \mu m$, which gives an optical confinement factor of $\Gamma = 0.4$. The length of the interferometer arms is 1.2 mm, which, combined with the relatively low confinement, limits the carrier modulation bandwidth to around 20 GHz. However, the device is almost completely polarization independent, and provides a very good coupling to tapered fiber, which results in high output power and a low input switching energy.

Fig. 7.7 (a-f) compares eye diagrams of the 10 Gb/s signal after propagating 0, 35, and 50 km on SMF. The left column (a-c) shows the case without regeneration (Tx-SMF-Rx), and the right column (d-f) shows the effect of the 3R regeneration (Tx-SMF-MZI-Rx). In Fig. 7.7 (g-l) the same comparison is made for the corresponding pulse patterns, where it is clear that the MZI operates in out-of-phase mode. XPM is a power dependent process, and thus the accumulated dispersion is reset at the output. This comes at the expense of added chirp, which can be detrimental when the MZI is operated in out-of-phase mode. However, by using a MZI with a built-in phase offset of π the signal polarity may be preserved, which improves the transmission properties significantly. The bias currents and average input powers remained the same for all transmission distances, namely $P_C/P_P/I_1/I_2/I_{3'}/I_{4'}/I_3/I_4 = -1.5$ dBm/ $-$ 3 dBm/ 100/120/100/110/250/80 mA. It should be noted that after 50 km the mark level varies by approximately 3 dB (see Fig. 7.7 (c) and (i)), which is well compensated for, indicating that the transfer function of the MZI is flat over at least 3 dB around the transmission minimum.

As pointed out previously, the RZ format provides a better receiver sensitivity than NRZ because a larger eye opening may be obtained for the same average power. This is illustrated and quantified in Fig. 7.8 (a), which shows

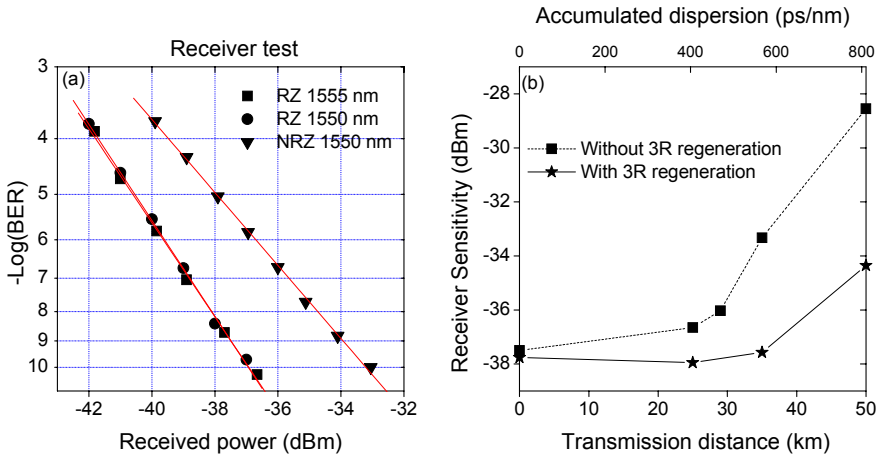

Figure 7.8: (a) Receiver test illustrating receiver sensitivity improvement obtained by using RZ over NRZ. (b) Evolution of sensitivity with transmission distance (accumulated dispersion) with and without 3R regeneration.

BER curves for back-to-back RZ signals at 1550 nm and 1555 nm to demonstrate the wavelength independence of the receiver, and a curve for an NRZ signal at 1550 nm. RZ signals with a certain amount of accumulated dispersion resemble NRZ signals - see e.g. the eye diagram after 35 km SMF in Fig. 7.7 (b) - and consequently the sensitivity is degraded by ≈3.5 dB simply due to the RZ→NRZ conversion. For this reason, the sensitivity degradation observed the first $30-35$ km in Fig. 7.8 (b) without 3R regeneration, can be ascribed primarily to the format conversion, whereas for distances beyond 35 km, intersymbol interference caused by the chromatic dispersion is responsible for the degradation.

7.4 Loop demonstration of 3R regeneration at 40 Gb/s

In an attempt to realize a 3R regenerator based exclusively on the standard mode of operation, with the added advantage of low polarization dependence and high IPDR, a XGM wavelength converter was cascaded with the active-passive MZI from section 6.2.1. The SOA is the same 800 μm long device used in section 6.1, but in this case a broader BPF with a bandwidth (FWHM) of 1.2 nm is used at the output, which provides a large output power needed in the next stage of the regenerator. The filter is only detuned slightly, thereby assisting the XGM response while maintaining the inverted polarity. A dual-stage configuration is necessary to obtain equal input and output wavelengths, required to test the regenerative performance in a recirculating loop. Moreover, the total transfer function of the XGM + MZI cascade is more nonlinear than a single MZI, which gives rise to a more efficient noise redistribution. The regenerator is controlled by only three bias currents (one for the SOA, and two for the MZI), which ensures easy control and low power consumption. A MZI + MZI configuration has an

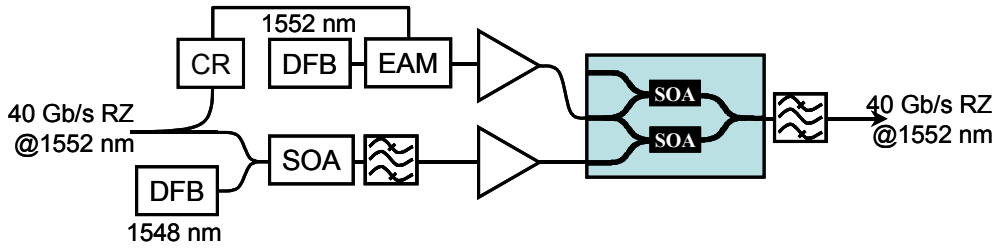

Figure 7.9: 3R regenerator consisting of a cascade of an SOA-XGM wavelength converter and an active-passive MZI with a clocked probe signal.

even more nonlinear transfer function [12, 13, 159], but suffers from an inherently low IPDR. Employing active input sections can compensate for this, but it comes at the expense of additional power consumption and the complexity of controlling the extra currents. Using the XGM as a first stage will to a great extent absorb fluctuations in the input signal power. In addition, XGM is less sensitive to polarization compared to XPM.

Fig. 7.9 shows the entire 3R regenerator. At the input a fraction of the power is tapped off for the Clock Recovery (CR) circuit, while the remaining signal power is merged with CW light at 1548 nm from a DFB laser, and launched into the SOA. The CR circuit consists of a photo diode, an electrical high-Q filter ($Q \approx 1000$) centered at 40 GHz, and an electrical amplifier driving an EAM, which transforms the electrical Sine into a 40 GHz train of optical pulses at 1552 nm. The DFB laser used in the CR circuit and the gain-switched DFB laser generating the input data signal are carefully matched, to make sure input and output wavelengths are identical. Before entering the MZI, the data and clock signals are amplified in EDFAs, and at the output the data signal is suppressed with a 0.8 nm filter.

The choice of target wavelength in the XGM wavelength conversion is a trade-off, since down-conversion gives rise to a larger ER, and sets the MZI up for up-conversion. On the other hand, a too large down conversion in the XGM stage will cause a problem for the MZI, which has a gain peak at ≈ 1560 nm. The choice of 1548 nm represents a compromise. The SOA is biased at 300 mA, and the signal and CW powers at the input are -2.8 dBm and 3 dBm, respectively. The MZI is biased at $I_3/I_4 = 260.8/749.9$ mA, which corresponds to an out-of-phase operating point, thus re-inverting the signal polarity.

The recirculating loop shown in Fig. 7.10 consists of two 40 km transmission spans of SMF, each followed by DCF to reset the dispersion. At the input side of the loop a 10 GHz clock from a GS-DFB laser is modulated with a PRBS of word length $2^{31} - 1$ and subsequently multiplexed to 40 Gb/s in a fiber-based interleaver. The signal passes through an acousto-optic (A.O.) switch controlling the access to the loop. An identical switch is placed inside the loop. As long as this switch is on (transmission state) the signal stays in the loop. After the signal has traversed the loop the desired number of times, the bit error rate test

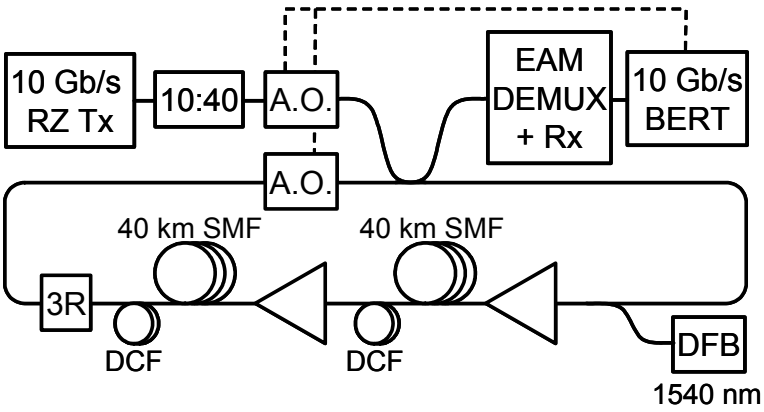

Figure 7.10: Recirculating loop setup emulating a cascade of 3R regenerators and 80 km fiber spans. A.O.: Acousto-optic switches.

set (BERT) starts measuring errors on the EAM-demultiplexed 10 Gb/s signal for a duration determined by the time of flight of the loop. The switch in the loop turns off, thereby emptying the loop, and following this, the input switch turns on and fills the loop with data. The switch in the loop turns on again and keeps the signal in the loop, etc. The A.O. switches and the BERT are controlled by a computer program, which takes the loop length and number of laps as parameters. Between emptying and reloading the loop, the gain of the EDFAs may have time to recover, which can result in detrimental transients. To avoid this, the EDFAs are loaded with a signal from a 1540 nm DFB laser to limit the gain excursion.

The SOA is packaged, whereas the MZI is a bare chip. This causes problems in the recirculating loop, because the setup is required to be stable for a longer time compared to single-regenerator experiments. Mechanical and thermal fluctuations influence the tapered fiber coupling to the chip, and also causes polarization changes, which become significant over many laps. Fig. 7.11 shows eye diagrams after 2 (a), 20 (b), 50 (c) and 100 (d) laps of 80 km. The eye diagram remains clear and open, which verifies the cascadability of the 3R regenerator.

Fig. 7.11 (e) shows the BER performance after 50 laps (4000 km), and reveals a 4 dB power penalty compared to back-to-back. The system remained stable for periods of a few seconds, which was not sufficient to measure errors lower than 10^{-9}. Individual 10 Gb/s tributaries of the regenerated signal cannot be distinguished, since there is no guarantee that the same tributary is demultiplexed each time the BER starts measuring errors. In other words, a BER measurement at the output of the loop represents an average of the 4 tributaries.

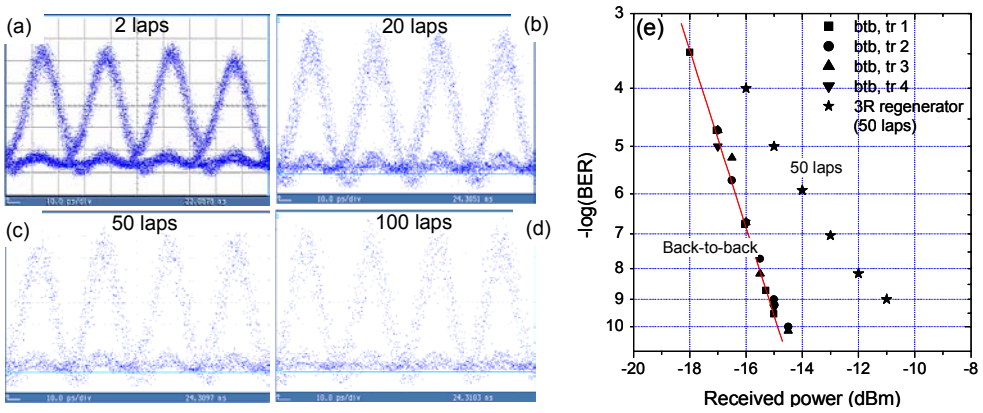

Figure 7.11: Eye diagrams of regenerated signal after (a) 2 laps, (b) 20 laps, (c) 50 laps, and (d) 100 laps. (e) BER curves: back-to-back, and regenerated signal after 50 laps.

7.5 2R regeneration using an MMI-SOA

In most all-optical SOA-based regeneration schemes, using e.g. MIs or MZIs, simultaneous wavelength conversion to a CW or clock signal is an inherent property. This is an advantage in a scenario where wavelength conversion is required anyway, but if the conversion is not desirable, an additional wavelength converter is needed to return to the original input wavelength. This complicates integration, and increases the physical size of the device considerably. So-called pass-through 2R regeneration schemes, in which wavelength conversion is not performed, have been demonstrated at up to 40 Gb/s using the MI and MZI [160], and with saturable absorbers [97]. In these schemes the data signal does not interact with additional signals, which means that a CW or clock source can be avoided at the input, and a filter is no longer necessarily needed at the output. This greatly reduces complexity and enables integration of a large number of regenerators for use in parts of the network where wavelength conversion is not necessary. Pass-through regenerators do not provide OSNR restoration, which is an inherent property of regenerative wavelength converters such as e.g. the MZI. One would think that this would seriously limit the cascadability. However, it is the in-band noise, i.e. the noise sharing the bandwidth with the signal, which is critical for the cascadability, since out-of band noise can be suppressed by simple filtering. The in-band noise is redistributed as explained in section 7.1, and thus its accumulated effect on the BER may be inhibited. This has been demonstrated in a loop experiment over 1 million km with a pass-through NLF-based 3R regenerator [14].

Here, dynamic measurements at 10 Gb/s on a novel type of all-optical pass-through type 2R regenerator are presented. The regenerator is based on an all-active $2x2$ multimode interference coupler (MMI-SOA), is very compact compared to the MZI 2R regenerator, and has a digital-like transfer function [161],

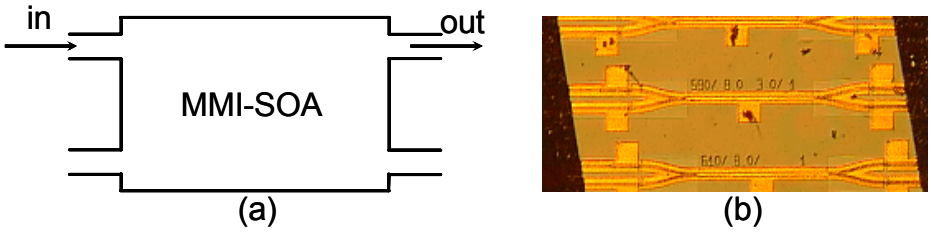

Figure 7.12: (a) Sketch of $2x2$ MMI-SOA. (b) Photo of chip (courtesy of Jan De Merlier)

which enables a more effective noise suppression in the logical zero level compared to the MZI and MI implementation of the pass-through scheme. Some of the results from this section are published in [p12].

7.5.1 Principle of operation

Fig. 7.12 (a) shows a sketch of the $2x2$ MMI-SOA, including input and output waveguides, and Fig. 7.12 (b) shows a photograph of the chip. The signal is launched into one of the inputs (here, the upper) where it excites a subset of the eigenmodes supported by the MMI waveguide. The excited eigenmodes will interfere as they propagate through the MMI, causing the transversal intensity pattern of the total excited field to produce periodic direct and mirrored self-images [152]. The propagation constants identifying the different eigenmodes depend on the transversal carrier density profile, which in turn is influenced by the input power. The length of the device is chosen such that, for input powers below the input saturation power, a mirrored self-image appears near the cross-state output waveguide. Thus, the output field interferes destructively at the bar-state output waveguide, and a minimum of power will exit through this port.

This is illustrated in Fig. 7.13 (a), which shows a simulation of the field intensity inside the MMI for an input power below saturation. As the input power is increased, the carrier density starts to saturate. This changes the real as well as the imaginary parts of the eigenmode propagation constants, causing a change of the relative phase relationship between the modes. As a result, the output field will evolve from interfering destructively at low input powers, to gradually interfere constructively in front of the bar-state output waveguide. This is observed in the evolution from Fig. 7.13 (a) through (c), which have been calculated for increasing input powers. Accordingly, the amount of power coupled out of the bar-state waveguide increases with the input power, and since this increase is highly nonlinear, regeneration can be obtained.

To assist in the design of the MMI-SOA, simulations based on a FD-BPM model like the one outlined in section 3.2 have been carried out. Unlike the 2D model in section 3.2, the model used to generate the results presented here, takes the inhomogeneous mode excitation by the ASE into account [162,163]. This is an important effect, since it influences the self-imaging properties of the MMI-SOA.

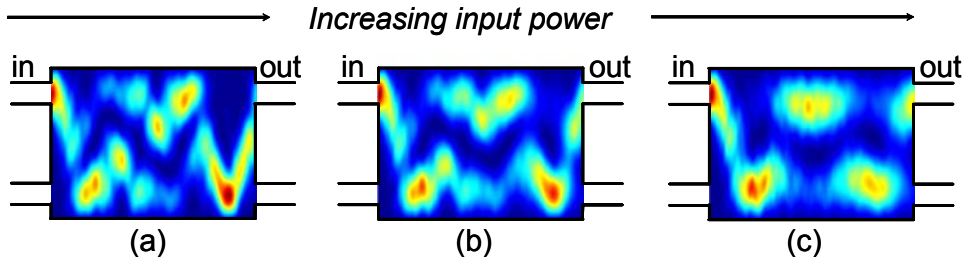

Figure 7.13: Field intensity inside MMI-SOA for increasing input power (courtesy of Jan De Merlier).

Based on the modeling, it was concluded that the width of the input waveguides should be as large as 3 μm for an MMI width of 8 μm, to obtain a sufficiently tolerant MMI design. The MMI-SOAs were fabricated with an active region consisting of eight 8 nm thick compressively strained quantum wells. Additional details about the fabrication process can be found in [164].

Static measurements of the regenerator transfer functions were first published in [161]. In this reference, a comparison between the simulated and measured transfer functions reveals good qualitative agreement, and it is reported that a static output ER of 22 dB can be achieved for an input ER of 7 dB.

7.5.2 Dynamic results at 10 Gb/s

Dynamic measurements at 10 Gb/s were performed on an MMI-SOA with a length of 550 μm. Including the access waveguides, this makes the total structure only ≈ 1.5 mm long. This should be compared to a total length of a MZI of $4-5$ mm. Fig. 7.14 (a) shows the experimental setup: the data signal is generated by modulating a 10 GHz pulse train from a gain switched DFB laser, emitting at a wavelength of 1554 nm, with a PRBS of word length $2^{31}-1$. The signal is first passed through a noise generator consisting of a variable attenuator followed by an EDFA and an optical bandpass filter. By controlling the amount of signal power launched into the EDFA, the output OSNR can be varied.

The signal then traverses the MMI-SOA, using lensed fibers to couple the light in and out of the chip. Finally, the signal is detected in a pre-amplified receiver.

As the input power to the EDFA is decreased, the OSNR obviously decreases. At the same time the ER decreases, since the unmodulated ASE generated by the EDFA adds to the base-line of the signal. This is clearly seen in Fig. 7.14 (b), which shows the optical eye diagram at the input of the regenerator, corresponding to an average signal power of -38 dBm into the noise generating EDFA. Fig. 7.14 (c) shows the eye diagram of the same signal, after it has traversed the MMI-SOA, and a clear suppression of the zero-level is observed.

In Fig. 7.15 (a) the ER of the signal is shown as a function of the input power to the noise generating EDFA, with and without the MMI-SOA in the

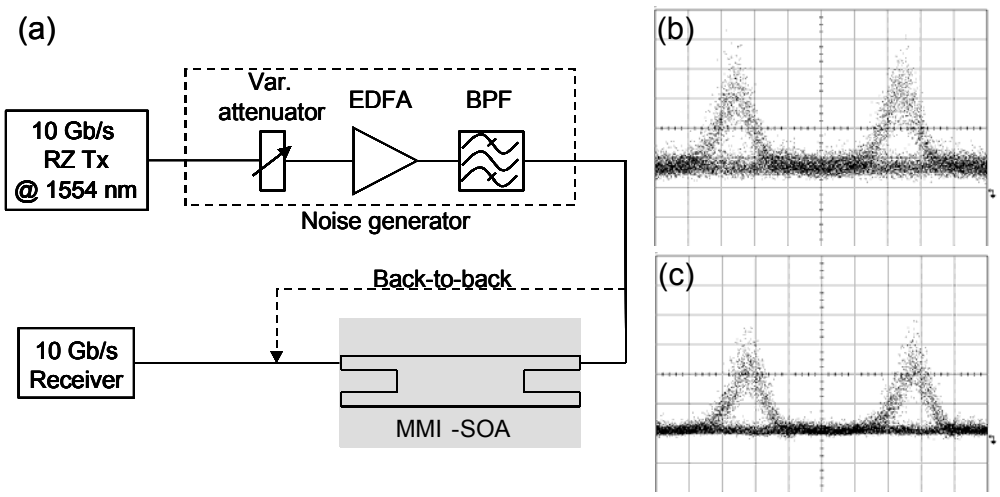

Figure 7.14: (a) Setup for experimental evaluation of MMI-SOA 2R regenerator at 10 Gb/s. (b-c) Comparison of input and output eye diagrams for −38 dBm of signal power into noise generator.

system. The ER improvement obtained by using the MMI-SOA is observed to be significant, and may be ascribed to the efficient noise redistribution of the pdf corresponding to the "0" level, as indicated in Fig. 7.14 (b-c).

The noise redistribution of the MMI-SOA is quantified in Fig. 7.15 (b) where the receiver sensitivity is shown with and without regeneration, as a function of the input power to the EDFA. As the input power is decreased, corresponding to decreasing the input OSNR, the sensitivity improvement increases. From Fig. 7.15 (a) it is seen that an input power to the EDFA of −27.5 dBm gives rise to an ER of ≈ 13 dB without regeneration and ≈ 14.5 dB with regeneration. This modest ER improvement does not by itself give rise to any noticeable sensitivity improvement, so it is clear that the improvement of more than 10 dB observed in Fig. 7.15 (b) is predominantly due to noise redistribution.

7.6 High-speed interferometric regenerators

All the interferometric switches described in Chapter 5 have a nonlinear transfer function, and thus posses the ability to regenerate the control signal. They are all based on a MZI structure, which means that the static[3] power transfer function, in terms of induced nonlinear phase shift $\Delta\phi_{NL}$ may be expressed as (see e.g. eq. (5.8))

$$T(\Delta\phi_{NL}) = \frac{1}{2}\left[1 + \cos\left(\Delta\phi_{NL} - \Phi_0\right)\right] \tag{7.7}$$

[3]For the differential-mode switches, a static transfer function cannot be measured, and T represents an input vs. output pulse energy transfer function.

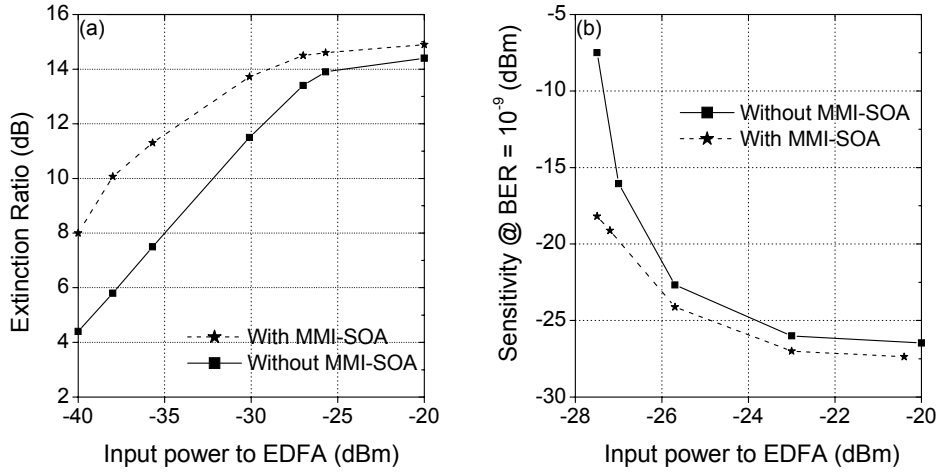

Figure 7.15: (a) Extinction ratio vs. input power to noise generating EDFA with and without MMI-SOA. (b) Receiver sensitivity at 10^{-9} vs. input power to EDFA with and without MMI-SOA.

where Φ_0 is a phase bias, obtained and tuned in different ways depending on the specific switch architecture. Notice that gain modulation is neglected in (7.7) for simplicity. Fig. 7.16 shows the relative transfer function vs. the nonlinear phase shift for $\Phi_0 = \pi$. The transfer function is plotted along with a linear function, and it is observed that the interferometric switches provide some degree of noise redistribution.

In [63] the nonlinearity of a MZI is estimated to a modest $\gamma \approx 0.64$, which should be compared to the BER-evolution curves in Fig. 7.3. In addition, the transfer function in (7.7) is only valid for static (or steady-state) input signals. Taking patterning effects into account, by noting that $\Delta\phi_{NL}$ depends on the preceding bit-pattern, the nonlinearity also becomes bit-pattern dependent. The effect of patterning on the BER evolution has been investigated for the DISC regenerator [165], and the regenerative advantage, compared to the linear gate, is found to decrease with the bitrate. In [165], the analysis was carried out for bitrates up to 40 Gb/s, for which a nonlinear phase shift $\Delta\phi_{NL}$ of π is still realistic. However, for bitrates exceeding 40 Gb/s, each control pulse cannot induce a phase shift of π, since the carrier density does not recover fully between excitations. Recent experimental results demonstrate a phase shift of $\approx \pi$ at 40 GHz periodic excitation [166]. However, the probe power was only -15 dBm, which is unrealistically low for excitation by a control signal modulated with random data, due to pattern effects. A lower peak phase shift implies that the signal does not experience the entire transfer function, which translates into a poor or non-existing noise redistribution in the mark-level. Although saturation will change the appearance of the transfer function in Fig. 7.16 somewhat, it seems clear that for an intermediate peak phase shift of around 0.5 π, the interferometric switch actually broadens the pdf of the mark-level, which is expected to have a detri-

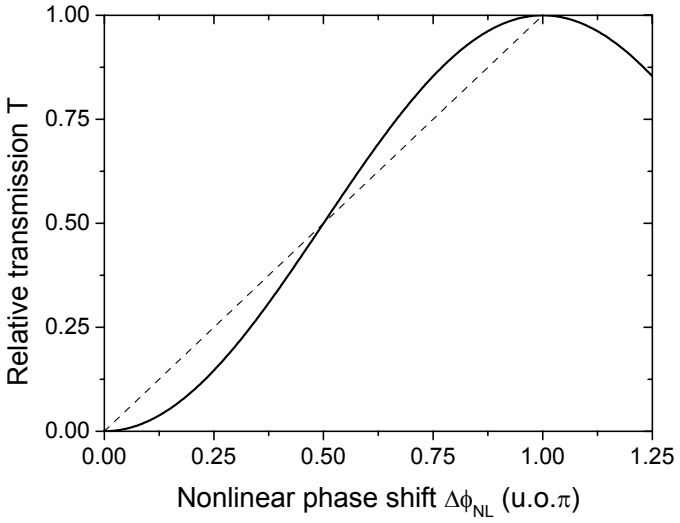

Figure 7.16: Relative transmission of MZI-based regenerator [eq. (7.7)] vs. nonlinear phase shift.

mental effect on the BER evolution in a cascade. Regardless of the magnitude of the phase shift the noise in the "0" level, or space-level, is decreased.

An expression providing the dependence of the phase shift $\Delta\phi_{NL}$ on a number of key parameters is given in [127] for a periodic control signal

$$\Delta\phi_{NL} \propto \frac{I\Gamma}{fHW} \tag{7.8}$$

where I is the bias current (assuming constant SOA length), f is the repetition frequency, and H and W are the height and width of the active region. From (7.8) it is clear that $\Delta\phi_{NL}$ is inversely proportional to the repetition frequency, which may be substituted with the bitrate B without loss of generality. Thus, as the bitrate is increased, the reduced phase shift must be compensated through an increase of the bias current, a reduction of the optical waveguide area HW/Γ, or by increasing the SOA length, while keeping the current density constant [127]. The absolute phase shift induced by a control pulse also depends on the input probe power, which determines the minimum level of saturation. As already discussed in Chapters 4 and 5, a large probe power is needed to reduce patterning effects, and may lead to a trade-off between efficient noise redistribution in the mark-level and low patterning for the "regenerated" signal.

The problems outlined here may be some of the reasons why all-optical regeneration with SOA-based devices has not been demonstrated in recirculating loop experiments at bitrates exceeding 40 Gb/s. The only loop demonstration of SOA-based 3R regeneration not employing a MZI, is described in [96] and uses a DISC, as well as two NLF-based 2R regenerators and a saturable absorber. The role of the DISC in this experiment was wavelength conversion and retiming only, whereas the reshaping functionality was left to the NLF-regenerators. The latter

do not introduce patterning effects, and the phase shift scales linearly with the peak power.

So far, the maximum bitrate at which an SOA-based gate has been employed as a 3R regenerator is 84 Gb/s, which was obtained using a PD-MZI (UNI) [93]. In this experiment, the tolerance towards timing jitter was investigated, but noise redistribution was not. Thus, the potential of SOA-based regenerators at bitrates above 40 Gb/s is still unclear.

7.7 Clock extraction from 40 Gb/s NRZ data

Clock recovery is a critically important part of optical receivers, as well as advanced all-optical functionalities such as e.g. Boolean logic, and all-optical regeneration [p13], [13]. The recovery of the base frequency $f = B$ (B: bitrate) from RZ data signals may be implemented using electronic, optoelectronic or all-optical techniques, using e.g. a high-Q electrical filter as in section 7.4, optical gates combined with a phase-locked loop (PLL) [167], and self-pulsating lasers [168], respectively. However, these techniques do not directly apply to the NRZ data format, since they depend on the existence of a frequency component in the RF spectrum at the bitrate frequency $f = B$, which does not exist for NRZ data.

An electronic solution to this problem is to detect the signal, band-pass filter it around $f/2$, i.e. in this case 20 GHz, followed by frequency doubling and subsequent high-Q filtering around 40 GHz [36]. This approach is quite power consuming and bulky, although parts of NRZ clock recovery circuits operating at 40 Gb/s have been integrated [38], and are now commercially available.

An alternative, all-optical solution is to pass the NRZ data through an 'edge trigger', which only allows transmission of the leading and/or trailing edges of succeeding '1's. The result is a so-called Pseudo-Return-to-Zero (PRZ) signal [169], which contains a spectral peak at $f = B$ that may be used to lock an oscillator, such as e.g. a mode-locked laser [170].

This type of signal has been generated by exclusive OR'ing (XOR'ing) 10 Gb/s NRZ data with itself, delayed by half a timeslot, using PM fiber [169] and a fiber-based asymmetric Mach-Zehnder interferometer [170]. A similar PRZ signal has been obtained by passing 5 Gb/s NRZ data through an SOA, and subsequently suppressing the optical carrier with an FBG [171]. A PRZ signal containing only the leading edges of the NRZ data, has been generated by cross-gain modulating a 10 Gb/s NRZ data signal with itself in an SOA, operated in a counter-propagating configuration [172], and by chirping (red-shifting) the leading edges of a 2.5 Gb/s NRZ signal by passing it through an SOA, and subsequently filtering out the red-shifted part [173].

Here, PRZ signals containing the leading or trailing edges of 40 Gb/s NRZ data are generated, using a scheme similar to those presented in [171] and [173]. Most of the results presented here are published in [p14].

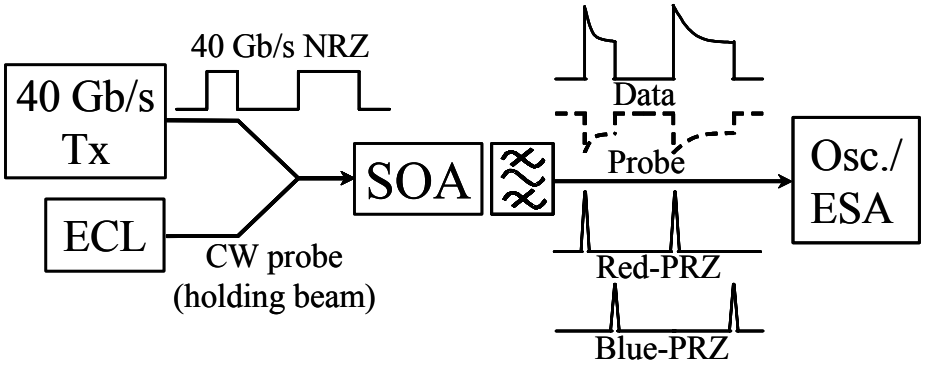

Figure 7.17: Experimental setup and principle of operation of PRZ generation. Osc: Sampling oscilloscope, ESA: Electrical Spectrum Analyzer.

7.7.1 Principle of operation

The experimental setup is shown in Fig. 7.17, which also aids in explaining the principle of operation. An optical 40 Gb/s transmitter, consisting of a 40 Gb/s PPG, a 40 Gb/s $LiNbO_3$ modulator, and an ECL, emits an NRZ PRBS of word length $2^{31} - 1$, at a wavelength of 1549.5 nm. This is combined with CW probe light at 1559.5 nm in a 50/50 coupler, before the signals are launched into a highly confined ($\Gamma = 0.6$), 4 mm long SOA.

Inside the SOA the data signal modulates the carrier density, which leads to an enhancement of the leading edge of the data signal itself due to gain saturation, accompanied by a SPM-induced spectral red-shift and blue-shift of the leading and trailing edges, respectively. The probe signal is cross-gain and cross-phase modulated by the data signal, and acquires a data pattern, which is inverted compared to the data signal, but with similar temporal distortions of the waveform. Moreover, the leading and trailing edges of the probe are also red and blue-shifted, respectively.

Before going into details about the effect of the band-pass filter (BPF) following the SOA, it should be mentioned that the data and probe signals at the output, illustrated in the two upper waveforms in Fig. 7.17, both contain a 40 GHz spectral component without any further processing. This was demonstrated in [171] for the data signal (no probe input), and is due to the asymmetry introduced by the enhanced leading edge of the waveform, which prevents the tone at $f = B$ from canceling out. However, significant improvement in terms of the Carrier-to-Modulation Ratio (CMR) may be obtained through optical filtering [171]. By detuning the 0.3 nm wide (FWHM) BPF after the SOA, the red or blue-shifted edges of the data signal or the wavelength converted probe signal may be selectively filtered out, thereby converting the frequency modulation (FM) into amplitude modulation (AM), and generating the 'edge trigger' signals labeled Red-PRZ and Blue-PRZ in Fig. 7.17.

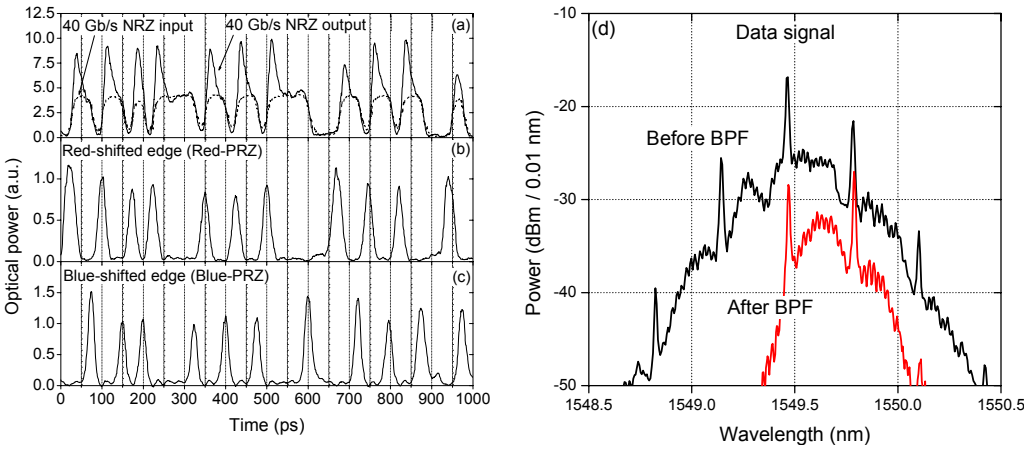

Figure 7.18: (a) 40 Gb/s input signal (dashed) and output signal in large optical bandwidth (solid). (b) Red-shifted PRZ data signal, and (c) Blue-shifted data PRZ. (d) Optical output spectrum of data signal before and after red-shifted BPF.

The CW probe not only allows for a wavelength converted PRZ signal, which may be a useful functionality, as it adds the ability to route the PRZ signal to a specific destination or simply adapt to the optimum operating wavelength of a mode-locked laser. It also serves as a holding beam [45, 174] that reduces the effective carrier lifetime to a level, which enables operation at 40 Gb/s. Actually, without the holding beam, the scheme does not work at 40 Gb/s.

7.7.2 Results

The SOA used in the experiment is very long by any standard, but it should be stressed that the results obtained here could have been obtained with a significantly shorter device. As an example, the 40 Gb/s wavelength conversion experiment presented in section 6.1, which exploits the same principle as explained here, was carried out with an 800 μm long SOA.

Fig. 7.18 (a-c) shows the results, in terms of pulse patterns measured with a 50 GHz photo diode, for the case where the SPM of the data signal is exploited. Thus, in this scenario the probe signal only works as a holding beam, and is not used at the output of the SOA. Fig. 7.18 (a) shows the 40 Gb/s NRZ data at the input (dashed), and the corresponding output pulse pattern (solid), which is measured using a wide 1.3 nm (FWHM) BPF centered on the optical carrier (1549.5 nm). A wide filter is used in this case to prevent shaping the waveform, thereby getting a true picture of the amplitude modulation. Notice that for succeeding '1's a steady-state is reached after only $\approx 25 - 30$ ps of the leading edge, and that the variation of the '1'-level is very low. Both observations are due to the fast carrier recovery, which is a direct consequence of the strong CW holding beam of $\approx$ 10 dBm. The average data power is $\approx$ 7 dBm. Fig. 7.18 (b) and (c) show the results of detuning a 0.3 nm wide filter by $\approx \pm 0.25$ nm

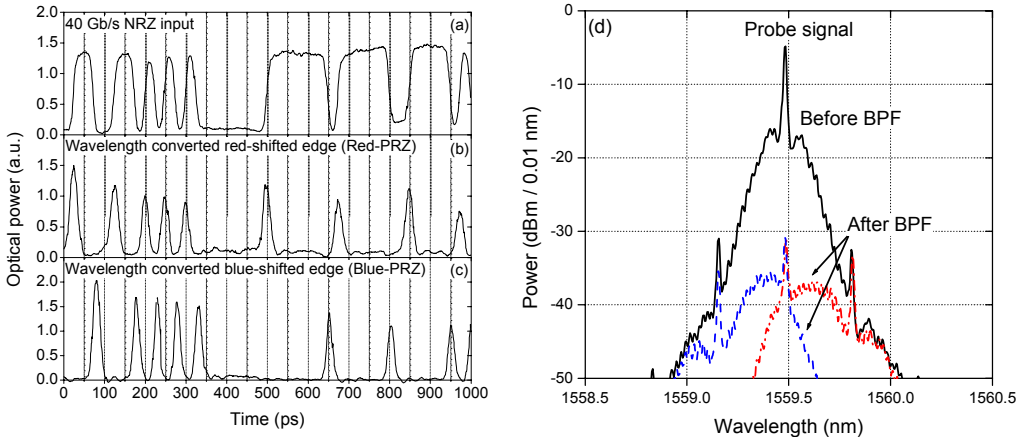

Figure 7.19: (a) 40 Gb/s NRZ input signal, (b) wavelength converted, red-shifted PRZ signal, and (c) blue-shifted PRZ signal. (d) Output probe spectrum before and after BPF for detuning to both red and blue side of the spectrum.

towards longer (red) and shorter (blue) wavelengths, respectively. The reason for the equal optimum detunings is that the spectrum is almost symmetrical. This is illustrated in Fig. 7.18 (d), which shows the optical spectrum of the data signal at the output of the SOA, and the corresponding spectrum after the BPF, shown for a detuning towards longer wavelengths. The symmetry is a result of the large holding beam power, which limits the spectral broadening. As observed, Fig. 7.18 (b) and (c) represent the leading and trailing edges of the NRZ signal, respectively. Even though no two pulses are closer than 50 ps, the timeslot is still 25 ps, which gives a strong 40 GHz component.

Fig. 7.19 shows the equivalent of Fig. 7.18 for the case where XPM of the probe is exploited. Thus, here the holding beam is optically filtered to obtain the PRZ signals. The average power levels used in this case are also $\approx 7/10$ dBm, respectively, for the probe and data, but a larger filter detuning of $\approx \pm 0.45$ nm was required here. This is due to a smaller spectral broadening of the probe, as observed in Fig. 7.19 (d). Thus, in order to obtain the necessary StC ratio for suppressing the DC contents of the probe signal, the filter must be detuned further.

The electrical power spectra in Fig. 7.20 correspond to the input NRZ signal (a), the blue-shifted PRZ data signal (b) and the blue-shifted PRZ probe signal (c). Only spectra of the blue-shifted signals are shown here, but the spectra of the red-shifted signals are close to identical. As indicated in Fig. 7.20 (a), the 40 GHz spectral component is missing from the input signal, whereas a clear component is observed in the spectra of the PRZ signals in Fig. 7.20 (b) and (c). In both cases, the CMR, measured from the peak of the clock to the peak of the remaining signal, is around 20 dB. This is equal to the figures obtained at 2.5 Gb/s in [173] and at 5 Gb/s in [171], and far exceeds the CMR at 10 Gb/s presented in [170] and [172]. Moreover, unlike the approach in [172], the performance of this scheme

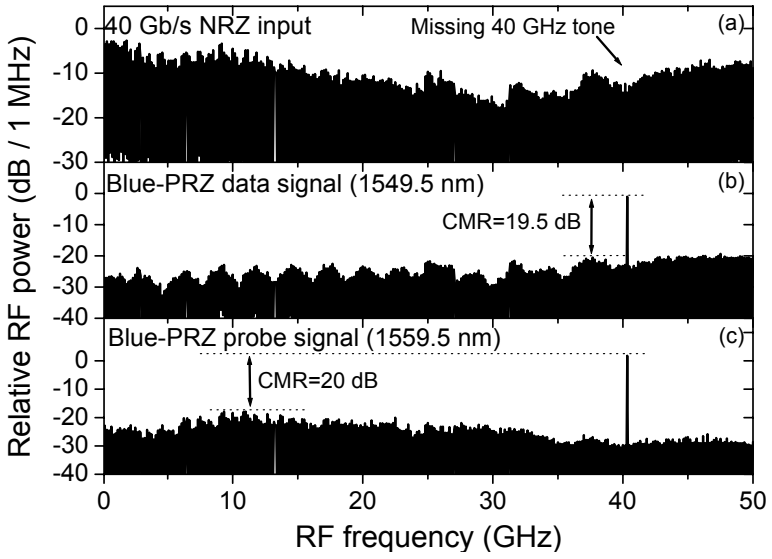

Figure 7.20: Electrical power spectra of input NRZ data (a), blue-PRZ data signal (b), and blue-PRZ probe signal.

is not limited by the transit time effects of counter-propagation [119], and is thus expected to work at bitrates in excess of 100 Gb/s.

The good results are believed to rely on the application of the holding beam, as well as choosing an optimum width and shape for the FM-to-AM conversion filter.

7.8 Summary

All-optical regeneration and enabling subsystems were investigated in this Chapter.

The principle of 2R regeneration, and the influence of the gate nonlinearity was explained, and it was noted that even a perfect "step-function" regenerator cannot reduce the BER. The effect of the regenerator is shaping the probability density functions to minimize the accumulation of errors, which is inevitable as noise is added by EDFAs. Single-regenerator experiments vs. loop experiments was discussed, and it was stipulated that a single regenerator does indeed provide insight into the noise redistributing properties of a nonlinear gate, as long as a noise source is inserted between the gate and the receiver. In practice this is always the case, as the receiver contains several noise sources.

As an example, the 2R regenerative capabilities of an active-passive MZI were investigated at 10 Gb/s. In addition, the tolerance of a 3R regenerator towards accumulated dispersion at 10 Gb/s was analyzed using an all-active MZI. A reduction of the power penalty of approximately 6 dB was achieved after transmission on 50 km of SMF. A 3R regenerator consisting of a cascade of a XGM

wavelength converter and an active-passive MZI, operated in the standard-mode, was tested in a recirculating loop experiment at 40 Gb/s. Mechanical fluctuations prohibited BER measurements beyond 50 laps of 80 km, and at this distance a power penalty of 4 dB was recorded.

A novel type of pass-through 2R regenerator, based on an all-active MMI-SOA, was described and tested at 10 Gb/s with reasonable results, and finally all-optical 40 GHz clock extraction from a 40 Gb/s NRZ signal was demonstrated by exploiting SPM and XPM in a long SOA, combined with FM-AM conversion in a detuned optical band-pass filter. In combination with a mode-locked semiconductor laser, the clock extraction scheme is a promising candidate for a high-speed, format transparent all-optical clock recovery circuit.

Chapter 8

All-optical logic

In future communications networks, optical solutions to simple logic functionalities are expected to present an alternative to present-day electronic signal processing. Optical logic is very immature compared to electronic logic, but potentially faster. Thus, the first optical logic functionalities in the networks are expected to be simple, i.e. consisting of relatively few Boolean logic gates, but operating at a very high bitrate.

In this Chapter, the implementation of the Boolean logic functions NOT, OR, AND, and XOR, using primarily interferometric switches, will be discussed. An experimental demonstration of logic AND at 20 Gb/s, using an all-active MZI is presented. Then, the MZI implementation of the exclusive-OR (XOR) function is analyzed in detail, experimentally as well as theoretically. In particular, the dependence of the XOR performance on the passive phase shift in the MZI, as well as the tolerance towards imperfect temporal pulse synchronism, is investigated numerically. Logic XOR with NRZ input data signals is also analyzed, and fundamental problems are identified.

The logic functions are combined to obtain slightly more advanced functionalities that may be applicable to all-optical networks. A 3− input XOR gate, implemented using two MZI-XOR gates is demonstrated experimentally. In addition, the two XOR gates also realize an all-optical encryption/decryption scheme. Then, a combination of Boolean AND and XOR in a single MZI-XOR gate is used to demonstrate all-optical bit-pattern recognition in segments of 10 Gb/s data. Finally, a compact, all-optical parity calculator, based on a MZI-XOR gate with a feedback, is demonstrated numerically and experimentally.

8.1 Boolean logic

Boolean logic gates are the fundamental building blocks of digital electronics, and realizing the Boolean functions all-optically is therefore a natural first step on the way to more complex digital optical functionalities. The obvious strength

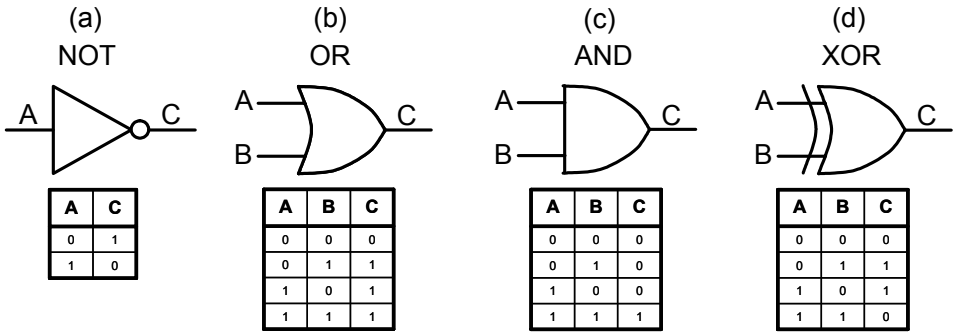

A	C
0	1
1	0

A	B	C
0	0	0
0	1	1
1	0	1
1	1	1

A	B	C
0	0	0
0	1	0
1	0	0
1	1	1

A	B	C
0	0	0
0	1	1
1	0	1
1	1	0

Figure 8.1: Equivalent symbols and truth tables for the Boolean logic gates (a) NOT, (b) OR, (c) AND, and (d) XOR.

of electronic logic is the ability to integrate thousands, or even millions, of gates on a single chip, enabling very advanced functions in a compact device. Before optical logic components reach a level of maturity enabling large scale integration, a number of fundamental problems must be solved. First, the size of the gates must be reduced. Currently, the smallest optical logic gates are still $1 - 4$ mm long, not counting necessary external hardware such as filters and polarization controllers. The second hurdle is the need for optical filtering. Most optical gates are switches driven by an optical control signal on a wavelength different from that of the switched signal. This implies the need for an optical filter at the output to distinguish the switched signal from the control signal, which adds significantly to the integration complexity. Moreover, filter tunability is needed when the gates are operated in a WDM environment. In addition to these two problems, which are particularly serious for high-scale integration, the optical gates must of course be able to operate at bitrates exceeding the limits of electronics, and be polarization independent, etc.

In the following, the pros and cons of different all-optical implementations of Boolean logic gates are discussed, with special focus on SOA-based gates.

8.1.1 The NOT gate

Together with the AND and OR gates, the NOT gate - the inverter - forms a set universal gates, from which all other Boolean functions can be formed.

All-optical implementations include all wavelength converters able to provide a polarity-inverted output, e.g. interferometric wavelength converters operated in out-of-phase mode. For the MZI, this is illustrated in Fig. 7.7 (j), which represents the logic NOT function of the data signal in Fig. 7.7 (g). In this example, the inverted signal is sampled by a clock, thereby preventing "dark" pulses, which may cause problems at the inputs of subsequent gate. Using a semiconductor based MZI as a NOT gate by launching a clock signal into the common arm, and data into one of the interferometer arms, was proposed as early as 1984 [175].

The simplest realization of the NOT gate is the XGM wavelength converter, or alternatively the DISC, if very high speed operation is required. Using the UNI, all-optical NOT has been demonstrated at 100 Gb/s [176]. Fig. 8.1 (a) shows the symbol for the NOT gate, along with its truth table.

8.1.2 The OR gate

The symbol and truth table for the OR gate is shown in Fig. 8.1 (b). Since the two-input OR gate only gives a "0" at the output if both input are "0", the function may be realized with a saturable device, i.e. a device for which the output power level is independent of whether the input level increases by a factor of two. The inverted OR gate, the NOR gate, may be realized by simple XGM [177, 178]. The two data signals participating in the NOR operation are launched into an SOA along with a probe signal at a different wavelength. The power level in the two data signals is such that if just one of the two goes high, the SOA gain is completely saturated, which pulls the output probe power low. If both inputs are high at the same time the outcome is the same.

Interferometric switches are also compatible with OR and NOR due to the nonlinear transfer function, which is flat around the maxima. The NOR function is obtained by operating on the negative (inverting) slope of the transfer function (see Fig. 5.3 (b)), whereas OR is realized by operating on the positive slope. Both functions have been demonstrated at 10 Gb/s using a UNI gate [179]. In addition, optical OR has been obtained with an all-active Michelson interferometer, also at 10 Gb/s [180].

8.1.3 The AND gate

As illustrated in Fig. 8.1 (c) the AND gate is unbalanced like the OR gate, as it only gives a "1" at the output in the event that both inputs are "1". From the truth table it is clear that the AND operation corresponds to sampling one signal with the other, and thus all-optical sampling techniques may be applied to obtain the AND function. For example, interferometric switches used for 3R regeneration may be configured as two-input AND gates by simply replacing the clock signal with another data signal. This has been demonstrated with a MZI at 10 Gb/s [181] using PRBS data, and at 20 Gb/s using short periodic 4−bit data patterns [182]. Again, this particular application of the MZI was suggested in 1984 [175].

Here, a demonstration of all-optical AND using an all-active MZI at 20 Gb/s, using PRBS data of word length $2^7 - 1$, is demonstrated. The experimental setup is shown in Fig. 8.2. The two 20 Gb/s RZ data signals are generated from two mode-locked locked lasers, emitting 10 GHz trains of ≈ 2 ps wide (FWHM) pulses at 1550 nm and 1544 nm, respectively. The pulse trains are independently modulated with 10 Gb/s PRBS data of word length $2^7 - 1$, then combined in a 3 dB coupler before being multiplexed up to 20 Gb/s in a fiber-based interleaver

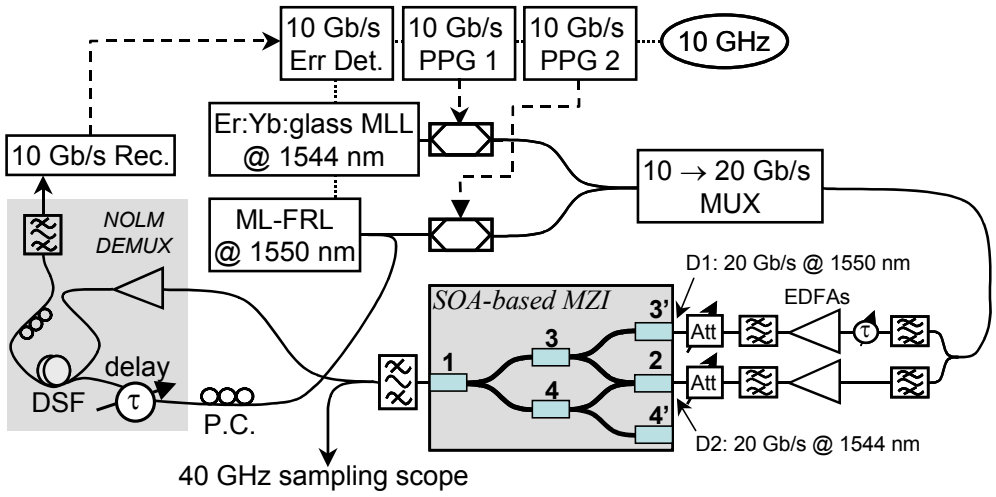

Figure 8.2: Setup for experimental demonstration of logic AND at 20 Gb/s using a MZI. MLL: mode-locked laser.

(MUX). At the output of the MUX, the wavelengths are separated by band-pass filtering, and the timeslots of the two 20 Gb/s data streams are aligned by means of an optical delay line. Both signals are amplified in EDFAs before being launched into ports $3'$ and 2 of the MZI. Inside the switch, which is the same device used for the experiment in section 7.3, the signal launched into port 2 (D2) interferes destructively at the output when no signal is applied to port $3'$ (D1 off). In other words, the interferometer is biased to in-phase operation. Turning D1 on opens the switching window, allowing transmission of D2, and thereby the function D1 AND D2 is obtained at the output of the MZI, after suppression of D1 in a BPF. Operating the MZI in out-of-phase mode does not provide the logic NAND, but represents the hybrid function NOT(D1) AND D2 [181].

The average input powers used were 3 dBm and 7 dBm for D1 and D2, respectively. The AND output is demultiplexed to the two 10 Gb/s tributaries in the NOLM, described in section 6.2.1, before pre-amplified reception and error detection. Boolean AND is unbalanced, i.e. the mark density is only 0.25, and the function D1 AND D2 is not a PRB sequence, which means that the error detector must be programmed. The correct sequence may be calculated on a computer and transferred to the error detector via the GPIB[1] interface. However, software for such an operation was not available, which means that the error detector must be programmed by manually keying in the calculated bit pattern. For practical reasons, this limited the word length to a relatively small number of bits, and in this case $2^7 - 1 = 127$ was used.

The input pulse patterns at 1550 nm (D1) and 1544 nm (D2) are shown in Fig. 8.3 (a) and (b), respectively. The output D1 AND D2 at 1544 nm is given

[1] GPIB: General Purpose Interface Bus

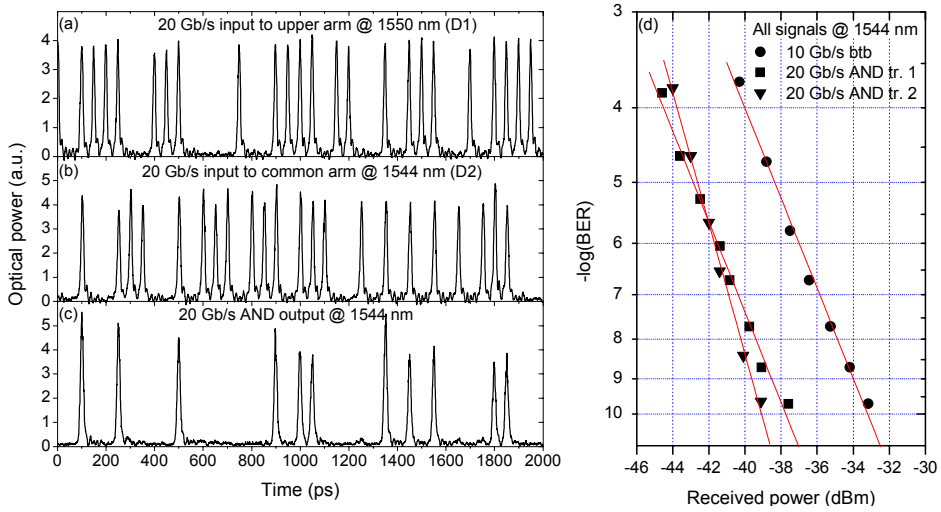

Figure 8.3: 20 Gb/s input signals to (a) upper arm at 1550 nm and (b) common arm at 1544 nm, and (c) logic AND output. (d) BER curves: back-to-back and demultiplexed 20 Gb/s AND tributaries.

in Fig. 8.3 (c). As can be observed, the extinction ratio is very high (> 13 dB), and an OSNR of 32 dB/0.1 nm is measured. The BER performance is illustrated in Fig. 8.3 (d), where the 10 Gb/s back-to-back (btb) curve is compared to the two BER curves of the two demultiplexed tributaries of the AND signal. The large sensitivity improvement of $\approx 4.5-5$ dB observed in Fig. 8.3 (d) has several contributions. First, the 10 Gb/s btb signal is a PRBS 2^7-1 with a mark density of 0.5, whereas the AND tributaries have a mark density of 0.25. Thus, for equal pulse energies (or eye opening) the average received power is a factor of 2 (3 dB) lower for the AND signal, which by itself gives rise to 3 dB sensitivity improvement. In addition, since the dominant noise source in the pre-amplified receiver is signal-spontaneous beat noise [158], and the power in the "0" level is very small, the variance of the pdf representing the "0" level, σ_0, is expected to be significantly smaller than the corresponding pdf, σ_1, for the "1" level. Consequently, by lowering the density of "1"s the total overlap between the pdfs, and thus the BER, decreases. Theoretically, a change of mark density from 0.5 to 0.25 reduces the BER by a factor not exceeding 2, which does not by itself give rise to the remaining sensitivity improvement. This is seen by noting that, assuming Gaussian pdfs, the BER may be expressed as

$$\begin{aligned} BER &= (1-p_1)p_{1/0} + p_1 p_{0/1} \\ &\approx \frac{1-p_1}{2}\,\mathrm{erf}\,c\left(\frac{z_D-E_0}{\sqrt{2}\sigma_0}\right) + \frac{p_1}{2}\,\mathrm{erf}\,c\left(\frac{E_1-z_D}{\sqrt{2}\sigma_1}\right) \end{aligned} \tag{8.1}$$

where p_1 is the mark density, $p_{1/0}$ and $p_{0/1}$ are the probabilities of detecting a "0" as a "1" and a "1" as a "0", respectively, and z_D, E_0, and E_1 are the decision threshold and "0" and "1" bit energies, respectively. For $z_D = E_0$

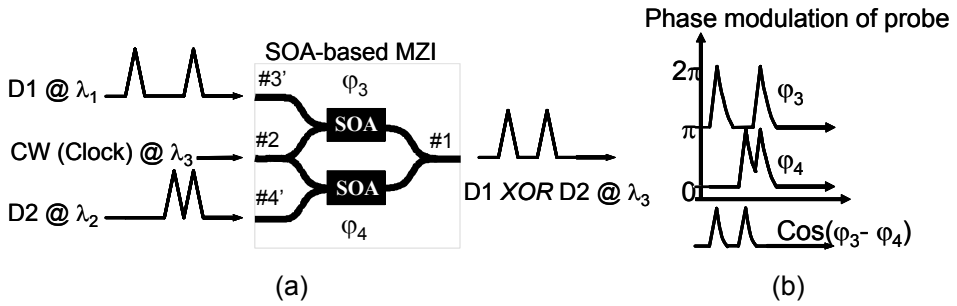

Figure 8.4: (a) Principle of logic XOR in MZI. (b) Probe phase in upper/lower arms, and corresponding phase difference.

the second term of (8.1) can be neglected, giving BER change of a factor of $(1-0.25)/(1-0.5) = 1.5$, i.e. an increase of 50%, when changing p_1 from 0.50 to 0.25. Analogously, the first term of (8.1) may be neglected for $z_D = E_1$, which modifies the BER by a factor of $0.25/0.5 = 0.5$, corresponding to a 50% decrease. The minimum BER is obtained for a value of z_D in between the two extremes, and by solving (8.1) for the optimum z_D numerically, it is found that for $\sigma_1 >> \sigma_0$ the minimum BER is reduced by close to 50% by reducing p_1 from 0.50 to 0.25. The improvement of the sensitivity, which is not already accounted for, is attributed to a dependence of the receiver on RF-spectral distribution of the signal.

All-optical AND has also been realized with 10 Gb/s RZ input signals using an EAM [183], in a setup that has also demonstrated 3R regeneration with simultaneous clock recovery [184]. A partial demonstration of logic AND between a 100 Gb/s data signal and a 100 GHz clock signal has been carried out with a UNI gate [176]. Finally, FWM in an SOA has been used to demonstrate AND at 10 Gb/s with NRZ input signals [185].

8.1.4 The XOR gate

The XOR gate, shown in Fig. 8.1 (d) including its truth table, gives a "1" at the output if one, and only one, of the two inputs is a "1". More generally, an XOR gate with an arbitrary number of inputs gives a "1" at the output if the parity of the input bits is 1, i.e. if the number of "1"s is odd. This property of the XOR gate makes it suitable for a wide variety of applications related to bit-comparison and encryption, which will be demonstrated in section 8.2.

As for the NOT and AND gates, the MZI implementation of the XOR gate was also suggested in 1984 [175]. The first experimental proof-of-principle demonstration of XOR with an integrated interferometric wavelength converter was made in 1997 with an SOA-based MZI using 5 Gb/s NRZ input data. Since then, operation at 10 and 20 Gb/s has been demonstrated with an all-active MZI [186], including BER measurements at 10 Gb/s with negligible power penalty, as well as with an all-active MI, employed in a label-swapping scheme at 10 Gb/s [22].

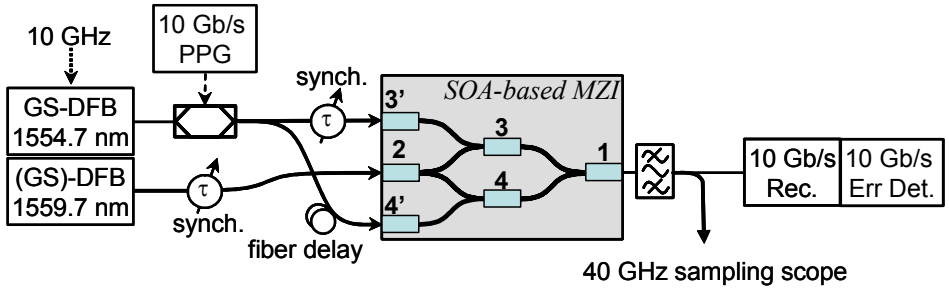

Figure 8.5: Setup for experimental demonstration of logic XOR in MZI, with CW or pused input probe signal.

Fig. 8.4 (a) illustrates the principle of operation of an MZI-based XOR gate. The interferometer is biased ti in-phase operation, which causes the probe - either CW or pulsed - to interfere destructively at the output when both data signals (D1 and D2) are off. Hence, when the data is turned on, a pulse in either data signal opens a switching window, allowing transmission of the probe. In the event that pulses in D1 and D2 are synchronized, equal phase shifts are introduced in both arms, which causes no net change of the phase difference. Thus, as detailed in Fig. 8.4 (b), two "1"s at the input gives rise to destructive probe interference at the output, which complies with the XOR truth table in Fig. 8.1 (d). Using the same arguments as above, one would think that the logic XNOR function, i.e. NOT(XOR), may be realized by operating the MZI on the inverting flank of the transfer function. However, this requires that the output remains "1" for (D1, D2) = ("1", "1"), and this is not possible, due to XGM in the interferometer arms.

The all-active MZI, used to demonstrate the AND function above, has also been employed as an XOR gate at 10 Gb/s. The experimental setup is sketched in Fig. 8.5, where EDFAs, attenuators, and polarization controllers at the inputs have been omitted for clarity. A gain-switched DFB laser emits a 10 GHz train of $\approx$ 25 ps wide (FWHM) pulses at 1554.7 nm, which is modulated with 10 Gb/s PRBS data of word length $2^7 - 1$. By splitting the data signal, and delaying one with respect to the other, the two data inputs D1 and D2 (see Fig. 8.4 (a)) are formed. The timeslots of D1 and D2 are aligned with a optical delay line, inserted into the path of D1. The probe signal can either be a clock signal or CW light, and the two options are compared by turning the gain-switching RF signal to a DFB laser at 1559.7 nm either on or off, respectively. When the laser is gain-switched it emits a 10 GHz pulse train of $\approx$ 25 ps wide (FWHM) pulses, which are aligned to the data pulses using an optical delay line. The BPF at the output of the MZI suppresses the data signals, and passes the XOR probe signal at 1559.7 nm on to a sampling oscilloscope and a receiver. As for the AND demonstration, the error detector is programmed to receive the XOR function between PRBS $2^7 - 1$ signals, delayed by 4 bits. However, PRB sequences are

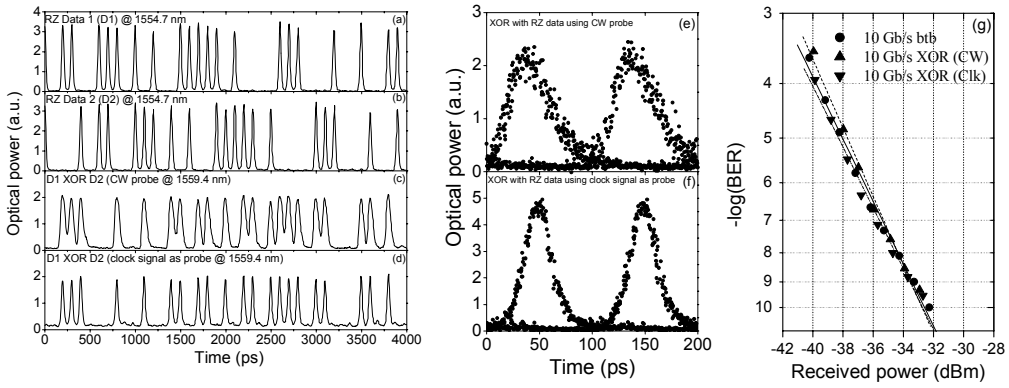

Figure 8.6: (a,b) Input signals at 10 Gb/s, (c) XOR output with CW probe, (d) XOR output with pulsed probe, (e,f) comparison of XOR eye diagrams employing CW and pulsed probe, respectively. (g) BER curves.

obtained by XOR'ing two or more outputs from a shift register, and feeding the result back to the input. In particular, the sequence of length $2^7 - 1$ is obtained like $X_n = X_{n-7} \oplus X_{n-6}$ [187], where X is the output bit and $\oplus$ denotes XOR. Had the delay between D1 and D2 been chosen as 6 (or 7) bits, the output of the MZI XOR gate would have been $Y_n = X_n \oplus X_{n-6} = X_{n-7} \oplus X_{n-6} \oplus X_{n-6} = X_{n-7}$, i.e. a PRB sequence of length $2^7 - 1$, delayed by 7 bits. This technique has been used to make BER measurements on a 10 Gb/s XOR result with two PRBS $2^{31} - 1$ inputs [188].

The experimental results are given in Fig. 8.6, in the form of bit patterns, eye diagrams and BER measurements. Figs. 8.6 (a-b) show the pulse patterns of input data signals D1 and D2, and Figs. 8.6 (c) and (d) show the output pattern, D1 XOR D2, for a CW probe and a pulsed probe, respectively. It is clear from the eye diagram in Fig. 8.6 (e), which corresponds to the pattern in Fig. 8.6 (c), that the CW probe gives rise to broadened, slightly asymmetric output pulses, due to the finite modulation bandwidth of the SOAs. Substituting the CW beam with a pulsed signal corresponds to sampling the eye diagram in Fig. 8.6 (e) with the clock pulses, and the result is given in the eye diagram of Fig. 8.6 (f) for comparison. However, as illustrated in the BER measurements in Fig. 8.6 (g), the receiver is insensitive to the minor variation of the pulse symmetry and width; both XOR signals are detected with no power penalty. The input powers and bias currents in the present experiment were $P_{C,3}/P_{C,4}/P_P/I_1/I_2/I_{3'}/I_{4'}/I_3/I_4 =$ 3 dBm/1.6 dBm/5.6 dBm/100/80/40/40/280/400 mA, and the OSNR at the output was 33 dB/0.1 nm.

As explained above, the MZI must operate in-phase. For a MZI based on $1x2$ and $2x1$ power splitters with no passive phase offset, the only way to obtain this is by introducing a π phase shift in one of the arms by biasing the long SOAs in the interferometer arms asymmetrically. This implies that the gain, and hence the effective carrier lifetime, is different in the two interferometer arms, which

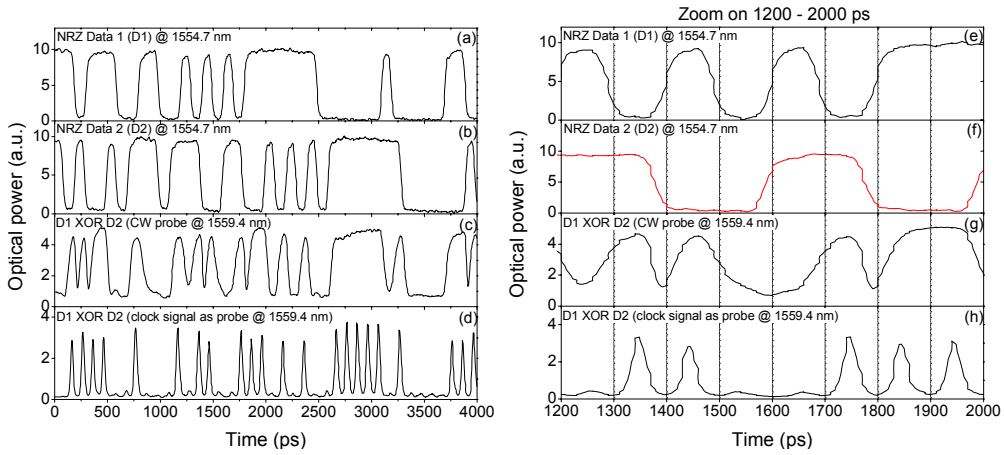

Figure 8.7: XOR with NRZ input data. (a,b) Input 10 Gb/s NRZ signals, (b) XOR output with CW probe, (d) XOR output with pulsed probe. (e-h): zoom on (a-d) in the range $1200 - 2000$ ps.

presents a problem when the MZI is employed as an XOR gate. In the following, the different lifetimes in the arms will be verified by considering NRZ input data, where the implications are the most noticeable. The interferometer arm with the highest/lowest bias current will be referred to as the fast/slow arm.

Fig. 8.7 (a-d) shows the equivalent of Fig. 8.6 (a-d), with RZ input data replaced by NRZ data. The pattern in Fig. 8.7 (c) represents D1 XOR D2, but by close inspection it is observed to be distorted by specific combinations of bit-transitions at the input. More specifically, problems occur when D1 goes from "0" to "1" while D2 goes from "1" to "0", and vice versa, during which the output is expected to remain "1". However, the phase shift associated with a "0"$\rightarrow$ "1" transition occurs on a time scale defined by the signal rise time and the stimulated carrier lifetime, whereas the phase shift brought about by a "1"$\rightarrow$ "0" transition is limited by carrier recovery. Thus, a "dip" in the output power is inevitable during the transition. This is clearly illustrated in Fig. 8.7 (e-h), which is a zoom on Fig. 8.7 (a-d) on the time span $1200 - 2000$ ps.

Moreover, since the carrier density in one interferometer arm recovers faster than in the other, the phase difference $\phi_3 - \phi_4$ changes on three different time scales. This is illustrated in Fig. 8.8 (a), where the probe phase in the two arms, ϕ_3 and ϕ_4, as well as the absolute phase difference $|\phi_3 - \phi_4|$ is sketched. The different phase recovery times of ϕ_3 and ϕ_4 are indicated by a dashed/dash-dotted exponential for ϕ_3 and ϕ_4, respectively. From the bottom trace of Fig. 8.8 (a) it is clear that the phase difference, and consequently the output signal, contains three distinct time constants. By close inspection of the experimental eye diagram in Fig. 8.8 (b) three distinct traces are visible, particularly in the rising flank, which verifies the existence of three different time constants. The phenomenon leads to pattern dependent timing jitter, which causes a BER floor around 10^{-7}. Decreasing the carrier lifetime by increasing the MZI arm length

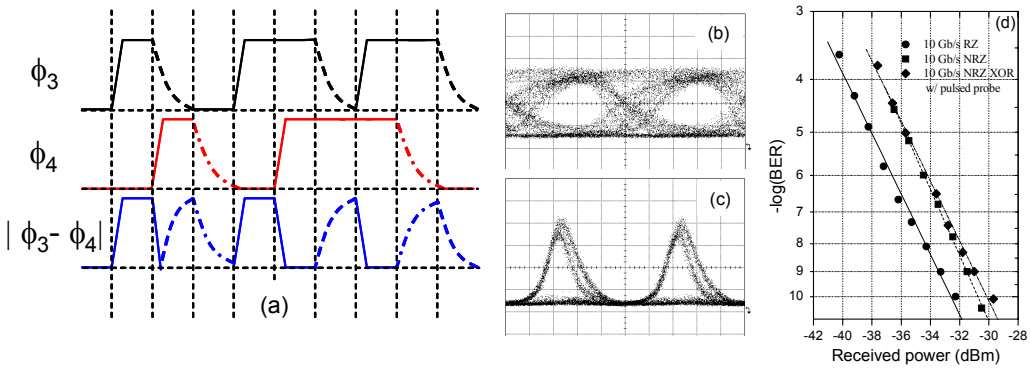

Figure 8.8: (a) Sketch of probe phases in the two interferometer arms of a MZI during XOR operation with NRZ data. (b,c) Comparison of XOR eye diagrams with and without pulsed probe signal, respectively. (d) BER curves.

and/or CW input power, and modifying the MZI design to facilitate equal SOA gains in the two arms, while maintaining a π phase offset, will equalize the "fast" and "slow" recovery times, and bring them closer to the stimulated lifetime.

By sampling the XOR switching window with a clock signal the pattern dependent jitter is reduced. Fig. 8.8 (c) shows the eye diagram corresponding to the pulse pattern in Fig. 8.7 (d), and the serious distortion is reduced to a double-trace. As explained previously, the RZ format gives rise to a better receiver sensitivity than NRZ, with a power penalty depending on the duty cycle. According to the BER measurements presented in Fig. 8.8 (d), the sampled NRZ XOR signal is detected with a power penalty of 2.3 dB compared to the 10 Gb/s RZ baseline, but only a 0.5 dB penalty compared to the NRZ baseline. In other words, due to the NRZ $\rightarrow$ RZ format conversion, the power penalty for the somewhat distorted signal represented by the eye diagram in Fig. 8.8 (c), is only 0.5 dB, compared to the input NRZ signal.

Synchronization

In the experiments presented above, the two data signals were synchronized manually with an optical delay line. In a practical implementation however, synchronization must be handled by an optical or optoelectronic subsystem, and the performance of these systems may be critical to the overall performance of the logic gate. These issues are investigated numerically in [p15] for an XOR gate based on a MZI with SOAs in the interferometer arms only, by evaluating the tolerance of the gate towards imperfect synchronism of the two signals participating in the XOR operation.

Fig. 8.9 (a) shows the excess power penalty vs. synchronization delay of the data signal to the slow interferometer arm for the XOR result between two 40 Gb/s RZ data signals. The signals consist of 5 ps wide (FWHM) Gaussian pulses modulated with PRB sequences of word length $2^5 - 1$. The parameter in Fig. 8.9

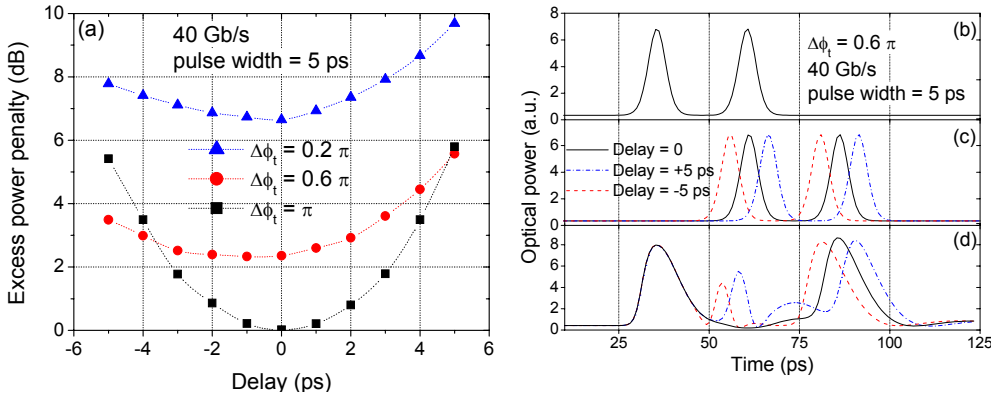

Figure 8.9: (a) Excess power penalty at 40 Gb/s of XOR signal vs. synchronization delay of RZ input signals, with the passive phase shift as a parameter. (b,c) signals to the fast and slow arms of the MZI, respectively, and (d) the corresponding XOR output.

(a) is the passive phase shift $\Delta\phi_t$. Not surprisingly the power penalty increases as $\Delta\phi_t$ is decreased from π, due to the reduced extinction (see e.g. Fig. 5.3). In addition, the penalty curve is observed to be symmetric for $\Delta\phi_t = \pi$, but asymmetric for $\Delta\phi_t < \pi$. The symmetry is obtained because the SOAs are biased equally for $\Delta\phi_t = \pi$, which means that the carrier lifetime is identical in the two arms. Thus, it makes no difference which of the SOAs is excited first. However, for $\Delta\phi_t < \pi$ the SOAs must be biased asymmetrically to obtain a π phase offset. As explained above, this leads to a "slow" and "fast" arm. Fig. 8.9 (b-d) shows part of the signal to the fast arm (b), slow arm (c), and the resulting XOR signal (d), for $\Delta\phi_t = 0.6\ \pi$. The signal to the slow arm is delayed by -5 ps (dashed), 0 ps (solid), and $+5$ ps (dash-dotted) compared to perfect timeslot synchronization to the signal in the fast arm.

As observed in Fig. 8.9 (d), the temporal misalignment leads to satellite pulses in the timeslot from $50 - 75$ ps, and the pulses contain more energy for positive delays. Since the SOAs are strongly saturated by a CW probe of 26 dBm, and data signal powers of around 20 dBm, the phase shift introduced in the two arms is almost identical. Thus, the difference observed for delays of $+5$ ps and -5 ps between the satellite pulses right after $t = 50$ ps in Fig. 8.9 (d) are solely due to patterning. The phase shift in the slow arm 'subtracts' from the trailing edge of the response in the fast arm for a negative delay, whereas for a positive delay the phase shift induced by the second pulse in the fast arm simply adds to the phase difference. Hence, whether the peak of the satellite pulse after $t = 50$ ps is higher for positive or negative delays depends on the bit patterns at the inputs. For long bit sequences this is completely symmetric, and consequently does not contribute to the asymmetry observed in Fig. 8.9 (a). However, if the signal to the slow arm arrives a little early (negative delay) the trailing edge of the "slow" phase response may cancel the trailing edge of the "fast" response, as shown by the dashed curve of Fig. 8.9 (d), corresponding to a delay of -5 ps. For the

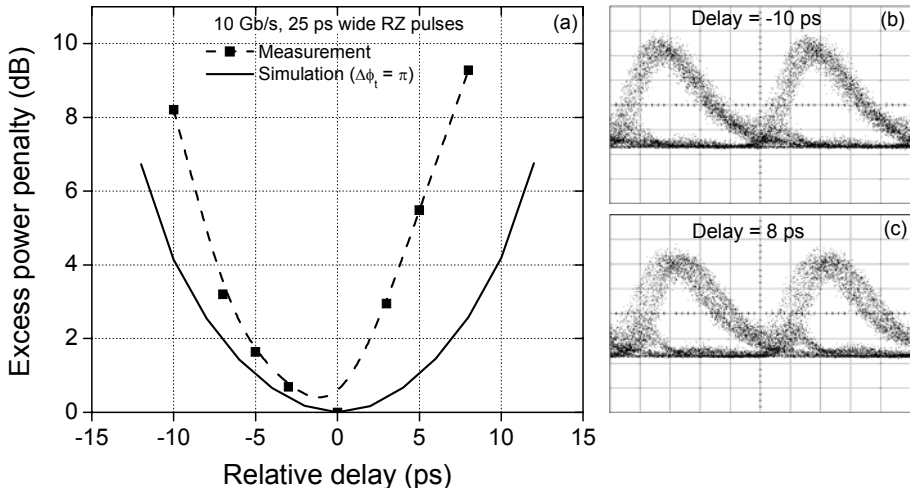

Figure 8.10: (a) Experimental (squares) and simulation (solid curve) of excess power penalty of 10 Gb/s XOR operation in MZI with RZ signals vs. synchronization delay. (b,c) experimental XOR eye diagrams for delay of −10 ps and 8 ps, respectively.

positive delay, +5 ps, the trailing edges of the "slow" and "fast" responses are misaligned, which causes the additional satellite peak around $t = 75$ ps, shown in the dash-dotted curve of Fig. 8.9 (d). This explains the asymmetric penalty curves in Fig. 8.9 (a).

Fig. 8.10 (a) shows a comparison at 10 Gb/s between the measured and simulated synchronization tolerance. The simulation is carried out for $\Delta\phi_t = \pi$, and overestimates the tolerance, which may in part be due to the choice of receiver parameters. Notice that the measured penalty curve is asymmetric as predicted in Fig. 8.9 (a), indicating that the passive phase difference is not equal to π. This is furthermore supported by the choice of bias currents, which is listed previously in this section. Fig. 8.10 (b) and (c) shows the measured XOR eye diagrams corresponding to delays of −10 ps and +8 ps, respectively. The before mentioned satellite peaks are visible, and more pronounced for positive delays, confirming the modeling results.

Alternative implementations

Boolean XOR may be obtained from Boolean AND and OR by the following operation

$$A \textbf{ XOR } B = A\underline{B} \textbf{ OR } B\underline{A} \tag{8.2}$$

where the underline denotes logical inversion (NOT). The equivalent diagram is shown in Fig. 8.11 (a).

Using (8.2), an all-optical XOR gate has been implemented in the Michelson interferometer structure shown in Fig. 8.11 (b) [189]. However, the principle of operation does not rely on interference. In the upper SOA, signal A is cross-gain

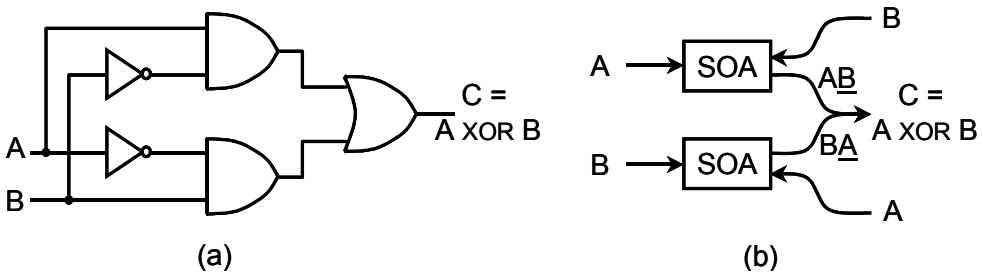

Figure 8.11: (a) Implementation of XOR gate from AND and XOR gates. (b) Optical equivalent with SOAs.

modulated (XGM'ed) by signal B, which yields $A\underline{B}$ at the output on the right-hand side. At the same time, signal B is XGM'ed by signal A in the lower SOA, whereby $B\underline{A}$ is obtained. Since no combination of A and B exists, for which $A\underline{B}$ and $B\underline{A}$ are both "1", the OR operation may be realized by simply merging the two products in a fiber coupler. This approach has been used to demonstrate XOR between 4 bit words at 10 Gb/s. Potential problems related to this scheme include bandwidth limitations due to transit-time effects, and the fact that two circulators or four isolators are required to implement the right-hand side of Fig. 8.11 (b). The requirement for circulators or isolators effectively prevents integration. Merging the two sub-products in a coupler presents a problem if A and B are at the same wavelength, since fluctuations may arise from interference if the extinction ratio is not large enough [p15],[p16]. In addition, the scheme requires synchronization at four interfaces, compared to just two for the MZI operated with a CW probe. However, unlike the MZI and other interferometric switches, no additional probe signal is needed, which is an advantage as it saves the cost of the additional laser.

Other interferometric switches are capable of carrying out the XOR operation. The UNI gate presented in section 5.2.3 may be configured as an XOR gate by injecting an additional data signal (see Fig. 5.15) aligned to the leading of the two delayed, orthogonal clock pulses. However, if the response time exceeds the timeslot, the phase shift imposed on the leading clock pulse is also experienced by the trailing pulse. Consequently, the UNI gate does not rely on a differential phase shift when operated as an XOR gate. This is inherent for single-SOA interferometric switches; the speed limitation is ultimately defined by the carrier recovery time, just as for the MZI implementation described above. This is the reason why XOR has only been demonstrated at moderate bitrates, using 20 Gb/s data and a 20 GHz clock signal as the two inputs [190], and at 40 GHz where the signal consisted of combinations of a 40 GHz clock and no signal (logic "0") [191]. In comparison, wavelength conversion and Boolean AND, where only one of the two split clock pulses is addressed, thus enabling a real differential phase shift, has been demonstrated up to 100 Gb/s [176].

The TOAD switch, illustrated in Fig. 5.14, suffers from the same speed limita-

tions when operated as an XOR gate, which is described in detail in [192]. So far, the TOAD has been used to demonstrate XOR at bitrates up to 10 Gb/s [193].

A novel scheme enabling Boolean XOR in an MZI operated in the differential mode, thus alleviating the speed limitation caused by linear patterning, has been proposed [194]. The principle is demonstrated at 10 GHz in [195], and verified with 40 Gb/s input data in [196], with significant patterning effects, however. The scheme involves launching both participating data signals into each data port ($3'$ and $4'$), with a differential delay of $+\tau$ in one port and $-\tau$ in the other. According to [194] this technique allows for all-optical XOR up to 100 Gb/s.

In a very recent demonstration, FWM in an SOA between differential phase shift keying (DPSK) modulated RZ data signals was exploited to obtain all-optical XOR at up to 20 Gb/s [197]. Since the gain modulation in the SOA is periodic, patterning effects are avoided. At higher bitrates the scheme is expected to benefit from using increasingly narrow pulses, since this will enhance intraband dynamic effects that are effective on a much shorter time scale (see eq. (3.1)).

Finally, it should be mentioned that by replacing the nonlinear element in the UNI or TOAD with a nonlinear fiber, XOR is feasible at higher bitrates, at the cost of increased switching energy. E.g., in a folded version of the UNI gate with DSF as the nonlinear medium, XOR was demonstrated at 40 Gb/s [188].

8.2 Logic functionalities for all-optical networks

By themselves, the logic gates presented in the previous section represent only limited functionality. However, by combining just a few gates it is possible to obtain functions that may be applicable in a future all-optical network. The literature contains plenty of examples of fairly advanced logic functions comprising only a few SOA-based gates, and in some cases, an optical feedback. Examples include regenerative all-optical memories [198–200], binary half- and full adders [201–203], a binary counter [204], Circulating Shift Registers (CSRs) [205–209], a pseudo-random number generator [192], a parity checker [210], all-optical flip-flops [211–214], and all-optical packet synchronization with address comparison [17]. Apart from the flip-flops, almost all the demonstrations listed above were carried out with fiber/SOA hybrid UNI or TOAD gates. However, all functions could equally well be implemented with integrated SOA-based switches, such as MZIs, which adds the advantage of reduced footprint.

This section describes experiments, giving examples of all-optical functionalities obtained by combining MZI-based logic gates are demonstrated. All experiments are carried out with the all-active MZIs used for the demonstrations in sections 7.3 and 8.1.4. These devices are designed for operation at 10 Gb/s [215], and although they are capable of operating at 20 Gb/s, the focus was on demonstrating functionality, rather than uncovering the speed potential. First, two MZIs are combined to form a 10 Gb/s 3-input XOR gate, which may be used to check the parity of 3-bit words, or to realize a 2-input XNOR gate. Moreover,

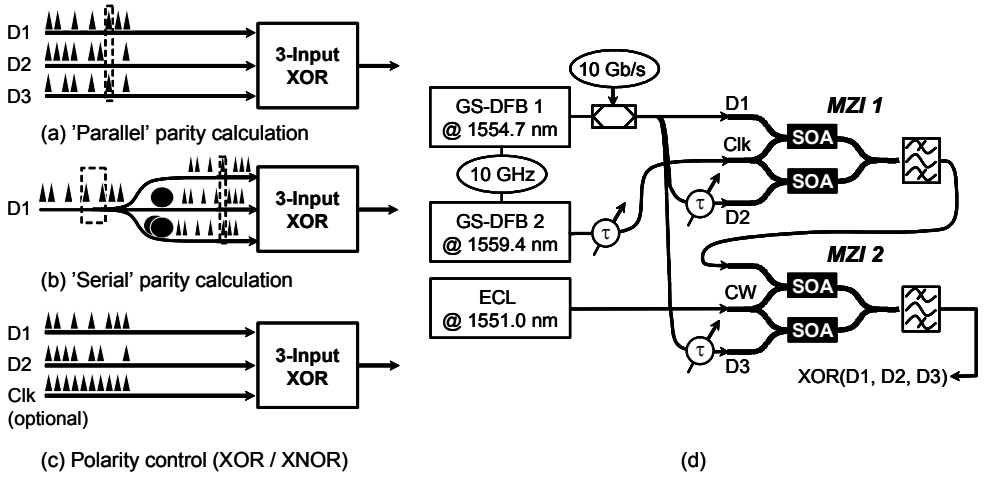

Figure 8.12: Applications of 3−input XOR gate: (a) parallel parity calculation, (b) serial parity calculation, and control of output polarity of 2−input XOR gate (XOR/XNOR). (d) Experimental setup for optical implementation of 3−input XOR gate.

the two XOR gates also simulate encryption and decryption. Then, a single MZI demonstrates bit-pattern recognition in *segments* of input data, defined by an external gating signal. Finally, an attempt is made at demonstrating all-optical parity calculation as in [210], employing a single all-active MZI with the peripheral SOAs used as feedback amplifiers. Logic and physical modeling assist the experiments in verifying the potential of the MZI for this application.

8.2.1 3-input XOR gate

This section demonstrates a 3-input XOR gate operating at 10 Gb/s. Parts of the results were published in [p16].

Fig. 8.12 (a-c) illustrates how the third input may be used to calculate the parity of 3-bit words defined by the three parallel data streams D1, D2, and D3, as shown in Fig. 8.12 (a). Alternatively, a single data stream, D1, can be parallelized as in Fig. 8.12 (b) by splitting it in three branches, and introducing an incremental delay of one timeslot between them. In this scheme, the output represents the parity of the bits within a 3-bit window of D1, which may be considered as a low level check of the data integrity, if D1 is coded accordingly. In other words, the function represented by Fig. 8.12 (b) could serve as a building block in a very primitive optical Forward Error Correction (FEC) scheme. As illustrated in Fig. 8.12 (c), the third input may also be used to invert the result of XOR between two other inputs, D1 and D2, to obtain the XNOR function.

As shown in the experimental setup in Fig. 8.12 (d) the 3-input XOR is realized by cascading two individual MZI-XOR gates: D1 XOR D2 XOR D3 = (D1 XOR D2) XOR D3. EDFAs and polarization controllers are omitted in the figure for simplicity. The three data signals (D1, D2, and D3) participating in the

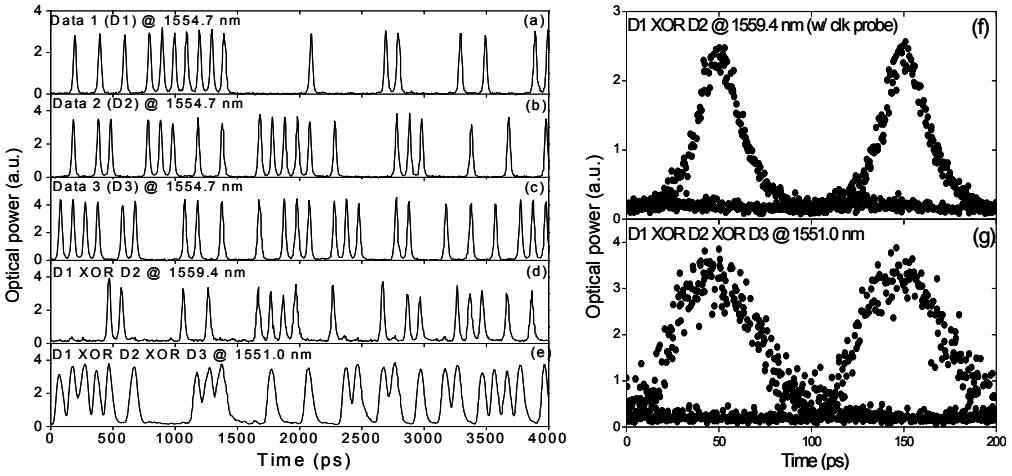

Figure 8.13: (a-c) Three 10 Gb/s input signals (D1, D2, and D3), (d) D1 XOR D2, (e) D1 XOR D2 XOR D3. (f,g) Eye diagrams corresponding to D1 XOR D2 and D1 XOR D2 XOR D3, respectively.

XOR operation all originate from the same gain-switched DFB laser (GS-DFB 1). This source emits a 10 GHz train of $\approx$ 25 ps wide (FWHM) pulses at a wavelength of 1554.7 nm, which is subsequently modulated with a PRB-sequence of word-length $2^7 - 1$. Variable delay lines in the arms carrying D2 and D3 align the data signals temporally, before they are coupled into the gates, denoted MZI 1 and MZI 2, respectively.

Focusing first on MZI 2, the XOR operation between D3 and the output of MZI 1 is obtained as explained in section 8.1.4, and the XOR switching window is probed by a CW signal at 1551 nm, which is launched into the common arm. It is important that the data signals launched into MZI 2 are of comparable pulse widths [p15], in order to obtain a high extinction for "1" XOR "1". Consequently, the output signal D1 XOR D2 from MZI must consist of pulses of width comparable to that of D3, i.e. $\approx$ 25 ps. As shown in Fig. 8.12 (d), this is ensured by launching a 10 GHz clock signal consisting of $\approx$ 25 ps wide pulses at a wavelength of 1559.4 nm from another gain-switched DFB laser (GS-DFB 2), into the common arm of MZI 1. This effectively samples the broader and asymmetrical pulses making up D1 XOR D2, as explained in section 8.1.4, and ensures that the pulse width of the output signal is defined by the width of the clock pulses.

Fig. 8.13 (a-e) show the results in terms of pulse patterns detected with a 40 GHz photodiode. The three inputs, D1, D2, and D3, are shown in Fig. 8.13 (a), (b), and (c), and Fig. 8.13 (d) and (e) show D1 XOR D2, and D1 XOR D2 XOR D3, respectively. Notice that the width of the pulses out of MZI 1 is indeed comparable to the width of the input pulses. This is also clear from Fig. 8.13 (f) and (g), which show the eye diagrams corresponding to D1 XOR D2 and D1 XOR D2 XOR D3, respectively. The fact that the "1"-level in Fig. 8.13 (g) is

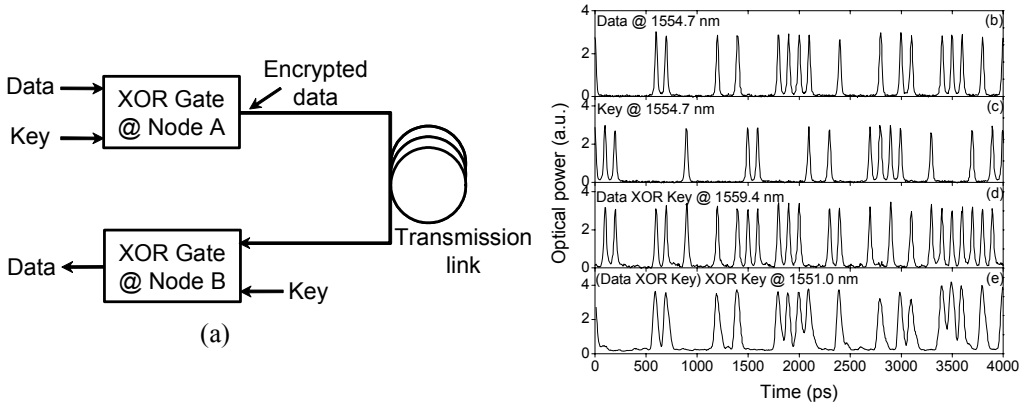

Figure 8.14: (a) Principle of encryption/decryption using XOR. (b,c) Input signal and encryption key, (d) encrypted data, and (e) decrypted data.

well-defined, and only consists of one "trace", is additional evidence that the two data inputs to MZI 2 consist of equally shaped pulses. The extinction ratio of D1 XOR D2 XOR D3 is ≈ 11 dB, and the OSNR at the output of both MZIs is 33 dB/0.1 nm.

The two all-active devices originate from the same wafer, and as expected they perform similarly. MZI 1, which is the same device used for the experiments in section 8.1.4, was biased at $P_{C,3}/P_{C,4}/P_P/I_1/I_2/I_{3'}/I_{4'}/I_3/I_4 = 3$ dBm/1.6 dBm/5.6 dBm/100/80/40/40/280/400 mA, and the bias conditions for MZI 2 are very similar: $P_{C,3}/P_{C,4}/P_P/I_1/I_2/I_{3'}/I_{4'}/I_3/I_4 = 2$ dBm/2.5 dBm/3.2 dBm/110/100/60/70/190/430 mA.

By considering MZI 1 as being part of a transmitting node (A), and MZI 2 as being part of a receiving node (B), the setup in Fig. 8.12 (d) can be used to demonstrate the scheme depicted in Fig. 8.14 (a). At node A, the data to be transmitted is encrypted by bit-wise XOR'ing with a key bit-stream before being transmitted onto the fiber link. If an unauthorized party at any point along the link should tap the fiber, the data will be safe, assuming the key is unknown to the perpetrators. At the receiving node B, XOR'ing the received signal with the same key used at the transmitting node decrypts the data.

The results are shown in Fig. 8.14 (b-e), again in the form of pulse patterns. From the top down, the two first rows (b, c) show the data signal at 1554.7 nm before encryption and the key stream, also at 1554.7 nm, respectively. The next row (d) shows the output of MZI 1, that is, the encrypted signal Data XOR Key. The bottom row shows the decrypted data signal, and it is confirmed that the pattern is logically identical to the originally transmitted data signal. As in the case of the 3-input XOR, a clock signal at 1559.4 nm is used as probe in MZI 1, whereas CW light at 1551 nm is used in MZI 2. It is clear that pulse broadening due to dispersion on the fiber link causes a potential problem to the decryption process, so a combination of dispersion compensation and adaptation

of the key-stream pulse width may be necessary for realistic fiber spans.

8.2.2 Bit-pattern recognition in data segments

Bit comparators can be implemented using either the Boolean AND or XOR gate, both of which have been demonstrated optically at bit rates $\geq$ 20 Gb/s using e.g. SOA-based interferometric switched, as mentioned earlier in this chapter. In [216], all-optical address recognition of 6-bit words at 100 Gb/s was demonstrated with an AND gate based on FWM in an SOA, and in [17] a UNI-XOR[2] gate was used as an address comparator at 12.5 Gb/s employing the pulse position modulation (PPM) format. There are advantages and disadvantages related to using the AND gate as well as the XOR gate as a comparator, which will be detailed in the following. To overcome these drawbacks, a novel bit-comparison scheme will be presented, which is based on a combination of AND and XOR that eliminates the disadvantages of the individual gates. The comparator is operated at 10 Gb/s, and is realized using a single all-active, polarization independent MZI. The concept was originally proposed in [181], and the results presented here are published in [p13].

Bit-wise comparison between an input pattern and a comparator sequence is shown in Fig. 8.15 using (a) an AND gate, (b) an XOR gate, and (c) a combination of the two gates. The input pattern is expected to contain the sequence "1011" at a specific time, indicated by the hatched area, but for some reason the second "1" bit is incorrect, and the timeslot contains a "0" instead (indicated by the dashed pulse). In all three implementations in Fig. 8.15, the comparators produce a pulse at the output for each erroneous bit detected. The output is detected by a photo detector (P.D.), and thus a surge in the photo current will correspond to an error. A high-bandwidth P.D. will be able to identify individual errors, whereas a cost-effective low-bandwidth solution will simply reveal the presence of errors, which may be sufficient for some applications.

When using an AND gate as a comparator for bit error detection, the comparator sequence must be the inverted of the expected sequence. In the present example this is a single pulse synchronized to the expected "0" in the input sequence. Fig. 8.15 (a) reveals the disadvantage of the AND-comparator: it is insensitive to bit-errors synchronized to "0"s in the comparator sequence. This means that the probability of detecting a single bit-error will be given by the ratio of "0"s to "1"s of the input sequence to be identified (in this case 25%). Using an XOR gate instead, as shown in Fig. 8.15 (b), with a comparator sequence equal to the expected sequence in the input pattern, all bit-differences are identified and result in a pulse at the output. However, since the XOR comparator sequence consists of "0"s outside the time span containing the expected sequence, all bits in the input pattern outside this time window will be transmitted to the output.

[2] the UNI gate was biased as an AND gate, but due to the PPM format, the gate performs the complementary XOR function

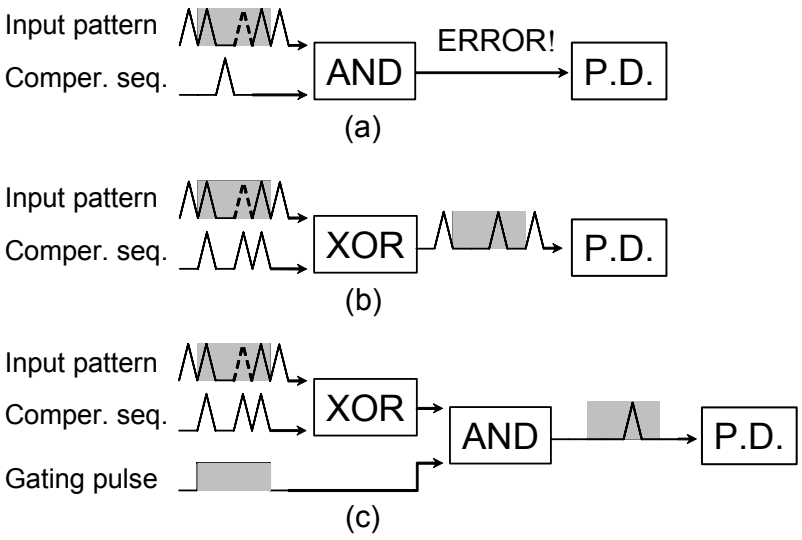

Figure 8.15: Schemes for bit comparison using (a) an AND gate, (b) an XOR gate, and (c) a combination of AND and XOR.

Consequently, a simple detection of P.D. power surge will not reveal the presence of errors. An additional gate is needed at the output to suppress the bits outside the window of interest, before the result can be detected. This gating procedure is obviously not needed with the AND-comparator, since the output is inherently "0" outside the time window of interest. This property of the AND gate can be exploited as shown in Fig. 8.15 (c), where the output of the XOR comparator is gated by a pulse equal in duration - and synchronized to – the time window of interest. Rather than using a separate AND gate, the gating function has been implemented using the same MZI that performs the XOR operation, thus reducing complexity and increasing cost-effectiveness.

The experimental setup is sketched in Fig. 8.16, where EDFAs and polarization controllers are omitted to maintain clarity. The MZI, which is the all-active device used to obtain the results in section 8.1.4, is biased to the in-phase operating condition, thereby enabling the XOR function between the two data inputs D1 and D2, launched into the upper and lower arm of the interferometer, respectively. The gating signal, G, launched into the common arm samples the switching window generated by D1 and D2, and consequently it is seen that the logic function obtained at the output of the filter is G AND (D1 XOR D2). The function depicted in Fig. 8.15 (c) can hence be realized with a single MZI, by injecting the synchronized gating pulse into the common arm.

As indicated in Fig. 8.16, the AND-XOR data segment comparator is demonstrated using two 10 Gb/s PPGs to drive two modulators independently. PPG 1 modulates a PRB-sequence of word length $2^7 - 1$ onto a 10 GHz train of ≈ 25 ps wide pulses emitted from a gain-switched DFB laser (GS-DFB 1) at a wavelength of 1554.7 nm. This signal is split in two, and forms the two input data signals D1

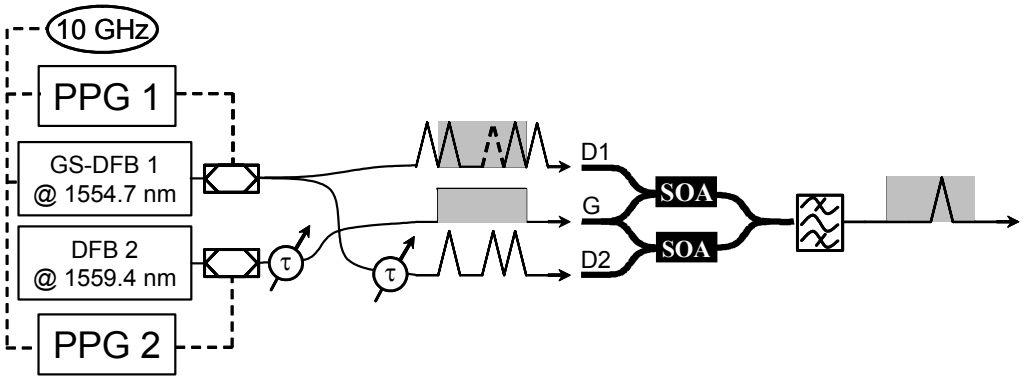

Figure 8.16: Setup for experimental evalution of bit-comparison in data segments using a combination of AND and XOR in a MZI.

and D2. A variable delay in the lower arm ensures synchronization between D1 and D2. PPG 2 modulates a periodic signal consisting of 63 NRZ "1"s followed by 64 "0"s onto a CW beam from a DFB laser (DFB2) at a wavelength of 1559.4 nm. This is the gating signal, G, which passes through a synchronizing optical delay line before being injected into the common arm of the MZI.

The result is shown in Fig. 8.17 (a-d) in the form of data pulse patterns, where the 3 rows from the top contain (a) D1, (b) D2, and (c) the gating signal G. The bottom row (d) shows the gated XOR-compared output G AND (D1 XOR D2). The output pulses are observed to be somewhat broader than the input pulses, but this may be compensated for by letting G consist of RZ pulses of width comparable to the input data signals.

The output extinction ratio is 10 dB and the OSNR is $\approx$ 30 dB/0.1 nm, which are indicators of a good signal quality. Measurement of BERs was not possible due to a technical problem with PPG 2. The BER performance of the gated XOR signal is expected to be slightly degraded compared to using a CW probe. The reason for this is that the peak power in the gating pulse cannot be as high as the (optimum) power of a corresponding CW beam, since the large contrast in the "0" to "1" transition gives rise to a gain-saturation induced temporal overshoot of the output, which leads to increased patterning. An average gate power of 1.1 dBm was used to obtain the pattern in Fig. 8.17 (d), which should be compared with the CW probe power of 5.6 dBm used in the XOR demonstration in section 8.1.4. This enhanced patterning could be reduced be injecting a holding beam into the common arm along with the gated probe, in order to reduce the available gain and speed-up the recovery. Fig. 8.17 (e) illustrates G AND (D1 XOR D2) on a larger time scale, where the 64 bit long segment constitutes the comparator window, and the remaining 63 bits of the period are efficiently suppressed.

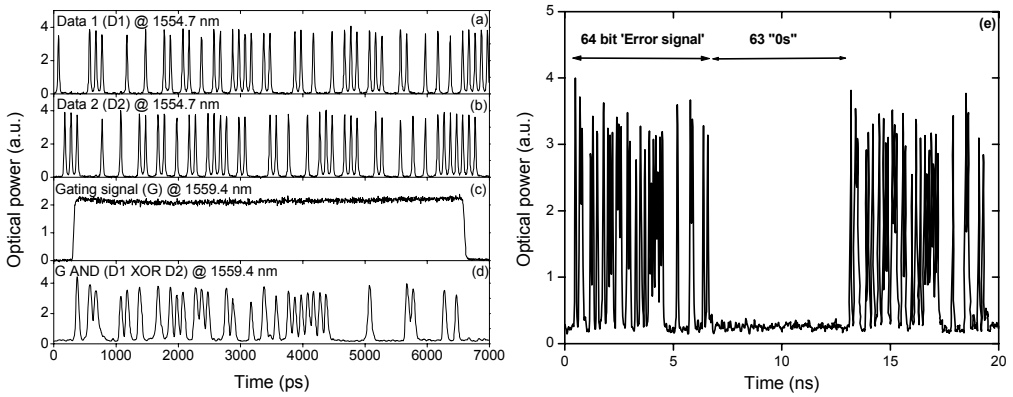

Figure 8.17: Two 10 Gb/s input signals (a,b) and gating signal defining comparator window (c), and (d) corresponding output of MZI. (e) Ouput on a larger time scale.

8.2.3 All-optical parity calculator

As mentioned in the introduction to section 8.2, optical switches based on SOA /fiber hybrid interferometers have been used to demonstrate advanced functionality incorporating memory in the form of an optical delay line, which feeds the output of an optical logic gate back to the input. The examples include an all-optical parity checker based on two TOADs [210], and a UNI based circulating shift register with an inverter [205, 209]. In both configurations, an EDFA amplifies the output, which is fed back to the switch as a control signal. Since an EDFA contains many meters of fiber, it represents the main contribution to the latency of the circuit. This was identified as a problem in [210], and a bit-differential design was employed, in which the m-bit input word was injected m times into the circuit before the parity of the word could be detected at the output. This is clearly not feasible in a real system, so for this type of scheme to be practical the total time-of-flight (TOF) of the switch and the feedback loop must be reduced – ideally to below the bit timeslot.

The only solution to this problem is integration, which leaves SOA-based interferometers as the prime candidates for the switches. Moreover, a feedback amplifier with a minimum TOF, but still with sufficient output power to facilitate the switching must be employed. Again, the natural choice is the SOA, since ultimately integration with the switch and the feedback waveguide is desirable to further minimize the total TOF. The replacement of the EDFA with an SOA has already been successfully demonstrated using a UNI as the switch [209], reducing the TOF in the feedback loop of an all-optical shift register to below 10 ns.

In this section the potential of the all-active MZI as an adjacent-bit parity calculator, i.e. a parity calculating circuit with a total TOF < 1 timeslot, is investigated experimentally and through simulations. In order to reduce the TOF the peripheral SOAs provide the necessary amplification in the feedback path. The results presented here are based, in part, on [p17].

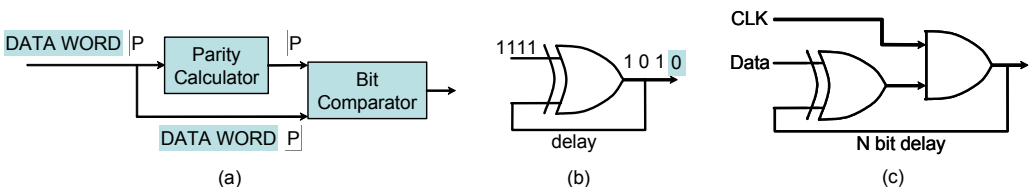

Figure 8.18: (a) application of parity calculator. Equvalent diagrams of (b) adjacent-bit parity calculator and N'th bit parity calculator.

Fig. 8.18 (a) illustrates an application of a bit-parity calculator. A data word, e.g. a packet, preceded by its parity bit is launched into an optical circuit that re-calculates the parity of the word, while a fraction of the input power bypasses the parity calculator. The original and re-calculated parity bits are synchronized and compared using e.g. the scheme outlined in Fig. 8.16, and the output of the bit comparator is an error signal representing a low-level check of the integrity of the data word. However, if an even number of bits are interpreted erroneously by the parity calculator, it will not be detected by this system.

A parity calculator may be realized by a single XOR gate with a feedback through a delay, as illustrates in Fig. 8.18 (b). Depending on the TOF of the feedback, the circuit has different applications. For a total delay D_T (incl. TOF through XOR gate) of one timeslot, the circuit is an adjacent-bit parity calculator/checker, where the 1^{st} bit is XOR'ed with the 2^{nd}, the result of which is XOR'ed with the 3^{rd}, etc. Assuming instead that the data consists of slotted packets of fixed length N (in number of bits) and that D_T is adjusted to match the TOF of one packet, bit $\#n$ in one packet will be XOR'ed with bit $\#n$ in the next packet etc., so that bit $\#n$ of the output packets contains the accumulated parity of the preceding input packets. Gating out the bit accounting for the parity of payload bit $\#n$ in packets $\#\ldots, X-2, X-1, X$ and inserting it into the header of packet $\#X$ before transmission, using a header re-writing technique such as described in e.g. [22] or [217], it will be possible to re-calculate the parity at the receiver side, and compare it to the control bit in the header of packet $\#X$, as illustrated in Fig. 8.18 (a). A discrepancy is an indication of an error, and this information may be used to monitor the signal quality.

The function represented by Fig. 8.18 (c) will be referred to as a gated parity calculator/checker, since the output from the XOR gate is sampled by a clock signal, CLK, before being fed back through an N-bit delay. The gated parity calculator is introduced here because the sampling of the XOR output is a necessary part of the MZI implementation presented below, in order to maintain the pulse shape and width of the feedback signal. In addition, the parity checker with bit-differential delay described in [210], which is the main source of inspiration for this work, is actually implemented exactly as shown in Fig. 8.18 (c). In [210], the N-bit delay was adjusted to fulfill $N = m + 1$, with m being the input word length, so that the 1^{st} bit of the 1^{st} period is synchronized to, and XOR'ed with,

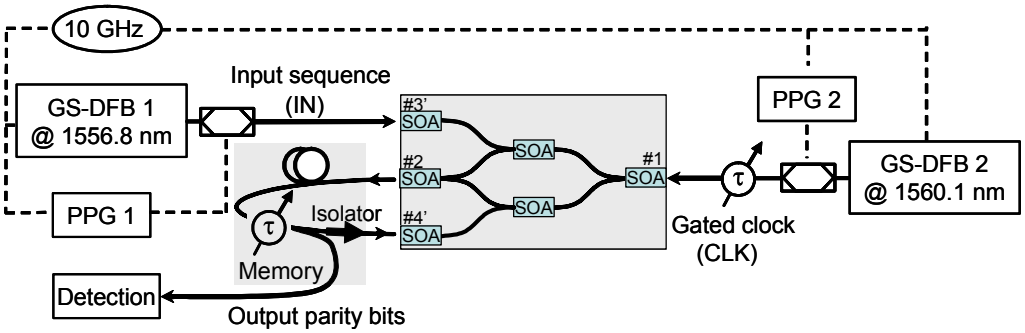

Figure 8.19: Experimental setup for MZI-based parity claculator.

the 2^{nd} bit of the 2^{nd} period, etc.

Fig. 8.19 shows the experimental setup. A gain-switched DFB laser (GS-DFB 1), emitting a 10 GHz clock of $\approx$ 25 ps wide pulses at 1556.8 nm is modulated with a sequence consisting of N_D bits at 10 Gb/s from pulse pattern generator 1 (PPG 1), and the periodic signal denoted IN is launched into port #3' of the all-active MZI. The active interferometer arms are 1200 μm long, while all peripheral SOAs are 400 μm long. Another GS-DFB (GS-DFB 2) emits a 10 GHz clock of $\approx$ 25 ps wide pulses at 1560.1 nm, which is modulated with a gating sequence of period N_G, containing just a single "1", effectively reducing the clock frequency of CLK to $(10/N_G)$ GHz, before it is injected into port #1 of the MZI switch, which it traverses in a counter propagating orientation compared to IN. Disregarding the feedback loop, the output from port #2 represents the logic function IN AND CLK, which has a period of $LCM(N_D, N_G)$ (LCM: Least Common Multiple).

By coupling this result into port #4' via the feedback fiber loop, exploiting the amplification of SOA #2 and SOA #4', and synchronizing the bits to the input sequence using an optical delay line, the output of the circuit will represent the adjacent-bit parity calculator if $N_G = 1$ and $D_T = 1$ (in timeslots of 100 ps). Alternatively, by setting $N_G = D_T =$ packet length N, the output will be the accumulated parity of a specific (payload) bit, and unlike shown in Fig. 8.18 (c), it will not be necessary to gate the output signal in an external AND gate, since this functionality is already included, due to the sampling by the gated clock. In [210], the additional TOAD gate was not used to reshape the pulses in the feedback loop, but it was needed to wavelength convert the XOR signal before launching it back into the TOAD-XOR gate, in order to facilitate distinction of the control signal and switched probe pulses. The MZI implementation does not encounter this problem, since the input signal and the sampling probe counter propagate, and consequently exit through different ports.

In general, the output will represent a non-trivial logic function F

$$F = f\left(N_D, N_G, D_T, \text{synch.}\right) \tag{8.3}$$

depending on N_D, N_G, D_T, and the relative synchronization between IN and

CLK. Since the input signals are periodic, it is clear that F represents a periodic sequence as well. A small piece of software has been made to investigate F logically, using the algorithm illustrated in Fig. 8.18 (c). This provides useful insight into the periodicity of F, as well as a being a means of verifying the output of the physical model. In order for the feedback to be active, the gating period N_G must divide the total delay D_T (in number of bits). This requirement corresponds to the output from port #2 arriving at port #4' synchronized to CLK at port #1, and if it is not fulfilled, F will simply be given by IN AND CLK, since the result of the XOR function will not be sampled by CLK.

The length of the fiber memory loop was ≈ 20 m, and no attempt was made to reduce it, since this would require an irreversible customization of a 3-fiber ribbon, while still not reducing D_T to below 1 timeslot. The TOF of the MZI is $\approx 35-40$ ps, which by a rough estimate leaves $60-65$ ps or $10-15$ ps for the TOF of the feedback loop for adjacent-bit parity calculation at 10 and 20 Gb/s, respectively. This is an estimate, since the fact that IN and CLK counter propagate adds to the latency of the circuit. This is explained further in connection with a discussion of the simulation results, where the exact latency is calculated. Integrating a waveguide between SOAs #2 and #4' with a delay as low as $10-15$ ps would be very challenging. Alternatively, the MZI could be placed in a planar lightwave circuit (PLC) containing a photonic crystal waveguide with sufficiently low loss, enabling very sharp bends. However, as indicated in Fig. 8.19 an isolator is required in the memory loop to prevent CLK from entering SOA #2. Although progress is being made in integrating optical isolators using non-reciprocal magneto-optic waveguides [218], an integration with SOAs remains to be demonstrated. Apart from hindering integration, the isolator also adds a significant delay, which makes it difficult to obtain a single-bit delay at high bitrates. One solution to this problem could be the DOMO-MZI, shown in Fig. 6.21, since in this design the counter propagating clock signal would traverse the MZI as a fundamental mode, and be guided exclusively towards SOA #2 by the mode couplers. Thus, ideally, CLK would only exit at SOA #2, and an isolator would not be required.

Another speed limiting factor is the counter-propagation induced transit time effects, explained in section 4.1.2. However, successful operation at 20 Gb/s in counter-propagation, also using a 1200 μm long SOA, has been demonstrated [219].

In order to visualize the output pulse pattern on a sampling oscilloscope the period N_F of the pattern must divide the trigger period N_{tr}. The sampling oscilloscope can be triggered by either PPG 1 (Anritsu MP1701A) or PPG 2 (HP 40843), which transmit trigger signals with periods of $LCM(N_D, 128)$ and $LCM(N_G, 256)$, respectively. Satisfying this requirement implies an optimization of D_T by means of the optical delay line in the memory loop, while changing the periods N_D and N_G of the input and gating sequences to meet the triggering requirement of one of the two PPGs. At best, this is very challenging, so to

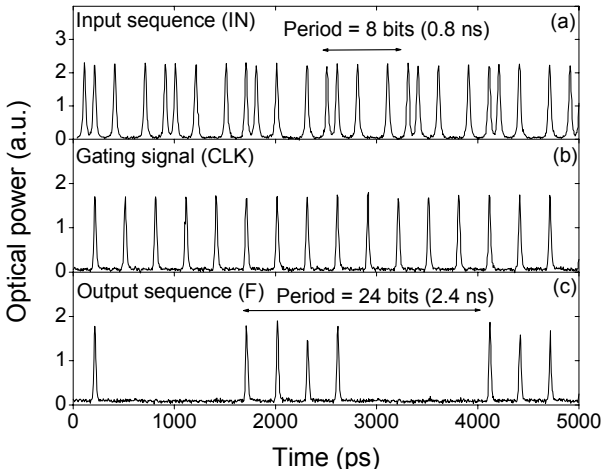

Figure 8.20: (a) 8−bit input sequence, (b) 3−bit gating signal, and (c) corresponding output sequence without synchronization between input and feedback signal.

visualize the output the combination $(N_D, N_G) = (8, 3)$ was chosen, which fulfills the triggering requirements using the trigger output from PPG 2, for an output period of IN AND CLK of $LCM(8, 3) = 24$.

Fig. 8.20 shows pulse traces of IN (a), CLK (b), and the output sequence F (c), which represents IN AND CLK. Fig. 8.20 does not by itself prove that the feedback loop is active, since the output sequence is the same as if the input to port #4' is disconnected. Changing the input to a PRBS of word length 2^7-1, the output sequence no longer satisfies the triggering requirements, and the output can only be visualized as an eye diagram. However, by varying the optical delay in the memory the effect of the feedback can be investigated by monitoring the eye diagram.

This is illustrated in Fig. 8.21 (a), which shows the gated pulses in the feedback, synchronized to the timeslot of the 10 Gb/s input signal IN, as well as to CLK, indicated by the dashed rectangular windows. If the feedback is synchronized to the timeslot of IN, but not to CLK an open eye diagram corresponding to IN AND CLK is expected, and this is illustrated in Fig. 8.21 (b) for a misalignment ΔD_T, compared to the gating window, of 1 timeslot (100 ps). In Fig. 8.21 (c) and (d) ΔD_T is 70 ps and 60 ps, respectively, and the eye diagram closes. It re-opens for $\Delta D_T = 0$, illustrated in Fig. 8.21 (e), which corresponds to perfect synchronization of the feedback signal. Decreasing the delay further to $\Delta D_T = -25$ ps, the eye diagram begins to close again, as shown in Fig. 8.21 (f). This evolution of the eye diagram proves that the feedback loop is active, since no change of eye diagram would have been observed otherwise. The transition of eye diagrams in Fig. 8.21 (b-f), and the fact that a similar transition occurs as the current to SOA #4' is varied, are clear indications that the XOR function is working, and that the output does indeed represent the accu-

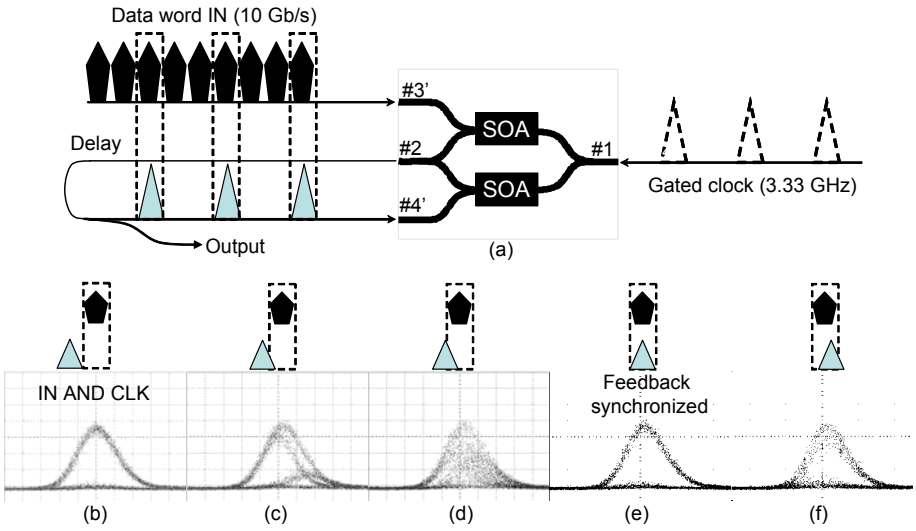

Figure 8.21: (a) Illustration of importance of synchronization between IN and feedback signal. Experimentally obtained eye diagrams for a relative misalignment of (b) 100 ps, (c) 70 ps, (d) 60 ps, (e) 0 ps, and (f) −25 ps.

mulating bit parity function. The eye diagrams in Fig. 8.21 were obtained with the bias condition $P_{C,3}/P_{C,4}/P_P/I_1/I_2/I_{3'}/I_{4'}/I_3/I_4$ = 1.1 dBm/−4.8 dBm/6 dBm/100/180/60/150/290/400 mA, where it should be noticed that an average power of −4.8 dBm, measured at the input of SOA #4', is sufficient to obtain switching when SOA #4' is biased at $I_{4'} = 150$ mA.

A numerical investigation has been undertaken to verify the experimental observations. In the model, the output power from port #2 was large enough to provide switching in SOA #4 without amplification in the peripheral SOAs, and thus in the following, only SOAs #3 and #4 are active. The passive phase shift in the MZI, $\Delta\phi_t$, is set to π to obtain symmetric bias conditions. Referring to Fig. 3.2, the coupler at port #4' with coupling ratio $r_{4'}^{FB}$, is tuned to obtain the same pulse energy at the input of SOA #4, as at the input of SOA #3. A perfect isolator is assumed in the feedback path to prevent clock-wise propagation in the loop. All physical dimensions of the active waveguides are equal to those of the device used in the experiment. Both signals consist of 25 ps Gaussian pulses, and the MZI is biased to $I_3 = I_4 = 300$ mA.

Fig. 8.22 shows a comparison between the result of the logic model (upper traces) and the physical model (lower traces) for (a) $D_T = 3$ bits, (b) $D_T = 4$ bits, (c) $D_T = 5$ bits, and (d) $D_T = 6$ bits. In all cases, the input signal is the periodic 8-bit word '11010010' ($N_D = 8$) and the gating signal is '100', i.e. $N_G = 3$. The gating pulse is synchronized to the second bit in IN. As observed in Fig. 8.22, the output patterns obtained with the two models are in agreement. Moreover, as explained above, the patterns only deviate from the IN and CLK pattern for total delays equal to multiples of N_G, in this case $D_T = 3$ and 6

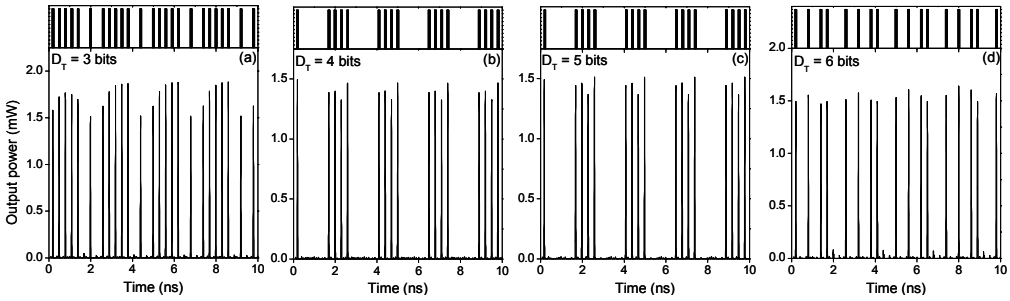

Figure 8.22: Logic simulation (upper) and physical simulation (lower) of parity calculator output for a total feedfack delay of (a) 3 bits, (b) 4 bits, (c) 5 bits, and (d) 6 bits.

bits. In these simulations, the average power of IN and CLK was -10 dBm and -13 dBm, respectively. The optimum relative delay between IN and CLK was 28 ps, which is slightly surprising considering the analytic results presented in section 4.1.2. There, the phase shift induced on a counter-propagating probe was found to peak at the output a time $2L/v_g$ after the delta-function pump pulse was launched from the opposite facet. This means that the a probe pulse should be injected $L/v_g = 13.2$ ps after the pump pulse to sample the maximum phase shift, which corresponds to the probe pulse entering the SOA as the pump pulse exits. However, in this simulation the pulses have finite widths (20 ps), which implies that the phase response functions, illustrated in Fig. 4.7, should be convoluted with the pump pulse in order to obtain the phase shift imposed on the counter propagating probe. This clearly broadens the response, which increases the optimum delay of the CLK signal. Physically, this corresponds to delaying the probe pulse until the entire[3] pump pulse has left the SOA.

The quite large relative delay between IN and CLK puts very demanding restrictions on the TOF of the external part of the feedback loop. Adding up the total internal latency amounts to 28 ps for the relative IN/CLK delay + 1.2 mm/v_g (= 13.2 ps) + 0.4 mm/v_g (= 4.4 ps) for the propagation delay of the 1.2 mm long interferometer arms and the 400 μm long SOA #2, respectively. This gives a total delay of 45.6 ps, relative to the time the first pulse in the IN signal entered SOA 3′. This leaves only 54.4 ps for the external feedback at 10 Gb/s, if an adjacent-bit parity checker is to be realized. Fig. 8.23 (a) and (b) show IN and the corresponding output, F, for a single-bit delay at 10 Gb/s, obtained by introducing an external delay of 54.4 ps. By inspection it may be verified that Fig. 8.23 (b) represents the accumulated parity of Fig. 8.23 (a). From the calculation of the internal delay above, only 4.4 ps is left for the external delay at 20 Gb/s, which is not realistic in practice. Moreover, due to distortions introduced by patterning effects at 20 Gb/s, it turns out to be advantageous for the feedback signal to arrive a few picoseconds early, which actually reduces

[3]This is a slightly simplistic view, since the carrier recovery actually begins before the pulse has completely left the SOA.

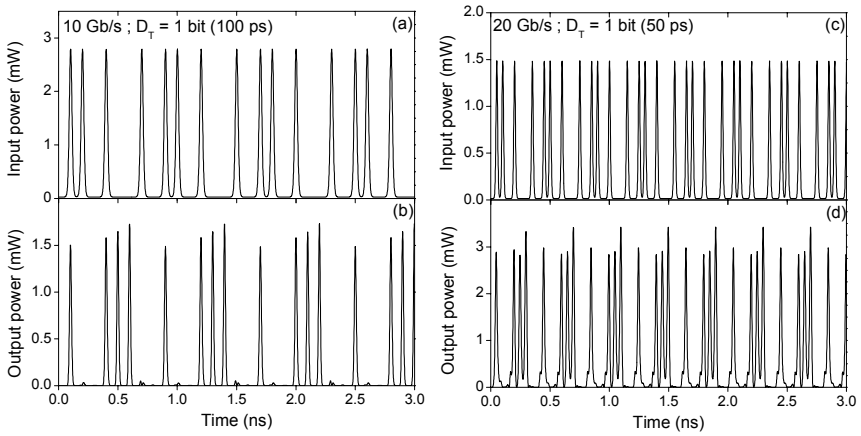

Figure 8.23: Simulation of adjacent-bit parity calculation at 10 Gb/s (a,b) and 20 Gb/s (c,d). Input signals (a,c) and accumulated parities (b,d).

the external delay to 1 ps. The results, in the shape of input and output pulse patterns, are shown in Fig. 8.23 (c) and (d), respectively.

The simulations of the adjacent-bit parity calculator above show that operation at 20 Gb/s is not possible with a MZI of the dimensions proposed here. Reducing the length of the interferometer arms reduces the internal latency, while at the same time alleviating the transit-time effects. On the other hand, the effective carrier lifetime increases, and will become the limiting factor if the arm length is decreased sufficiently, as illustrated in Fig. 4.5 (a). Thus, the interferometer arm length is a subject for optimization.

As explained in section 8.1.4, a misalignment of timeslots at the input of a MZI-XOR gate leads to distortion of the output pulses. When feeding the distorted output back to the input, the distortion will either accumulate or stabilize, depending on the amount of initial distortion. This is investigated by varying the external delay around the optimum at 10 Gb/s. The result is given in Fig. 8.24 as the ER of the adjacent-bit parity output vs. the delay relative to 54.4 ps. An ER $\gtrapprox$ 10 dB can be maintained for a relative delay between -4 ps and $+8$ ps, giving a total synchronization tolerance of 12 ps. This value has been found to depend highly on the input power to port $4'$, and the power giving rise to the best ER for perfect synchronization does not necessarily provide the best synchronization tolerance. However, the 12 ps represents the highest obtained value.

8.3 Summary

This Chapter reviewed the current state of all-optical logic, and presented experimental examples of logic gates and functionalities, based on SOA-based MZI gates.

Implementations of the Boolean logic gates NOT, OR, AND, and XOR were

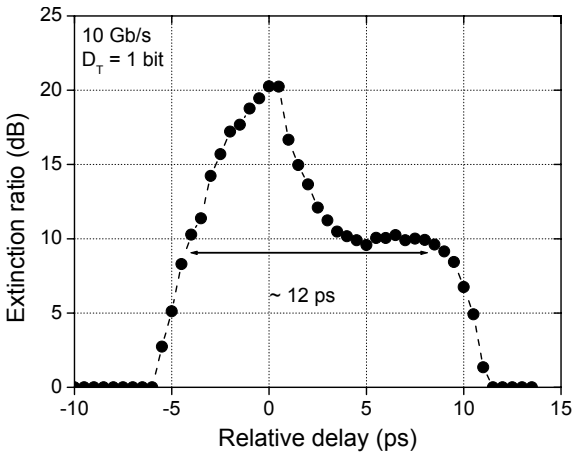

Figure 8.24: Tolerance towards variation of feedback delay for adjacent-bit operation at 10 Gb/s.

discussed with special attention to the realization by MZIs. In particular, logic AND was demonstrated at 20 Gb/s, whereas the XOR function was investigated at 10 Gb/s, using RZ as well as NRZ input data, with CW and pulsed probes. A pulsed probe ensures that the pulse shape and width is maintained across the gate, which is critical for the cascadability of logic gates. Whereas operation with RZ data works well, NRZ input data introduces a form of pattern dependent jitter, which is particularly pronounced if the carrier lifetime is high. Employing a pulsed probe in connection with NRZ input data enhances the performance considerably, at the expense of NRZ $\rightarrow$ RZ format conversion.

The tolerance of a MZI-XOR gate towards synchronization of RZ input data was investigated numerically at 40 Gb/s. The results depend on the passive phase shift between the arms of the interferometer, since this leads to a necessary asymmetric biasing. For a passive phase shift of π, the bias currents are symmetric, and the ≤ 1 dB power penalty tolerance becomes $\approx \pm 2$ ps. Asymmetric bias currents reduce the tolerance if the signal to the 'slow' arm (low current) is lagging the signal to the 'fast' arm (high current). This was verified experimentally at 10 Gb/s.

Logic functionalities involving more than a single Boolean gate have been demonstrated with all-active MZIs. A 3-input XOR gate for parallel or serial parity calculation/checking was demonstrated at 10 Gb/s by cascading two 2-input MZI-XOR gates. The same setup was used to demonstrate all-optical data encryption/decryption. In another scheme, bit-pattern recognition in segments of data was demonstrated at 10 Gb/s by implementing a logic function combining AND and XOR in a single MZI. Finally, the potential for implementing an all-optical adjacent-bit parity calculator/checker, capable of providing the parity bit of a data word by launching it only once into a MZI-based circuit, was investigated. This required using the peripheral SOAs as amplifiers for the feedback signal, which was illustrated experimentally. Simulations revealed a bitrate

limitation for adjacent-bit operation of below 20 Gb/s, due to a combination of internal latency in the chip and counter-propagation induced transit-time effects. The requirement of an isolator in the feedback path poses another problem, which may be resolved by using the DOMO-MZI.

Chapter 9

Conclusions

It has been argued that a potential increase of the line rate, from the current maximum of 10 Gb/s to 40 Gb/s and beyond, offers a reduction in the cost per bit. For this reason alone, it is very likely that implementation of 40 Gb/s systems will be initiated when the telecom market recovers, since operators will require cost-effective solutions for upgrading the network capacity, in order to remain competitive.

With an upgrade to 40 Gb/s and beyond, it becomes increasingly advantageous to move functionality from the electrical to the optical domain, since unnecessary termination of WDM channels consumes an increasing amount of power, and consequently takes up more space, as the bitrate increases, which is unsustainable as the need for capacity grows. Technologies such as optical MEMS space switches, and at a later stage, all-optical wavelength converters, regenerators and simple optical logic processors, provide solutions that may overcome the limitations of optoelectronic approaches, ensuring transparency and better scalability of future networks.

This thesis has investigated all-optical approaches to high-speed switching, based on Semiconductor Optical Amplifiers (SOAs), theoretically as well as experimentally. The main focus of the theoretical work has been on explaining the phenomena limiting the performance of different SOA-based switch configurations, in terms of speed, and point to potential solutions. On the other hand, the experimental studies have primarily aimed at demonstrating functionality and providing a means of verifying trends observed theoretically. Combining the two disciplines has been an invaluable help, since the modeling has benefitted from laboratory experience, and vice versa.

The basis for the theoretical work was described thoroughly in the beginning of the thesis. Then, a simpler model was employed to analytically investigate the small-signal response of a continuous wave (CW) probe signal co-propagating or counter-propagating through an SOA with a modulated control signal. The influence of waveguide loss on the evolution of the modulation bandwidth was analyzed, and analytical formulas for the bandwidth were given for both co-

and counter-propagating signals. Large-signal modeling of cross-gain modulation (XGM) was shown to comply with the small-signal modeling. In particular, for co-propagation, small-signal modeling predicted a −3 dB bandwidth of 70 GHz for a 3 mm long SOA, and the power penalty of cross-gain modulated probe at 80 Gb/s decreased to a minimum around 4.5 dB at a length of 3.5 mm. However, for longer SOAs, ASE was found to limit the performance, which cannot be predicted by a small-signal analysis. An equivalent analysis confirmed small-signal predictions that the modulation bandwidth is reduced to below 40 Gb/s when the signals counter-propagate.

Patterning effects were introduced and divided into linear and nonlinear contributions, where the former is related to the finite rate of carrier recovery, and the latter to the effect of saturation. It was argued that linear patterning can be completely compensated for by employing the so-called differential control scheme, and that nonlinear patterning may be alleviated using holding beam techniques.

Three types of interferometric switches, the MZI operated in standard-mode (SM-MZI), differential-mode (DM-MZI), and the Delayed-Interference Signal Converter (DISC) were investigated numerically at 80 Gb/s. Compared to XGM, the SM-MZI switch represents a significant improvement due to the nonlinear transfer function, which provides an enhanced extinction ratio. As an example, the minimum power penalty obtained with 2 mm long SOAs was reduced from 7 dB to 3.5 dB. The limiting factor for the SM-MZI switch is the linear patterning effects, which manifest as intersymbol interference. Operating the MZI in the differential mode, by launching a delayed and attenuated copy of the data signal into the other interferometer arm, the trailing edge of the phase response may be cancelled out, thus eliminating linear patterning effects. In this case, the performance is limited by the remaining nonlinear patterning, which materializes as fluctuations of the mark-level.

The DISC is found to be fundamentally different from the DM-MZI in several regards. The phase response in the arms of the asymmetric MZI (AMZI) are equal, and thus the trailing edges do not fully cancel. As a consequence, a detrimental satellite pulse is introduced after each switched pulse. The amplitude of the satellite pulses may be reduced by limiting the input data power, but this is at the expense of the switched output power. However, due to a very effective ASE filtering, compared to the DM-MZI, the low output power from the DISC translates into an acceptable OSNR. An analytical expression for the ratio of transmitted ASE power for the DM-MZI and DISC switches was presented, and the ratio was found to be around 10 dB, independently of the bitrate. In my personal opinion, the comparison of the DM-MZI and DISC switches is one of the main results of the thesis.

Using the DISC as an example, analytical formulas relating the parameters of the SOA and AMZI to the obtainable small-signal bandwidth were derived. A bandwidth enhancement factor, was defined as the factor by which the AMZI

improves the small-signal modulation bandwidth of an SOA, and the factor was expressed analytically. A new approach to small-signal analysis, based on the analysis of the field envelope, was presented and applied to all-optical switches based on a single SOA and an optical filter. This approach provided a convenient means of analyzing the effect of an arbitrary filter on the small-signal frequency response. In particular, the importance of the filter phase response was demonstrated by showing that the bandwidth enhancement effect of the asymmetric MZI filter relies on a discontinuous phase shift of π. Moreover, for a filter with a continuous phase response, such as e.g. a Band-Pass Filter (BPF), it was shown that the highest bandwidth is obtained by suppressing one of the sidebands. The predictions of the small-signal analysis should be regarded as upper limits, since nonlinear patterning and the OSNR degradation that follows from e.g. detuning a filter at the output of an SOA, was not included in the analysis. For all filter types, and particularly for BPFs, a clear trade-off between modulation bandwidth and OSNR exists.

The small-signal analysis of the DISC and the generalization to arbitrary filters is considered a main result of the thesis.

Following the theoretical description, an account for the experimental results obtained with wavelength converters was given. A simple wavelength converter based on a single SOA and a commercially available BPF, detuned 0.5 nm towards the blue side of the probe spectrum, was demonstrated at 40 Gb/s with only 3 fJ of data pulse energy. The data polarity and the RZ format was preserved, and the experiment verifies the theoretical predictions based on the small-signal analysis. An active-passive and an all-active MZI, both operated in the standard-mode, were demonstrated at 40 Gb/s with good results in terms of fast response and large tunability. For the all-active MZI, a narrow BPF, slightly detuned towards the blue-side of the spectrum, enhanced the response and provided narrow pulses for the converted signal. An attempt was made at realizing 80 Gb/s standard-mode wavelength conversion with an all-active MZI with subsequent pulse shaping by a narrow BPF, but a bit error-rate (BER) floor at 10^{-9} was encountered due to a low extinction ratio. The all-active MZI was also used to demonstrate $2x20$ Gb/s to 40 Gb/s WDM-to-OTDM translation and multiplexing with good results. A numerical investigation, using the two-dimensional FD-BPM, of the dual-mode (DOMO) wavelength converter operated in XGM, was presented. Due to the inherently larger cross-section area of a dual-mode waveguide, the DOMO wavelength converter is found to be slightly inferior compared to the single-mode SOA, since the gain recovery time scales with the optical area. One of the claimed advantages of the DOMO wavelength converter is its ability to 'convert' to the same wavelength. However, for small wavelength detunings between the data and probe signals a mode-beating induced cross-talk mechanism was identified, and found to be detrimental for detunings below a certain critical detuning, which was expressed analytically. The cross-talk mechanism is able to explain previously published experimental results. The effect of transverse carrier diffusion was in-

vestigated and found to reduce the cross-talk by averaging out asymmetries in the carrier distribution. It was concluded that the effect of cross-talk could be reduced by employing DOMO-SOAs in an interferometer, since this reduces the required data power, and thus the absolute cross-talk power.

All-optical 2R and 3R regeneration was also addressed theoretically and experimentally. The principle of 2R regeneration - reshaping - and the influence of the gate nonlinearity on the accumulation of the BER was explained. In particular, it was noted that a regenerator, regardless of the nonlinearity, cannot reduce the BER. The validity of single-regenerator experiments was discussed, and it was concluded that a single regenerator does indeed provide insight into the noise redistributing properties of a nonlinear gate, as long as a noise source is inserted between the gate and the receiver. To some extent this will always be the case, since the receiver itself adds noise. The reshaping capabilities of an active-passive MZI was verified at 10 Gb/s, and the tolerance of an all-active MZI-based 3R regenerator towards accumulated chromatic dispersion was analyzed, also at 10 Gb/s. Moreover, a 3R regenerator consisting of a cascade of a XGM wavelength converter and an active-passive SM-MZI, was evaluated at 40 Gb/s in a recirculating loop experiment. After 50 laps of 80 km, a power penalty of 4 dB was recorded. For regenerators based on interferometric switches, such as e.g. the MZI, regeneration is accompanied by wavelength conversion, which may present a problem for some applications. A novel type of pass-through 2R regenerator, based on a compact all-active $2x2$ Multi-Mode Interference (MMI) coupler, where regeneration is not accompanied by wavelength conversion, was evaluated at 10 Gb/s, and the reshaping effect was verified through BER measurements. Furthermore, a subsystem capable of extracting the 40 GHz harmonic from a 40 Gb/s NRZ signal was demonstrated by exploiting Self-Phase Modulation (SPM) and Cross-Phase Modulation (XPM) in a 4 mm long SOA, combined with Phase Modulation (PM) to Amplitude Modulation (AM) conversion in a detuned BPF. Operation at 40 Gb/s was enabled by the use of an intense holding beam.

Finally, implementation of the Boolean logic gates, and realization of optical logic functionalities involving combinations of Boolean gates, was discussed and illustrated through simulations and experiments. In particular, an all-active MZI was used to demonstrate Boolean logic AND at 20 Gb/s, and XOR at 10 Gb/s, using both RZ and NRZ input data. XOR operation with RZ data works well, and power penalty-free operation at 10 Gb/s was demonstrated, whereas NRZ input data introduces a pattern dependent jitter. The tolerance of a MZI-XOR gate towards synchronization of RZ input data was investigated numerically at 40 Gb/s. The result was found to depend on the passive phase shift between the interferometer arms, since this determines the level of asymmetry of the gains in the two arms. For a passive phase shift of π, the bias currents are symmetric, and the ≤ 1 dB power penalty tolerance is found to be $\approx \pm 2$ ps. For asymmetric bias currents the tolerance is smaller if the signal to the 'slow'

arm (low current) is lagging the signal to the 'fast' arm (high current). This was verified experimentally at 10 Gb/s.

Functions made up of several Boolean gates were demonstrated with all-active MZIs. A 3-input XOR gate for parallel or serial parity calculation/checking was demonstrated at 10 Gb/s by cascading two 2-input MZI-XOR gates. The same setup was used to demonstrate all-optical data encryption/decryption. In addition, bit-pattern recognition in data segments was demonstrated at 10 Gb/s by implementing a logic function combining AND and XOR in a single MZI. Finally, an all-optical adjacent-bit parity calculator/checker, capable of providing the parity bit of a data word by launching it only once into a MZI-based circuit, was investigated. Adjacent-bit operation was found to be limited to below 20 Gb/s, due to a combination of internal latency in the chip and counter propagation induced transit-time effects. The requirement of an isolator in the feedback increases the latency further, but by employing a DOMO-MZI the isolator may be avoided.

Just a few years back, integrated SOA-based MZIs were obvious choices for possible implementation of optical signal processing. However, new solutions have emerged, such as e.g. the PD-EAM, which appears very attractive in terms of footprint, power consumption, and performance. Moreover, progress in existing technologies, such as PPLN waveguides, is making these approaches realistic alternatives for e.g. wavelength conversion. Nonetheless, SOA technology remains one of a few serious candidates for future commercialization. A number of challenges must be faced before SOA-based devices can be turned into products. Since optical signal processing is unlikely to offer significant cost savings at 40 Gb/s, optical solutions may need to operate at 80 or 160 Gb/s to make economic sense. At bitrates of this magnitude nonlinear patterning effects pose a serious challenge, and additional research is needed to solve this problem. As mentioned in Chapter 5, exploiting the correlation between the pulse energy, chirp, and polarization state of pulses switched by an SOA-based configuration could potentially eliminate nonlinear patterning, and pave the way for ultra-high speed all-optical signal processing with SOA-based devices.

Appendix A

Model interfaces

The interfaces to the switch model are shown in the block diagram in Fig. 3.1, and include an optical input signal generator, a signal processing toolbox, and a receiver model. In the following the contents of the three blocks will be reviewed.

A.1 Optical input signals

The signal generator part generates up to 4 independent optical signals, one per input/output of the switch. The options for each input signal is listed in Table A.1 where A/N denotes "any number". The entries in Table A.1 should be self-explanatory.

Apart from the parameters in Table A.1, the relative timing of the 4 input signals may also be adjusted. This is crucial for simulating e.g. the MZI differential-mode of operation, 3R regeneration and logical functionalities, and will be used extensively in Chapters 5 and 8. When operated in the differential-mode, where the data signal is launched into both port $3'$ and $4'$, the 'Average

Parameter	**Value**
Average power	A/N (dBm)
OSNR	A/N (dB)
Wavelength	1490-1590 nm
Bitrate	A/N
Data format	RZ/NRZ/CW
Pulse shape (RZ)	Gauss/Sech^2/Square
Pulse width (RZ)	0-1/Bitrate (ps)
Data type	PRBS/Clock/Code word
PRBS pattern length	$2^n - 1$. n = 3 - 9
Rise/fall time (NRZ and RZ square)	0-1/Bitrate (ps)
Extinction ratio	>0 dB

Table A.1: Options for signal generator

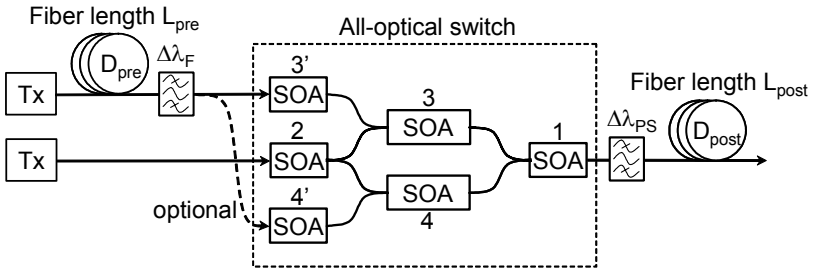

Figure A.1: Illustration of MZI switch with optional fiber spans and filters at the input and output.

power' entry in Table A.1 for input port $4'$ is replaced by a 'relative attenuation compared to input $3'$', which allows for simpler optimization.

A.2 Signal processing toolbox

The signal processing toolbox is capable of propagating the input signals on fiber before they are launched into the all-optical switch, which is either a MZI or a single SOA, as well as propagate the switched signal, in order to simulate the effect of chromatic dispersion. In the treatment of the signals, fiber nonlinearities and loss is neglected, and consequently the effect of dispersion on the complex field amplitude is governed by the operation [48]

$$A_{out}(t) = \mathbf{F}^{-1}\left[\mathbf{F}\left\{A_{in}(t)\right\}\exp(-j\frac{D\lambda^2}{4\pi c_0}\omega^2 L)\right] \tag{A.1}$$

where $A_{in}(t)$ is the field envelope at the input of the fiber, and $A_{out}(t)$ is the corresponding output after propagating a distance L on a fiber with dispersion parameter D. Nonlinear effects may be introduced in a straight-forward manner by using a split-step approach [48].

As illustrated in Fig. A.1, the optional fiber spans may be placed before input $3'$ and at the output, but when the MZI is operated in the differential-mode, the dispersed signal is injected into port $4'$ as well. Since narrowband filtering has a beneficial effect on dispersed signals, the output of the fiber may be passed through an optional filter before entering the MZI. If the OSNR is finite the width of the filter should be equal to $\Delta\lambda_F$, cf. eq. (3.48), but is otherwise unrestricted. At the output of the MZI, another optional filter of width $\Delta\lambda_{PS}$ shapes the switched pulses (PS: pulse shaping).

The dispersion parameter D and the fiber length L can be set independently for the two fibers spans, i.e. $D = D_{pre}$ and $L = L_{pre}$ for the input span, and $D = D_{post}$ and $L = L_{post}$ for the output fiber. For the optional filtering at the input and output, a total of six filter shapes have been implemented: Lorentzian (Lor), Gaussian (Gaus), Trapezoid (Trpz), Square (Sqre), second-order Polynomial on a logarithmic scale (LogPoly), and Asymmetric MZI (AMZI), where the

Parameters/Filter shapes	Lor.	Gaus.	Trpz.	Sqre.	LogPoly	AMZI
$\Delta\lambda_{BW}$ (nm)	x	x	x	x	x	-
$\Delta\lambda_{DET}$ (nm)	x	x	x	x	x	-
Gauss-order	-	x	-	-	-	-
Decay ($10n$ dB/decade)	-	-	x	-	-	-
Suppression ratio (dB)	x	x	x	x	x	-
AMZI phase offset (u.o.π)	-	-	-	-	-	x
AMZI rel. delay (ps)	-	-	-	-	-	x
AMZI output coupling	-	-	-	-	-	x

Table A.2: Available filter types and parameters

parentheses correspond to the abbreviations in Table A.2, which summarizes adjustable parameters for the different filter shapes. A 'x' in Table A.2 indicates that a parameter applies to the particular filter.

In the table, $\Delta\lambda_{BW}$ and $\Delta\lambda_{DET}$ are the bandwidth (FWHM) and detuning from the carrier, respectively, which apply to all filter types except the AMZI. The Gauss-order sets the order of the super-Gaussian filter shape, Decay is the slope, in multiples of 10 dB/decade of the Trapezoid filter, the suppression ratio sets the maximum contrast between the maximum and minimum transmission of all the BPFs, and the phase offset, relative delay, and output coupling ratio of the AMZI obviously only apply to the AMZI filter.

A.3 Receiver model

A simple model for calculating the Bit Error-Rate (BER) in a direct detection system consisting of an ideal photodiode, an electrical low-pass filter, and a sampling/decision circuit, is presented. The noise terms responsible for erroneously detected bits are listed, and the method for determining the optimum sampling time is explained.

Without optical amplification, there are two contributions to the noise incident on the photodiode: thermal noise and shot noise from the incident signal. These may be described in terms of the corresponding variance of the Equivalent Photo Current (EPC) [158]

$$\sigma_{th}^2 = N_{th}B_e \tag{A.2}$$

$$\sigma_{s-shot}^2 = 2eB_e i_s \tag{A.3}$$

where N_{th} is the thermal noise spectral density, B_e is the bandwidth of the electrical filter, e is the elementary charge, and i_s is the EPC of the input signal power $P_{in}(t)$, defined as $i_s = |[R_{rec}P_{in}(t)] \otimes h_{rec}(t)|$, where $h_{rec}(t)$ is the impulse response corresponding to the transfer function $H_{rec}(f)$ of a 4^{th} order Bessel low-pass filter

$$H_{rec}(f) = \frac{105}{105 + 105s + 45s^2 + 10s^3 + s^4} \tag{A.4}$$

Here, $s = 2.11j\frac{f}{B_e}$, which leads to a -3 dB electrical power bandwidth of B_e. If an optical amplifier, as e.g. an SOA, precedes the photodiode three additional noise terms come into play, namely shot noise from spontaneous emission, signal-spontaneous beat noise, and spontaneous-spontaneous beat noise, here quantified by the variances of the EPC [158]

$$\sigma^2_{sp-shot} = 2eB_e i_{sp} \quad (A.5)$$

$$\sigma^2_{s-spon} = 4i_s i_{sp}\frac{B_e}{B_o} \quad (A.6)$$

$$\sigma^2_{sp-sp} = i^2_{sp}B_e\frac{2B_o - B_e}{B_0^2} \quad (A.7)$$

Here, i_{sp} is the EPC of the ASE power, i.e. $i_{sp} = |[R_{rec}P_{sp}(t)] \otimes h_{rec}(t)|$, where $P_{sp}(t)$ is the ASE power in the optical bandwidth B_o. Expressing P_{sp} as $P_{sp} = \widetilde{P}_{sp}B_0$, where $\widetilde{P}_{sp}$ is the spectral density of the ASE, it becomes clear that $\sigma^2_{sp-shot}$ and σ^2_{sp-sp} may be reduced by filtering the ASE as tightly as possible, whereas σ^2_{s-spon} is independent of B_o. For a non-preamplified receiver as the one described here, the thermal noise σ^2_{th} and signal-spontaneous beat noise σ^2_{s-sp} dominate, but including all the five terms the total noise variance becomes

$$\sigma^2_{tot} = \sigma^2_{th} + \sigma^2_{s-shot} + \sigma^2_{sp-shot} + \sigma^2_{s-spon} + \sigma^2_{sp-sp} \quad (A.8)$$

Assuming that the noise distributions are Gaussian, the minimum BER may be approximated with [158]

$$BER = \frac{1}{\sqrt{2\pi}}\frac{\exp(-Q^2/2)}{Q} \quad (A.9)$$

where the Q value is defined as

$$Q = \frac{i_{s,1} - i_{s,0}}{\sqrt{\sigma^2_{tot,0}} + \sqrt{\sigma^2_{tot,1}}} \quad (A.10)$$

with $i_{s,0}$, $i_{s,1}$, $\sigma^2_{tot,0}$, and $\sigma^2_{tot,1}$ being the EPCs and the total noise variances corresponding to the "0" and "1" levels of the signal, respectively, for a specific delay of the sampling process. In order to find the optimum sampling delay, corresponding to sampling where the eye diagram is the most open, the expected bit sequence is first identified in the incoming signal, and the Q value is calculated for the 1^{st} sample of the 1^{st} timeslot, 1^{st} sample of the 2^{nd} timeslot, etc, and 2^{nd} sample of the 1^{st} timeslot, 2^{nd} sample of the 2^{nd} timeslot, etc. For each delay the lowest Q value, corresponding to the most pessimistic eye opening for that particular delay, is noted, and the highest of these Q values is used to calculate the BER. This way the BER is based on the worst-case eye opening, i.e. the lowest "1" level and the highest "0" level, but sampled with the optimum delay.

By attenuating the signal and ASE power and recalculating the optimum BER repeatedly, the receiver sensitivity at $BER = 10^{-9}$, i.e. the input signal power corresponding to a BER of 10^{-9} ($Q \approx 6$), is identified.

Appendix B

Gain model

The material gain model is taken from Agrawal and Dutta [104], and includes contributions from recombination of electron-light hole, as well as electron-heavy hole pairs

$$g(\lambda, N) = g_{lh}(\lambda, N) + g_{hh}(\lambda, N) \tag{B.1}$$

Both contributions are given by

$$g_\gamma(\lambda, N) = \frac{e^2 \left|M_b\right|^2 \lambda}{4\pi^2 \varepsilon_0 m_0^2 n_a c_0^2} \rho_\gamma(\lambda) \left(f_c(E_{c,\gamma}) + f_v(E_{v,\gamma}) - 1\right) \tag{B.2}$$

where $\gamma = lh, hh$, m_0 is the free electron mass, n_a is the refractive index of the active region, $|M_b|^2$ is the average matrix element for the Bloch states, ρ_γ is the joint density of states, and f_c and f_v are the Fermi distributed occupation probabilities of electrons and holes in the conduction and valence bands, respectively. The arguments to the Fermi functions are the energies of the electrons $E_{c,\gamma}$ and holes $E_{v,\gamma}$, which form electron-hole pairs satisfying the $\Delta k = 0$ selection rule, with an energy difference of hc_0/λ. The matrix element is given by

$$\left|M_b\right|^2 = \frac{E_g(E_g + \Delta)m_0^2}{6(E_g + \frac{2}{3}\Delta)m_c} \tag{B.3}$$

where E_g, Δ, and m_c is the bandgap energy, the spin-orbit splitting energy, and the effective electron mass in the conduction band (parabolic bands are assumed). The joint density of states can be expressed

$$\rho_\gamma(\lambda) = \sqrt{\left(h\frac{c_0}{\lambda} - E_g\right)\left(\frac{8\pi^2}{h^2} m_{r,\gamma}\right)^3} \tag{B.4}$$

with $m_{r,\gamma}$ being the reduced masses

$$m_{r,\gamma} = \frac{m_c m_{v,\gamma}}{m_c + m_{v,\gamma}} \tag{B.5}$$

and $m_{v,\gamma}$ is effective light-hole or heavy-hole mass. The Fermi distributions are

$$\begin{aligned} f_c(E_{c,\gamma}) &= \left(\exp\left(\frac{E_{c,\gamma}-E_{qF,c}}{k_BT}\right)+1\right)^{-1} \\ f_v(E_{v,\gamma}) &= \left(\exp\left(\frac{E_{v,\gamma}-E_{qF,v}}{k_BT}\right)+1\right)^{-1} \end{aligned} \tag{B.6}$$

where k_B is the Boltzmann constant, T is the absolute temperature, and $E_{c,\gamma}$ and $E_{v,\gamma}$ are the electron and hole energies, which can be expressed

$$\begin{aligned} E_{c,\gamma} &= \frac{m_{r,\gamma}}{m_c}\left(h\frac{c_0}{\lambda}-E_g\right) \\ E_{v,\gamma} &= \frac{m_{r,\gamma}}{m_{v,\gamma}}\left(h\frac{c_0}{\lambda}-E_g\right) \end{aligned} \tag{B.7}$$

The quasi-Fermi levels E_{qF} in (B.6) are approximated by the empirical formulas

$$\begin{aligned} E_{qF,c} &= k_BT\left(\ln\left(\frac{N}{N_c}\right)+\frac{N}{N_c}\left(64+0.05524\frac{N}{N_c}\left(64+\sqrt{\frac{N}{N_c}}\right)\right)^{-\frac{1}{4}}\right) \\ E_{qF,v} &= k_BT\left(\ln\left(\frac{N}{N_v}\right)+\frac{N}{N_v}\left(64+0.05524\frac{N}{N_v}\left(64+\sqrt{\frac{N}{N_v}}\right)\right)^{-\frac{1}{4}}\right) \end{aligned} \tag{B.8}$$

where N_c and N_v are the effective density of states

$$\begin{aligned} N_c &= 2\left(\frac{2\pi m_c k_BT}{h^2}\right)^{3/2} \\ N_v &= 2\left(\frac{2\pi k_BT}{h^2}\right)^{3/2}\left(m_{v,lh}^{3/2}+m_{v,hh}^{3/2}\right) \end{aligned} \tag{B.9}$$

and N is the carrier density, under the assumption of charge neutrality, i.e. equal hole and electron concentration in the active region. The temperature T enters explicitly into (B.6) and (B.9). In steady state operation, recent measurements show that the temperature is a linear function of the carrier density N [220]

$$T = a_T N + T_0 \tag{B.10}$$

with parameters $a_T = 52\cdot 10^{-24}\ \frac{K}{m^3}$, and $T_0 = 230\ K$. Since this may not be an accurate description for dynamic calculations, the feature can be turned on and off from the input files. The bandgap energy E_g shrinks at high carrier concentrations due to an increasing overlap of the electronic wave functions [104]

$$E_g = e\left(E_{g,0}-1.3\cdot 10^{-10}N^{1/3}\right) \tag{B.11}$$

where $E_{g,0}$ is the bandgap energy at zero doping

$$E_{g,0} = e\left(1.35 - 0.72Y + 0.12Y^2\right) \tag{B.12}$$

and Y is the mole fraction of As in lattice matched $In_{1-X}Ga_XAs_YP_{1-Y}$. The mole fraction Y of Ga is connected to X through the lattice matching requirement

$$X = \frac{0.4526Y}{1 - 0.031Y} \tag{B.13}$$

The mole fractions are calculated based on the desired bandgap energy, and once they are known the band structure parameters introduced above can be determined as [104]

$$\begin{aligned}
n_a &= \sqrt{(1-Y)\left(8.4X + 9.6\left(1-X\right)\right) + Y\left(13.1X + 12.2\left(1-X\right)\right)} \\
\Delta &= e\left(0.11 + 0.31Y - 0.09Y^2\right) \\
m_c &= \left(0.080 - 0.039Y\right)m_0 \\
m_{hh} &= \left(\left(1-Y\right)\left(0.79X + 0.45\left(1-X\right)\right) + Y\left(0.45X + 0.4\left(1-X\right)\right)\right)m_0 \\
m_{lh} &= \left(\left(1-Y\right)\left(0.14X + 0.12\left(1-X\right)\right) + Y\left(0.082X + 0.026\left(1-X\right)\right)\right)m_0
\end{aligned} \tag{B.14}$$

Appendix C

Implementation of numerical models

In this appendix, details about the implementation of the one and two dimensional models, described in Chapter 3, are provided. The one-dimensional model includes ASE, which propagates in both directions, and this requires an iterative approach before the carrier density in each section attains a stable value. The two-dimensional model does not include ASE, and if diffusion is turned off, $D_x = 0$, the steady-state carrier density associated with a specific grid point only depends on the intensity at this point. However, for $D_x \neq 0$, the carrier density at that point also depends on the density in the neighboring points, which again calls for an iterative approach.

C.1 One-dimensional model

The dynamic input signals always begin with a number of logic "0"s, where the exact number is an input parameter to the model. Based on the average power, data format, rise/fall time for NRZ, pulse shape for RZ, pulse width for RZ, and extinction ratio, the steady-state power corresponding to a logic zero is calculated. This result represents the initial condition for obtaining the steady state solution. As shown in the left part of the flow chart in Fig. C.1, the calculated power, as well as all SOA-specific parameters such as physical dimensions, confinement factor, and bias currents, are inputs to the process labeled "Propagate 1 time step". The process propagates all input signals one time step through SOA $\#i$ of the MZI structure, and is repeated for all 6 SOAs. The time step assumes a value much larger than the transit time Δt of a single section, in order to accelerate convergence towards a steady-state solution.

The propagation step contains several sub steps, which is illustrated in Fig. C.2. First, based on the input power to each section j of SOA i at the time $t - \Delta t$, the single-pass gains and phase changes of all N_z sections are calculated. This is done

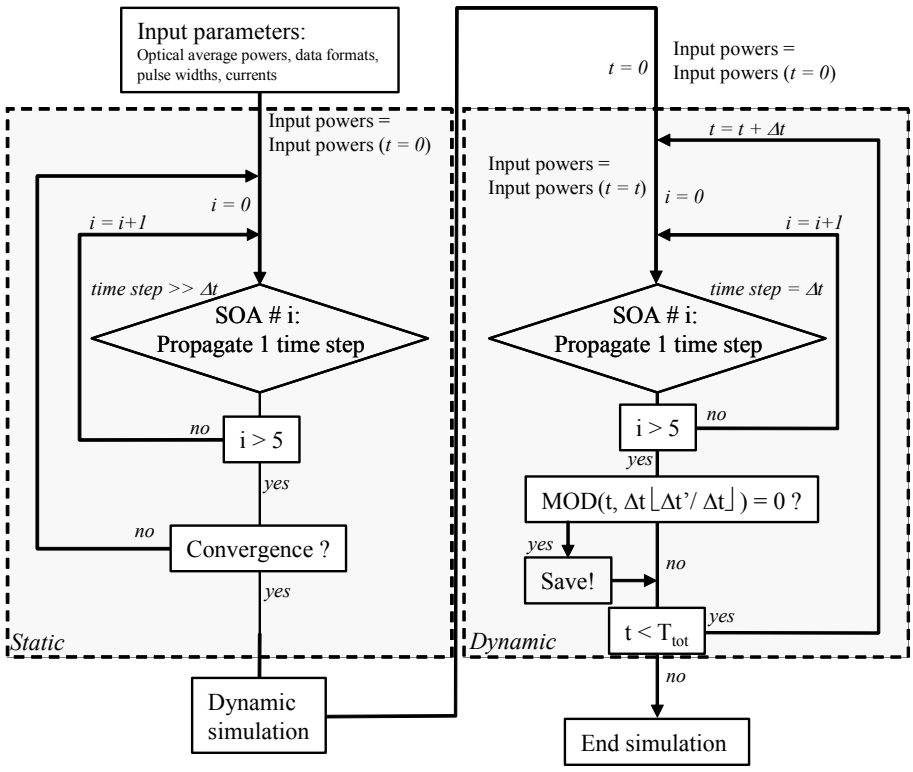

Figure C.1: Flow chart of the algorithm. The static part to the left obtaines a steady-state solution, before the input signals become dynamic in the right part of the figure.

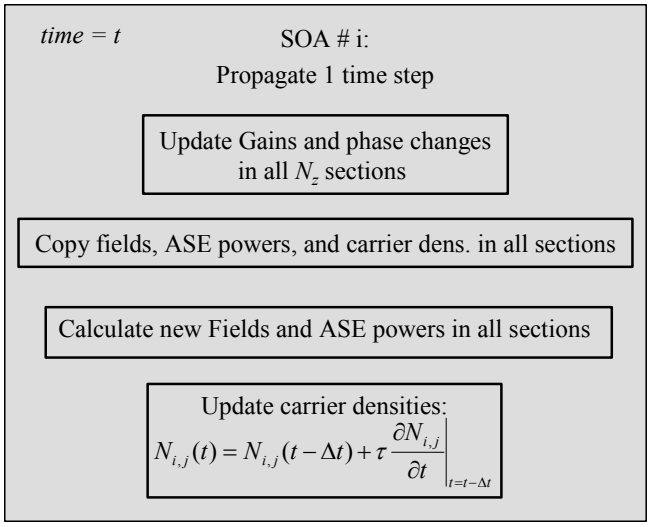

Figure C.2: Flow chart of the propagation procedure.

very fast, since, as a start-up procedure, the program creates dense (N, λ) look-up tables for the material gain and spontaneous-emission factor. Then, the existing signal powers, ASE spectra, and carrier densities at each section boundary are copied, before the optical powers are updated using the newly calculated section gains and phase shifts. Finally, the carrier densities are updated, using the old values to calculate the time derivative. If the MZI contains less than 6 SOAs, the missing amplifiers are simply made transparent by setting the single pass gain in all sections to unity. Only phase changes stemming from the propagation itself are included.

As illustrated in Fig. C.1, propagation of the signal powers corresponding to $t = 0$ is repeated until the carrier density in all sections of the MZI has converged. This is obtained by requiring

$$\sum_i \sum_j \left| \frac{N_{i,j} - N_{i,j}^{old}}{N_{i,j}^{old}} \right| < K \tag{C.1}$$

where K is chosen significantly low.

The input signals now become time dependent, and the arrow is followed to the right part of the flowchart in Fig. C.1. Here, the simulation procedure is repeated with a time step equal to Δt, until the time exceeds the duration of the input signal. As shown in Fig. C.1, the fields and ASE powers can be saved with a user defined (approximate) resolution $\Delta t'$.

The transit time Δt of one section is the elementary time constant, as all time spans are integer multiples of Δt. This means that no phenomenon varying on a time scale smaller than τ can be resolved. However, this is not a limitation, since Δt can be made infinitely small by simply increasing N_z. The real limitation

comes from the fact that only interband carrier dynamics is taken into account, which set a lower limit for the pulse width, given by (3.1). The integration of the carrier rate equation is approximated by the linear expression in the bottom of Fig. C.2, which is good approximation as long as Δt is significantly smaller than the time scale on which the carrier density varies.

C.2 Two-dimensional model

An overview of the algorithm of the two-dimensional model given by the flowchart in Fig. C.3. Based on the definition of the two-dimensional refractive index the lateral confinement factor Γ_y is calculated, as outlined in section E.2. Moreover, the transversal input field distributions are calculated as eigenmodes of an access waveguide with user-defined dimensions.

For dynamic calculations the approach is similar to what was described in section C.1 The field distributions of the control signal and the probe are launched into the multi-moded waveguide containing power corresponding to a logic zero and the fixed CW power, respectively. The carrier density profile of the first row $j = 0$ is calculated based on the input distributions, and the corresponding gain and phase changes are used to propagate the field to the second row, etc. When the field have propagated through the structure twice, it is tested whether the carrier densities have converged, using the criterion in (C.1), where i represents the transversal grid points in the core of the waveguide. The fields are propagated through the structure until the criterion is fulfilled.

Propagation of the dynamic signal is handled in the same way as in the one-dimensional model, except that the retarded time frame (3.58) allows for propagating the time-incremented input signal through the entire structure.

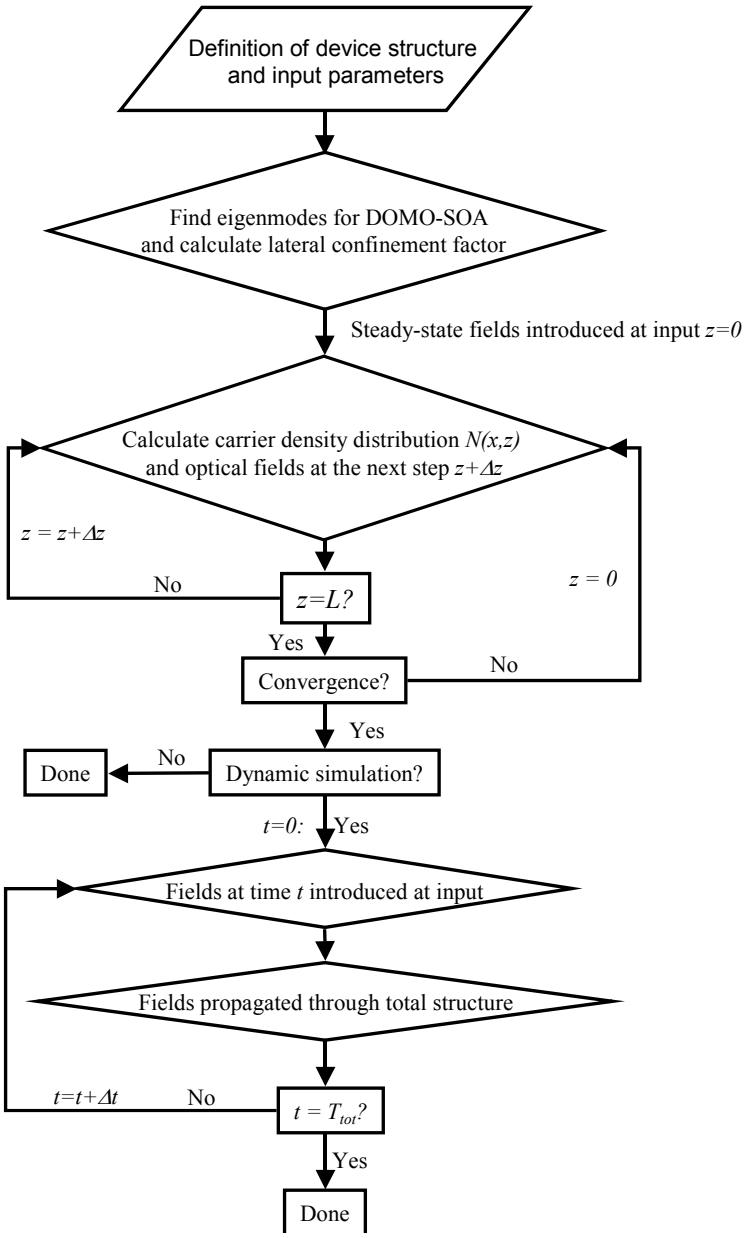

Figure C.3: Flow chart of the two-dimensional model.

Appendix D

Simulation parameters

Here, simulation parameters not specified in the text for the one- and two-dimensional models, and the receiver model, are provided.

D.1 One-dimensional model

Parameter	**Symbol**	**Unit**	**Value**
Mode index	$\overline{n}$	-	3.2
Group index	n_g	-	3.3
Differential core index	$\partial n_{core}/\partial N$	m^{-3}	$-2 \cdot 10^{-26}$
Reference wavelength	λ_r	μm	1.55
Reference carrier density	N_r	m^{-3}	$1.5 \cdot 10^{24}$
Bandgap energy ($hc_0/E_{g,0}$)	$\lambda_{g,0}$	μm	1.57
Free electron mass	m_0	kg	$9.11 \cdot 10^{-31}$
Loss coefficients	a_{1_1}	m^{-1}	5600
$a_1 = a_{1\_1} - a_{1\_2}L$	a_{1_2}	m^{-2}	$1.33 \cdot 10^{6}$
$a_2 = a_{2\_1} - a_{2\_2}L$	a_{2_1}	m^{2}	$4.35 \cdot 10^{-21}$
	a_{2_2}	m	$1.33 \cdot 10^{-18}$
	a_3	m^{-1}	$3 \cdot 10^{3}$
Recombination coefficients	c_1	s^{-1}	$1 \cdot 10^{8}$
	c_2	$s^{-1}m^3$	$9 \cdot 10^{-16}$
	c_3	$s^{-1}m^6$	$5 \cdot 10^{-41}$
Coupling ratios	r_1	-	0.50
	r_2	-	0.50
	$r_3^{'}$	-	0.50
	$r_4^{'}$	-	0.50
Power reflection coefficients	R_1	-	0
	R_2	-	0
Temperature	T	K	293
ASE spectrum resolution	$\Delta\lambda$	nm	10
Coupling loss	ξ_L	dB	0

D.2 Two-dimensional model

Parameter	**Symbol**	**Unit**	**Value**
Differential gain	$\partial g/\partial N$	m^2	$5 \cdot 10^{-20}$
Linewidth enhancement factor	α	-	5.0
Carrier density at transparency	N_{tr}	m^{-3}	$1 \cdot 10^{24}$
Loss coefficient	a_l	m^{-1}	$3 \cdot 10^{3}$
Recombination coefficients	c_1	s^{-1}	$1 \cdot 10^{8}$
	c_2	$s^{-1}m^3$	$9 \cdot 10^{-16}$
	c_3	$s^{-1}m^6$	$5 \cdot 10^{-41}$
Cladding index	n_{clad}	-	3.17
Reference index	n_0	-	3.17
Number of transversal grid points	N_x	-	97
Propagation step	Δz	μm	1.0
Fundamental transversal grid size	d_{core}	μm	0.10
Maximum transversal grid size increase	$R_{\max}$	-	2.0
Group refractive index	n_g	-	3.3

D.3 Receiver parameters

Parameter	Symbol	Unit	Value
Thermal noise spectral density	σ_{th}^2	A^2Hz^{-1}	$2.2 \cdot 10^{-22}$
Electrical -3 dB bandwidth	B_e	$-$	$Bitrate$
Photodiode responsivity	R_{rec}	A/W	1.0

Appendix E

Effective index method

The effective-index method (EIM) is a way of solving a 2D waveguide problem by dividing it into two 1D problems. In the present context the EIM will be used to eliminate one of the dimensions of a rectangular waveguide. This is done by ascribing an *effective* index to every point on the remaining axis, in order to account for the wave-guiding in the eliminated dimension. Eliminating a dimension reduces the level of complexity, and consequently the amount of CPU-time necessary for obtaining a result. It is important to stress, however, that the EIM is an approximation, which means that the reduction of complexity comes at a price.

E.1 Derivation of eigenmodes

The starting point is the scalar wave equation introduced in (3.54)

$$\nabla^2 E + n^2 k_0^2 E = 0 \tag{E.1}$$

where E is the Fourier transform of the electric field, and n is the refractive index, which is assumed to be a real number, corresponding to a passive waveguide. The free-space wave number k_0 is defined as $k_0 = \frac{2\pi}{\lambda_0}$, λ_0 being the free-space wavelength. The electric field is assumed to be separable in x and y as in (3.51)

$$E = \phi(y)\psi(x)\exp(i\beta z) \tag{E.2}$$

where β is the propagation constant. By using the method of separation of variables, and assuming that the refractive index profile is $z-$invariant, (E.1) can be expanded to

$$\frac{\partial^2 \phi}{\partial y^2} + k_0^2 \left[n^2(x,y) - n_{eff}^2(x) \right] \phi = 0 \tag{E.3}$$

$$\frac{\partial^2 \psi}{\partial x^2} + k_0^2 \left[n_{eff}^2(x) - \overline{n}^2 \right] \psi = 0 \tag{E.4}$$

The effective index n_{eff} is the separation variable, and $\overline{n} = \frac{\beta}{k_0}$ is the mode-index of a specific eigenmode. A waveguide with a rectangular cross section of (W, H) will now be considered. The longest dimension W is along the x-axis, which means that (E.3) must be solved for the effective index for all values of x [221]. The general solution of (E.3) is given by

$$\phi(y) = \begin{cases} A_1 \cos(\kappa_y y) + B_1 \sin(\kappa_y y) & ; \quad |y| \leq H/2 \\ A_2 \exp\left[-\gamma_y(|y| - H/2)\right] & ; \quad |y| > H/2 \end{cases} \tag{E.5}$$

where κ_y is the lateral propagation constant, γ_y is the lateral attenuation constant, H is the height of the waveguide, and A_1, A_2, and B_1 are arbitrary constants to be determined by the boundary conditions. κ_y and γ_y are related to the refractive indices in the following way [104]

$$\kappa_y^2 = k_0^2(n_{core}^2 - n_{eff}^2) \qquad ; \qquad \gamma_y^2 = k_0^2(n_{eff}^2 - n_{clad}^2) \tag{E.6}$$

n_{core} and n_{clad} being the refractive indices of the core and cladding, respectively. Here, H is small enough to support only the fundamental mode in the y-direction. Since the fundamental mode is even, $B_1 = 0$ in (E.5). The rest of the constants are found from the boundary conditions that the electromagnetic field must obey on any surface where the constitutive parameters undergo discontinuous changes.

Assuming the electric field is polarized along the x - axis, it is completely tangential to the boundary, and thus $\phi(y)$ is continuous across the discontinuities at $\pm H/2$. The tangential z-component of the magnetic flux density H is proportional to $\frac{\partial \phi}{\partial y}$, and is continuous as well, assuming there are is no current on the surface [222]. These two conditions yield the eigenvalue equation that determines the effective index

$$\gamma_y = \kappa_y \tan(\kappa_y H/2) \tag{E.7}$$

In order to find the mode-indices $\bar{n}$ and the corresponding field distributions in the x-direction, (E.4) is solved. The solution is identical to (E.5), except that n_{core}, n_{eff}, and H have to be replaced by n_{eff}, $\bar{n}$,and W, respectively, where W is the width of the waveguide. Since the electric field is perpendicular to the surface $\psi(x)$ is not continuous across the discontinuities, but the electric flux density D is, which provides the following relationship, assuming

$$n_{clad}^2 \psi(\pm\frac{W^-}{2}, y) = n_{eff}^2 \psi(\pm\frac{W^+}{2}, y) \tag{E.8}$$

However, in the EIM the magnitude of the electric field, and its derivative, are assumed continuous across discontinuities along both axes, although the solution obtained is inaccurate around the boundaries. The problem is of minor importance though, as long as the mode considered is well-confined (far from cutoff).

The eigenvalue equations determining the mode-indices are

$$\begin{array}{ll} \gamma_x = \kappa_x \tan(\kappa_x W/2) & \text{even modes} \\ \gamma_x = -\kappa_x \cot(\kappa_x W/2) & \text{odd modes} \end{array} \tag{E.9}$$

where κ_x and γ_x are defined like (E.6) with the substitutions described above. Now the eigenmodes in the x-direction can be found by inserting the solutions to (E.9) into the x-equivalent of (E.5). This approach is used in section 6.4 to calculate the input field distributions to the dual-moded SOA.

E.2 Confinement factor

From the equations in the previous section, an expression for the lateral optical confinement factor Γ_y can now be found. Γ_y is defined as the fraction of the modal power which overlaps with the core of the waveguide

$$\Gamma_y = \frac{\int_{-H/2}^{H/2} |\phi(y)|^2 \, dy}{\int_{-\infty}^{\infty} |\phi(y)|^2 \, dy} \tag{E.10}$$

Using (E.5) and (E.10), Γ_y can be expressed as

$$\Gamma_y = \frac{H/2 + \sin(\kappa_y H)/(2\kappa_y)}{H/2 + \sin(\kappa_y H)/(2\kappa_y) + \cos^2(\kappa_y H/2)/\gamma_y} \tag{E.11}$$

This expression is used in all the simulations of the DOMO wavelength converter.

Appendix F

PhD publications

p1 M. L. Nielsen, D. J. Blumenthal, and J. Mørk, "A Transfer Function approach to the Small-Signal Response of Saturated Semiconductor Optical Amplifiers", IEEE J. Lightwave Technology, vol. 18, no. 12, pp. 2151-2157, 2000.

p2 M. L. Nielsen and J. Mørk, "Increasing the Modulation Bandwidth of Semiconductor Optical Amplifier based Switches using Optical Filtering", Submitted to J. Opt. Soc. Am. B, 2003.

p3 S. Bischoff, M. L. Nielsen, and J. Mørk, "Improved All-optical Response of SOAs using Modulated Holding Beam", Accepted for publication in IEEE J. Lightwave Technology, 2004.

p4 M. L. Nielsen, B. Lavigne, and B. Dagens, "Polarity-preserving Wavelength Conversion at 40 Gb/s using Band-Pass Filtering", IEE Electronics Letters, vol. 39, no. 18, pp 1334-1335, 2003.

p5 Mads Lønstrup Nielsen, Bengt-Erik Olsson, and Daniel J. Blumenthal, "Pulse Extinction Ratio Improvement using SPM in an SOA for OTDM Systems Applications", in Proc. ECOC 2000, Munich, Germany, 2000.

p6 M. L. Nielsen, Bengt-Erik Olsson, and Daniel J. Blumenthal, "Pulse Extinction Ratio Improvement using SPM in an SOA for OTDM Systems Applications", IEEE Photonics Techn. Letters, vol. 14, no.2, pp. 245-247, 2002.

p7 B. Dagens, A. Labrousse, S. Fabre, B. Martin, S. Squedin, B. Lavigne, R. Brenot, M. L. Nielsen, and M. Renaud, "New Modular SOA-based active-passive integrated Mach-Zehnder interferometer and first standard-mode 40 Gb/s all-optical wavelength conversion on the C-band", in Proc. ECOC 2002 (Post-Deadline Papers), Copenhagen, Denmark, 2002.

p8 A. Labrousse, B. Dagens, R. Brenot, B. Lavigne, S. Squedin, B. Martin, S. Fabre. M. L. Nielsen, and M. Renaud, "Standard-mode 40 Gbit/s Performance Analysis of Evanescent Coupling 'active-passive' Mach-Zehnder Interferometer for All-optical Regeneration", IEE Electronics Letters, vol. 39, no. 16, pp. 1201-1202, 2003.

p9 M. L. Nielsen, M. Nord, M. N. Petersen, B. Dagens, A. Labrousse, R. Brenot, B. Martin, S. Squedin, and M. Renaud, "40 Gbit/s Standard-Mode Wavelength Conversion in All-active MZI with Very Fast Response", IEE Electronics Letters, vol. 39, no. 4, pp. 385-386, 2003.

p10 M. L. Nielsen, J. D. Buron, M. Nord, and M. N. Petersen, "SOA-based Functional Devices for Future Optical Networks", in Techn. Digest SSDM 2003, paper F-9-1 (invited), Tokyo, Japan, 2003.

p11 M. L. Nielsen, D. Wolfson, A. Kloch, S. Bischoff, and J. Mørk, "Numerical Analysis and Optimization of a Dual-Order Mode All-optical Wavelength Converter", in Proc. ECOC 2001, Amsterdam, Holland, 2001.

p12 M. L. Nielsen, J. De Merlier, G. Morthier, and R. Baets, "Experimental Demonstration of All-optical 2R Regeneration at 10 Gb/s in a Novel MMI-SOA based device", in Techn. Digest OFC 2002, Anaheim, CA., USA, 2002.

p13 M. L. Nielsen, T. Fjelde, J. Buron, and B. Dagens, "All-optical Bit-Pattern Recognition in Data Segments using an All-active MZI Wavelength Converter", in Proc. ECOC 2002, Copenhagen, Denmark, 2002.

p14 M. L. Nielsen, J. D. Buron, J. Mørk, and B. Dagens, "All-optical Extraction of 40 GHz component from 40 Gb/s NRZ data using Signal Processing in an SOA combined with optical filtering", submitted to OECC 2004.

p15 M. L. Nielsen, J. Mørk, T. Fjelde, and B. Dagens, "Numerical Analysis of an All-optical Logic XOR gate based on an active MZ interferometer", in Techn. Digest CLEO 2002, Long Beach, CA., USA, 2002.

p16 M. L. Nielsen, J. Buron, and B. Dagens, "Demonstration of an All-optical 3-input XOR gate and a Data Encryption scheme at 10 Gb/s based on All-active Mach-Zehnder interferometers", in Techn. Digest OAA, Vancouver, BC., Canada, 2002.

p17 M. L. Nielsen, M. N. Petersen, M. Nord, and B. Dagens, "Compact All-optical Parity calculator based on a single all-active Mach-Zehnder Interferometer with an all-SOA amplified feedback", Techn. Digest OFC2003, Atlanta, Ga, USA, 2003.

p18 T. Fjelde, D. Wolfson, A. Kloch, M. L. Nielsen, and H. Wessing, "SOA-based Functional Devices", in Proc. ITCom2001, Denver, Co., USA, 2001.

p19 T. Fjelde, M. L. Nielsen, H. Wessing, and D. Wolfson, "Wavelength Conversion and All-optical Logic", DOPS-NYT, vol. 16, 2001.

p20 M. L. Nielsen, A. T. Clausen, T. Fjelde, L. Oxenlöwe, A. Kloch, H. Poulsen, and D. Wolfson, "All-optical Signal Processing employing Interferometric Structures", Proc. of OSP/COST International workshop, Copenhagen, Denmark, 2001.

p21 J. Mørk, S. Bischoff, T. W. Berg, and M. L. Nielsen,"Ultrafast Optical Signal Processing using Semiconductor Optical Devices", in Proc. NUSOD2002, Zürich, Switzerland, 2002.

p22 J. Mørk, S. Bischoff, T. W. Berg, M. L. Nielsen, and F. Öhman, "Modeling of Semiconductor Optical Amplifiers", in Techn. Digest OSA 2002 Annual meeting, Orlando, Fl., USA, 2002.

p23 J. Mørk, M. L. Nielsen, and T. W. Berg, "The Dynamics of Semiconductor Optical Amplifiers: Modeling and Applications", OSA OPN Magazine, pp. 42-48, July 2003.

p24 M. Nord, S. Bjørnstad, M.L. Nielsen, and B. Dagens. "Novel strictly non-blocking Node Designs for asynchronous OPS MAN", in Proc. Photonics in Switching 2003 (PS'2003), PD paper 1, 2003, Versailles, France.

p25 M. Nord, S. Bjørnstad, M.L. Nielsen, and B. Dagens. "Demonstration of Optical Packet Switching scheme for header-payload separation and Class-based Forwarding", in Techn. Digest OFC 2004, TuQ2, 2004, Los Angeles, 2004.

p26 M. Nord, S. Bjornstad, and M.L. Nielsen, "Performance of an Asynchronous Optical Packet Switching Metropolitan Area Network with Active Nodes and Distributed MAC Protocol", Submission to J. Lightwave Technology, Spec. Issue on Metro & Access Networks, to appear in Nov. 2004.

p27 Jesper Mørk, Tommy W. Berg, Mads L. Nielsen, and Alexander V. Uskov, "The Role of Fast Carrier Dynamics in SOA-based Switches" (invited), to appear in IEICE transactions, special issue in Ultrafast Photonics, 2004.

References

[1] P. Hill, "Downturn Puts a Break on Component Start-Ups", *Opto and Laser Europe*, September 2001.

[2] Fiber.Org News and Analysis, "`www.Fibers.Org`", September 2002.

[3] J. Devaney, "The Great Telecoms Crash: Where Did It All Go Wrong?", *FibreSystems Europe*, pp. 40–42, September 2002.

[4] C. Rasmussen, S. Dey, D. Liu, J. Bennike, B. Mikkelsen, P. Mamyshev, M. Kimmitt, K. Springer, D. Gapontsev, and V. Ivshin, "Transmission of 40x42.7 Gbit/s over 5200 km UltraWave Fiber with Terrestrial 100 km Spans Using Turn-Key ETDM Transmitter and Receiver", in *Proc. Of ECOC 2002, Post Deadline Paper PD4.4*, Copenhagen, Denmark, 2002.

[5] Christian Rasmussen, Tina Fjelde, Jon Bennike, Fenghai Liu, Supriyo Dey, Benny Mikkelsen, Pavel Mamyshev, Peter Serbe, Paul Van der Wagt, Youicho Akasaka, David Harris, Denis Gapontsev, Vladlen Ivshin, and Peter Reeves-Hall, "DWDM 40G Transmission over Trans-Pacific Distance (10,000 km) Using CSRZ-DPSK, Enhanced FEC and All-Raman Amplified 100 km UltraWave Fiber Spans", in *Techn. Digest OFC 2003, Post Deadline Paper PD18-1*, Atlanta, USA, 2003.

[6] Computer World Online, "`www.computerworld.com`", November 2003.

[7] J. Lively, "2003 Ends with a Bang, Setting Stage for a Positive 2004, RHK Research Brief", March 2004, `www.rhk.com`.

[8] N. McKeown, "Scalability of IP Routers", in *Techn. Digest of OFC 2001*, Anaheim, CA., USA, 2001, p. MN1.

[9] Calient Networks, "`www.Calient.net`", June 2003.

[10] T. S. El-Bawab and J.-D. Shin, "Optical Packet Switching in Core Networks: Between Vision and Reality", *IEEE Communications Magazine*, pp. 60–65, September 2002.

[11] C. Guillemot, M. Renaud, P. Gambini, C. Janz, I. Andonovic, R. Bauknecht, B. Bostica, M. Burzio, F. Callegati, M. Casoni, D. Chiaroni, F. Clerot, S. L. Danielsen, F. Dorgeuille, A. Dupas, A. Franzen, P. B. Hansen, D. K. Hunter, A. Kloch, R. Krahenbuhl, B. Lavigne, A. Le Corre, C. Raffaelli, M. Schilling, J.-C. Simon, and L. Zucchelli, "Transparent Optical Packet Switching: The European ACTS KEOPS project approach", *IEEE J. Lightwave Technology*, vol. 16, no. 12, pp. 2117 –2134, 1998.

[12] B. Lavigne, P. Guerber, P. Brindel, E. Balmefrezol, and B. Dagens, "Cascade of 100 Optical 3R Regenerators at 40 Gbit/s based on All-active Mach Zehnder Interferometers", *Proc. ECOC 2001*, vol. 3, pp. 290 –291, 2001.

[13] O. Leclerc, B. Lavigne, E. Balmefrezol, P. Brindel, L. Pierre, D. Rouvillain, and F. Seguineau, "Optical Regeneration at 40 Gb/s and Beyond", *IEEE J. Lightwave technology*, vol. 21, no. 11, pp. 2779–2790, 2003.

[14] G. Raybon, Y. Su, J. Leuthold, R.-J. Essiambre, T. Her, C. Joergensen, P. Steinvurzel, K. Dreyer, and K. Feder, "40 Gbit/s Pseudo-Linear Transmision Over One Million Kilometers", in *Techn. Digest OFC 2002*, Anaheim, USA, 2002, pp. 930–932.

[15] D. J. Blumenthal, J. E. Bowers, L. Rau, H.-F. Chou, S. Rangarajan, W. Wang, and H. N. Poulsen, "Optical Signal Processing for Optical Packet Switching Networks", *IEEE Communications Magazine*, vol. 41, no. 2, pp. S23, 2003.

[16] L. Dittmann, C. Develder, D. Chiaroni, F. Neri, F. Callegati, W. Koerber, A. Stavdas, M. Renaud, A. Rafel, J. Sole-Pareta, W. Cerroni, N. Leligou, L. Dembeck, B. Mortensen, M. Pickavet, N. Le Sauze, M. Mahony, B. Berde, and G. Eilenberger, "The European IST Project DAVID: A Viable Approach Toward Optical Packet Switching", *IEEE J. Sel. Areas in Communications*, vol. 21, no. 7, pp. 1026–1040, 2003.

[17] S. A. Hamilton, B. S. Robinson, T. E. Murphy, S. J. Savage, and E. P. Ippen, "100 Gb/s Optical Time-Division Multiplexed Networks", *IEEE J. Lightwave Technology*, vol. 20, no. 12, pp. 2086–2100, 2002.

[18] A. E. Willner, "All-optical Signal Processing for Implementing Network Switching Functions", *All-Optical Networking: Existing and Emerging Architecture and Applications/Dynamic Enablers of Next-Generation Optical Communications Systems/Fast Optical Processing in Optical Transmission/VCSEL and Microcavity Lasers. 2002 IEEE/LEOS Summer Topical Meeting*, pp. TuC1–9, 2002.

[19] E. McGeehan, M. C. Hauer, A. B. Sahin, and A. E. Willner, "Multiwavelength-channel Header Recognition for Reconfigurable WDM

Networks using Optical Correlators based on Sampled Fiber Bragg Gratings", *IEEE Photonics Techn. Letters*, vol. 15, no. 10, pp. 1464–1466, 2003.

[20] D. J. Blumenthal, "All-optical Label Swapping for the Future Internet", *Optics and Photonics News*, vol. 13, no. 3, pp. 22–25, 2002.

[21] L. Rau, S. Rangarajan, D. J. Blumenthal, H.-F. Chou, Y.-J. Chiu, and J. E. Bowers, "Two-hop All-optical Label Swapping with variable length 80 Gb/s Packets and 10 Gb/s Labels using Nonlinear Fiber Wavelength Converters, Unicast/Multicast output and a single EAM for 80- to 10 Gb/s Packet Demultiplexing", *Techn. Digest OFC 2002*, pp. FD2–1, 2002.

[22] T. Fjelde, A. Kloch, D. Wolfson, B. Dagens, A. Coquelin, I. Guillemot, F. Gaborit, F. Poingt, and M. Renaud, "Novel Scheme for simple Label-swapping employing XOR Logic in an Integrated Interferometric Wavelength Converter", *IEEE Photonics Techn. Letters*, vol. 13, no. 7, pp. 750–752, 2001.

[23] T. Durhuus, B. Mikkelsen, C. Jørgensen, S. L. Danielsen, and K. E. Stubkjær, "All-Optical Wavelength Conversion by Semiconductor Optical Amplifiers", *IEEE J. Lightwave Technology*, vol. 14, pp. 942–954, 1996.

[24] M. Nord, S. Bjørnstad, and C. M. Gauger, "OPS or OBS in the Core Network?", in *Proceedings of ONDM 2003*, Budapest, Hungary, 2002, pp. 179–198.

[25] Mintera Optical Networks, "Myths and Realities About 40G Optical Technology", *White paper*, 2002.

[26] N. Le Sauze, M. Nodr, M. S. Berger, H. Christiansen, J. Fernandez-Palacios, J. Solé-Pareta, and S. Spadaro, "IST DAVID Report: Network Concepts Validation and Benchmarking", Tech. Rep. D101, 2003.

[27] Xerox, "`www.Xeroxtechnology.com`", March 2004.

[28] Fujitsu, "`www.Fujitsu.com`", March 2004.

[29] R. Ramaswami and K. N. Sivarajan, *Optical Networks - A Practical Perspective*, chapter 8, Academic Press, 1998.

[30] C. Fenger and V. B. Iversen, "Wavelength Conversion by Using Multiple Fibres", in *Proc. ECOC 2002*, Copenhagen, Denmark, 2002, p. 2.4.2.

[31] J. Strand, R. Doverspike, and L. Guangzhi, "Importance of Wavelength Conversion in an Optical Network", *Optical Networks Magazine*, vol. 2, no. 3, pp. 33–44, 2001.

[32] N. Wauters, W. Van Parys, B. Van Caenegem, and P. Demeester, "Reduction of Wavelength Blocking through Partitioning with Wavelength Converters", *Techn. Digest of OFC 1997*, pp. 122 –123, 1997.

[33] C. M. Assi, A. A. Shami, M. A. Ali, Z. Zhensheng, and Xinyi Liu, "Impact of Wavelength Converters on the Performance of Optical Networks", *Optical Networks Magazine*, vol. 3, no. 2, pp. 22–30, 2002.

[34] Yuanqiu Luo and N. Ansari, "Split Restoration with Wavelength Conversion in WDM Networks", *IEEE Intern. Conf. on Communications 2003*, vol. 2, pp. 1423–1427, 2003.

[35] S. L. Danielsen, B. Mikkelsen, C. Joergensen, T. Durhuus, and K. E. Stubkjaer, "WDM Packet Switch Architectures and Analysis of the influence of Tunable Wavelength Converters on the Performance", *IEEE J. Lightwave Technology*, vol. 15, no. 2, pp. 219 –227, 1997.

[36] W. Kuebart, B. Lavigne, M. Witte, G. Veith, and O. Leclerc, "40 Gb/s Transmission over 80000 km Dispersion Shifted Fibre using Compact Opto-Electronic-3R Regeneration", in *Proc. ECOC 2003*, Rimini, Italy, 2003.

[37] D. Chiaroni, "Packet Switching Matrix: A Key element for the Backbone and the Metro", *IEEE J. Sel. Areas in Communications*, vol. 21, no. 7, pp. 1018–1025, 2003.

[38] I. Aoko, S. Kobayashi, T. Yakihari, H. Matsuura, and A. Miura, "Development of HBT-IC Modules for 50 GBPS Optical Communication Systems (White Paper)", March 2004, `http://www.Yokogawa.com/rd/pdf/TR/rd-Tr-R00034-001.pdf`.

[39] B. Lavigne, E. Balmefrezol, P. Brindel, B. Dagens, R. Brenot, L. Pierre, J.-L. Moncelet, D. de la Grandiere, J.-C. Remy, J.-C. Bouley, B. Thedrez, and O. Leclerc, "Low Input Power All-Optical 3R Regenerator Based on SOA Devices for 42.66 Gbit/s ULH WDM RZ Transmissions with 23 dB Span Loss and All-EDFA Amplification", *Techn. Digest OFC 2003*, pp. PD15–1, 2003.

[40] B. Lavigne, E. Balmefrezol, L. Pierre, B. Dagens, R. Brenot, B. Thedrez, M. Renaud, and O. Leclerc, "Operation Margins of a SOA-based 3R Regenerator for 42.66 Gbit/s ULH transmission Systems", in *Proc. ECOC 2003*, Rimini, Italy, 2003.

[41] S. Kodoma, T. Ito, N. Watanabe, S. Kondo, H. Takeutchi, H. Ito, and T. Ishibashi, "2.3 Picosecond Optical Gate Monolithically Integrating Photodiode and Electroabsorption Modulator", *IEE Electronics Lett.*, vol. 37, no. 19, pp. 1185–1186, 2001.

[42] T. Yoshimatsu, S. Kodama, K. Yoshino, and H. Ito, "100 Gbit/s Full-Rate Operation of PD-EAM Optical Gate for Retiming Function", in *Techn. Digest SSDM 2003*, Tokyo, Japan, 2003, pp. 882–883.

[43] R. Slusher, "Controlling Light with Light: Nonlinear Optics Applications in Optical Communications", in *Techn. Digest CLEO 2002*, Long Beach, CA., USA, 2002, p. 482.

[44] J. Leuthold, D. Marom, S. Cabot, R. Ryf, P. Bernasconi, F. Baumann, J. Jaques, D. T. Neilson, and C. R. Giles, "All-Optical Wavelength Converter Based on a Pulse Reformatting Optical Filter", in *Techn. Digest OFC 2003, Paper PD41*, Atlanta, USA, 2003.

[45] R. J. Manning, A. D. Ellis, A. J. Poustie, and K. J. Blow, "Semiconductor Laser Amplifiers for Ultrafast All-Optical Signal Processing", *J. Opt. Soc. Am. B*, vol. 14, no. 11, pp. 3204–3216, 1997.

[46] Leif K. Oxenlöwe, *Optical Signal Processing with Semiconductor Components*, PhD thesis, Research Center COM, Technical University of Denmark, 2002.

[47] M. Itoh, Y. Shibata, T. Kakitsuka, Y. Kadota, and Y. Tohmori, "Polarization-insensitive SOA with a Strained Bulk active layer for Network Device Application", *IEEE Photonics Techn. Letters*, vol. 14, no. 6, pp. 765–767, 2002.

[48] Govind P. Agrawal, *Nonlinear Fiber Optics*, Academic Press, San Diego, 2001.

[49] K. P. Hansen, J. R. Jensen, C. Jakobsen, H. R. Simonsen, J. Broeng, P. M. W. Skovgaard, and A. Petersson, "Highly Nonlinear Photonic Crystal Fiber with Zero-Dispersion at 1.55 micro meters", in *Techn. Digest OFC 2002, Post Deadline Papers*, Anaheim, CA., USA, 2002, pp. FA9–1–3.

[50] W. Belardi, J. H. Lee, K. Furusawa, Z. Yusoff, P. Petropoulos, M. Ibsen, T. M. Monroe, and D. J. Richardson, "A 10 Gb/s Tuneable Wavelength Converter Based on Four-Wave Mixing in Highly Nonlinear Holey Fibre", in *Proc. ECOC 2002, Post Deadline Papers*, Copenhagen, Denmark, 2002, p. PD1.2.

[51] K. S. Berg, L. K. Oxenlöwe, A. Siahlo, A. Tersigni, A. T. Clausen, C. Peucheret, P. Jeppesen, K. P. Hansen, and J. R. Hansen, "80 Gb/s Transmission over 80 km and Demultiplexing Using a Highly Non-Linear Photonic Crystal Fibre", in *Proc. ECOC 2002*, Copenhagen, Denmark, 2002, p. 2.1.5.

[52] W. Wang, H. N. Poulsen, L. Rau, H.-F. Chou, J. E. Bowers, D. J. Blumenthal, and L. Gruner-Nielsen, "Regenerative 80-Gb/s Fiber XPM Wavelength Converter using a hybrid Raman/EDFA Gain-enhanced Configuration", *IEEE Photonics Techn. Letters*, vol. 15, no. 10, pp. 1416–1418, 2003.

[53] J. Yu and P. Jeppesen, "80-Gb/s Wavelength Conversion Based on Cross-Phase Modulation in High-Nonlinearity Dispersion-Shifted Fiber and Optical Filtering", *IEEE Photonics Techn. Letters*, vol. 13, no. 8, pp. 833–835, 2001.

[54] J. Yu and P. Jeppesen, "Wavelength Conversion by use of Four-Wave Mixing in a Novel Optical Loop Configuration", *Optics Lett.*, vol. 25, no. 6, pp. 393–395, 2000.

[55] M. H. Chou, K. R. Parameswaran, M. M. Fejer, and I. Brener, "Multiple Channel Wavelength Conversion Using Engineered Quasi-Phasematching Structures in $LiNbO_3$ waveguides", in *Techn. Digest CLEO 1999*, Baltimore, USA, 1999, p. 219.

[56] J. Yamawaku, H. Takara, T. Ohara, K. Sato, A. Takada, T. Morioka, O. Tadanaga, H. Miyazawa, and M. Asobe, "Simultaneous 25 GHz-Spaced DWDM Wavelength Conversion of 1.03 Tbit/s (103 x 10 Gbit/s) Signals in PPLN Waveguide", *IEE Electronics Lett.*, vol. 39, no. 15, pp. 1144–1145, 2003.

[57] H. Suche, G. Schreiber, Y.L. Lee, V. Quiring, R. Ricken, W. Sohler, A. Paoletti, F. Carbone, D. Caccioli, and A. Schiffini, "Efficient Ti:PPLN Multi-Wavelength Converter for High Bitrate WDM-Transmission Systems", *Proc. ECOC 2001, Post Deadline Papers, vol 6*, pp. 42–3, 2001.

[58] L. Razzari, C. Liberale, I. Cristiani, R. Tediosi, and V. Degiorgio, "Wavelength Conversion and Pulse Reshaping through Cascaded Interactions in an MZI Configuration", *IEEE J. Quantum Electronics*, vol. 39, no. 11, pp. 1486–1491, 2003.

[59] K. R. Parameswaran, R. K. Route, J. R. Kurz, R. V. Roussev, M. M. Fejer, and M. Fujimura, "Highly Efficient SHG in Buried Waveguides Formed Using Annealed and Reverse Proton Exchange in PPLN", in *Proc. IEEE LEOS Annual Meeting 2001*, 2001, p. ThL3.

[60] M. C. Cardakli, A. B. Sahin, O. H. Adamczyk, A. E. Willner, K. R. Parameswaran, and M. M. Fejer, "Wavelength Conversion of Subcarrier Channels Using Difference Frequency Generation in a PPLN Waveguide", *IEEE Photonics Techn. Letters*, vol. 14, no. 9, pp. 1327–1329, 2002.

[61] Fabrizio Carbone, Luciano Socci, Marco Romagnoli, Ilaria Cristiani, and Vittorio Degiorgio, "Polarization-insensitive Wavelength Conversion in a Lithium Niobate Waveguide by the Cascading Technique", *Techn. Digest OFC 2002*, vol. 70, pp. 728–730, 2002.

[62] A. Schiffini, A. Paoletti, D. Caccioli, P. Minzioni, P. Griggio, C. Lorenzetto, S. Cascelli, M. Guglielmucci, F. Matera, G. Tosi-Beleffi, H. Suche, Y. Lee, V. Quiring, and W. Sohler, "Field Demonstration of All optical in-line Wavelength Conversion in a WDM 40 Gbit/s Dispersion Managed link using a Polarization insensitive Ti:PPLN Converter", *Techn. Digest OFC 2003*, pp. 291–293, 2003.

[63] P. Ohlen and E. Berglind, "Noise Accumulation and BER Estimates in Concatenated Nonlinear Optoelectronic Repeaters", *IEEE Photonics Techn. Letters*, vol. 9, no. 7, pp. 1011 –1013, 1997.

[64] S. Oka, S. Kobayashi, T. Yakihari, H. Matsuura, and A. Miura, "Development of HBT-based Ultra-High speed Electron Devices (White Paper)", March 2004, `http://www.Yokogawa.com/rd/pdf/TR/rd-Tr-R00034-002.pdf`.

[65] S. L. Danielsen, C. Joergensen, M. Vaa, B. Mikkelsen, K. E. Stubkjaer, P. Doussiere, F. Pommerau, I. Goldstein, R. Ngo, and M. Goix, "Bit Error Rate Assessment of 40 Gbit/s All-Optical Polarisation Independent Wavelength Converter", *IEE Electronics Lett.*, vol. 32, no. 18, pp. 1688–1689, 1996.

[66] B. Dagens, C. Janz, D. Leclerc, V. Verdrager, F. Poingt, I. Guillemot, F. Gaborit, and D. Ottenwälder, "Design Optimization of All-Active Mach-Zehnder Wavelength Converters", *IEEE Photonics Techn. Letters*, vol. 11, pp. 424–426, 1999.

[67] B. Mikkelsen, M. Vaa, H. N. Poulsen, S. L. Danielsen, C. Joergensen, A. Kloch, P. B. Hansen, K. E. Stubkjaer, K. Wünstel, L. Daub, E. Lach, G. Laube, W. Idler, M. Schilling, and S. Bouchoule, "40 Gbit/s All-Optical Wavelength Converter and RZ-to-NRZ Format Adapter Realised by Monolithic Integrated Active Michelson Interferometer", *IEE Electronics Lett.*, vol. 33, no. 2, pp. 133–134, 1997.

[68] Y. Shibata, N. Kikuchi, S. Oku, I. Ito, H. Okamoto, Y. Kawaguchi, Y. Kondo, Y. Suzuki, and Y. Tohmori, "Filter-free All-optical Wavelength Conversion using Sagnac Interferometer integrated with Parallel-Amplifier Structure (SIPAS)", *IEE Electronics Lett.*, vol. 38, no. 21, pp. 1273–1275, 2002.

[69] N. S. Patel, K. A. Rauschenbach, and K. L. Hall, "40-Gb/s Demultiplexing Using an Ultrafast Nonlinear Interferometer (UNI)", *IEEE Photonics Techn. Letters*, vol. 8, no. 12, pp. 1695–1697, 1996.

[70] K. Tajima, S. Nakamura, and Y. Ueno, "Ultrafast All-Optical Signal Processing with Symmetric Mach-Zehnder Type All-Optical Switches", *Optical and Quantum Electronics*, vol. 33, pp. 875–897, 2001.

[71] J. P. Sokoloff, P. R. Prucnal, I. Glesk, and M. Kane, "A Terahertz Optical Asymmetric Demultiplexer (TOAD)", *IEEE Photonics Techn. Letters*, vol. 5, no. 7, pp. 787–790, 1993.

[72] M. Eiselt, "Optical Loop Mirror with Semiconductor Laser Amplifier", *IEE Electronics Letters*, vol. 28, no. 16, pp. 1505 –1507, 1992.

[73] Y. Ueno, S. Nakamura, K. Tajima, and S. Kitamura, "3.8 THz Wavelength Conversion of Picosecond Pulses Using a Semiconductor Delayed-Interference Signal-Wavelength Converter (DISC)", *IEEE Photonics Techn. Letters*, vol. 10, no. 3, pp. 346–348, 1998.

[74] Y. Ueno, S. Nakamura, H. Hatakeyama, T. Tamanuki, T. Sasaki, and K. Tajima, "168 Gb/s OTDM Wavelength Conversion Using an SMZ-Type All-Optical Switch", in *Proc. ECOC 2000, Paper 1.1.1.*, Munich, Germany, 2000.

[75] J. Leuthold, B. Mikkelsen, G. Raybon, C. H. Joyner, J. L. Pleumeekers, B. I. Miller, K. Dreyer, and R. Behringer, "All-Optical Wavelength Conversion Between 10 and 100 Gb/s with SOA Delayed-Interference Configuration", *Optical and Quantum Electronics*, vol. 33, pp. 939–952, 2001.

[76] A. D. Ellis, A. E. Kelly, D. Nesset, D. Pitcher, D. G. Moodie, and R. Kashyap, "Error Free 100Gbit/s Wavelength Conversion using Grating Assisted Cross-gain Modulation in 2 mm long Semiconductor Optical Amplifiers", *IEE Electronics Lett.*, vol. 34, no. 20, pp. 1958–1959, 1998.

[77] S. Watanabe, S. Takeda, and T. Chikama, "Interband wavelength conversion of 320 Gb/s (32x10 Gb/s) wdm signal using a polarization-insensitive fiber four-wave mixer", in *Proc. ECOC 1998, Post Deadline Papers*, 2000.

[78] J. Inoue, H. Sotobayashi, W. Chujo, and H. Kawaguchi, "Picosecond 80-Gbit/s OTDM Signal Transmission over 208-km Standard fiber using Midspan Optical Phase Conjugation", *Techn. Digest CLEO 2002, vol. 1*, p. 496, 2002.

[79] A. E. Kelly, A. D. Ellis, D. Nesset, R. Kashyap, and D. G. Moodie, "100Gbit/s Wavelength Conversion using FWM in a MQW Semiconductor

Optical Amplifier", *IEE Electronics Lett.*, vol. 34, no. 20, pp. 1955–1956, July 1998.

[80] A. E. Kelly, D. D. Marcenac, and D. Nesset, "40 Gbit/s Wavelength Conversion over 24.6nm using FWM in a Semiconductor Optical Amplifier with an Optimised MQW Active Region", *IEE Electronics Lett.*, vol. 33, no. 25, pp. 2123–2124, 1997.

[81] T. J. Morgan, R. S. Tucker, and J. P. R. Lacey, "All-Optical Wavelength Translation over 80 nm at 2.5 Gb/s Using Four-Wave Mixing in a Semiconductor Optical Amplifier", *IEEE Photonics Techn. Letters*, vol. 11, no. 8, pp. 982–984, 1999.

[82] R.B. Lee, D.F. Geraghty, M. Verdiell, M. Ziari, A. Mathur, and K.J. Vahala, "Cascaded Wavelength Conversion by Four-wave Mixing in a Strained Semiconductor Optical Amplifier at 10 Gb/s", *IEEE Photonics Techn. Letters*, vol. 9, no. 6, pp. 752 –754, 1997.

[83] L. Xu, L. K. Oxenlowe, N. Chi, J. Mork, P. Jeppesen, K. Hoppe, and J. Hanberg, "Experimental Characterisation of Wavelength Conversion at 40 Gb/s based on Electroabsorption Modulators", *LEOS Annual Meeting 2002*, vol. 1, pp. 111–112 vol.1, 2002.

[84] K. Nishimura and M. Usami, "All optical Wavelength Conversion using Electro-absorption Modulators", *LEOS Annual metting 2003*, vol. 1, pp. 431–432, 2003.

[85] C. Schubert, R. Ludwig, S. Watanabe, E. Futami, C. Schmidt, J. Berger, C. Boerner, S. Ferber, and H. G. Weber, "160 Gbit/s Wavelength Converter with 3R-Regenerating Capability", *IEE Electronics Lett.*, vol. 38, no. 16, pp. 903–904, 2002.

[86] J. Yu, P. Jeppesen, and N. S. Knudsen, "80 Gbit/s Pulsewidth-maintained Wavelength Conversion based on HNL DSF-NOLM including Transmission over 80 km of conventional SMF", *IEE Electronics Lett.*, vol. 37, no. 9, pp. 577 –579, 2001.

[87] I. Brener, B. Mikkelsen, G. Raybon, R. Harel, K. Parameswaran, J. Kurz, and M. M. Fejer, "Parametric Wavelength Conversion and Phase Conjugation in $LiNbO_3$ Waveguides", *LEOS Annual meeting 2000*, vol. 2, pp. 766–767 vol.2, 2000.

[88] O. Leclerc, B. Lavigne, E. Balmefrezol, P. Brindel, L. Pierre, D. Rouvillain, and F. Seguineau, "All-optical Signal Regeneration: From First Principles to a 40 Gbit/s System Demonstration", *Comptes Rendus Physique*, vol. 4, no. 1, pp. 163–173, 2003.

[89] B. Lavigne, D. Chiaroni, L. Hamon, C. Janz, and A. Jourdan, "Experimental Analysis of SOA-based 2R and 3R Optical Regeneration for Future WDM Networks", in *Techn. Digest OFC 1998*, 1998, pp. 324 –325.

[90] I. White, R. Penty, M. Webster, Y. J. Chai, A. Wonfor, and S. Shahkooh, "Wavelength Switching Components for future Photonic Networks", *IEEE Communications Magazine*, vol. 40, no. 9, pp. 74–81, 2002.

[91] A. Dupas, L. Billes, J. C. Simon, B. Landousies, M. Henry, I. Valiente, F. Ratovelomanana, A. Enard, and N. Vodjdani, "2R All-optical Regenerator assessment at 2.5 Gbit/s over 3600 km Using Only Standard Fibre", *IEE Electronics Lett.*, vol. 34, no. 25, pp. 2424 –2425, 1998.

[92] A. Kloch and K. E. Stubkjær, "Accumulation of Jitter in Cascaded Wavelength Converters based on Semiconductor Optical Amplifiers", in *Techn. Digest OFC 1999, Paper FB4*, 1999, pp. 33–35.

[93] Y. Ueno, S. Nakamura, and K. Tajima, "Penalty-Free Error-Free All-Optical Data Pulse Regeneration at 84 Gbps with Symmetric-Mach-Zehnder-Type Regenerator", in *Techn. Digest OFC 2001, Paper MG5-1*, Anaheim, CA., USA, 2001.

[94] H. J. Thiele, A. D. Ellis, and I. D. Phillips, "Recirculating loop Demonstration of 40 gbit/s All-optical 3R Data Regeneration using a Semiconductor Nonlinear Interferometer", *IEE Electronics Lett.*, vol. 35, no. 3, pp. 230 –231, 1999.

[95] J. Leuthold, B. Mikkelsen, R. E. Behringer, G. Raybon, C. H. Joyner, and P. A. Besse, "Novel 3R Regenerator Based on Semiconductor Optical Amplifier Delayed-Interference Configuration", *IEEE Photonics Techn. Letters*, vol. 13, no. 8, pp. 860–862, 2001.

[96] J. Leuthold, G. Raybon, Y. Su, R. Essiambre, S. Cabot, J. Jaques, and M. Kauer, "40 Gbit/s Transmission and Cascaded All-optical Wavelength Conversion over 1000000 km", *IEE Electronics Lett.*, vol. 38, no. 16, pp. 890–892, 2002.

[97] T. Otani, T. Miyzaki, and S. Yamamoto, "40 Gbit/s Signal Transmission using Optical 3R Regenerator based on Electroabsorption Modulators", *Techn. Digest OFC 2000*, vol. 3, pp. 226 –228 vol.3, 2000.

[98] S. Boscolo, S. K. Turitsyn, and K. J. Blow, "All-optical Passive 2R Regeneration for N x 40 Gbit/s WDM Transmission using NOLM and Novel Filtering Technique", *Optics Communications*, vol. 217, no. 1, pp. 227–232, 2003.

[99] N. Chi, L. Xu, L. Oxenloewe, T. Tokle, and P. Jeppesen, "2R Regenerator based on High Non-linear Dispersion-imbalanced Loop Mirror", *Optics Communications*, vol. 206, no. 4-6, pp. 295–300, 2002.

[100] P. V. Mamyshev, "All-Optical Data Regeneration based on Self-phase Modulation effect", in *Proc. ECOC 1998*, 1998, vol. 1, pp. 475 –476.

[101] S. Watanabe, F. Futami, R. Okabe, Y. Takita, S. Ferber, R. Ludwig, C. Schubert, C. Schmidt, and H. G. Weber, "160 Gbit/s Optical 3R-Regenerator in a Fiber Transmission Experiment", in *Techn. Digest OFC 2003*, 2003, pp. PD16–1.

[102] A. Mecozzi and J. Mørk, "Saturation Induced by Picosecond Pulses in Semiconductor Optical Amplifiers", *J. Opt. Soc. Am. B*, vol. 14, no. 4, pp. 761–770, 1997.

[103] G. P. Agrawal and N. A. Olsson, "Self-Phase Modulation and Spectral Broadening of Optical Pulses in Semiconductor Laser Amplifiers", *IEEE J. Quantum Electronics*, vol. 25, no. 11, pp. 2297–2306, 1989.

[104] G. P. Agrawal and N. K. Dutta, *Long-Wavelength Semiconductor Lasers*, Van Nostrand Reinhold Company, New York, 1986.

[105] B. Fernier, "1.5 micro meter Laser with High Quantum Efficiency and Controlled Emission Wavelength", in *IEE Proceedings*, 1987, vol. 134, pp. 27–34.

[106] C. J. Viedecrantz, *Optical Amplification and Processing in High-Capacity Photonic Networks*, PhD thesis, Technical University of Denmark, 1997.

[107] D. Marcenac and A. Mecozzi, "Switches and Frequency Converters Based on Cross-Gain Modulation in Semiconductor Optical Amplifiers", *IEEE Photonics Techn. Letters*, vol. 9, no. 6, pp. 749–751, 1997.

[108] A. W. Snyder and J. D. Love, *Optical Waveguide Theory*, Chapman and Hall, London, 1983.

[109] R. Scarmozzino, A. Gopinath, R. Pregla, and S. Helfert, "Numerical Techniques for Modeling Guided-Wave Photonic Devices", *IEEE J. Sel. Top. Quantum Electronics*, vol. 6, no. 1, pp. 150–162, January 2000.

[110] R. Scarmozzino and R. M. Osgood Jr., "Comparison of Finite-Difference and Fourier-Transform Solutions of the Parabolic Wave Equation with Emphasis on Integrated Optics Applications", *J. Opt. Soc. Am. A*, vol. 8, no. 5, pp. 724–731, 1991.

[111] B. H. Bransden and C. J. Joachain, *Introduction to Quantum Mechanics*, Longman, Essex, 1989.

[112] J. Hedegaard Poulsen, "Personal communication", 2000.

[113] K. Kawano and T. Kitoh, *Introduction to Optical Waveguide Analysis*, Wiley, New York, 2001.

[114] T. Rasmussen, J. H. Poulsen, and Anders Bjarklev, "Accurate Finite Difference Beam Propagation Method for Complex Integrated Optical Structures", *IEEE Photonics Techn. Letters*, vol. 5, pp. 339–342, 1993.

[115] D. A. Neamen, *Semiconductor Physics and Devices: Basic Principles*, Irwin, Chicago, 1997.

[116] A. Uskov, J. Mørk, and J. Mark, "Wave Mixing in Semiconductor Laser Amplifiers Due to Carrier Heating and Spectral hole-burning", *IEEE J. Quantum Electronics*, vol. 30, no. 8, pp. 1769–1781, August 1994.

[117] N. Peyghambarian, S. Koch, and A. Mysyrowicz, *Introduction to Semiconductor Optics*, Prentice-Hall, Inc., New Jersey, 1993.

[118] A. Mecozzi, "Small-Signal Theory of Wavelength Converters Based on Cross-Gain Modulation in Semiconductor Optical Amplifiers", *IEEE Photonics Techn. Letters*, vol. 8, pp. 1471–1473, 1996.

[119] D. Marcenac, "Travelling Wave Effects for Wavelength Conversion by Cross-Gain Modulation and Cross-Phase Modulation in Optical Amplifiers", *Intern. J. Optoelectronics*, vol. 10, no. 5, pp. 325–329, 1995.

[120] K. I. Kang, T. G. Chang, I. Glesk, and P. R. Prucnal, "Comparison of Sagnac and Mach-Zehnder Ultrafast All-Optical Interferometric Switches Based on a Semiconductor Resonant Optical Nonlinearity", *Applied Optics*, vol. 35, no. 3, pp. 417–426, 1996.

[121] J. Mørk, "Personal communication", 2003.

[122] J. Pleumeekers, M. Kauer, K. Dreyer, C. Burrus, A. G. Dentai, S. Shunk, J. Leuthold, and C. H. Joyner, "Acceleration of Gain Recovery in Semiconductor Optical Amplifiers by Optical Injection Near Transparency Wavelength", *IEEE Photonics Techn. Letters*, vol. 14, no. 1, pp. 12–14, 2002.

[123] Svend Bischoff and Jesper Mørk, "Reduction of Pattern Effects in SOA-Based All Optical Switches by Using Cross-Gain Modulated Holding Signal", in *Techn. Digest CLEO 2002, Paper CWA53*, Long Beach, CA., USA, 2002.

[124] K. Obermann, D. Breuer, and K. Petermann, "Theoretical Estimation of the Cascadability of Wavelength Converters Based on Cross-Gain Modulation in Semiconductor Optical Amplifiers", in *Techn. Digest CLEO 1998*, 1998, pp. 388–389.

[125] C. C. Wang, M. A. Summerfield, and R. S. Tucker, "Performance of Cascaded Wavelength Converters", in *Techn. Digest LEOS 2000*, 2000, pp. 631–632.

[126] D. D. Marcenac, A. E. Kelly, and D. Nesset, "Nonlinear Optical Amplifiers for Ultra-High Speed All-Optical Wavelength Conversion and Switching", in *OSA TOPS on OAA*, vol. 5. OAA Program Committee, 1996.

[127] Y. Ueno, S. Nakamura, and K. Tajima, "Nonlinear Phase Shifts Induced by Semiconductor Optical Amplifiers with Control Pulses at Repetition Frequencies in the 40-160 GHz Range for Use in Ultrahigh-Speed All-Optical Signal Processing", *J. Opt. Soc. Am. B*, vol. 19, no. 11, pp. 2573–2589, 2002.

[128] K. Tajima, "All-Optical Switch with Switch-Off Time Unrestricted by Carrier Lifetime", *Jpn. J. Appl. Phys.*, vol. 32, no. 12A, pp. L1746–L1749, Part 2, 1993.

[129] S. Nakamura, Y. Ueno, and K. Tajima, "Error-Free Demultiplexing at 336 Gb/s with a Hybrid-Integrated Symmetric-Mach-Zehnder Switch", in *Techn. Digest OFC 2002, Post Deadline, FD3-1*, Anaheim, CA., USA, 2002.

[130] R. J. Manning, A. Antonopoulos, R. Le Roux, and A. E. Kelly, "Experimental Measurement of Nonlinear Polarisation Rotation in Semiconductor Optical Amplifiers", *IEE Electronics Lett.*, vol. 37, no. 4, pp. 229 –231, 2001.

[131] H. J. S. Dorren, D. Lenstra, Yong Liu, M. T. Hill, and G.-D. Khoe, "Nonlinear Polarization Rotation in Semiconductor Optical Amplifiers: Theory and Application to All-optical Flip-Flop Memories", *IEEE J. Quantum Electronics*, vol. 39, no. 1, pp. 141–148, 2003.

[132] S. Nakamura and K. Tajima, "Bit-Rate-Transparent Non-Return-to-Zero All-Optical Wavelength Conversion at up to 42 Gb/s by Operating Symmetric-Mach-Zehnder Switch with a New Scheme", in *Techn. Digest OFC 2004*, Los Angeles, CA., USA, 2004, p. FD3.

[133] F. Ginovart, J. C. Simon, and I. Valiente, "Gain Recovery Dynamics in Semiconductor Optical Amplifiers", *Optics Communications*, vol. 199, pp. 111–115, 2001.

[134] J. Mørk and A. Mecozzi, "Theory of the Ultrafast Optical Response of Active Semiconductor Waveguides", *J. Opt. Soc. Am. B*, vol. 13, no. 8, pp. 1803–1816, 1996.

[135] P. S. Cho, D. Mahgerefteh, J. Goldhar, and G. L. Burdge, "Wavelength Conversion Using a Noninterferometric Semiconductor-Optical-Amplifier/Fiber-Bragg-Grating Device", in *Techn. Digest of CLEO 1998, Paper CThZ4*, San Francisco, CA., USA, 1998.

[136] J. Leuthold, R. Ryf, D. N. Maywar, S. Cabot, J. Jaques, and S. S. Patel, "Nonblocking All-optical Cross Connect based on Regenerative All-optical Wavelength Converter in a Transparent Demonstration over 42 nodes and 16800 km", *IEEE J. Lightwave Technology*, vol. 21, no. 11, pp. 2863–2870, 2003.

[137] Y. Ueno, S. Nakamura, and K. Tajima, "Spectral Phase-Locking in Ultrafast All-Optical Mach-Zehnder-Type Semiconductor Wavelength Converter", *Jpn. J. Appl. Phys.*, vol. 38, no. 11A, pp. 1243–1245, 1999.

[138] H.-Y. Yu, D. Mahgerefteh, P. S. Cho, and J. Goldhar, "Optimization of the Frequency Response of a Semiconductor Optical Amplifier Wavelength Converter Using a Fiber Bragg Grating", *IEEE J. Lightwave Technology*, vol. 17, no. 2, pp. 308–315, 1999.

[139] B. E. Olsson, P. Ohlen, L. Rau, and D. J. Blumenthal, "A Simple and Robust 40 Gb/s Wavelength Converter using Fiber Cross-Phase Modulation and Optical Filtering", *IEEE Photonics Techn. Letters*, vol. 12, no. 7, pp. 846–848, July 2000.

[140] T. Tekin and M. Schlak, "Design of Monolithically Integrated GS-MZI for Ultrafast All-Optical Switching", *submitted to OFC 2002*, 2002, found at www.hhi.frauenhofer.de.

[141] T. Tekin, M. Schlak, W. Brinker, B. Maul, and R. Molt, "Monolithically Integrated MZI comprising band gap shifted SOAs: A new Switching scheme for Generic All-optical Signal Processing", *Proc. ECOC 2000*, pp. 123–4 vol.3, 2000.

[142] T. Tekin, M. Schlak, W. Brinker, J. Berger, C. Schubert, B. Maul, and R. Molt, "Ultrafast All-optical Demultiplexing performance of Monolithically integrated band gap shifted Mach-Zehnder Interferometer", *Proc. ECOC 2001*, vol. 4, pp. 504–505 vol.4, 2001.

[143] T. Tekin, "Personal communication", 2004.

[144] T. Fjelde, A. Kloch, D. Wolfson, B. Dagens, R. Brenot, A. Labrousse, E. Roux, F. Gaborit, F. Poingt, and M. Renaud, "Simultaneous 2x10 to 20 Gbit/s Time-Division Multiplexing and Wavelength Conversion Using an Integrated SOA-Based Mach-Zehnder Interferometer", in *Proc. OECC/IOOC 2001, Paper TueL.4*, Sydney, Australia, 2001.

[145] A. Kloch, P. B. Hansen, D. Wolfson, S. L. Danielsen, K. E. Stubkjaser, J. Y. Emery, F. Pommerau, M. Renaud, and M. Schilling, "Assessment of Dual-Stage Wavelength Converter in OXC at 20 Gb/s", in *Proc. ECOC 1998*, Madrid, Spain, 1998, pp. 659–660.

[146] J. Leuthold, J. Eckner, P. A. Besse, G. Guekos, and H. Melchior, "Dual-Order Mode (DOMO) All-Optical Space Switch for Birectional Operation", in *Techn. Digest OFC 1996*, San Jose, CA., USA, 1996, pp. 271–272.

[147] C. Janz, F. Poingt, F. Pommereau, F. Gaborit, D. Ottenwider, I. Guillemot, B. Dagens, and M. Renaud, "All-active Dual-Order Mode Mach-Zehnder Wavelength Converter for Power-efficient, Co-propagative operation", *Proc. ECOC 1998*, pp. 661–2 vol.1, 1998.

[148] C. Janz, F. Poingt, F. Pommereau, W. Grieshaber, F. Gaborit, D. Leclerc, I. Guillemot, and M. Renaud, "New All-active Dual-Order Mode (DOMO) Mach-Zehnder Wavelength Converter for 10 Gbit/s operation", *Proc. ECOC 1999*, pp. 172–3 vol.2, 1999.

[149] D. Wolfson, T. Fjelde, A. Kloch, C. Janz, F. Poingt, F. Pommereau, I. Guillemot, F. Gaborit, and M. Renaud, "Detailed Experimental Investigation of All-active Dual-Order Mode Mach-Zehnder Wavelength Converter", *IEE Electronics Lett.*, vol. 36, no. 15, pp. 1296 –1297, 2000.

[150] M. L. Nielsen, "Semiconductor Optical Switches Employing Transverse Modes", Master's thesis, Research Center COM, Technical University of Denmark, 2000.

[151] A. Kloch, *Circuit Switched Optical Networks (LD8)*, PhD thesis, COM, Technical University of Denmark, 1999.

[152] L. B. Soldano and E. C. M. Pennings, "Optical Multi-Mode Interference Devices Based on Self-Imaging: Principles and Applications", *IEEE J. Lightwave Technology*, vol. 13, no. 4, pp. 615–627, April 1995.

[153] R. Ulrich and G. Angele, "Self-imaging in Homogeneous Planar Optical Waveguides", *Appl. Physics Lett.*, vol. 27, pp. 337–339, 1975.

[154] J. Leuthold, J. Eckner, E. Gamper, P. A. Besse, and H. Melchior, "Multimode Interference Couplers for the Conversion and Combining of Zero- and First-Order Modes", *IEEE J. Lightwave Technology*, vol. 16, no. 7, pp. 1228–1239, July 1998.

[155] Velocium 43 GHz Broadband Amplifier AUH232, "`Http://Www.Velocium.com/clientImages/22211/Wireless_Datasheets/auh232rev12.03.pdf`", 2004.

[156] J. Mørk, Filip Öhman, and Svend Bischoff, "Analytical Expression for the Bit-Error-Rate of Cascaded All-optical Regenerators", *IEEE Photonics Techn. Letters*, vol. 15, 2003.

[157] G. P. Agrawal, *Fiber-Optic Communication Systems*, vol. I, Wiley, New York, 1997.

[158] N. A. Olsson, "Lightwave Systems with Optical Amplifiers", *IEEE J. Lightwave Technology*, vol. 7, no. 7, pp. 1071 –1082, 1989.

[159] O. Leclerc, "Optical Regeneration and WDM Dispersion-Managed Transmission Systems", *Proc. ECOC 2001*, vol. 5, pp. 46–79, 2001.

[160] D. Wolfson, P. B. Hansen, A. Kloch, T. Fjelde, C. Janz, A. Coquelin, I. Guillemot, F. Garorit, F. Poingt, and M. Renaud, "All-optical 2R Regeneration at 40 Gbit/s in an SOA-based Mach-Zehnder Interferometer", *Techn. Digest OFC/IOOC 1999, Post Deadline Papers*, p. PD36/1, 1999.

[161] J. De Merlier, G. Morthier, T. Van Caenegem, R. Baets, I. Moerman, and P. Van Daele, "Experimental Demonstration of 15 dB Extinction Ratio Improvement in a new 2R Optical Regenerator based on an MMI-SOA", *Proc. ECOC 2001*, vol. 4, pp. 574 –575 vol.4, 2001.

[162] J. De Merlier, Van D. Thourhout, G. Morthier, and R. Baets, "Amplified Spontaneous Emission in index-guided Multimodal Waveguide Structures", *IEEE J. Quantum Electronics*, vol. 39, no. 9, pp. 1099–1105, 2003.

[163] J. De Merlier, G. Morthier, and R. Baets, "The Influence of Lateral Carrier Diffusion and Surface Recombination on the Behavior of Semiconductor Optical Amplifier (SOA)-based MMIs", *IEEE J. Quantum Electronics*, vol. 39, no. 7, pp. 880–885, 2003.

[164] J. De Merlier, *Optical Signal Regenerators Based on Integrated Amplifying Interferometers*, PhD thesis, University of Gent, Belgium, 2003.

[165] S. Bischoff, B. Lading, and J. Mork, "BER Estimation for All-optical Regenerators influenced by Pattern Effects", *IEEE Photonics Techn. Letters*, vol. 14, no. 1, pp. 33–35, 2002.

[166] L. Schares, C. Schubert, C. Schmidt, H. G. Weber, L. Occhi, and G. Guekos, "Phase Dynamics of Semiconductor Optical Amplifiers at 10-40 GHz", *IEEE J. Quantum Electronics*, vol. 39, no. 11, pp. 1394–1408, 2003.

[167] L. K. Oxenlowe, C. Schubert, C. Schmidt, E. Hilliger, J. Berger, U. Feiste, R. Ludwig, and H. G. Weber, "Optical Clock Recovery employing an optical PLL using Cross-Phase Modulation in a Sagnac-interferometer", *Techn. Digest CLEO 2001*, pp. 525 –526, 2001.

[168] O. Brox, S. Bauer, C. Bobbert, G. Bramann, J. Kreiss, and B. Sartorius, "160 to 40 Gb/s Demultiplexing using a Self Pulsating Laser based Clock Recovery", *Techn. Digest OFC 2003*, pp. 105–106, 2003.

[169] C.-H. Lee and H. K. Lee, "Passive All-optical Clock Signal Extractor for Non-Return-to-Zero Signals", *IEE Electronics Lett.*, vol. 34, no. 3, pp. 295–297, 1998.

[170] H. K. Lee, J. T. Ahn, M. Y. Jeon, K. H. Kim, D. S. Lim, and C.-H. Lee, "All-Optical Clock Recovery from NRZ Data of 10 Gb/s", *IEEE Photonics Techn. Letters*, vol. 11, no. 6, pp. 730–732, 1999.

[171] W. Mao, M. Al-Mumin, X. Wang, and G. Li, "All-Optical Enhancement of Clock and Clock-to-Data Suppression Ratio of NRZ Data", *IEEE Photonics Techn. Letters*, vol. 13, no. 3, pp. 239–241, 2001.

[172] A. Bilenca, D. Dahan, J. Lashri, G. Eisenstein, and D. Ritter, "High Bit Rate Clock Recovery of NRZ Data by All-Optical Processing in a Semiconductor Optical Amplifier and Direct Optical Injection Locking of a Self-Oscillating Phototransistor", *IEEE Photonics Techn. Letters*, vol. 14, no. 3, pp. 399–401, 2002.

[173] H. J. Lee, H. G. Kim, J. Y. Choi, and H. K. Lee, "All-Optical Clock Recovery from NRZ Data with Simple NRZ-to-PRZ Converter Based on Self-Phase Modulation of Semiconductior Optical Amplifier", *IEE Electronics Lett.*, vol. 35, no. 12, pp. 989–990, 1999.

[174] R. J. Manning and G. Sherlock, "Recovery of a pi Phase Shift in Approximately 12.5 ps in a Semiconductor Laser Amplifier", *IEE Electronics Lett.*, vol. 31, no. 4, pp. 307 –308, 1995.

[175] H. A. Haus and N. A. Whitaker, "All-Optical Logic in Optical Waveguides", *Philosophical Transactions of the Royal Society of London. Series A, Mathematical and Physical Sciences*, vol. 313, no. 1525, pp. 121–129, 1984.

[176] K. L. Hall and K. A. Rauschenbach, "100-Gbit/s Bitwise Logic", *Optics Letters*, vol. 23, no. 16, pp. 1271–1273, 1998.

[177] A. Sharaiha, H. W. Li, F. Marchese, and J. Le Bihan, "All-Optical Logic NOR Gate Using a Semiconductor Laser Amplifier", *IEE Electronics Lett.*, vol. 33, no. 4, pp. 323–325, 1997.

[178] A. Hamie, A. Sharaiha, M. Guegan, and B. Pucel, "All-Optical Logic NOR Gate Using Two-Cascaded Semiconductor Optical Amplifiers", *IEEE Photonics Techn. Letters*, vol. 14, no. 10, pp. 1439–1441, 2002.

[179] N. S. Patel, K. L. Hall, and K. A. Rauschenbach, "40-Gbit/s Cascadable All-Optical Logic with an Ultrafast Nonlinear Interferometer", *Optics Letters*, vol. 21, no. 18, pp. 1466–1468, 1996.

[180] T. Fjelde, D. Wolfson, A. Kloch, C. Janz, A. Coquelin, I. Guillemot, F. Poingt, B. Dagens, and M. Renaud, "10 Gbit/s All-Optical Logic OR in Monolithically Integrated Interferometric Wavelength Converter", *IEE Electronics Lett.*, vol. 36, no. 9, pp. 813–815, 2000.

[181] T. Fjelde, *Traffic Analysis and Signal Processing in Optical Packet Switched Networks*, PhD thesis, Research Center COM, Technical University of Denmark, 2001.

[182] B. K. Kang, J. H. Kim, Y. H. Park, S. Lee, Y. M. Jhon, D. H. Woo, S. H. Kim, and S. H. Park, "All-optical Logic AND in a SOA-based Mach-Zehnder All-optical Wavelength Converter", *LEOS Annual Meeting 2000*, vol. 1, pp. 117–118 vol.1, 2000.

[183] E. S. Awad, P. S. Cho, and J. Goldhar, "An all-optical AND gate using nonlinear transmission of electro-absorption modulator", in *Techn. Digest CLEO 2001*, 2001, p. CMS6.

[184] E. S. Awad, P. S. Cho, N. Moulton, and J. Goldhar, "3R Optical Regeneration with Simultaneous Optical Clock Recovery and All-optical Wavelength Conversion using a Single Electro-absorption Modulator", *Techn. Digest CLEO 2002*, pp. 611 –612, 2002.

[185] D. Nesset, M. C. Tatham, and D. Cotter, "All-Optical AND Gate Operating on 10 Gbit/s Signals at the Same Wavelength Using Four-Wave Mixing in a Semiconductor Laser Amplifier", *IEE Electronics Lett.*, vol. 31, no. 11, pp. 896–897, 1995.

[186] T. Fjelde, D. Wolfson, A. Kloch, B. Dagens, A. Coquelin, I. Guillemot, F. Gaborit, F. Poingt, and M. Renaud, "Demonstration of 20 Gbit/s All-optical logic XOR in Integrated SOA-based Interferometric Wavelength Converter", *IEE Electronics Lett.*, vol. 36, no. 22, pp. 1863 –1864, 2000.

[187] Peter Alfke, "Efficient Shift Registers, LFSR Counters, and Long Pseudo Random Sequence Generators", Tech. Rep. XAPP 052, Xilinx, 1996.

[188] B. S. Robinson, S. A. Hamilton, S. J. Savage, and E. P. Ippen, "40 Gbit/s All-optical XOR using a Fiber-based Folded Ultrafast Nonlinear Interferometer", *Techn. Digest OFC 2002*, pp. 561–563, 2002.

[189] J. H. Kim, Y. M. Jhon, Y. T. Byun, S. Lee, D. H. Woo, and S. H. Kim, "All-optical XOR gate using Semiconductor Optical Amplifiers without Additional Input Beam", *IEEE Photonics Techn. Letters*, vol. 14, no. 10, pp. 1436 –1438, 2002.

[190] C. Bintjas, M. Kalyvas, G. Theophilopoulos, T. Stathopoulos, H. Avramopoulos, L. Occhi, L. Schares, G. Guekos, S. Hansmann, and R. Dall'Ara, "20 Gb/s All-optical XOR with UNI gate", *IEEE Photonics Techn. Letters*, vol. 12, no. 7, pp. 834 –836, 2000.

[191] G. Theophilopoulos, K. Yiannopoulos, M. Kalyvas, C. Bintjas, G. Kalogerakis, H. Avramopoulos, L. Occhi, L. Schares, G. Guekos S., Hansmann, and R. Dall'Ara, "40 GHz All-optical XOR with UNI gate", *Techn. Digest OFC 2001*, vol. 1, pp. MB2/1, 2001.

[192] A. J. Poustie and R. J. Manning, "All-optical Pseudorandom Number Generator", *Optics Communications*, vol. 159, no. 4-6, pp. 208–214, 1999.

[193] T. Houbavlis, K. Zoiros, A. Hatziefremidis, H. Avramopoulos, L. Occhi, G. Guekos, S. Hansmann, H. Burkhard, and R. Dall'Ara, "10 Gbit/s All-optical Boolean XOR with SOA Fibre Sagnac gate", *IEE Electronics Lett.*, vol. 35, no. 19, pp. 1650 –1652, 1999.

[194] H. Chen, G. Zhu, Q. Wang, J. Jaques, J. Leuthold, A. B. Piccirilli, and N. K. Dutta, "All-optical Logic XOR Functionality in an Integrated SOA-MZI", *Proc. SPIE 2002*, vol. 4870, pp. 137–143, 2002.

[195] H. Chen, G. Zhu, Q. Wang, J. Jaques, J. Leuthold, A. B. Piccirilli, and N. K. Dutta, "All-optical logic XOR using Differential Scheme and Mach-Zehnder Interferometer", *IEE Electronics Lett.*, vol. 38, no. 21, pp. 1271–1273, 2002.

[196] R. P. Webb, R. J. Manning, G. D. Maxwell, and A. J. Poustie, "40 Gbit/s All-optical XOR gate based on Hybrid-integrated Mach-Zehnder Interferometer", *IEE Electronics Lett.*, vol. 39, no. 1, pp. 79–81, 2003.

[197] K. Chan, C.-K. Chan, L. K. Chen, and F. Tong, "Demonstration of 20-Gb/s All-Optical XOR Gate by Four-Wave Mixing in Semiconductor Optical Amplifier with RZ- DPSK Modulated Inputs", *IEEE Photonics Techn. Letters*, vol. 16, no. 3, pp. 897–899, 2004.

[198] A. J. Poustie and R. J. Manning, "Storage Threshold and Amplitude Restoration in an All-optical Regenerative Memory", *Optics Communications*, vol. 146, no. 1-6, pp. 262–267, 1998.

[199] R. J. Manning, I. D. Phillips, A. D. Ellis, A. E. Kelly, A. J. Poustie, and K. J. Blow, "10 Gbit/s All-optical Regenerative Memory using Single SOA-based Logic Gate", *IEE Electronics Lett.*, vol. 35, no. 2, pp. 158 –159, 1999.

[200] K. L. Hall and K. A. Rauschenbach, "All-optical Buffering of 40-Gb/s Data Packets", *IEEE Photonics Techn. Letters*, vol. 10, no. 3, pp. 442 –444, 1998.

[201] A. J. Poustie, K. J. Blow, A. E. Kelly, and R. J. Manning, "All-optical Binary Half-adder", *Optics Communications*, vol. 156, no. 1, pp. 22–26, 1998.

[202] J. Hun Kim, Y. Tae Byun, Y. Min Jhon, S. Lee, D. Ha Woo, and S. Ho Kim, "All-optical Half Adder using Semiconductor Optical Amplifier based Devices", *Optics Communications*, vol. 218, no. 4-6, pp. 345–349, 2003.

[203] A. J. Poustie and A. E. Kelly, "All-optical Full Adder with Bit-Differential Delay", *Optics Communications*, vol. 168, no. 1-4, pp. 89–93, 1999.

[204] A. J. Poustie, K. J. Blow, A. E. Kelly, and R. J. Manning, "All-optical Binary Counter", *Proc ECOC 1999*, pp. 246–7 vol.1, 1999.

[205] K. L. Hall, J. P. Donnelly, S. H. Groves, C. I. Fennelly, R. J. Bailey, and A. Napoleone, "40-Gbit/s All-optical Circulating Shift Register with an Inverter", *Optics Letters*, vol. 22, no. 19, pp. 1479–81, 1997.

[206] A. J. Poustie, R. J. Manning, and K. J. Blow, "All-optical Circulating Shift Register using a Semiconductor Optical Amplifier in a Fibre Loop Mirror", *IEE Electronics Lett.*, vol. 32, no. 13, pp. 1215 –1216, 1996.

[207] R. J. Manning, K. J. Blow, and D. Nesset, "Semiconductor Optical Amplifier based Nonlinear Optical Loop Mirror with feedback: Two Modes of Operation at high Switching Rates", *Optics Communications*, vol. 157, no. 1-6, pp. 45–51, 1998.

[208] R. J. Manning, I. D. Phillips, A. D. Ellis, A. E. Kelly A. J., Poustie, and K. J. Blow, "All-optical Clock Division at 40 GHz using Semiconductor Optical Amplifier based Nonlinear Interferometer", *IEE Electronics Lett.*, vol. 35, no. 10, pp. 827 –829, 1999.

[209] R. J. Manning and A. J. Poustie, "40 GHz All-optical Shift Register with Semiconductor Optical Amplifiers for Switching and Feedback", *Techn. Digest OFC 2001*, vol. 54, no. 1, pp. MB3/1–MB3/3, 2001.

[210] A. J. Poustie and A. E. Kelly, "All-optical Parity Checker with Bit-Differential Delay", *Optics Communications*, vol. 162, no. 1-3, pp. 37–43, 1999.

[211] Y. Liu, M. T. Hill, H. de Waardt, G. D. Khoe, D. Lenstra, and H. J. S. Dorren, "All-optical Flip-Fflop Memory based on Two Coupled Polarisation Switches", *IEE Electronics Lett.*, vol. 38, no. 16, pp. 904–906, 2002.

[212] M. T. Hill, H. de Waardt, G. D. Khoe, and H. J. S. Dorren, "All-optical Flip-Flop based on Coupled Laser Diodes", *IEEE J. Quantum Electronics*, vol. 37, no. 3, pp. 405 –413, 2001.

[213] Y.-I. Kim, J.H. Kim, S. Lee, D. H. Woo, S. H. Kim, and T.-H. Yoon, "Broad-Band All-Optical Flip-Flop Based on Optical Bistability in an Integrated SOA/DFB-SOA", *IEEE Photonics Techn. Letters*, vol. 16, no. 2, pp. 398–400, 2004.

[214] M. Takenaka and Y. Nakano, "Realization of All-optical Flip-Flop using Bistable laser diode with Nonlinear Directional Coupler", *IEEE 18th International Semiconductor Laser Conference, 2002*, pp. 121–122, 2002.

[215] C. Janz, B. Dagens, A. Bisson, F. Poingt, F. Pommereau, F. Gaborit, I. Guillemot, and M. Renaud, "Integrated All-active Mach-Zehnder Wavelength Converter with Record Signal Sensitivity and Large Dynamic Range at 10 Gbit/s", *Techn. Digest OFC/IOOC 1999,*, pp. 30 –32, vol.4, 1999.

[216] D. Cotter J. K., Lucek, M. Shabeer, K. Smith, D. C. Rogers, D. Nesset, and P. Gunning, "Self-routing of 100 Gbit/s Packets using 6 bit 'keyword' Address Recognition", *IEE Electronics Lett.*, vol. 31, no. 17, pp. 1475 –1476, 1995.

[217] P. Öhlen, B. E. Olsson, and D. J. Blumenthal, "All-optical Header Erasure and penalty-free Rewriting in a Fiber-based High-speed Wavelength Converter", *IEEE Photonics Techn. Letters*, vol. 12, no. 6, pp. 663 –665, 2000.

[218] N. Bahlmann, M. Lohmeyer, M. Wallenhorst, H. Dotsch, and P. Hertel, "An Improved Design of an Integrated Optical Isolator based on Non-reciprocal Mach-Zehnder interferometry", *Optical and Quantum Electronics*, vol. 30, no. 6, pp. 323–334, 1998.

[219] D. Wolfson and K. E. Stubkjaer, "Bit error rate Assessment of 20 Gbit/s All-optical Wavelength Conversion for Co- and Counter-directional Coupling scheme", *IEE Electronics Lett.*, vol. 34, no. 23, pp. 2259 –2261, 1998.

[220] J. N. Fehr, M. A. Dupertuis, T. P. Hessler, L. Kappei, D. Marti, F. Salleras, M. S. Nomura, B. Deveaud, J. Emery, and B. Dagens, "Hot Phonons and Auger Related Carrier Heating in Semiconductor Optical Amplifiers", *IEEE J. Quantum Electronics*, vol. 38, no. 6, pp. 674–681, 2002.

[221] T. Rasmussen, *Integrated Optical structures for optical communications*, PhD thesis, Dept. of Electromagnetic Systems, Technical University of Denmark (FN139), 1994.

[222] S. Ramo, J. R. Whinnery, and T. Van Duzer, *Fields and Waves in Communication Electronics*, Wiley, New York, 1994.